MEDICINE MEETS ENGINEERING

Studies in Health Technology and Informatics

This book series was started in 1990 to promote research conducted under the auspices of the EC programmes' Advanced Informatics in Medicine (AIM) and Biomedical and Health Research (BHR) bioengineering branch. A driving aspect of international health informatics is that telecommunication technology, rehabilitative technology, intelligent home technology and many other components are moving together and form one integrated world of information and communication media. The complete series has been accepted in Medline. Volumes from 2005 onwards are available online.

Volume 133

Recently published in this series

Vol. 132. J.D. Westwood, R.S. Haluck, H.M. Hoffman, G.T. Mogel, R. Phillips, R.A. Robb and K.G. Vosburgh (Eds.), Medicine Meets Virtual Reality 16 – parallel, combinatorial, convergent: NextMed by Design

Vol. 131. R. Latifi (Ed.), Current Principles and Practices of Telemedicine and e-Health

Vol. 130. J.I. Westbrook, E.W. Coiera, J.L. Callen and J. Aarts (Eds.), Information Technology in Health Care 2007 – Proceedings of the 3rd International Conference on Information Technology in Health Care: Socio-technical Approaches

Vol. 129. K.A. Kuhn, J.R. Warren and T.-Y. Leong (Eds.), MEDINFO 2007 – Proceedings of the 12th World Congress on Health (Medical) Informatics – Building Sustainable Health Systems

Vol. 128. P.J. Murray, H.-A. Park, W.S. Erdley and J. Kim (Eds.), Nursing Informatics 2020: Towards Defining Our Own Future – Proceedings of NI2006 Post Congress Conference

Vol. 127. L. Bos and B. Blobel (Eds.), Medical and Care Compunetics 4

Vol. 126. N. Jacq, H. Müller, I. Blanquer, Y. Legré, V. Breton, D. Hausser, V. Hernández, T. Solomonides and M. Hofmann-Apitius (Eds.), From Genes to Personalized HealthCare: Grid Solutions for the Life Sciences – Proceedings of HealthGrid 2007

Vol. 125. J.D. Westwood, R.S. Haluck, H.M. Hoffman, G.T. Mogel, R. Phillips, R.A. Robb and K.G. Vosburgh (Eds.), Medicine Meets Virtual Reality 15 – *in vivo*, *in vitro*, *in silico*: Designing the Next in Medicine

ISSN 0926-9630

Medicine Meets Engineering

Proceedings of the 2nd Conference on Applied Biomechanics
Regensburg

Edited by

Joachim Hammer

University of Applied Sciences Regensburg, Faculty of Mechanical Engineering

Michael Nerlich

University of Regensburg, Department for Trauma and Surgery

and

Sebastian Dendorfer

University of Applied Sciences Regensburg, Faculty of Mechanical Engineering

IOS Press

Amsterdam • Berlin • Oxford • Tokyo • Washington, DC

ISBN 978-1-58603-828-1
Library of Congress Control Number: 2007943786

Publisher
IOS Press
Nieuwe Hemweg 6B
1013 BG Amsterdam
Netherlands
fax: +31 20 687 0019
e-mail: order@iospress.nl

Distributor in the UK and Ireland
Gazelle Books Services Ltd.
White Cross Mills
Hightown
Lancaster LA1 4XS
United Kingdom
fax: +44 1524 63232
e-mail: sales@gazellebooks.co.uk

Distributor in the USA and Canada
IOS Press, Inc.
4502 Rachael Manor Drive
Fairfax, VA 22032
USA
fax: +1 703 323 3668
e-mail: iosbooks@iospress.com

PRINTED IN THE NETHERLANDS

Medicine Meets Engineering
J. Hammer et al. (Eds.)
IOS Press, 2008

Preface

Biomedical Engineering is defined as the science that integrates medical and engineering sciences to improve diagnosis and treatment of patients. Only by this integration can progress be achieved. Both medical and engineering sciences comprise a huge diversity in topics, so understandably, in combining these two areas of science, Biomedical Engineering is even more huge. If research between several medical disciplines is called multidisciplinary it is rational to call research in Biomedical Engineering megadisciplinary. Thanks to this megadisciplinary approach many breakthroughs can be achieved. More and more research groups are realising this and starting new research projects, resulting in a rapid increase in knowledge, which can only benefit the main aim of Biomedical Engineering, improving the diagnosis and treatment of patients when it is spread and applied.

Conferences are a valuable means in distributing knowledge. Since Biomedical Engineering is a multidisciplinary science it is important to reach both medical and engineering specialists. This requirement is very difficult to realise as both research groups often focus only on their own research field, which hinders the essential integration of knowledge.

The 2nd Regensburg Applied Biomechanics conference is special in that it realised both the distribution of new knowledge and the essential integration of medical and engineering specialists. The first step for that was to have not one, but two, congress chairmen, one medical and one technical: Prof. Nehrlich and Prof. Hammer. They made a unique program around the central topic ‘Applied Biomechanics’. This topic was well chosen, because it was challenging for and could be understood by both groups, which is not obvious, since both groups have a different culture and language. It also attracted many young scientists and since they are the future, this was very good to note.

The conference dealt with the latest results in applied biomechanics, ranging from fundamental bone strength properties via bone remodelling phenomena to new implants that replace lost human functions. Also, new research areas like robot surgery and tissue engineering were discussed.

This conference is an excellent example of the activities of ESEM, the European Society for Engineering and Medicine that aims at stimulating and integrating research in Biomedical Engineering. One of the ways ESEM is stimulating research is by awarding excellent presentations, and during this conference an ESEM scientific award was issued.

The only drawback in organising a successful conference is that everybody expects that next year it will be organised again…

Prof. Dr. Bart Verkerke
ESEM president

European Society for

Engineering

and

Medicine

This page intentionally left blank

Contents

Medicine Meets Engineering
J. Hammer et al. (Eds.)
IOS Press, 2008

Biomechanical characterisation of osteosyntheses for proximal femur fractures: helical blade versus screw

Amir A. AL-MUNAJJED [a,1], Joachim HAMMER [a], Edgar MAYR [b], Michael NERLICH [c] and Andreas LENICH [b,c]

[a] *University of Applied Sciences Regensburg, Labor für Werkstoffkunde und Metallographie, Germany*

[b] *Clinical Centre Augsburg, Department for Trauma and Reconstructive Surgery, Germany*

[c] *Clinical Centre University of Regensburg, Department for Trauma and Surgery, Germany*

Abstract. Proximal femur fractures are of main concern for elderly and especially osteoporotic patients. Despite advanced implant modifications and surgical techniques, serious mechanical complication rates between 4 - 18% are found in conventional osteosyntheses of proximal femur fractures. Clinical complications such as the rotation of the femoral head and the cut-out phenomenon of the fracture fixation bolt are often diagnosed during post-operative treatments. Therefore, efforts in new intramedulary techniques focus on the load bearing characteristics of the implant by developing new geometries to improve the implant-tissue interface. The objective of this investigation was to analyse the osteosynthesis/femur head interaction of two commonly used osteosyntheses, one with a helical blade and the other one with a screw design under different loading conditions.

For the comparative investigation the helical blade of the Proximal Femur Nail Antirotation was investigated versus the screw system of the Dynamic Hip Screw. After implantation in a femoral head the loads for rotational overwinding of the implants were analysed. Pull-out forces with suppressed rotation were investigated with analysis of the influence of the previous overwinding. All investigations were performed on human femoral heads taken of patients with average age of 70.3 $\pm$ 11.8. The bone mineral densities of the human specimens were detected by QCT-scans (average BMD: 338.9 $\pm$ 61.3 $\frac{mg}{cm^3}$). Prior to cadaveric testing the experimental set-up was validated and special influences were analysed by the use of synthetic foam blocks (Sawbone). The helical blade showed a significant higher torque for the rotation of the femoral head compared to the screw system. The pull-out forces of the blade were substantially lower than of the comparative screw.

Taken together the helical blade showed a higher potential of rotational stability, but after a rotation the lower pull-out forces demonstrate a higher degree of damage to the femoral head.

Keywords. proximal femur fractures, osteosynthesis, helical blade

[1]Corresponding Author: Amir Al-Munajjed, Royal College of Surgeons in Ireland, Department of Anatomy, 123 St. Stephens Green, Dublin 2, Ireland; E-mail: aalmunajjed@rcsi.ie

1. Introduction

Trochanteric fractures are a main concern in our society [1]. A significant morbidity and mortality in elderly patients due to hip fractures is caused by a decrease in quality of the functional structure of the spongious bone [2, 3]. Due to this decrease higher demands are placed on fracture fixation implants in the proximal femur. Continuous improvements have been made in proximal femur implants since their inception. While first fracture healing processes were supported by Kirschner wires [4], side plates, screw bolts and static plates [1], the need for special proximal femur osteosyntheses was of special interest. The use of angled plates and extramedular ostheosynthesis also showed material and clinical problems [5]. Intramedular osteosynthesis reduced due to their favorable working point the rotational loads on the implant [6]. Furthermore, intramedullary fixation of proximal femur fractures is a minimally invasive technique that preserves the blood supply of the periosteum and soft tissue while simultaneously providing strong fixation [1]. It is also recommended for fracture treatments in osteoporotic bone because its central location distributes loads uniformly [1]. Next to these theoretical advantages of intramedullary osteosyntheses they also show better clinical results [7] and have gained popularity [8]. An additional sliding system in the implant enables the possibility of closing the fracture gap during the first load applications to the femur. Experimental and clinical results of sliding nails are often discussed in literature. Friedl and Clausen [7] compared in vitro results of the Dynamic Hip Screw (DHS, Synthes), the Proximal Femur Nail (PFN, Synthes), the Gamma Nail (GN, Stryker) and the Gliding Nail (Plus Orthopedics). Simmermacher *et al.* [9] described differences and effects in the treatment of femoral fractures by GN versus the PFN [9]. Presently no clinical or biomechanical investigation has shown one intramedular osteosyntheses significantly better than any other [10, 11]. There are still common clinical complications with the use of sliding nails often concerning the undefined point of load transfer and the gliding mechanism [12]. The present focus of investigations is to replace the screw design of the fracture fixation bolt with a helical blade as seen in the Trochanter Fixation Nail (TFN, Synthes) and the novel Proximal Femur Nail Antirotation (PFNA, Synthes).

In documented proximal femur fractures, serious complication rates between 4 - 18% were reported, regarding only mechanical failures [9, 13-16]. The major post-operative complication reported is the cutting-out of the head and neck, whereby the osteosynthesis breaks through the corticalis of the femoral head [13, 17]. This can cause severe injuries in hard as well as in soft tissues surrounding the hip joint. However, a rotation of the femoral head prior to the cutting-out has been investigated in a previous study assuming the cause for implant failure is the destruction of the trabecular bone due to the rotation of the femoral head [18]. Eccentric implantations of osteosyntheses within the surgical tolerance due to differences in the individual geometry of proximal femurs can cause high rotational moments in the hip joint and therefore on the fixation of proximal femur fractures [14, 18, 19]. These torques are high enough to lead to a rotation of the femoral head [14].

The objective of this investigation was to characterise two different fracture fixation bolts, one with a helical blade and one with a screw design. In a first experiment the rotational stability of the two osteosyntheses was analysed by overwinding the implanted blade and screw. Afterwards the implants were pulled out to investigate the axial stability as an index for the destruction caused by the rotation.

2. Material and Methods

2.1. Osteosyntheses

Modern osteosyntheses for proximal femur fractures usually consist of an intramedular nail, a bolt for the fixation of the femoral head segment and a distal fixation screw. In this investigation the helical blade of the Proximal Femur Nail Antirotation (PFNA) and the screw of the Dynamic Hip Screw (DHS) have been characterised, figure 1. All are part of sliding nails with a special device for fixing the axial rotation. Both systems have only one bolt for the stabilization of the fracture segments. The length of the thread of the PFNA is approximately 32mm; the DHS' thread is 23mm long. The manuals of the DHS instruct a pre-drilling before implantation.

Figure 1. Bolt for fixation of the femoral head segment of the Dynamic Hip Screw (DHS, Synthes) and the Proximal Femur Nail Antirotation (PFNA, Synthes).

2.2. Specimen

In order to examine the reproducibility of the investigated implant characterisation, two types of material were used, a synthetic foam block (Sawbone) with the density of $200\frac{mg}{cm^3}$ (dimension: 30mm x 30mm x 40mm) and human bone. The biological specimen used in this study was fresh frozen human femoral heads (n=16) obtained from patients who underwent a total hip replacement. The individual density of the human material was measured with a QCT-scanner (XCT 900 Stratec). Because of the individual local densities the zone of the measured density was narrowed to the central femoral head (figure 2a.)). Measurements were made at three different depths (figure 2b.)). The measurements and following investigations were made after a defrosting period of 12 hours.

2.3. Experimental modus

The human specimens were prepared for the tests by removing the soft tissue from the cortical bone. The femoral neck was cut using a handsaw to get a defined plane surface. The femur heads were fixed in a custom made embedding system with Moldostone cement (Heraeus Kulzer Dentist Product Devision), EN 23873 with a compressive strength

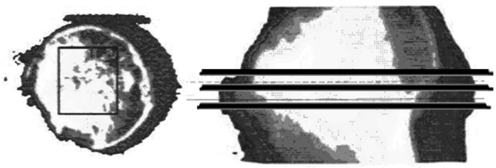

Figure 2. Bone mineral density measurement with a QCT-scanner (XCT 900 Stratec) with the (a) limitation of each measuring zone to the centre of the femoral head and (b) the three steps of the investigated zones

of 54 $\frac{N}{mm^2}$. The dry out time of the cement was 120 Minutes. The special conical geometry of the embedding system forced a form- and pressfit of the specimen in the system.

The characterisation of the blade and the screw stabilisation in synthetic foam blocks and human bone was divided in three consecutive sequences. First the osteosyntheses were implanted into the femoral head and neck. Then the osteosyntheses were rotated in the femur. At last the osteosyntheses were extracted out of the femur. Osteosyntheses were implanted 32mm into the femoral head as per manufacturers' manuals. A forced axial rotation of the femoral head was executed with a speed of $1^o/sec$. During the rotation the axial movement of the embedded sample was blocked. This experiment was divided in left (+60^o) and right (-60^o) rotations (figure 3). After 60^o of rotation the movement was stopped. The last step was the complete axial extraction of the osteosyntheses out of the femoral head (figure 3). No rotation of the implant or the specimen was allowed. During these three steps displacement [mm], angle [^{o}], force [N] and torque [Nm] in a 3-Dimension coordinate system were measured. One mechanical setup was designed for all experiments. All tests were performed in a biaxial servo hydraulic test system by Instron with an Interlaken controller, an Instron load and torque cell.

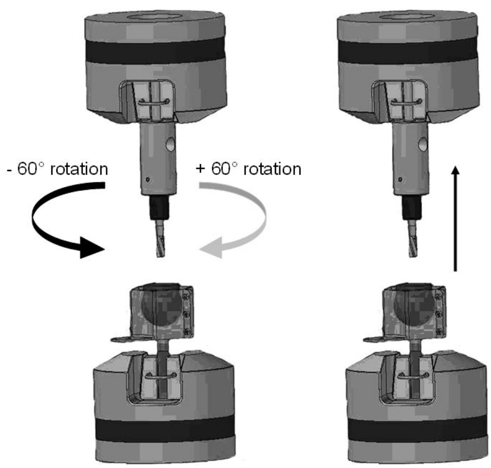

Figure 3. Schematic experimental modus of the mechanical tests for +60^o and -60^o rotation and pull out of the helical blade and screw after rotation.

2.4. Statistical analysis

All data was subjected to statistical analyses with SPSS. Correlations between variables were evaluated using one-way ANOVA with Tukey posthoc test, significance was set as $p < 0.05$.

3. Results

3.1. Bone mineral density

The average bone mineral density (BMD) of the femoral heads was 338.9 ± 61.3 mg/cm3 (n = 16). The average age of the patients was 70.3 ± 11.8 with a male- female distribution of 7 - 9 in total.

3.2. Synthetic foam tests

In the synthetic foam blocks the helical blade showed a maximum of 8Nm in the mean torque at 20^o in $+60^o$ direction and 10Nm at 10^o in -60^o direction, figure 4. After an initial increase, the screw showed a constant torque of 2.9Nm in the $+60^o$ and 4.3Nm in the -60^o direction (figure 4).

The maximum tensile forces of the helical blade were 0.5kN after $+60^o$ rotation and 0.2kN after -60^o rotation (figure 5). The maximum for the screw design were 1.4kN after $+60^o$ rotation and 1.3kN after the -60^o rotation (figure 5).

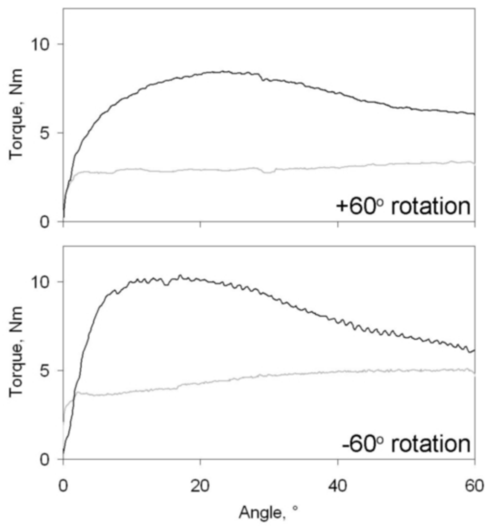

Figure 4. Torque-angle diagram of the helical blade and the screw in synthetic foam blocks at (a) $+60^o$ (n=6) and (b) -60^o rotation (n=6).

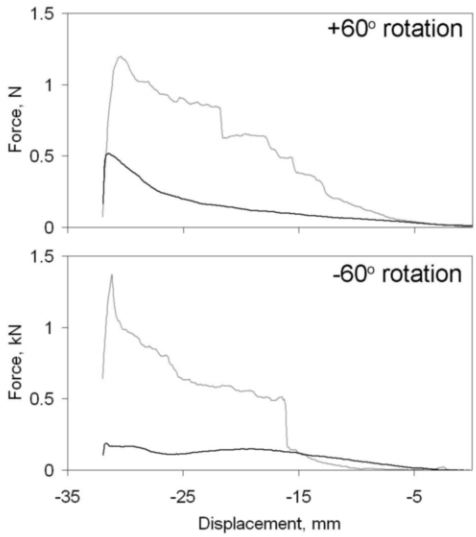

Figure 5. Force-displacement diagram of the helical blade and the screw in synthetic bone after (c) +60^o (n=6) and (d) -60^o rotation (n=6).

3.3. *Cadaveric femoral tests*

In the cadaveric bone specimen, the helical blade showed a maximum of 12Nm in the mean torque at 30^o in the +60^o, and 20Nm at 30^o in the -60^o direction, figure 6. The torque decreased after the maxima at approximately 30^o. The screw design showed a constant linear behavior after an initial slope. A mean torque of up to 6Nm for both

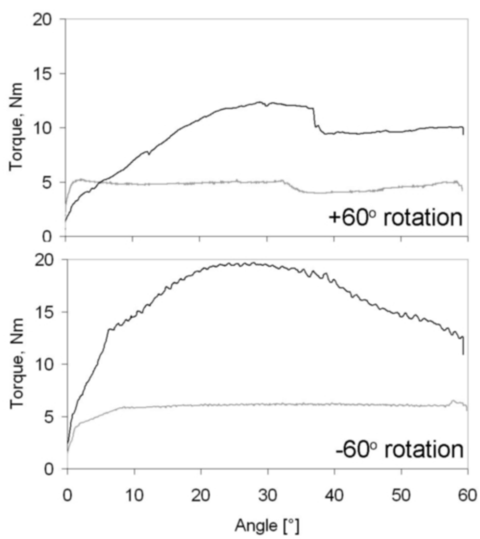

Figure 6. Torque-angle diagram of the helical blade and the screw in human cadaveric bone at (a) +60^o (n=4) and (b) -60^o rotation (n=4)

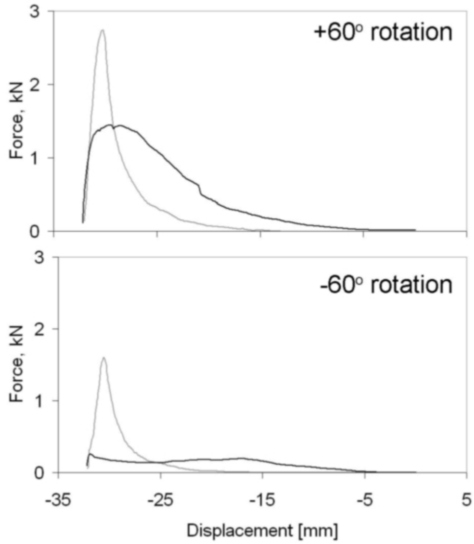

Figure 7. Force-displacement diagram of the helical blade and the screw in human bone after (c) +60^o (n=4) and (d) -60^o rotation (n=4).

directions could be seen, figure 6.

A maximum of the mean tensile forces for the helical blade of 0.3kN after the +60^o rotation and 1.4kN after the -60^o rotation was measured, respectively. The maximum of the mean values for the screw after the +60^o rotation was 2.7N and 1.6kN after the -60^o rotation (figure 7). Characteristically for the investigated implants the loads decreased after an initial peak to 0 N.

4. Discussion

Proximal femur fractures still cause a high rate of serious complications and a significant rate of morbidity and mortality in elderly patients [2, 3]. Many different implant types are currently used to stabilise these fractures [1]. The present focus of osteosynthese such as the TFN and the PFNA is to replace the screw design of the fracture fixation bolts with helical blades to ensure a better rotational stability of the femoral head. The objective of this investigation was to analyse two different fracture fixation bolts that are currently used in various clinics. The performance of a fracture fixation bolt with a helical blade and a bolt with a screw has been investigated under rotational and axial loadings. Taken together, the results indicate that the helical blade shows a better fixation stability for proximal femur fracture compared to the screw design, particularly in rotational failure .

Cadaveric tests indicated that the rotational stability of the helical blade was significantly better than the screw. Due to its geometrical difference the blade showed values 2 to 4 times higher than the screw. However a significant difference in the rotational direction was seen using the blade. The helical blade showed a torque almost twice as high in -60^o compared to the +60^o direction. Tests in synthetic foam blocks also showed a significant difference in the results. The experiments indicated that in the -60^o direction the helical blade cut further into the trabecular bone and, therefore increased the stability of the fixation, while in +60^o direction the contact between bone and implant was lost and the implant became loose.

Pull out tests indicated that after a rotation of 60^o in both directions the blade showed a significantly lower axial stability. The screw showed tensile forces 2 to 7 times higher than the helical blade. Both cadaveric and synthetic bone tests indicated a significant influence of the previous rotation direction for the helical blade on the tensile forces. This was also supported by the rotational results. Morphology and architecture of the trabecular meshwork gives the stability in the bone of the proximal femur [13]. By overwinding the implant in the femoral head, this spongious structure is destroyed. Experiments conducted into the extraction of the implant provide a measure of the degree of structural damage to the trabecular bone. High forces for the extraction show a minimal destruction of bone material during insertion. Low forces testify a high structural damage of the femoral head.

The trabecular morphology and quality of the spongious tissue in the femur head plays a major role in the load bearing capacity of implants [14]. The bone mineral density of the specimens was $338.9 \pm 63 \frac{mg}{cm^3}$, which is only about half of the typical value reported for the femoral neck of $560 \frac{mg}{cm^3}$ with a range from 260 - $750 \frac{mg}{cm^3}$ [13]. The average age of 74 ± 13 years in Morgan *et al.* is similar to the present investigation of 70.3 $\pm$ 11.8 years. The reason for this could be seen in the fact that the specimens were taken from patients who received a total hip replacement and therefore serious bone resorption processes might have already been acting. Nevertheless, the use of this biomaterial is still reasonable and practicable because the patients treated with these osteosyntheses are expected to have comparable material properties. The variations in the experimental results indicate the possible range which is observed in every day clinical practice. A full relation between local mineral bone density and mechanical properties could not been found. Concepts of skeletal structure-function relationships have been investigated with stiffness optimising [15] or by strain energy density optimising [16]. A prior BMD measurement with QCT to the implantation of an osteosynthesis showed no significant relevance to the stability of the implant in the fracture. A detailed investigation of the trabecular structure seems to be more effective, in particular the point transmission of force on the trabecular themselves. The experiments with the synthetic Sawbone foam blocks (density of 200 $\frac{mg}{cm^3}$) proved the accuracy and reproducibility of the test set-up, although the values of the maximum tensile forces and torques are not comparable to fresh biological tissue. To examine real clinical complications, the use of human bone is still necessary.

In a perfect environment no torques act at the centre of the hip joint. All forces are directed straight to the centre of the femoral head and therefore no lever arms act. Eccentric positions of the fracture fixation bolts however can cause lever arms. According to these static results an eccentricity of the helical blade or screw in the femoral head is critical for rotational failure under daily activities. This clearly demonstrates the importance of highly precise positioning of the osteosynthesis in the middle of the femoral head [17]. The helical blade showed an enormous higher potential for rotational stability. This investigation points out the values of structural failures at static loads. This effect becomes even more pronounced under cyclic loading and results in dramatically reduced failure loads [18].

5. Conclusion

Clinical complications due to implant failure are caused by damage of the trabecular structures in the bone due to overloading, fatigue or movements of implants in the femoral head. This investigation successfully investigated the loads for stable static conditions of helical blades and screws as a first guide line. Two common osteosyntheses for proximal femur fractures, the PFNA with a helical blade and the DHS with a screw were analysed. As most loading cases in the human body are not static, further dynamic investigations have to be performed to better understand the behaviour of proximal femur osteosyntheses. The results show in particular a better rotational stability of the helical blade in human bone compared to the screw.

Acknowledgements

We are grateful for the support of implants and implantation devices from Synthes, Switzerland. We also appreciate the helpful support from Felix Häussler (Clinical Centre Augsburg) and Niamh Plunkett (Royal College of Surgeons in Ireland).

References

[1] Curtis R, Goldhahn J, Schwyn R, Regazzoni P, Suhm N (2005) Fixation principles in metaphyseal bone–a patent based review. Osteoporos Int 16 Suppl 2:S54-64
[2] Johnell O, Kanis J (2005) Epidemiology of osteoporotic fractures. Osteoporos Int 16 Suppl 2:S3-7
[3] Dennison E, Cooper C (2000) Epidemiology of osteoporotic fractures. Horm Res 54 Suppl 1:58-63
[4] Kirschner R (1971) [The use of internal wire fixation for vertebral fractures to restore the natural stability of the cervical vertebrae]. Z Orthop Ihre Grenzgeb 108:563-567
[5] Sanders R, Regazzoni P, Ruedi TP (1989) Treatment of supracondylar-intracondylar fractures of the femur using the dynamic condylar screw. J Orthop Trauma 3:214-222
[6] Steinberg EL, Blumberg N, Dekel S (2005) The fixion proximal femur nailing system: biomechanical properties of the nail and a cadaveric study. J Biomech 38:63-68
[7] Friedl W, Clausen J (2001) [Experimental examination for optimized stabilisation of trochanteric femur fractures, intra- or extramedullary implant localisation and influence of femur neck component profile on cut-out risk]. Chirurg 72:1344-1352
[8] Rao JP, Banzon MT, Weiss AB, Rayhack J (1983) Treatment of unstable intertrochanteric fractures with anatomic reduction and compression hip screw fixation. Clin Orthop Relat Res:65-71
[9] Simmermacher R., Ch. Wvd (2005) Trochanteric hip fractures - Gamma nail versus proximal femoral nail. Orthopedic trauma dir 03:11-17
[10] Bridle SH, Patel AD, Bircher M, Calvert PT (1991) Fixation of intertrochanteric fractures of the femur. A randomised prospective comparison of the gamma nail and the dynamic hip screw. J Bone Joint Surg Br 73:330-334
[11] Mahomed N, Harrington I, Kellam J, Maistrelli G, Hearn T, Vroemen J (1994) Biomechanical analysis of the Gamma nail and sliding hip screw. Clin Orthop Relat Res:280-288
[12] Schneider E, Michel MC, Genge M, Zuber K, Ganz R, Perren SM (2001) Loads acting in an intramedullary nail during fracture healing in the human femur. J Biomech 34:849-857
[13] Werner-Tutschku W, Lajtai G, Schmiedhuber G, Lang T, Pirkl C, Orthner E (2002) [Intra- and perioperative complications in the stabilization of per- and subtrochanteric femoral fractures by means of PFN]. Unfallchirurg 105:881-885
[14] Lenich A, Fierlbeck J, Al-Munajjed A, Dendorfer S, Mai R, Fuchtmeier B, Mayr E, Hammer J (2006) First clinical and biomechanical results of the Trochanteric Fixation Nail (TFN). Technol Health Care 14:403-409

[15] Baumgaertner MR, Curtin SL, Lindskog DM (1998) Intramedullary versus extramedullary fixation for the treatment of intertrochanteric hip fractures. Clin Orthop Relat Res:87-94

[16] Steindl A, Schörghuber L (2000) Treatment of per- and subtrochanteric fractures by gliding nail and PFN - early results and analysis of problems. In: Osteosynthese international. p 86-94

[17] Baumgaertner MR, Curtin SL, Lindskog DM, Keggi JM (1995) The value of the tip-apex distance in predicting failure of fixation of peritrochanteric fractures of the hip. J Bone Joint Surg Am 77:1058-1064

[18] Lenich A, Mayr E, Ruter A, Mockl C, Fuchtmeier B (2006) First results with the Trochanter Fixation Nail (TFN): a report on 120 cases. Arch Orthop Trauma Surg

[19] Park SY, Park J, Rhee DJ, Yoon HK, Yang KH (2007) Anterior or posterior obliquity of the lag screw in the lateral view–does it affect the sliding characteristics on unstable trochanteric fractures? Injury 38:785-791

[20] Morgan EF, Bayraktar HH, Keaveny TM (2003) Trabecular bone modulus-density relationships depend on anatomic site. J Biomech 36:897-904

[21] Frigg R (2004) Product development for osteoporosis - Key factors that increase the stability of an osteosynthesis implant in osteoporotic bone. In: AO-Dialogue. p 23

[22] Fyhrie DP, Vashishth D (2000) Bone stiffness predicts strength similarly for human vertebral cancellous bone in compression and for cortical bone in tension. Bone 26:169-173

[23] Carter DR, Fyhrie DP, Whalen RT (1987) Trabecular bone density and loading history: regulation of connective tissue biology by mechanical energy. J Biomech 20:785-794

[24] Cleveland M, Bosworth DM, Thompson FR, Wilson HJ, Jr., Ishizuka T (1959) A ten-year analysis of intertrochanteric fractures of the femur. Am J Orthop 41-A:1399-1408

[25] Haddock SM, Yeh OC, Mummaneni PV, Rosenberg WS, Keaveny TM (2004) Similarity in the fatigue behavior of trabecular bone across site and species. J Biomech 37:181-187

Medicine Meets Engineering
J. Hammer et al. (Eds.)
IOS Press, 2008

DEVELOPMENT OF A COLLAGEN CALCIUM-PHOSPHATE SCAFFOLD AS A NOVEL BONE GRAFT SUBSTITUTE

Amir A. AL-MUNAJJED [a,b,1], John P. GLEESON [a,b] and Fergal J. O'BRIEN [a,b]
[a] *Royal College of Surgeons in Ireland, Department of Anatomy, Ireland*
[b] *Trinity College Dublin, Trinity Centre of Bioengineering, Ireland*

Abstract. Previous investigations have shown that collagen shows excellent biological performance as a scaffold for tissue engineering. As a primary constituent of bone and cartilage, it demonstrates excellent cell adhesion and proliferation. However, in bone tissue engineering, it has insufficient mechanical properties for implantation in a load-bearing defect. The objective of this preliminary study was to investigate the possibility of developing a collagen/calcium-phosphate composite scaffold which would combine the biological performance and the high porosity of a collagen scaffold with the high mechanical stiffness of a calcium-phosphate scaffold.
Collagen scaffolds were produced by a lyophilisation process from a collagen slurry. The scaffolds were soaked for different exposure times in solutions of 0.1 M, 0.5 M or 1.0 M $NaNH_4HPO_4$ followed by 0.1 M, 0.5 M or 1.0 M $CaCl_2$. Mechanical tests of each scaffold were performed on a uniaxial testing system. Young's moduli were determined from stress-strain curves. The pore structure and porosity of the scaffolds were investigated using micro-computed tomography. A pure collagen scaffold served as a control.
All scaffolds showed a significantly increased compressive stiffness relative to the pure collagen scaffolds. The exposure to the 0.5 M solutions showed significantly superior results compared to the other groups. Analysis of the pore structure indicated a decrease in the overall porosity of the composite scaffolds relative to the controls. Regarding mechanical stiffness and porosity, scaffolds after 1 hour exposure to the 0.5 M solutions showed the best properties for bone tissue engineering. Further work will involve producing a scaffold with a more homogeneous calcium phosphate distribution.

Keywords. scaffold design, collagen, calcium phosphate, composite

1. Introduction

Every year, up to 4 million bone replacement procedures are performed worldwide which require the use of either a bone graft or bone graft substitute. The most common situation

[1]Corresponding Author: Amir Al-Munajjed, Royal College of Surgeons in Ireland, Department of Anatomy, 123 St. Stephens Green, Dublin 2, Ireland; E-mail: aalmunajjed@rcsi.ie

is whereby bone is taken from the patient‘s own body and re-implanted, namely an autograft. However, there is a limited amount of bone which can be removed from a particular donor site and extra invasive surgery needs to be performed. Another option is the use of an allograft whereby bone is removed from an organ donor. The drawbacks with this approach include a risk of infectious disease being transmitted and fewer growth factors present to stimulate the growth of new bone as the graft does not contain any living cells. Recently the focus has changed to bone tissue engineering.

Scaffolds in tissue engineering must ensure a sufficient porosity and permeability to allow ingrowth of host tissue and nutrient flow through the tissue [1]. The scaffold also requires adequate mechanical integrity to withstand both the implantation procedure and the mechanical forces when implanted in load-baring areas [1, 2 & 3]. Hydroxyapatite and Calcium-Phosphate (CP) scaffolds are commonly used in bone tissue engineering because of their high mechanical stiffness and biocompatibility. However, the rigidity, brittleness and poor resorbability of ceramics have restricted their use in this area. Currently, no final consensus has been reached concerning the question of which substitute graft material might be the best for clinical application [1, 2]. Previous investigations in our laboratory have shown that scaffolds fabricated from collagen, a normal constituent of bone and cartilage, show excellent biological performance, promoting cell adhesion and growth due to their high porosity of 99.5% [4, 5 & 6]. However, they have insufficient mechanical properties for bone tissue engineering. Scaffolds based on CP show excellent mechanical stability for implantation in a load-bearing defect [7, 8]. Therefore combining both materials might produce a scaffold with the optimal properties for bone tissue engineering.

The objective of this preliminary study was to investigate the possibility of developing a collagen/CP composite scaffold by coating collagen scaffolds with CP. The specific goals were (1) to improve the mechanical stiffness of pure collagen scaffolds and (2) to maintain the high porosity and permeability of the composite scaffolds in comparison to the pure collagen scaffolds.

2. Material and Methods

2.1. Fabrication of pure collagen scaffolds

Pure collagen scaffolds were fabricated from a collagen suspension using a freeze drying method that has been previously described [4, 5 & 9]. Briefly, the suspension was produced from microfibrillar type I collagen, isolated from bovine tendon (Integra Life-Sciences, Plainsboro, NJ, USA) and mixed at 15,000 rpm in an overhead blender (IKA Works, Inc., Wilmington, NC, USA). To prevent denaturation of the collagen fibres, the temperature of the suspension was held at 4^{o}C using a cooling system during the blending procedure (Lauda, Westbury, NY, USA). The slurry was poured into a stainless steel tray which was placed into a freeze-dryer (VirTis Co., Gardiner, NY, USA) at room temperature. The temperature was then lowered at a constant cooling rate of 0.9^{o} C/min to the final temperature. The influence of varying freeze-drying temperatures on the pore size of the scaffolds has been previously described [4]. Consequently, a final freeze-drying temperature of -40^{o}C was used to produce scaffolds with a mean pore size of approximately 95 μm [5]. The shelf and chamber temperature were then held constant at the final temperature for 60 minutes to complete the freezing process. The shelf temperature was then ramped up to 0^{o}C for 160 minutes. The ice phase was then sublimated under a vacuum of approximately 200 mTorr at 0^{o}C for 17 hours to produce the porous collagen scaffold.

2.2. Calcium phosphate coating

Calcium chloride ($CaCl_2$) and ammonium sodium hydrogen phosphate ($NaNH_4HPO_4$) (Sigma Aldrich, Germany) solutions were prepared by mixing in Tris buffer at a pH of 7.4 (50 mM Tris, 1% NaN_3) according to Yaylaoglu *et al.*[10]. Three concentrations of each solution were prepared (0.1, 0.5 and 1.0 M). A preliminary investigation showed that a significantly superior CP coating resulted using a process when starting with an initial exposure to $NaNH_4HPO_4$, followed by a second exposure to $CaCl_2$ and repeating these steps [11]. Consequently this treatment was also chosen in this study. Each scaffold was immersed first in the phosphate solution, followed by the calcium chloride solution. This process was then repeated, as seen in Table 1. The influence of the exposure duration was also investigated by using a short exposure of 1 h and a long exposure of 22 h. Thus, in this study three different concentrations, as well as two different exposure times were compared, resulting in six scaffolds (A - F) as demonstrated in Table 1.

Table 1. Explanation of the durations and concentrations for the calcium phosphate coating on the collagen scaffolds.

Exposure	**1^{st} Exposure $NaNH_4HPO_4$**	**2^{nd} Exposure $CaCl_2$**	**3^{rd} Exposure $NaNH_4HPO_4$**	**4^{th} Exposure $CaCl_2$**
Scaffold type (Duration)	**Concentration**	**Concentration**	**Concentration**	**Concentration**
A (1 h)	0.1 M	0.1 M	0.1 M	0.1 M
B (22 h)	0.1 M	0.1 M	0.1 M	0.1 M
C (1 h)	0.5 M	0.5 M	0.5 M	0.5 M
D (22 h)	0.5 M	0.5 M	0.5 M	0.5 M
E (1 h)	1.0 M	1.0 M	1.0 M	1.0 M
F (22 h)	1.0 M	1.0 M	1.0 M	1.0 M

2.3. Mechanical testing

Mechanical characterisation of the scaffolds (n=6) was performed on a uniaxial testing system (Zwick Z005 with a 5 N load cell). Compression tests were performed at room temperature in a water bath after immersion in phosphate buffered saline. Young‘s moduli were determined between strains of 2 and 5% by finding the slope of the interpolated stress-strain curve. Statistical analysis was performed using one-way ANOVA tests from SPSS with the Tukey Post Hoc test. The level for significance was chosen as $p < 0.05$.

2.4. Micro-computed tomography

The three-dimensional structure of the scaffolds (n=2) was analyzed using micro-computed tomography (μ-CT). Scans were performed on a Scanco Medical 40 Micro-

CT system (Bassersdorf, Switzerland) with 70 kVP X-ray source and 112 μA. Morphological calculations were carried out on the reconstructed sections using the standard Scanco software package to calculate the porosity from the total number of voxels.

3. Results

3.1. Mechanical testing

The compressive moduli of the different scaffold variants are shown in Figure 1. All composite scaffolds showed a significantly increased compressive stiffness relative to the pure collagen scaffolds (0.3 kPa) due to the addition of the CP phase.
Increasing the exposure times from 1 to 22 h showed no significant difference between the 0.1 M and the 1.0 M solution treatments. However, a trend of increased stiffness could be seen. This trend was significant for the 0.5 M solutions comparing scaffold C (1 h) and D (22 h).
The scaffolds after the treatment with the 0.5 M solutions showed significantly higher moduli compared to all other groups. In particular, the scaffolds produced after 22 h exposure to the 0.5 M solutions showed the highest compressive moduli.

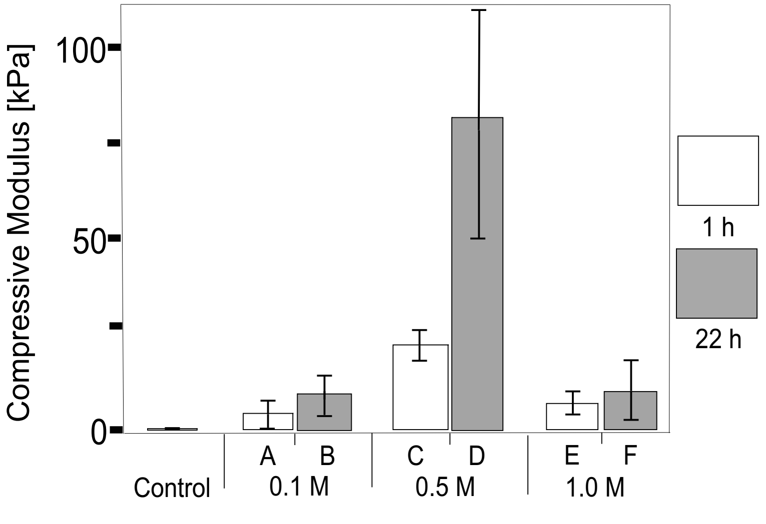

Figure 1. Compressive moduli of pure collagen scaffolds and composite scaffolds after exposure to 0.1 M, 0.5 M and 1.0 M solutions for 1 and 22 h.

3.2. Micro-computed tomography

2D images obtained of the scaffolds using μ-CT show the effect of the different coating treatments (Figure 2, 3 & 4). White areas represent CP, while black areas show regions where no CP is present. All scaffolds showed a CP coating on the collagen struts.

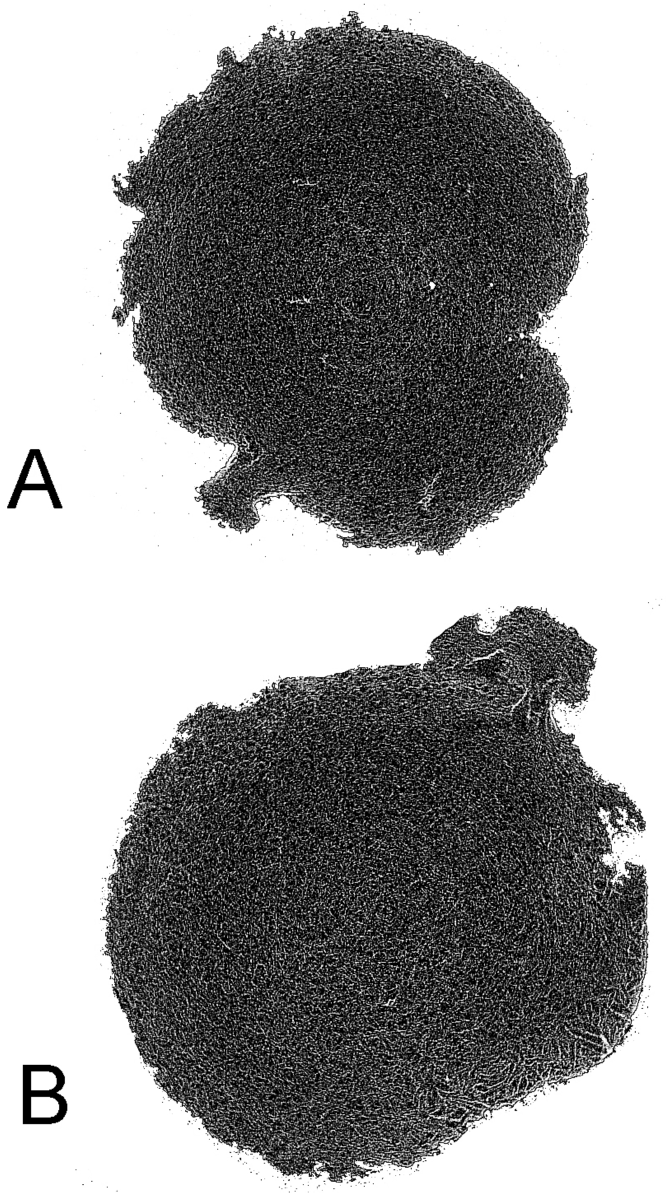

Figure 2. 2D μ-CT slices of Scaffold A (1 h) and B (22 h) after coating with 0.1 M phosphate and calcium solutions.

Figure 2 demonstrates the results of the coating treatments with the 0.1 M concentrations (Scaffold A and B). Both scaffolds show a relatively homogeneous CP distribution. No clear difference is observed between A and B. This is consistent with the mechanical test data.

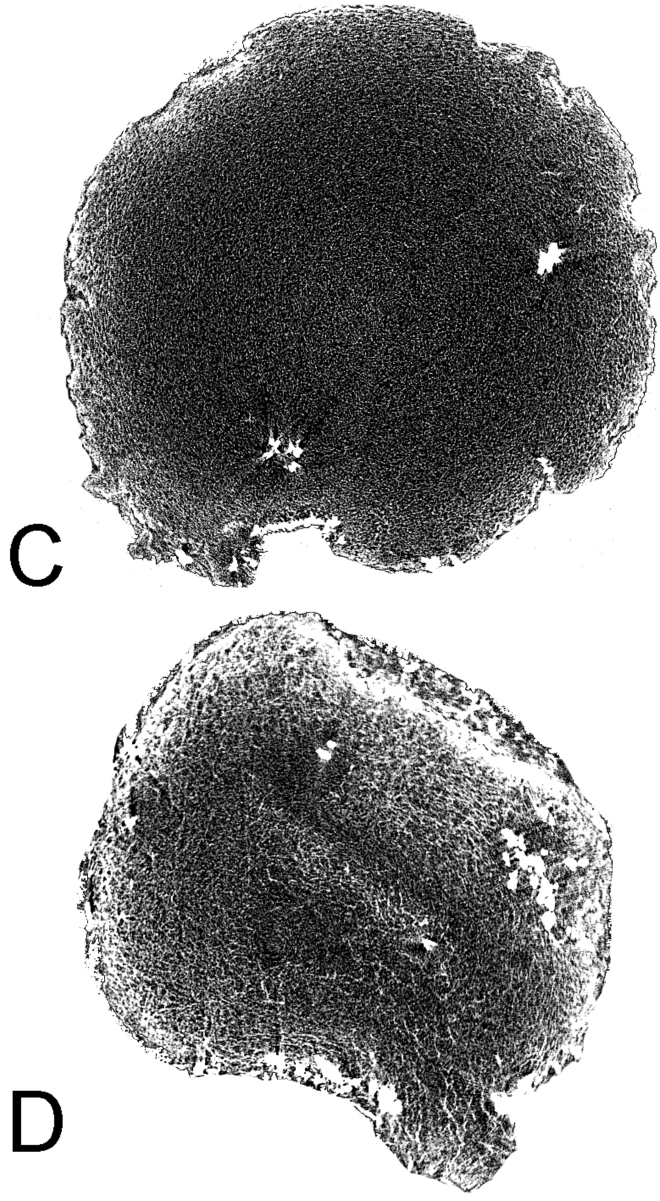

Figure 3. 2D μ-CT slices of Scaffold C (1 h) and D (22 h) after coating with 0.5 M phosphate and calcium solutions.

Figure 3 demonstrates the results of the coating treatments with the 0.5 M concentrations (Scaffold C and D). Both scaffolds showed a more heterogeneous distribution of CP in comparison to Figure 2. Scaffold C had a very homogeneous CP structure in the central area, while in the outer area some concentrated CP amounts can be seen. Scaffold D shows greater levels of localised CP clusters throughout the sample.

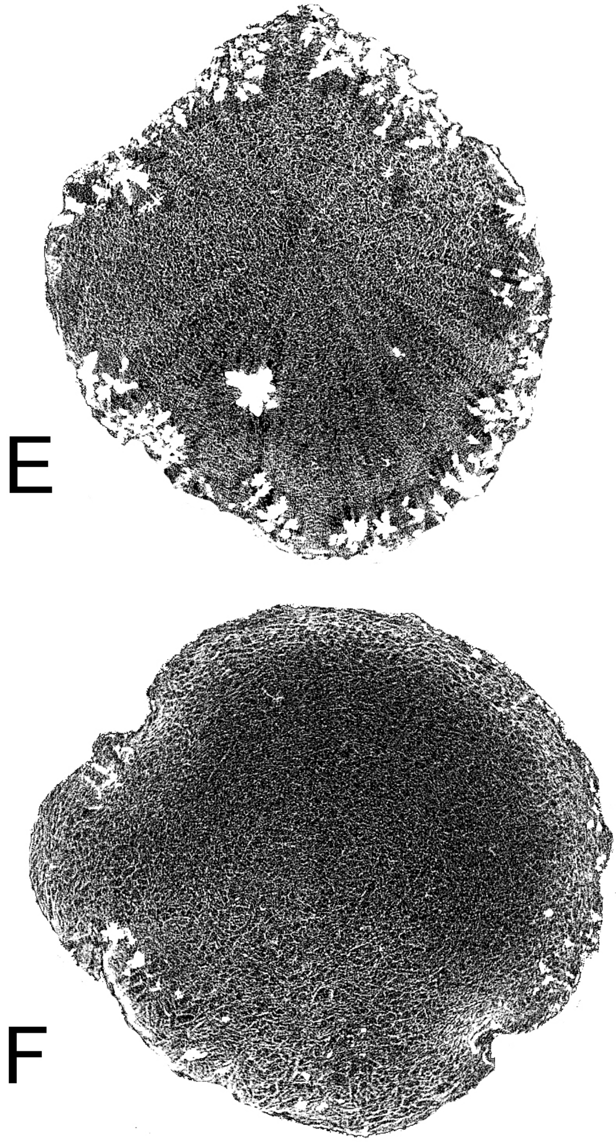

Figure 4. 2D μ-CT slices of Scaffold E (1 h) and F (22 h) after coating with 1.0 M phosphate and calcium solutions.

Figure 4 demonstrates the results of the coating treatments with the 1.0 M concentrations (Scaffold E and F). Scaffold E shows a very heterogeneous CP distribution throughout. In particular high levels of CP clusters were observed in the circumference. Scaffold F however, showed a homogeneous CP distribution in the central area, and small concentrated CP amounts in the outer area.

The overall scaffold porosity as well as the porosity in the outer surface and in the central area of the scaffolds are shown in Table 2.
Scaffold types that had been treated with the 0.1 M solution (Scaffolds A and B) had the highest overall porosity. Scaffold D, coated for 22 h in the 0.5 M solutions showed the lowest overall porosity.

Table 2. Preliminary results of the overall, central and surface porosity of the collagen scaffolds after exposure to 0.1 M, 0.5 M and 1.0 M solutions for 1 and 22 h (n=2).

		Porosity		
Duration		**0.1 M Concentration**	**0.5 M Concentration**	**1.0 M Concentration**
		A	C	E
	overall	59 ± 1 %	49 ± 0 %	18 ± 4 %
1 h	centre	80 ± 2 %	80 ± 4 %	31 ± 6 %
	surface	52 ± 7 %	22 ± 9 %	10 ± 5 %
		B	D	F
	overall	63 ± 5 %	13 ± 4 %	36 ± 6 %
22 h	centre	81 ± 6 %	43 ± 11 %	51 ± 16 %
	surface	51 ± 10 %	5 ± 3 %	15 ± 7 %

4. Discussion

Bone tissue engineering has had limited clinical success to date. In order for a scaffold to be successful in bone tissue engineering, a trade-off between mechanical properties and porosity is required. For implantation in load-bearing areas, mechanical stability is essential, as well as a high porosity and permeability to facilitate nutrient flow through the scaffold [1, 12]. The objective of this study was to investigate the possibility of developing a collagen/calcium-phosphate composite scaffold by coating a collagen scaffold with CP. The results indicate a significant increase in the mechanical properties of the scaffolds, although a reduction in porosity was observed relative to the control scaffold. CP could be detected using μ-CT in all scaffolds after coating.
The treatments using the lowest concentration (0.1 M) showed the lowest increase in mechanical properties. However, compared with pure collagen scaffolds, this increase was significant. The overall, central and surface porosity was the highest in this embodiment compared to all other composite scaffolds. Furthermore, the distribution of the CP was homogeneous (Figure 2).
Scaffolds that were treated with 0.5 M solutions showed the highest compressive moduli, although the overall porosity was decreased. The scaffolds after the 1 h exposure maintained a relatively high porosity, in particular in the central area. After 22 h of exposure to the 0.5 M solutions, a large reduction in porosity was observed. In particular the scaffolds possessed a dense outer surface of CP. This treatment therefore seems inadvisable for bone tissue engineering by reducing the ability of the scaffold to satisfactorily promote cellular penetration.
This investigation indicated that using 1.0 M concentrations leads to higher compressive moduli compared to the pure collagen scaffold, but the reduction in porosity results in

a scaffold unsuitable for tissue engineering. This reduction in porosity is insufficient for seeding the scaffolds with cells, as well as limiting nutrient flow throughout the scaffold. The results from this preliminary investigation indicate that the recommended treatment for CP coatings is 1 h exposure to the 0.5 M phosphate and the 0.5 M calcium chloride solution. Although a reduced porosity was observed, the magnitude of the decrease in porosity was lower than in the other groups making this coating technique superior to the other treatments. However, further work is necessary to obtain a more homogeneous CP distribution throughout the scaffolds as well as an increased porosity. This may be realised by increasing the pore size of the collagen scaffolds prior to coating using techniques that are well established in our laboratory [4, 5]. Furthermore, the influence of CP coating on cellular activity needs to be investigated by analysing the biological compatibility, specifically cell adhesion and proliferation.

With a similar CP process and commercially available Gelfix scaffolds, Yaylaoglu *et al.,* Kose *et al.* and Du *et al.* showed similar results of increased mechanical properties [9, 13 & 14]. However no data on the mechanical properties of these scaffolds is available. Using scaffolds with a initial porosity of 60 %, a final porosity of 50 % was achieved after their CP treatment. The best scaffold from our preliminary investigation (Scaffold C) showed an overall porosity of 50 % and in the central area more than 80 % indicating the potential of these first generation collagen/calcium-phosphate composite scaffolds for bone tissue engineering applications.

5. Conclusion

This preliminary investigation has successfully developed a composite scaffold by coating pure collagen scaffolds with calcium-phosphate. While a reduction of 50 % in the porosity of the scaffolds was obtained, an increase of almost 7000 % in the mechanical properties of the scaffolds was found indicating the potential of the scaffold for future studies.

Acknowledgements

We are grateful for the funding for this study provided by the Research Frontiers 07 program from Science Foundation Ireland. Technical support for the μ-CT from Oran Kennedy and Peter O'Reilly is also acknowledged.

References

[1] Frenkel, S. R., and Di Cesare, P. E.: Scaffolds for articular cartilage repair. Ann Biomed Eng, 32(1): 26-34, 2004.

[2] Hunziker, E. B.: Articular cartilage repair: basic science and clinical progress. A review of the current status and prospects. Osteoarthritis Cartilage, 10(6): 432-63, 2002.

[3] Rezwan, K.; Chen, Q. Z.; Blaker, J. J.; and Boccaccini, A. R.: Biodegradable and bioactive porous polymer/inorganic composite scaffolds for bone tissue engineering. Biomaterials, 27(18): 3413-31, 2006.

[4] O'Brien, F. J.; Harley, B. A.; Yannas, I. V.; and Gibson, L.: Influence of freezing rate on pore structure in freeze-dried collagen-GAG scaffolds. Biomaterials, 25(6): 1077-86, 2004.

[5] O'Brien, F. J.; Harley, B. A.; Yannas, I. V.; and Gibson, L. J.: The effect of pore size on cell adhesion in collagen-GAG scaffolds. Biomaterials, 26(4): 433-41, 2005.

[6] Farrell, E.; O'Brien, F. J.; Doyle, P.; Fischer, J.; Yannas, I.; Harley, B. A.; O'Connell, B.; Prendergast, P. J.; and Campbell, V. A.: A collagen-glycosaminoglycan scaffold supports adult rat mesenchymal stem cell differentiation along osteogenic and chondrogenic routes. Tissue Eng, 12(3): 459-68, 2006.

[7] El-Ghannam, A.: Bone reconstruction: from bioceramics to tissue engineering. Expert Rev Med Devices, 2(1): 87-101, 2005.

[8] Kim, H. W.; Knowles, J. C.; and Kim, H. E.: Hydroxyapatite porous scaffold engineered with biological polymer hybrid coating for antibiotic Vancomycin release. J Mater Sci Mater Med, 16(3): 189-95, 2005.

[9] Yannas, I. V.; Lee, E.; Orgill, D. P.; Skrabut, E. M.; and Murphy, G. F.: Synthesis and characterization of a model extracellular matrix that induces partial regeneration of adult mammalian skin. Proc Natl Acad Sci U S A, 86(3): 933-7, 1989.

[10] Yaylaoglu, M. B.; Yildiz, C.; Korkusuz, F.; and Hasirci, V.: A novel osteochondral implant. Biomaterials, 20(16): 1513-20, 1999.

[11] Al-Munajjed, A.; Gleeson, J.P.; and O'Brien, F. J.: Development of a collagen calcium- phosphate scaffold as a novel bone graft substitute. In Bioengineering in Ireland 13, pp. 46. Edited by Buchanan, F.; Dunne, N.; and Orr, J.; Enniskillen, Co. Fermanagh, Northern Ireland, The School of Mechanical and Aerospace Engineering; Queen's University Belfast; Northern Ireland, 2007.

[12] O'Brien F, J.; Harley, B. A.; Waller, M. A.; Yannas, I. V.; Gibson, L. J.; and Prendergast, P. J.: The effect of pore size on permeability and cell attachment in collagen scaffolds for tissue engineering. Technol Health Care, 15(1): 3-17, 2007.

[13] Kose, G. T.; Korkusuz, F.; Ozkul, A.; Soysal, Y.; Ozdemir, T.; Yildiz, C.; and Hasirci, V.: Tissue engineered cartilage on collagen and PHBV matrices. Biomaterials, 26(25): 5187-97, 2005.

[14] Du, C.; Cui, F. Z.; Zhu, X. D.; and de Groot, K.: Three-dimensional nano-HAp/collagen matrix loading with osteogenic cells in organ culture. J Biomed Mater Res, 44(4): 407-15, 1999.

Medicine Meets Engineering
J. Hammer et al. (Eds.)
IOS Press, 2008

Occlusal convergence and strain distribution on the axial surface of cemented gold crowns

S ASBIA [a,*], R IBBETSON[a] and R.L.REUBEN[b]

[a] *University of Edinburgh, Postgraduate Dental Institute, Edinburgh, UK.*
[b] *Heriot-Watt University, School of Engineering and Physical Sciences, Edinburgh, UK.(E.mail:s0096711@sms.ed.ac.uk OR salimasbia@hotmail.com)*
[*] *Corresponding author.*

Abstract
The overall thrust of this work is concerned with the performance of the adhesives used to simulate cementation of gold crowns onto nickel chromium dies under static and dynamic compression. A measurement system, based on the mounting of strain gauges on the outer surface of the crowns, has been developed allowing an indirect semi-quantitative estimate of the state of adhesion.

This paper reports an investigation of the effect of increased total occlusal convergence (TOC) of the nickel chromium dies from 12^{o} to 24^{o} with different degrees of cementation, a) un-cemented, b) partially cemented and c) fully cemented.

Four nickel chromium dies (12^{o}TOC) and five nickel chromium dies (24^{o}TOC) for each convergence were fabricated using the lost wax technique. The axial height of all dies was 6mm. Two miniature gauges were installed on opposing axial surfaces of each gold crown 1 mm above the crown margin. Axial loading and unloading of the crowns was repeated five times for each crown and the values for strain recorded.

The results showed an increase in strain at the axial surfaces with increasing TOC, providing useful design information for the durability of restorative crowns. These findings, along with the findings of earlier work are consistent with a simple model of load transfer between the crown and the die.

Keywords: Restorative dentistry, adhesives, stress-strain behaviour, total occlusal convergence, taper.

Introduction

Tooth preparation is an important aspect of restorative dentistry as it establishes the foundation for the restoration that is being replaced. Long term service is an essential characteristic of fixed partial dentures. Since luting cements provide little or no adhesion, full veneer crowns depend on relatively parallel axial walls for retention. Cements enhance this frictional fit by filling the minor discrepancies between the castings and the axial walls of the preparation providing a keying-type load transfer. The shear strength of the cement is a key factor in retention of the crown.

Taper describes the gradual decrease in width of an elongated object. Whilst the total occlusal convergence (TOC) is the angle formed between two external opposing prepared axial surfaces. Theoretically, the more nearly parallel the opposing walls of a preparation, the greater the retention, with the most retentive preparation being one with parallel walls. Kaufman et al. [1] and Jorgensen [2] elucidated experimentally the inverse relationship between taper and retention.

Surprisingly, there is no close agreement between authors as to the ideal taper. Historically, the recommended TOC has ranged between 4^{o} and 14^{o} (Shillingburg et al. [3], Rosenstiel et al. [4]). El-Ebrashi et al. [5] emphasised that the taper should be between 2.5^{o} and 6.5^{o} to minimise stress, with only a slight increase in stress as the taper increased from 0^{o} to15^{o}. At 20^{o}, the stress concentration was found to increase sharply. Shillingburg et al. [3] described resistance and retention as interrelated and often inseparable qualities. To maximise these two qualities, they recommended a taper of 6^{o}.

The literature therefore supports the use of a minimal convergence angle. This was based on research involving removing a cemented crown from a simulated prepared tooth (in the form of metallic or plastic dies) by pulling along the long axis of the tooth, Jorgensen [2] and Wilson and Chan [6]. However, Rosenstiel et al. [4] and Dodge et al. [7] have stated that the forces that tend to remove cemented restorations along their path of withdrawal are small compared to those that tend to seat or tilt those restorations.

It has been determined that the TOC produced by dental practitioners, dental students, general practice residents and prosthodontists usually are not ideal. Instead, the angles range between 12^{o}-17^{o}; Smith et al. [8], Noonan and Goldfogel (1991)[9], Kent *et al* (1988)[10], and Nordlander et al. [11]. Ohm and Silness [12] measured microscopically the bucco-lingual and mesio-distal convergence angles of vital and root filled teeth. They found that the mean total convergence in vital teeth was approximately 19^{o}-27^{o}, whilst the root filled teeth were between 12^{o} and 37^{o}. Kent et al. [10] evaluated the taper of 418 dies of preparations made over 12 years made by Shillingburg. This study included posterior full crowns, inlays, onlays and posterior metal ceramic crowns. The taper ranged between 8.6^{o}-26.6^{o}, with average of 14.3^{o} depending upon the location and in the mouth and visual accessibility.

Goodacre [13] reported that there are number of factors that affect the amount of TOC and make it more difficult to achieve the goal of 10^{o}-20^{o}. Preparation of posterior teeth often leads to greater TOC than anterior teeth (Kent et al. [10] and Nordlander et al. [11]). Further, mandibular tooth preparation leads to greater TOC teeth compared with that of the maxillary teeth, Smith et al. [8], Nordlander et al. [11], and Kent *et al*. [10].

Goodacre et al. [14] reported that, after anatomic reduction, most teeth have specific geometric forms when viewed occlusally. Prepared mandibular molars are rectangular in shape; maxillary molars are rhomboidal, whilst premolars and anterior teeth frequently are oval. They added that these geometric shapes have traditionally provided resistance to dislodging forces on individual crowns and fixed partial dentures. Hegdahl and Silness [15] compared the area that created resistance on conical and pyramidal tooth preparations, and reported that pyramidal tooth preparations provided increased resistance because of their edges. They concluded that the use of large convergence angles resulted in small resisting areas and should be avoided.

The literature and clinical experience confirm that small convergence angles are difficult to produce clinically and that somewhat greater convergence angles do not seem to be directly associated with levels of failure.

The purpose of the current study is to extend the findings of previous work (Asbia et al. [16]) which sought to determine the relationship between strain measured on the outside of a model crown-die system as the degree of coverage by luting cement was varied. Here, we introduce a new geometrical factor, total occlusal convergence, in order to assess how this variable affects the relationship already established.

Materials and methods

For compatibility with earlier work, this study aimed to evaluate the resultant strain in opposing axial walls of cemented full gold crowns mounted on dies of 12^{o} TOC and 24^{o} TOC, respectively both sets of dies being of 6 mm axial height and maximum diameter 10mm. In order to facilitate comparisons, an idealised system was adopted, consisting of truncated conical dies, made from a nickel-chromium alloy with corresponding gold crowns cemented on them using zinc phosphate cement.

a) Die preparation

The method for production of nickel chromium dies was as described in Asbia et al. [16]. Four nickel chromium dies of 12^{o} taper and five of 24^{o} taper were produced. All dies had 6 mm axial wall height and bottom diameter 10mm, Figure 1.

Figure1: Nickel chromium dies, 12^{o} taper (left), 24^{o} taper (right).

b) Crown fabrication

For each produced nickel chromium die, a gold crown of total thickness 0.5mm was cast using the lost wax technique, the detailed method again being as described in Asbia et al. [16].

c) Strain gauge installation

Two miniature linear strain gauges (EA-06-031EC-350, Measurements Group) were bonded (M-Bond 200, Measurements Group) opposite each other about 1 mm above the crown margin. Each gauge was amplified independently, and calibrated on an Aluminium-Copper alloy strip of known elastic modulus (72.4GPa). The calibration curves for the two amplifiers used are shown in Figure 2, and, as can be seen, the measurements on increasing and decreasing load (shown as different symbol types) were reproducible with little or no hysteresis.

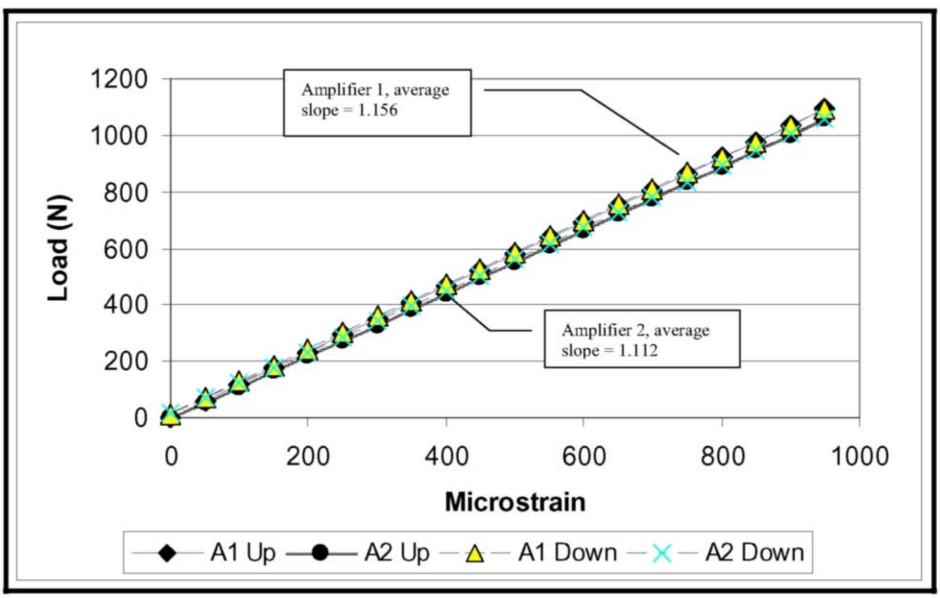

Figure 2: Calibration of amplifiers used. Diamond and circle symbols represent Amplifier 1 and triangle and cross symbols, Amplifier 2.

d) Cementation procedure:

The cement used was a zinc phosphate (De Trey®Zinc, Dentsply Ltd.) and conformed with ISO specification 9917:1991. The cement was mixed on a glass slab which had been cooled by immersion in tap water for 2 minutes, and the room temperature during mixing was 19±2ºC. The powder to liquid ratio was according the manufacturer's recommendations and the mixing was carried out according to the recommendations of Eames et al. [17]. Each increment of powder was incorporated into the liquid at 15 second intervals and the time until completion of the mix was 1½ minutes. Cross-sections of typical cemented crowns on their dies are shown in Figure 3. The same procedure of cementation was used as described in Asbia et al. [16], involving the production of crowns which are uncemented, partially cemented (with no cement on the occlusal surface) and fully cemented. All crowns were produced with a spacer designed to give a 25μm gap between crown and die.

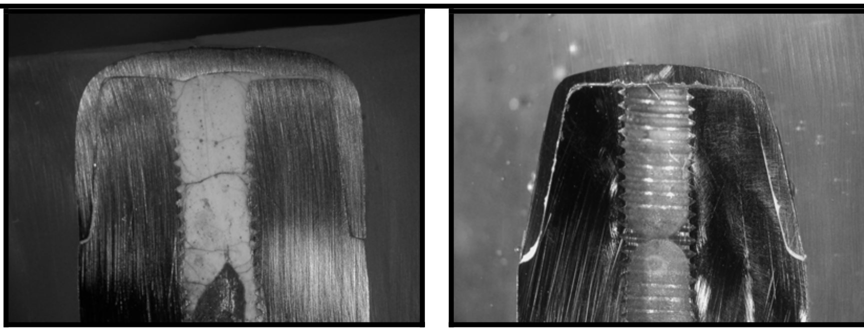

Cross section of fully cemented gold crown on nickel chromium die of 12^0 total occlusal convergence.

Cross section of fully cemented gold crown on nickel chromium die of 24^0 total occlusal convergence.

Figure 3: Cross section of fully cemented gold crowns on their nickel chromium dies with two different taper models

e) Load application and experimental procedure

The load application procedure was again as described in Asbia et al. [16], with a static compression (Figure 4) being applied to each crown in increments of 10N starting from 0N to 220N . The loading was applied using an Instron testing machine.

Cemented sample under test

Figure 4: Crown-die assembly and testing

f) Data collection
The data was collected manually from the screen of the amplifiers for each loading increment, for each of the five runs on each crown. The strain readings were calibrated according to the calibration factors; the mean of the five repeats was taken and plotted as microstrain (με) against load (N).

Results

The results are displayed in Figures 5, 6 and 7 for the uncemented crowns, partially cemented crowns and fully cemented crowns, respectively, each plot showing both the 12° and 24° TOC.

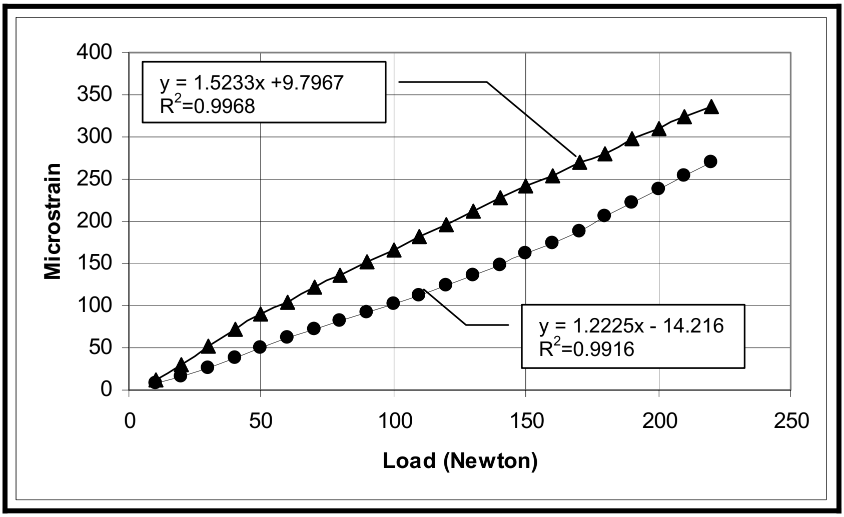

Figure 5: Load strain behaviour of un-cemented crowns
(Circle 12° TOC& Triangle 24° TOC)

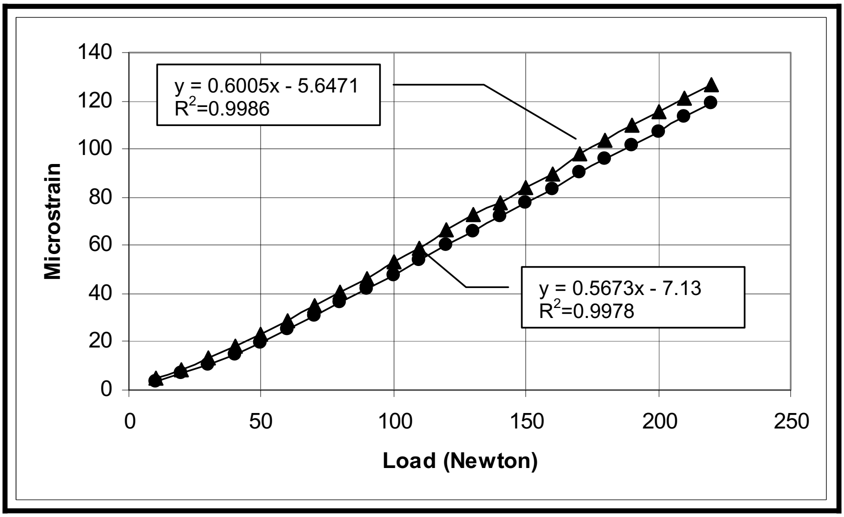

Figure 6: Load strain behaviour of partially cemented crowns
(Circle 12° TOC& Triangle 24° TOC)

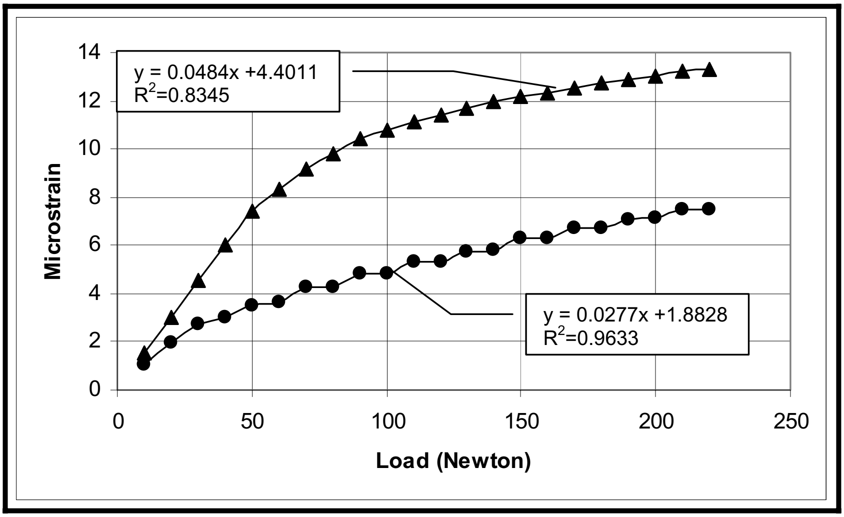

Figure 7: Load strain behaviour of fully cemented crowns.
(Circle 12° TOC& Triangle 24° TOC)

The results show consistently higher strains for a given load on the axial surface of the non cemented, partially cemented, and fully cemented crowns with 24° TOC than for the 12° TOC crowns. The ratios of the slopes (24° TOC: 12° TOC) of the strain-load graph is around 1.24 for uncemented crowns, 1.06 for partially cemented crowns, and 1.75 for fully cemented crowns, although it might be noted that the strain levels for fully cemented crowns are rather low and the results could be affected significantly by zero drift or plastic slip at the cement interfaces.

Discussion

For the purposes of understanding the effect of the degree of cementation, the gold crown (Young's modulus, E_{crown}=90GPa) on its nickel chromium die (E_{die}=220GPa) can be roughly represented by an inverted cup-shaped cylinder sitting on the finish line over a solid cylinder. The hollow cup is held onto the solid die using zinc phosphate cement (Shear modulus G_{cem}= 8.14GPa), and the bond relies on mechanical interlocking into the irregularities of the metal surfaces as the zinc phosphate cement neither adheres to gold nor to nickel chromium. The overall geometrical arrangement, including the approximate placement of the strain gauges is shown schematically in Figure 8, which also shows where luting cement is present in the uncemented, partially cemented and fully cemented crowns.

In the uncemented case, it might be expected the compressive stress to be given approximately by the force divided by the annular cross-sectional area of the crown, giving an axial compressive strain of $\varepsilon_u = \dfrac{F}{AE}$. Thus the slope of the strain force graph might be expected as shown in equation no. [1] to be around:

$$\frac{\varepsilon}{F} = \frac{1}{\pi dtE} = \frac{1}{\pi \times 10 \times 0.5 \times 90 \times 10^3} \cong 0.73 \mu\varepsilon / N \,. \quad [1]$$

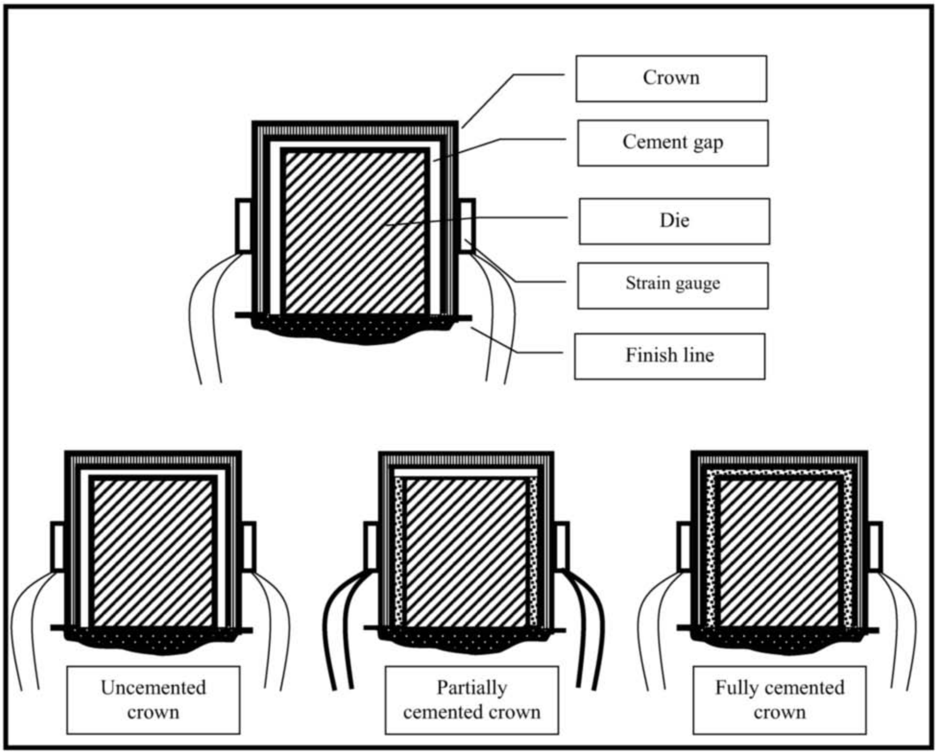

Figure 8: Simplified cylindrical model of crowns.

The fact that the strain in the uncemented crowns is larger than this is attributable to the effect of the taper angle which decreases the cross-sectional area at the strain gauge from that determined by the nominal diameter, d (10 mm). For a taper angle of 6°, the diameter at the top of the crown is 8.74mm (0.874 of original xsa), and, for a taper angle of 12°, it is 7.45mm (0.745 of original xsa). Given that the centre of strain gauge is about half-way up the crown, it might be expected that the strain to increase for a given load by a factor of about 1.07 for 12° TOC and about 1.15 for 24° TOC. Although this does not precisely account for the observed strain and for the ratio between the TOC angles, it clearly shows the expected direction, the difference probably being accountable by inward bending of the crown wall.

For the partially-cemented crowns, a simplified solution for the tension/compression in one member of a single lap joint (Her [18]) can be used (adapted for the particular geometry considered as shown in equation no. [2]:

$$C_{crown} = P\left[-\frac{1}{2}\frac{\sinh(\lambda x)}{\sinh(\lambda l)} + \frac{E_{die}r_{die} - E_{crown}t_{crown}}{2\left(E_{die}r_{die} + E_{crown}t_{crown}\right)}\frac{\cosh(\lambda x)}{\cosh(\lambda l)} + \frac{E_{crown}t_{crown}}{\left(E_{die}r_{die} + E_{crown}t_{crown}\right)}\right] \quad [2]$$

where C_{crown} is the compressive force in the crown wall as a function of the dimension x, which is measured axially from the approximate position of the strain gauge, mid-way axially between the top ($x = -l/2$) and bottom ($x = l/2$) of the cylinder, negative towards the top of the crown. The parameter λ is shown in equation no. [3]:

$$\lambda = \sqrt{\frac{G_{cem}}{t_{cem}}\left(\frac{1}{E_{die}r_{die}} + \frac{1}{E_{crown}t_{crown}}\right)} = 0.434 t_{cem}^{-1/2} mm^{-1} \quad [3]$$

where the elastic moduli have been defined earlier and the *t*s are the thicknesses of the crown, the cement and the die (effectively its radius), and *P* is the applied compressive load. Figure 9 shows the calculated ratio of C_{crown} /P (which is essentially the ratio of slope between a partially cemented and uncemented crown (found to be about 2 to 2.5 in the experiments) following this model, and it can be seen that the load transfer is rather better than is observed even for a very thick cement layer.

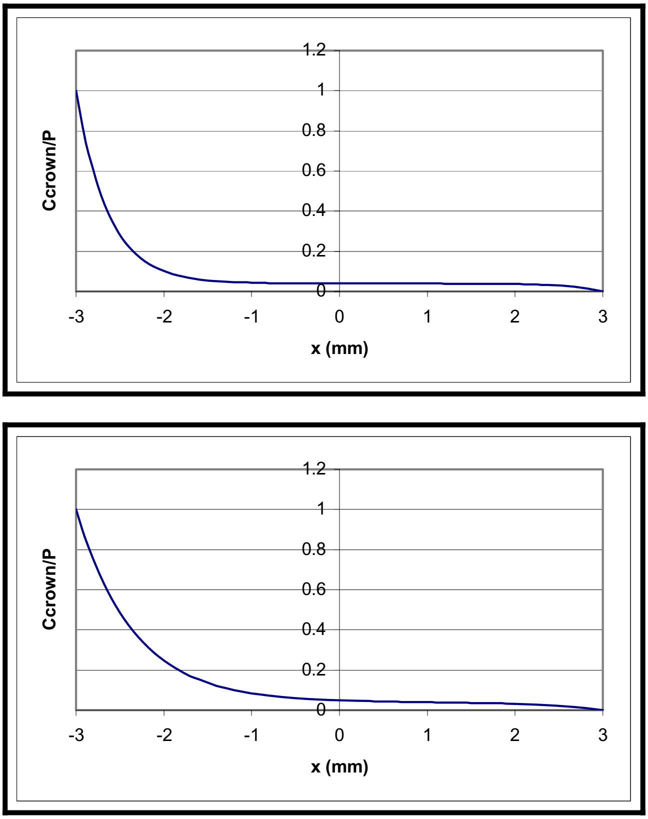

Figure 9: Compressive force in adhesively bonded partially cemented crown, for 25µm thick adhesive (top) and for 80 µm thick adhesive (bottom).

This poor load transfer is partly attributable to the quality of the cement coverage, but, probably more significantly, to the fact that the cement is not an adhesive and can therefore permit much more slip at the cement-die and cement-crown interfaces than would an adhesive.

A fully cemented crown can be regarded as a compound cylinder is made up of three series elements; I, II and III, the last two of which are themselves made up of parallel sub-elements, Figure 10. If a compressive force, *F*, is applied to the compound cylinder, it will be carried through all of the series elements, but will be shared between the parallel sub-elements according to their cross-sectional areas and elastic moduli.

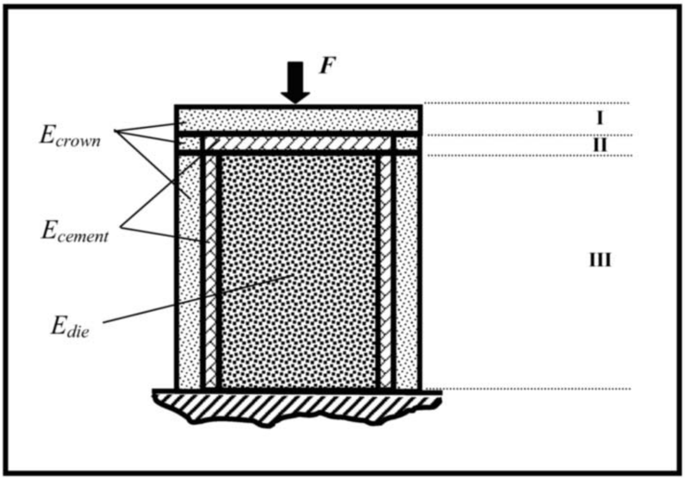

Figure 10: Schematic compound cylinder model for fully cemented crown.

By considering the compound model described above, the compressive strain in the crown wall can be expressed in terms of the compressive force, F, and the Young's moduli, *E*, and cross-sectional areas, *A*, of the crown, the die and the cement as shown in equation no. [4]:

$$\varepsilon_{crown} = \frac{F}{E_{crown}A_{crown} + E_{cement}A_{cement} + E_{die}A_{die}} \quad [4]$$

and so the strain per unit load calculation is shown in equation no. [5]:

$$\frac{\varepsilon_{crown}}{F} = \frac{1}{\pi dt_{crown}E_{crown} + \pi dt_{cement}E_{cement} + \pi d^2 E_{die}/4} = 1.4\times10^{-2}\,\mu\varepsilon/N \quad [5]$$

so the strain in a fully cemented crown is much lower than either a partially cemented or an uncemented crown. Also, neither the cement nor the crown has much effect on the strain measured in the crown. Again, the calculated compliance is a factor of about 2-2.5 smaller than that observed, which can be explained only partly by the effect of taper angle. Since the crown is constrained against bending inwards by the cement in the gap, it is unlikely that the difference will be due to this effect, and it is rather more likely that the outer of the three cylinders in Element III, behaves more independently than the compound model would suggest due to slip between the cement and the metal components.

The fact that greater TOC produces more axial strain in the walls of the crown might have an adverse effect on the long term survival of a cemented crown in the clinical situation. This is in accord with Hegdahl and Silness [15] who concluded that the use of large convergence angles resulted in small resisting areas and hence poorer long-term performance.

Metal (specifically a nickel chromium alloy) dies were used in this work because of its hardness and abrasion resistance under repeated cementation and crown removal, Chan [19], Lockwood [20] and Cassidy [21]. Wax was applied directly onto the metal dies, because of the degree of adaptation or misfit of a crown waxed onto a metal die is less than one waxed on a stone die (Fusayama et al. [22]). Eden et al. [23] showed that base metal alloys have inferior fit on metal dies, and so a noble metal crown was chosen. The dip technique was used for waxing of the gold crown, because it has been shown to give a reproducible crown thickness of about 0.5 mm, Kovarik et al. [24]. The control of crown thickness was seen to be important, following Sugita et al. [25], who emphasised that, as metal thickness increased, the deformation of the crown decreased and the cement failure load increased. These choices, whilst ensuring control over the experimental conditions, will have an effect on the conclusions. Also, different cement types, especially those which have greater adhesion to the die and/or crown might be expected to give rather different results.

The main methods used in dental experimental mechanics for strain assessment are strain gauges, brittle lacquer and photoelastic techniques. Palamara et al. [26] reported on the importance of the size of the strain gauge relative to the surface area of the sample, and on the difficulty in attaching very small gauges to make sufficiently accurate measurements. The gauges used in this experiment covered a substantial proportion of the axial length, but this has had the advantage of permitting a certain amount of averaging of the effect of the luting cement and a reduced dependence on local variations in thickness or coverage in what is, after all, a crafted artefact. In separate work by Asbia [27], to be published, an analysis of variance has shown that the variability around the circumference in the measured strain at a given load for a given crown is as much as the verifiability between builds of nominally identical crowns.

Conclusions

1) The degree of cementation in cast dental restorations has an effect on the axial strain on the outer wall of the crown, partially cemented crowns being about half as compliant as uncemented ones, and fully cemented ones being about one fortieth as compliant.
2) The total occlusal convergence (TOC) has an effect on the axial strain on the outer wall of the crown, larger angles producing higher strains in uncemented, partially cemented and fully cemented crowns.
3) The qualitative observations 1 and 2 can be explained using simple mechanical models, differences being accountable in terms of the interface between the cement and the crown and/or the die.
4) Future work in this area should consider the effect of different cement types on the load transfer as this has an effect on the shear stresses in the adhesive, better load transfer resulting in higher shear stresses and hence a greater rate of deterioration of the cement under sustained repeated loading.

Acknowledgments

The principal author acknowledges the continuing generous support of the Libyan Education Ministry.

Correspondence to: Dr S Asbia, Edinburgh postgraduate Dental Institute, Lauriston Building, Lauriston Place, Edinburgh, EH3 9HA, UK.

References

[1] Kaufman E G, Coelho D H and Colin L: Factors influencing the retention of cemented gold castings. *J. Prosthet. Dent*. 1961: **11**: 487-502.

[2] Jorgensen K D: The relationship between retention and convergence angle in cemented veneer crowns. *Acta Odontol. Scand*. 1955; **13**: 35-40.

[3] Shillingburg H T, Hobo S and Whitsett L D: *Fundamentals of fixed prosthodontics*. Quintessence; Chicago: 1997.

[4] Rosenstiel S F, Land M F and Fujimoto J: *Contemporary fixed prosthodontics*. Mosby Publishing Co.; St. Louis: 1995.

[5] El-Ebrashi M K, Craig R G and Peyton F A: Experimental stress analysis of dental restorations. IV. The concept of parallelism of axial walls. *J. Prosthet. Dent.* 1969; **22**: 346-53.

[6] Wilson A H and Chan DC: The relationship between preparation convergence and retention of extracoronal retainers. *J. Prosthodont*. 1994; **3**: 74-8.

[7] Dodge W W, Weed R M, Baez R J and Buchanan R N: The effect of convergence angle on retention and resistance form. *Quintessence Int.* 1985; **16**: 191-194.

[8] Smith C T, Gary J J, Conkin J E and Franks H L: Effective taper criterion for the full veneer crown preparation in preclinical prosthodontics. *J. Prosthodont*. 1999; **8**: 196-200.

[9] Noonan J E and Goldfogel M H: Convergence of the axial walls of full veneer crown preparations in a dental school environment. *J. Prosthet. Dent*. 1991; **66**: 706-8.

[10] Kent W A, Shillingburg H T and Duncanson M G: Taper of clinical preparations for cast restorations. *Quintessence Int*. 1988; **19**: 339-45.

[11] Nordlander J, Weir D, Stoffer W and Ochi S: The taper of clinical preparations for fixed prosthodontics. *J. Prosthet. Dent*. 1988; **60**: 148-51.

[12] Ohm E and Silness J: The convergence angle in teeth prepared for artificial crowns. *J. Oral Rehabil*. 1978 ; 5: 371-5.
[13] Goodacre C J: Designing tooth preparations for optimal success. *Dent. Clin. North Am*. 2004; **48**: 359-385.

[14] Goodacre C J, Campagni W V and Aquilino S A: Tooth preparations for complete crowns: an art form based on scientific principles. *J. Prosthet. Dent*. 2001; **85**: 363-76.

[15] Hegdahl T and Silness J: Preparation areas resisting displacement of artificial crowns. *J. Oral Rehabil*. 1977; **4**: 201-7.

[16] Asbia S, Ibbetson R and Reuben R L: Compressive stress-strain behaviour of cast dental restorations in relation to luting cement distribution. *Technol. Health Care*. 2006; **14**: 439-48.

[17] Eames WB, Monroe SD, Roan JD, O'Neal SJ. Proportioning and mixing of cements: a comparison of working times. Opera Dent. 1977; **2**, 97-104.

[18] Her S-C: Stress analysis of adhesively-bonded lap joints. *Composite Structures*. 1999; **47**: 673-678.

[19] Chan NC (1982). Electropneumatic vibration and cementation of full crowns. MSc project report, University of London.

[20] Lockwood KWI (1984). The cementation of a full crown with glass ionomer cement. MSc project report, University of London.

[21] Cassidy M (1985). Effect of marginal design on crown seatings. MSc project report, University of London.

[22] Fusayama T, Ide K, Kurosu A, Hosoda H.: Cement thickness between cast restorations and preparation walls. J prosthet Dent. 1963; **13**:354-64.

[23] Eden GT, Franklin OM, Powell JM, Ohta Y, Dickson G.Fit of porcelain fused-to-metal crown and bridge castings. J Dent Res. 1979;**5**:2360-2368.

[24] Kovarik RE, Breeding LC, Caughman WF Fatigue life of three core materials under simulated chewing conditions. J Prosthet Dent. 1992;**68**:584-90.

[25] Sugita T, Takakuda K, Miyairi H.: Mechanical behaviour of the cement layer of a cast crown--effect of the mechanical properties of casting alloy. Kokubyo Gakkai Zasshi. 2000;**67**: 52-7.[Abstract from the pub med. Article in Japanese].

[26] Palamara JE, Wilson PR, Thomas CD, Messer HH.: A new imaging technique for measuring the surface strains applied to dentine. J Dent. 2000 ;**28**:141-6.

[27] Asbia S: Short and long-term behaviour of cast dental restorations under compressive stresses, PhD Thesis, University of Edinburgh, to be published.

Medicine Meets Engineering
J. Hammer et al. (Eds.)
IOS Press, 2008

Strain adaptive bone remodelling: Influence of the implantation technique

B.-A. BEHRENS[a], A. BOUGUECHA[a,1], I. NOLTE[b], A. MEYER-LINDENBERG[b], C. STUKENBORG-COLSMAN[c] and T. PRESSEL[c]
[a] *Institute of Metal Forming and Metal-Forming Machines, Leibniz Universität Hannover, Germany*
[b] *Small Animal Clinic, University of Veterinary Medicine Foundation Hannover, Germany*
[c] *Department of Orthopaedic Surgery, Hannover Medical School, Germany*

Abstract Total hip arthroplasties (THA) can be performed with cemented and uncemented femoral components. Aseptic loosening of the joint replacement still illustrates a problem for both implantation techniques. This loosening can be caused, among other factors, by resorption of the bone surrounding the implant due to stress shielding. In order to analyse the absolute influence of the implantation technique on the bone degeneration in the periprosthetic femur, the strain adaptive bone remodelling after THA was investigated in a three-dimensional finite element (FE) simulation of a femur provided with a cemented and uncemented BICONTACT (Aesculap, Tuttlingen, Germany) femoral component. For this, a bone density evolution theory was implemented in the FE code MSC.MARC®. In these static FE simulations, the muscle and hip resultant forces represent the maximum loading situation in the normal walking cycle. To describe the mechanical properties of the bone, an isotropic material law dependent upon density was used. The situation directly after implantation without any bone ingrowth was simulated. The cemented femoral component was bonded to the bone by a homogenous cement mantle. The numerical results show that proximally, the bone resorption areas surrounding the BICONTACT stem are heavily dependent upon anchoring technique. Furthermore, no significant bone remodelling is calculated in the distal periprosthetic femur in both models.

Keywords Bone remodelling, Finite element analysis, Total hip arthroplasty, BICONTACT, Implantation technique

Background

Total hip replacement is a successful surgical option for treatment of painful osteoarthritis of the hip or long-term consequences of trauma [1]. The bone cement introduced by Charnley allowed reproducible and stable anchorage of total hip replacements. In the beginning of 1980s, the uncemented anchoring of prostheses was more widely used due to problems removing the cement in revision surgery and

[1] Corresponding Author: Dipl.-Ing. Anas Bouguecha, Department of Numerical Methods, Institute of Metal Forming and Metal-Forming Machines, An der Universität 2, 30823 Garbsen, Leibniz Universität Hannover, Germany; E-mail: bouguecha@ifum.uni-hannover.de

improved uncemented prosthesis designs. Nowadays, both techniques are established, and there are prostheses which can be implanted with or without cement [2,3]. The total replacement of the hip, no matter which technique is used, has an influence on the load distribution in the bone. One resulting phenomenon is called stress shielding [4]. As the metal material of the prosthesis is very rigid, compared to cortical or cancellous bone, it takes over most of the stresses. Hypothesized by Wolff's law [5], lower stresses in the bone cause resorption of the surrounding bone tissue. This can contribute to a loosening of the implant. Prosthesis loosening is painful for the patient, and cost intensive revision surgery is needed. Therefore, it is generally believed that a physiological load distribution in the periprosthetic femur may lead to reduced loosening rates.

Several study groups have been engaged in reducing the effect of the strain changes in the periprosthetic bone tissue by optimising the design of the implants [6,7,8]. Finite element analysis (FEA) is an appropriate computer-aided method to improve the implants in the constructional phase and to analyse their structure compatibility [9,10,11,12]. It is a rational and timesaving alternative to theoretical biomechanical simulations of the intact and the endoprosthetic provided femur [6,7,9,12,13,14,15]. Prendergast and Taylor [14], for example, used the FEA to compare the stress distributions in proximal medial femora provided with prostheses with different Young's modules. Tai et al. [7] computed femoral stresses after implantation of conventional and femoral neck prostheses. Huiskes and co-workers [4,12,16,17,18,19,20] led clinical and numerical investigations concerning bone remodelling after THA. They have studied among other factors the influence of prosthesis coating and the implant material on this process [4,17,20]. Their work was focused on uncemented stems [16,18,19].

The available numerical biomechanical studies usually compare cemented and uncemented prostheses with different designs, so that differences in stress and strain distributions could also be attributed to different prosthesis geometries. Therefore, the aim of this study was to compare periprosthetic strains of a cemented and uncemented femoral prosthesis component featuring the same geometry by FE modelling for quantifying the hypothesized differences between cemented and uncemented anchoring techniques.

Methods

For the numerical calculations, a three-dimensional (3D) FE model of a femur was developed based on computed tomography (CT) data of a human patient. The examination was performed in preparation for robot assisted total hip replacement. After informed consent was obtained, the caudal pelvis and the femur were scanned with a slice thickness of 2 mm (SOMATOM PLUS 4, Siemens, Erlangen, Germany). With the image analysis programme ANALYZE (Mayo Clinic Biomedical Imaging Resource, Rochester MN, USA) 3D surfaces of the image data were created in stereolithography format (STL). Based on this data, a solid FE mesh was generated using the preprocessor software HYPERMESH (Altair Engineering, Böblingen, Germany). The meshing was carried out using four-noded tetrahedral elements with single Gauss integration point.

To design the elastic behaviour of the bone, an isotropic material law based upon apparent bone density (ABD), ρ [20, 21] was used (Eq. 1).

$$\begin{cases} \nu = 0.3 \\ E = \alpha \cdot \rho^3 \end{cases} \tag{1}$$

Where the variable α is a constant, E the Young's modulus and ν the Poisson's ratio of the bone.

Own measurements showed that the density of the cortical bone in the human femur exhibited an approximately constant value of $1.96\ \mathrm{g/cm^3}$. Compression tests at compact bone samples showed that a Young's modulus of 22,500 MPa remained constant throughout the femoral shaft. This implies that the parameter α is equal to 2921 $[\mathrm{MPa/(g/cm^3)^3}]$. In order to simulate the bone remodelling after implantation of a hip prosthesis in comparison with the physiological situation, first a static simulation of an intact femur was performed. As femoral strains are different when muscle forces are neglected [22], a simplified loading regime modelling the forces of the abductors of the hip, the tensor fasciae latae and vastus lateralis was used [24] (Figure 1). The muscle forces and hip resultant force (F_1, F_2, F_3, F_4, F_5) representing a human weighing 85 kg were taken from the work of Heller and co-workers [24]. They conform to the muscle forces which are effective on the human femur at a maximum hip joint load while walking [23,24].

The elastic 3D-simulations were performed with the solver MSC.MARC (MSC.SOFTWARE, Santa Ana CA, USA). The elastic strain energy density (ESED), D_{ref} in the intact femur was calculated via Eq. 2.

$$D_{ref} = \frac{1}{2} \cdot \underline{\sigma}^T \cdot \underline{\varepsilon} = \frac{1}{2} \cdot \underline{\varepsilon}^T \cdot \underline{\underline{C}} \cdot \underline{\varepsilon} \tag{2}$$

Where $\underline{\varepsilon}$ and $\underline{\sigma}$ are the strain and stress tensor respectively and $\underline{\underline{C}}$ the stiffness matrix.

Hence the elastic strain energy per unit mass (ESEUM) in the intact bone, S_{ref} was computed using Eq. 3.

$$S_{ref} = \frac{D_{ref}}{\rho_{ref}} \tag{3}$$

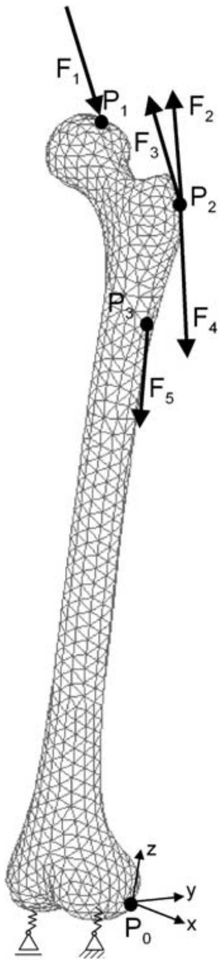

Force [N]:	Components x	y	z	Acts at point
Hip contact (F_1)	451	268	-1916	P_1
Abductor (F_2)	-485	-36	723	P_2
Tensor fascia latae, proximal part (F_3)	-60	-97	110	P_2
Tensor fascia latae, distal part (F_4)	4	6	-159	P_2
Vastus lateralis (F_5)	8	-155	-777	P_3

Point:	x	y	z
P_0	0	0	0
P_1	-69	5	441
P_2	-1.5	-4	399.2
P_3	-11.6	1	355

Figure 1: Loading of the femur (data obtained from [15])

For the FE simulation of the contact between bone and implant, a BICONTACT femoral component (Aesculap, Tuttlingen, Germany) was used which is available for cemented and uncemented implantation (Figure 2).

A 3D FE-model was constructed from computer aided design (CAD) data of the prosthesis. The implantation of the prosthesis into the femur was accomplished with the pre-processor HYPERMESH. The cementless stem is proximally porous-coated with titanium. The cemented stem is made of steel and exhibits a polished surface. In this study, we intended to simulate the situation directly after THA when no bony ingrowth

Figure 2: BICONTACT standard implants for cementless and cemented hip replacement

of the femoral components has occurred so the effect of ingrowth of the prostheses into the bone is not accounted for. Hence, the uncemented stem is only fixed proximally in the coated region [2,3]. The cemented femoral component is bonded to the bone by a homogenous cement mantle in the proximal and subproximal regions [2,3]. The same boundary conditions (joint and muscle forces) were chosen as for the simulation of the intact femur. The prostheses were modelled using a homogenous and isotropic material law (for titanium $E = 110{,}000$ MPa, $\nu = 0.3$, for steel $E = 210{,}000$ MPa, $\nu = 0.3$). For cement the mechanical parameters of PALACOS G (Heraeus Medical, Hanau, Germany) were used ($E = 2{,}600$ MPa and $\nu = 0.3$). For a numerical comparison of calculated ABD in different regions of the femur, the bone in each FE model was subdivided into three regions of interest (ROI): proximal, subproximal and distal (Figure 4).

For the quantification of the bone remodelling after THA, the ABD in the periprosthetic femur was determined using an iteration algorithm. In each step the ESEUM in the periprosthetic bone, S_{pro} is computed. From the result the stimulus ξ to bone remodelling is calculated according to Eq. 4.

$$\xi = \frac{S_{pro}}{S_{ref}} \qquad (4)$$

In order to determine the density evolution rate of the bone $\dot{\rho}$ a material law taken from the reference [20] using Eq. 5 was applied.

$$\dot{\rho} = \begin{cases} \left(\xi - 1 - \frac{z}{2}\right) \text{ if } \xi \geq 1 + \frac{z}{2} \\ \left(\xi - 1 + \frac{z}{2}\right) \text{ if } \xi \leq 1 - \frac{z}{2} \\ 0 \text{ if } 1 - \frac{z}{2} \leq \xi \leq 1 + \frac{z}{2} \end{cases} \tag{5}$$

Here the parameter z represents the dead zone and is assigned the value 0.7 [25]. The simulation is terminated if the average ABD value in the periprosthetic femur converges (Figure 3).

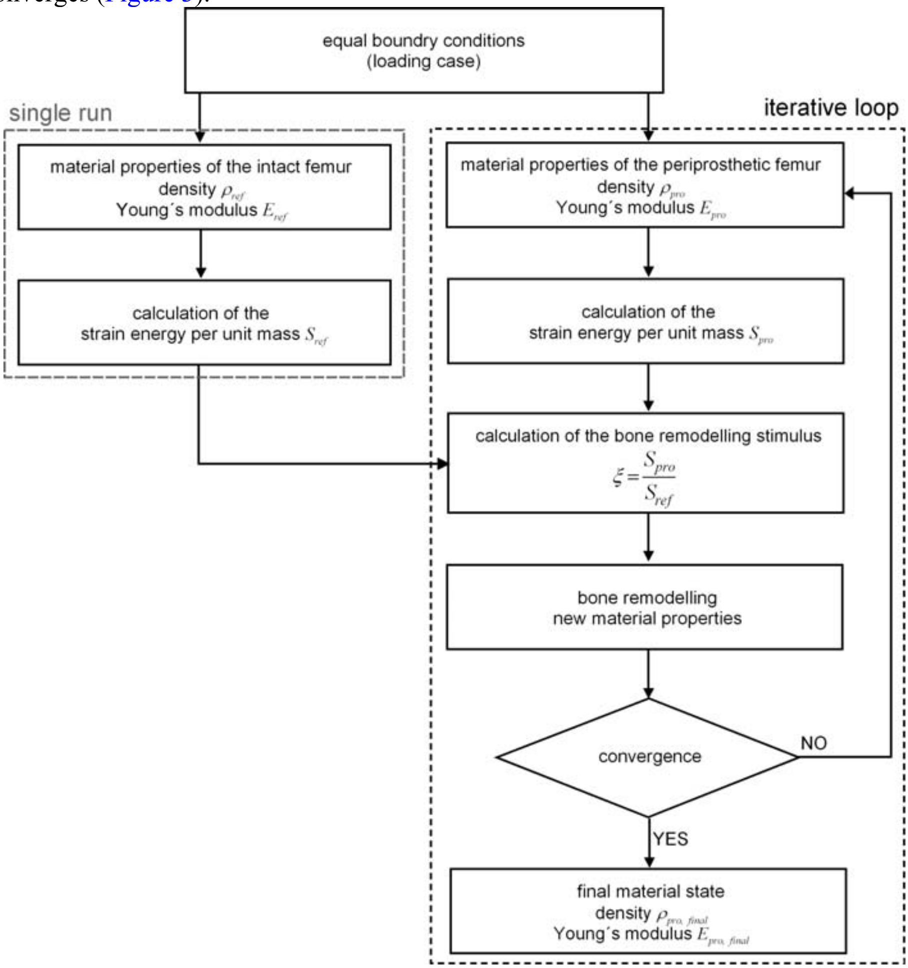

Figure 3: Schematic representation of the procedure for the bone remodelling simulation

Mean calculated ABD for each region of interest at each simulation step were calculated and tested for differences between the cemented and uncemented anchoring technique by a single-factorial analysis of variance (ANOVA).

Results

The distribution of the ESED in the intact bone is shown in Figure 4, acting as a reference. In order to illustrate the ESED distributions within the femur, a transverse section (TS) of the bone is shown. A maximum of the ESED of 0.06 mJ/mm^3 was found.

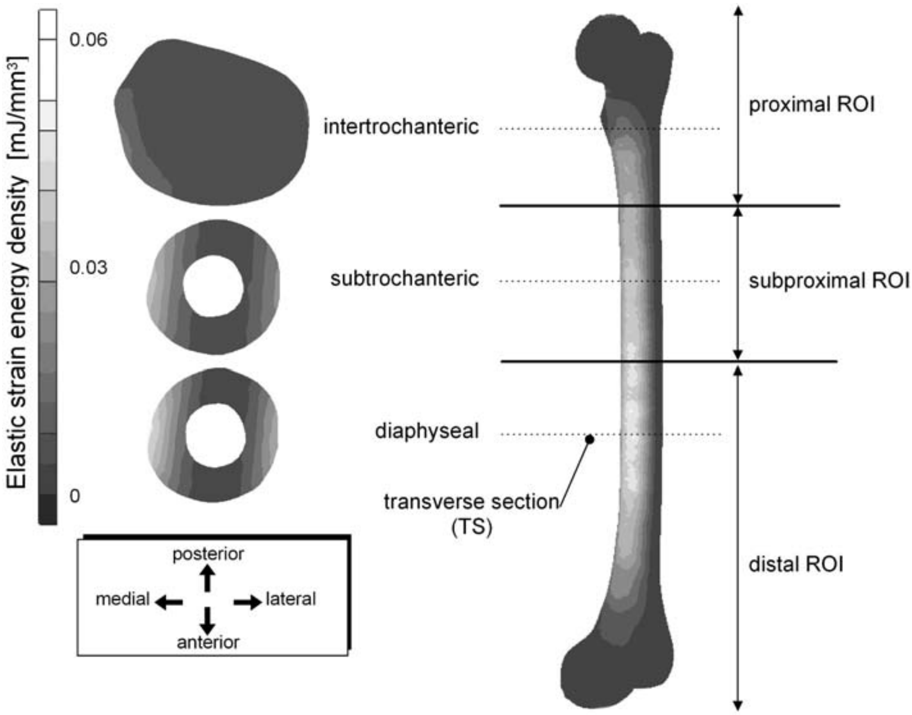

Figure 4: Distribution of the ESED in the intact femur

In Figure 5 the distribution of the ABD in the periprosthetic femora is illustrated. Bone densities at each simulation step in the three regions of interest are shown in Figure 6: Calculated and measured moments in the transversal plane left hip. Proximally both implantation techniques caused marked bone remodelling due to the ESED changes in the bone surrounding the implant. In the subproximal region, slight density changes were observed in the femur provided with the uncemented BICONTACT stem. The densities were significantly different between the cemented and uncemented prosthesis ($p < 0.001$). The ABDs in the model with the uncemented femoral stem were found to be significantly larger ($p < 0.05$). In the distal ROI, both models demonstrated no difference in the distribution of the ESED compared to the intact femur, so that no change of bone remodeling compared to the intact femur was calculated in this zone (Figure 5 and Figure 6: Calculated and measured moments in the transversal plane left hip). However, the slight differences in ABD in this region were still highly significant ($p < 0.001$).

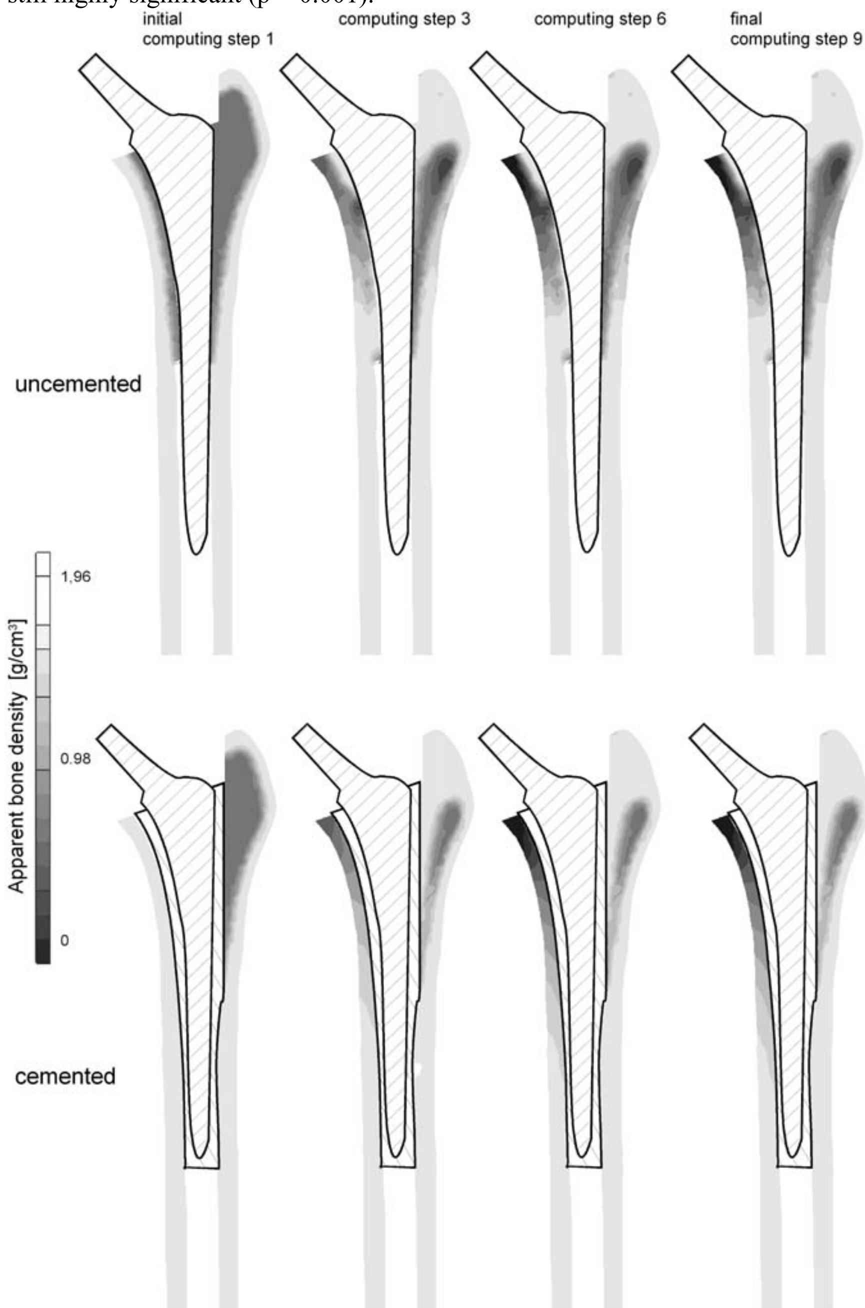

Figure 5: Distributions of ABD in the periprosthetic femora

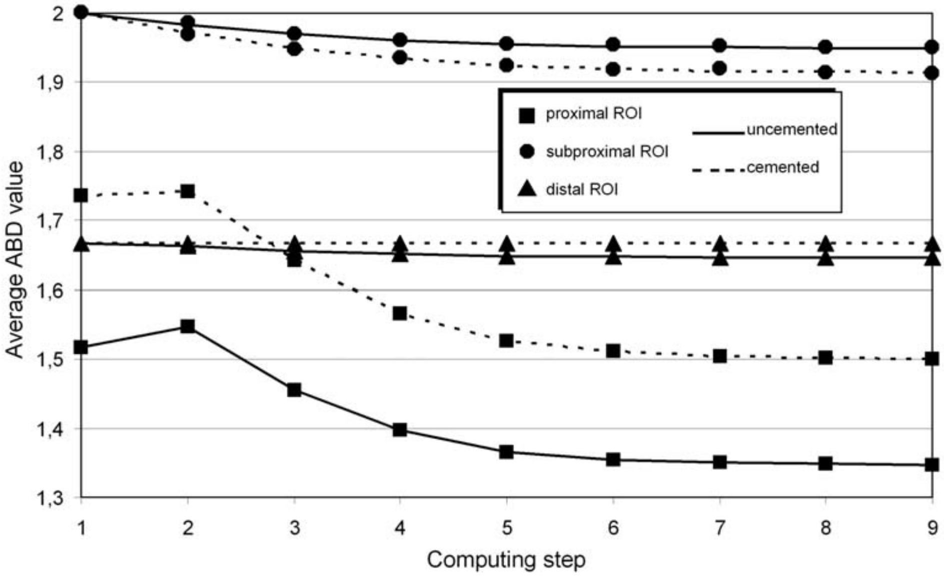

Figure 6: Calculated and measured moments in the transversal plane left hip

Discussion

In the study presented here, computer models of a femur after implantation of a cemented and uncemented BICONTACT femoral component were constructed and ABD changes over time were simulated by FE modelling. In the uncemented stem the situation after the implantation of the prosthesis was investigated when the femoral component was only fixed in the metaphyseal region. Therefore, the effect of ingrowth of the cementless prosthesis into the bone was not accounted for in this study so that the real strain energy distribution at the end of the remodelling simulation might be different from reality. However, as the uncemented femoral component exhibits a polished surface at the distal stem, no relevant diaphyseal fixation is expected.

Further simplifications were made concerning the hip joint forces and muscles. In this study, a simplified loading regime comprising three muscle forces according to Heller et al. [24] was used. Nevertheless, the large variations in the elastic properties of the bone among different individuals should exceed the error which is caused by these modelling simplifications.

In the literature, different mathematical approaches to compute the bone density evolution rate from mechanical stimuli are used (Figure 7: Mathematical material law for the bone remodelling simulation).

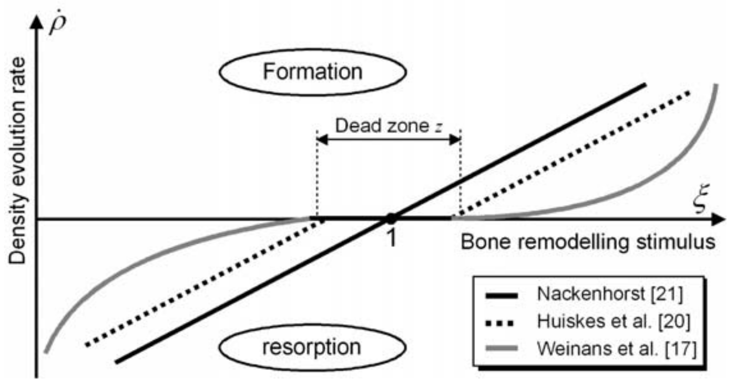

Figure 7: Mathematical material law for the bone remodelling simulation

On the one hand many clinical studies report that to a certain threshold, loading changes cause no bone remodelling [17,18,25] which supports a neutral or dead zone (Figure 7: Mathematical material law for the bone remodelling simulation). On the other hand the experimental determination of the density evolution rate as a function of the loading variation is extremely difficult [21]. For these reasons the model according to Huiskes et al. [16] was used in this work.

Kroger and coworkers [26] reported a decrease in periprosthetic bone density of 10% to 24% in the first postoperative year. In our study, the bone density was reduced by 11% and 14% in uncemented and cemented models, respectively. Nishii et al. [27] published a similar density decrease ranging from 9% to 24% after one year.The results of the clinical studies of Weise et al. [2] and Fritz et al. [3] indicate that there is no significant difference between the aseptic loosening rates of cemented and uncemented BICONTACT femoral components. In contrast, in our study we found small but highly significant differences between the cemented and uncemented anchoring techniques in periprosthetic bone densities over time. This underlines that bone remodelling is only one possible factor contributing to aseptic loosening. While finite element modelling is an appropriate method for evaluating the mechanical effects of new prosthetic designs, the biological reaction to an implant has to be included for a comprehensive investigation of femoral prosthetic components. Long-term clinical studies are needed for the evaluation of endoprosthetic designs in humans.

Acknowledgement

The study was realised in the framework of the collaborative research centre (SFB) 599 "Sustainable degradable and permanent implants made of metallic and ceramic materials". The authors thank the German Research Foundation (Deutsche Forschungsgemeinschaft) for the financial support of the project.
The authors also wish to thank the company AESCULAP AG & CO. KG for providing CAD data of the BICONTACT femoral component.

References

[1] F. Adam and D. Kohn, Computergestützte Entwicklung eines anatomischen Hüftprothesenschaftes, in Magazin Forschung, pp. 41-48 (Universität des Saarlandes, VMK- Verlag für Marketing und Kommunikation GmbH, Saarbrücken, Germany, 2000).

[2] K. Weise, C. Eingartner and E. Winter, Cemented versus uncemented hip replacement- rational decision making using the BICONTACT total hip system, in Zentralblatt für Chirurgie, 46-52 (Barth Verlage Heidelberg GmbH, Stuttgart, Germany, 2003).

[3] St. Fritz, R. Volkmann, E. Winter and C. Bretschneider, The BICONTACT hip endoprosthesis- a universal system for hip arthroplasty for traumatic and idiopathic indications results after 10 years, in European Journal of Trauma- E-Supplement, 18-22 (Urban & Vogel, Munich, Germany, 2001).

[4] R. Huiskes, H. Weinans, B. van Rietbergen: The relationship between stress shielding and bone resorption around total hip stems and the effects of flexible materials. Clin.Orthop. 274 (1992), 124-134.

[5] J. Wolff, Das Gesetz der Transformation der Knochen, (Hirschwald, Berlin, 1892).

[6] C. Mattheck, U. Vorberg and C. Kranz, Effects of hollow shaft endoprosthesis on stress distribution in cortical bone, in Biomedizinische Technik, pp. 316-319 (Fachverlag Schiel Schon, Berlin, Germany, 1990).

[7] C. L. Tai, C. H. Shih, W. P. Chen, S. S. Lee, Y. L. Liu and P. H. Hsieh, Finite element analysis of the cervico-trochanteric stemless femoral prosthesis, in Clinical Biomechanics, pp. S53-S58 (Elsevier Sci Ltd, Oxon, UK, 2003).

[8] W. Thomas, L. Lucente, N. Mantegna and H. Grundei, ESKA (CUT) endoprosthesis, in Orthopade, pp. 1243-1248 (Springer, New York NJ, 2004).

[9] N. Goetzen, F. Lampe, R. Nassut and M. M. Morlock, Load-shift-numerical evaluation of a new design philosophy for uncemented hip prostheses, in Journal of Biomechanics, pp. 595-604 (Elsevier Sci Ltd, Oxon, UK, 2005).

[10] S. K. Senapati and S. Pal, Finite element analysis: an effective tool for prostheses design, in Trends in Biomaterials and Artificial Organs, pp. 141-148 (Society for Biomaterials and artificial organs, Thiruvananthapuram, India, 2004).

[11] O. Mikhailov, L. N. Tkachenko, M. B. Shtern and V. A. Dubok, Optimization of the composition and geometric shape of implants based on computer modelling, in Powder Metallurgy and Metal Ceramics, 9-13 (Consultants Bureau, New York NJ, 2003).

[12] R. Huiskes, H. Weinans, H.J. Grootenboer, M. Dalstra, B. Fudala, T.J. Slooff: Adaptive bone-remodeling applied to prosthetic-design analysis. J.Biomech. 20 (1987), 1135-1150.

[13] M. Doblare and J. M. Garcia, Application of an anisotropic bone-remodelling model based on a damage-repair theory to the analysis of the proximal femur before and after total hip replacement, in Journal of Biomechanics (2001), 1157-1170.

[14] P. J. Prendergast and D. Taylor, Stress analysis of the proximo-medial femur after total hip replacement, in Journal of Biomedical Engineering 1990, 379-382.

[15] M. Taylor, K. E. Tanner, M. A. Freeman and A. L. Yettram, Cancellous bone stresses surrounding the femoral component of a hip prosthesis: an elastic-plastic finite element analysis, in Medical Engineering & Physics 1995, 544-550.

[16] R. Huiskes, H. Weinens, M. Dalstra: Adaptive bone remodeling and biomechanical design considerations for noncemented total hip arthroplasty. Orthopedics 12 (1989), 1255-1267.

[17] H. Weinans, R. Huiskes, H.J. Grootenboer: Effects of material properties of femoral hip components on bone remodeling. J.Orthop.Res. 10 (1992), 845-853.

[18] B. van Rietbergen, R. Huiskes, H. Weinans, D.R. Sumner, T.M. Turner, J.O. Galante: ESB Research Award 1992. The mechanism of bono remodeling and resorption around press-fitted THA stems. J.Biomech. 26 (1993), 369-382.

[19] H. Weinans, R. Huiskes, B. van Rietbergen, D.R. Sumner, T.M. Turner, J.O. Galante: Adaptive bone remodeling around bonded noncemented total hip arthroplasty: a comparison between animal experiments and computer simulation. J.Orthop.Res. 11 (1993), 500-513.

[20] R. Huiskes, B. van Rietbergen: Preclinical testing of total hip stems. The effects of coating placement. Clin.Orthop. 319 (1995), 64-76.

[21] U. Nackenhorst: Numerical simulation of stress simulated bone remodeling, Technische Mechanik, Band 17, Heft 1 (1997), 31-40.

[22] G. N. Duda, M. Heller, J. Albinger, O. Schulz, E. Schneider and L. Claes: Influence of muscle forces on femoral strain distribution, in Journal of Biomechanics 31 (1998), 841-846.

[23] G. Bergmann, G. Deuretzbacher, M.O. Heller, F. Graichen, A. Rohlmann, J. Strauss, G.N. Duda: Hip contact forces and gait patterns from routine activities. J.Biomech. 34 (2001), 859-871.

[24] M. O. Heller, G. Bergmann, J. P. Kassi, L. Claes, N. P. Haas, G. N. Duda, Determination of muscle loading at the hip joint for use in pre-clinical testing, Journal of Biomechanics 38 (2005), 1155-1163.

[25] J. Kerner, R. Huiskes, G.H. van Lenthe, H. Weinans, B. van Rietbergen, C.A. Engh, A.A. Amis: Correlation between pre-operative periprosthetic bone density and post-operative bone loss in THA can be explained by strain-adaptive remodelling. J.Biomech. 32 (1999), 695-703.
[26] H. Kroger, P. Venesmaa, J. Jurvelin, H. Miettinen, O. Suomalainen, E. Alhava: Bone density at the proximal femur after total hip arthroplasty. Clin Orthop Relat Res 1998, 66-74.
[27] T. Nishii, N. Sugano, K. Masuhara, T. Shibuya, T. Ochi, S. Tamura: Longitudinal evaluation of time related bone remodeling after cementless total hip arthroplasty. Clin Orthop Relat Res 1997, 121-131.

Medicine Meets Engineering
J. Hammer et al. (Eds.)
IOS Press, 2008

Evaluation of Biaxial Tension Tests of Soft Tissues

Jiri BURSA[1], Miroslav ZEMANEK
Institute of Solid Mechanics, Mechatronics and Biomechanics, FME, BUT, Brno, Czech Republic

Abstract. Soft tissues are pseudoelastic anisotropic materials; various formulas for their strain energy density have been proposed for modelling of their constitutive behaviour. However, the individual variance of elastic parameters is often more pronounced than their anisotropy, so that their constitutive relations can be modelled as either isotropic or orthotropic. Any hyperelastic model requires more mechanical tests to be input for an identification of its parameters than mere uniaxial tension tests; especially biaxial tension tests are very important also for isotropic hyperelastic materials. A design of a testing rig produced in cooperation of our institute with some local companies is presented. It enables us to carry out not only equibiaxial tension tests, but also some other biaxial tensile tests, because displacements in both mutually perpendicular directions can be controlled independently. The proposal of various types of biaxial tests is presented in the paper, with examples of their realization with porcine aortic wall tissue. The contribution focuses on ways of evaluation of the results and on identification of parameters of various constitutive models. The use of more mechanical tests in identification of constitutive parameters can improve the predictive capability of the models substantially.

Keywords. Mechanical testing, biaxial tension test, hyperelastic materials, soft tissue, strain energy density.

Introduction

In general, soft tissues are biological materials showing large strains and displacements. In most of these materials, their loading and unloading curves differ mutually only slightly and they stabilize themselves after several loading cycles, called "pre-conditioning". These materials are called pseudoelastic and are mostly modelled as hyperelastic or viscoelastic (with time-dependent deformation). If the dissipative part of the strain energy can be neglected then the material is modelled as hyperelastic, it means a strain energy density function is postulated.

1. Experimental Equipment

The experimental equipment (Figure 1) consists of a bedplate with two step motors and orthogonally oriented ball screws, four carriages, equipment for clamping of the

[1] Corresponding Author: Jiri Bursa, Brno University of Technology, Faculty of Mechanical Engineering, Technicka 2, 61669 Brno, Czech Republic; E-mail: bursa@fme.vutbr.cz.

specimens, specimen bath with physiological saline solution, support stand with programmable camera and computer with software system for test control.

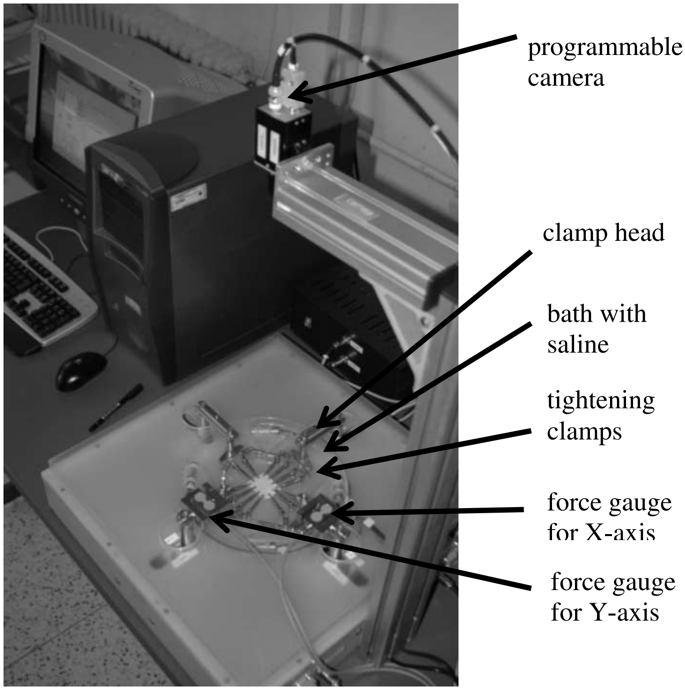

Figure 1. Biaxial testing rig

Equipment for clamping of the specimens consists of four carriages with four clips each and two sensing heads with force gauges. The specimen can be clamped by two or four clips on every edge; a system of levers ensures a uniform distribution of load among the clamps. The force of clamping is adjusted with a torque spanner to hold the specimen damage as low as possible. The specimen can be immersed in physiological saline solution with fixed temperature. As a contactless strain evaluation is necessary at soft tissues, several markers are located in the central part of the specimen, where the uniformity of the stress-strain state is not deteriorated by local effects in the surroundings of clamps. The position of markers is scanned in preset time intervals by a programmable CCD camera and recorded together with the corresponding values of forces which are measured in each of the directions by an S-shaped force gauge. Evaluation of strains (or more preciously, stretch ratios, i.e. components of deformation gradient tensor) is based on evaluation of positions of the markers (or, more exactly, their centres of gravity) before and during the loading.

2. The Process of Testing

The biaxial testing rig was used for testing of specimens of porcine thoracic aorta (Figure 2). The specimen with a square or another rectangular shape is cut-out from the

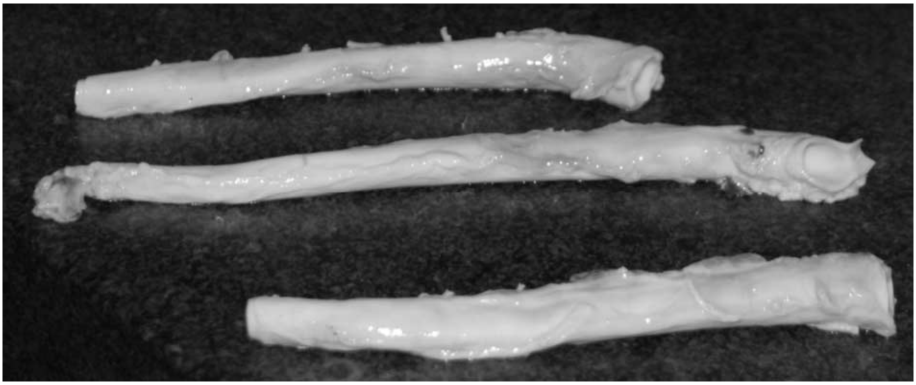

Figure 2. Porcine thoracic aortas

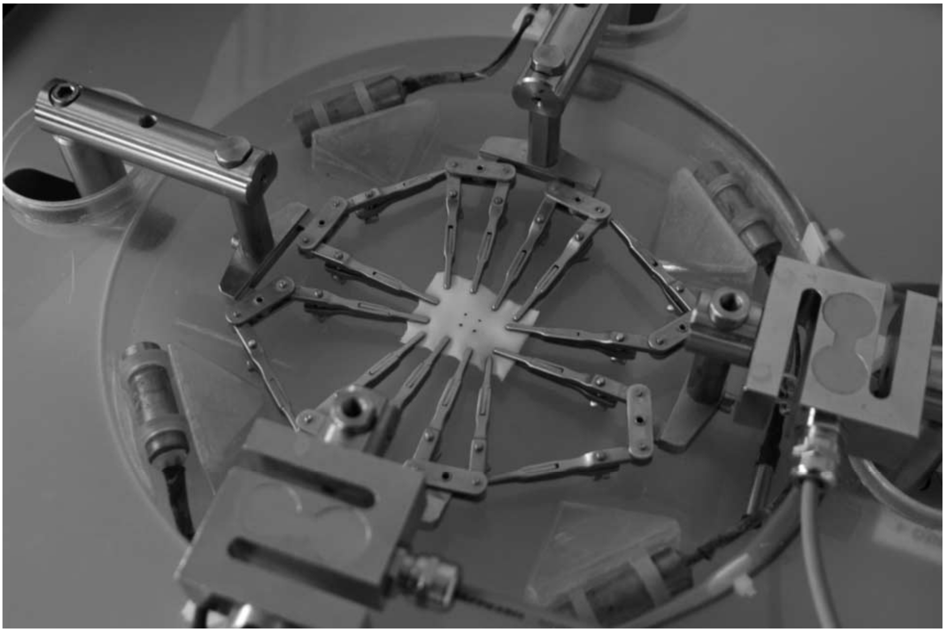

Figure 3. Gripped rectangle specimen with the reference points

aorta and circumferential and axial directions of aorta are recorded. Four reference markers are located in the central part of the specimen; these are either black points [1] marked on the specimen surface (Figure 3), or 1 mm diameter steel balls ([2],[3]) glued onto the specimen surface. Then the specimen is loaded by controlled forces or displacements. Positions of reference points or steel balls are on-line monitored by the CCD camera and these images are recorded. After having finished the experiment, the recorded images can be processed by the special software (Tibixus) for off-line image analysis. The data comprehend also information on loads and dimensions of the specimen, so that the results consist of stretch ratios (inferred from the positions of the markers), loading forces and Cauchy (true) stresses. In the end, principal stresses vs. principal components of deformation gradient tensor can be displayed.

3. Types of Tests

Mechanical tests of soft tissues are realized using a specimen „in vitro“. The independent control of displacements in both directions enables us to obtain the stress-strain characteristics for various states of biaxial tension, not only for equibiaxial tests. It is possible to obtain stress-strain characteristics (see [4], [5]) e.g. in the following types of tests (Figure 4):

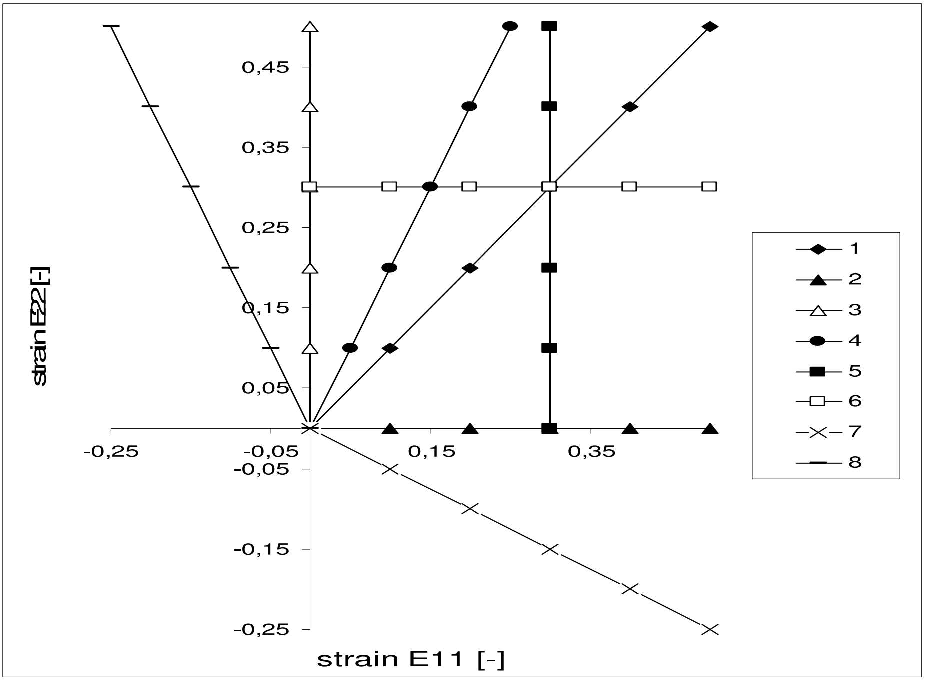

Figure 4. Changes of strain components in various types of tests

a) equibiaxial tension test - with equal strains in both principal directions (curve 1)
b) biaxial tension test with constrained (zero) transversal contraction (curves 2, 3)
c) biaxial tension test with proportional strain components (curve 4)
d) biaxial tension test with constant non-zero strain in one direction (curves 5, 6)
e) uniaxial tension test (curves 7, 8).

It is known in the theory of elasticity, that some different stress-strain states (and consequently tests as well) are mutually equivalent for isotropic incompressible materials; e.g., equibiaxial tension is equivalent to uniaxial compression, uniaxial tension is equivalent to equibiaxial compression, pure or simple shears are equivalent to tension or compression under plain strain conditions. In general, however, these equivalences are not valid for orthotropic materials. Fortunately, all the real stress states in arterial wall correspond to various types of biaxial tension, with a relatively low compression in radial direction only.

However, another feature of these tests should be emphasized. Tests of hyperelastic material should cover all the range of strains expected in the real body. Also the density of experimental points in all the parts of this range should be sufficiently high to prevent false values calculated by the constitutive model what is possible especially at polynomial models of higher orders (more complex shapes of stress-strain curves). However, if the real stress-strain state does not correspond to uniaxial tension conditions, then stresses in both principal directions (as well as strain energy density) depend on both components of strains. It means the constitutive relation is represented graphically not only by a curve, but by a general skew surface (see figure 5). And if such a surface is required to be described (modelled) by an analytical function, than it should be covered with a sufficient density of experimental points in all the regions in question. Therefore more types of mechanical tests are required in the case of hyperelastic, especially anisotropic materials.

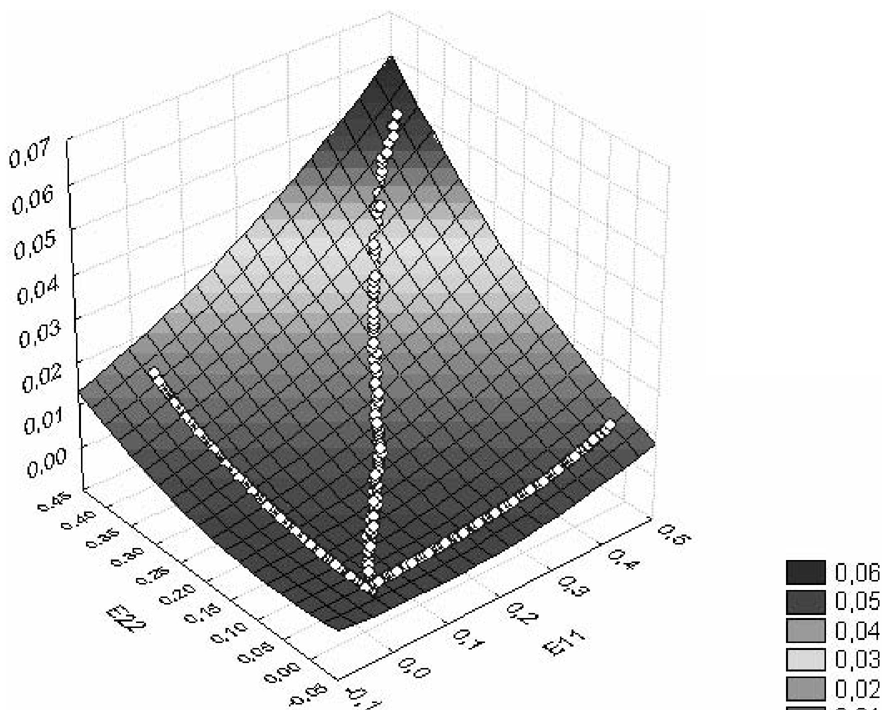

Figure 5. The regression surface of the strain energy function

4. Overview of Frequent Types of Constitutive Relations

Appropriate constitutive relations are needed for computational modelling of different types of stress-strain states in arteries. Hyperelastic constitutive relations, isotropic as well as orthotropic, represent a mathematical description of relations among stress and strain components that are derived from the strain energy density function W. If such a strain-energy function exists, the stress components can be obtained as derivatives of W with respect to the corresponding strain components:

$$S_{11} = \frac{\partial W}{\partial E_{11}} \qquad S_{22} = \frac{\partial W}{\partial E_{22}} \tag{1}$$

where S_{ij} is a component of the 2nd Piola-Kirchhoff stress tensor (conjugated with Green-Lagrange strain tensor E_{ij}).

For an identification of parameters from experimental data, a selection of a convenient constitutive model is necessary. These models can be either phenomenological, or based on some information on the tissue structure (histology). For soft tissue applications, the most frequent phenomenological orthotropic constitutive models are defined on the base of the following strain energy density functions (see [1],[6]):

- Polynomial model [7]:

$$W = c_1 E_{11}^2 + c_2 E_{11} E_{22} + c_3 E_{22}^2 + c_4 E_{11}^3 + c_5 E_{11}^2 E_{22} + c_6 E_{11} E_{22}^2 + c_7 E_{22}^3 \tag{2}$$

- Exponential model:

$$W = \frac{C}{2}.\left(e^{Q} - 1\right) \tag{3}$$

where either $Q = c_1 E_{11}^2 + c_2 E_{22}^2 + 2.c_3 E_{11} E_{22}$ (4)

represent a two-dimensional form ([8] or [9]), or

$$Q = c_1 E_r^2 + c_2 E_t^2 + c_3 E_z^2 + 2c_4 E_t E_r + 2c_5 E_t E_z + 2c_6 E_z E_r \tag{5}$$

in the more general 3D form used in [10].

- Logarithmic model[2] [11]:

$$W = -C.\ln(1 - Q) \quad , where\ Q = \frac{1}{2} c_1 E_{11}^2 + \frac{1}{2} c_2 E_{22}^2 + c_3 E_{11} E_{22} \tag{6}$$

- While the above models are phenomenological, the model proposed (in [12]) for the individual layers of arterial wall is based on some histological information on (collagen) reinforcing fibres in the layer. The strain energy density formula consists of an isotropic and an anisotropic parts (Eq. 7a); the isotropic part is expressed in neo-Hookean form (Eq. 7b), while the anisotropic part is described by an exponential function (Eq. 7c):

$$W = W_{iso} + W_{aniso} \tag{7a}$$

[2] The logarithmic model is limited by maximum strain values on the order of 10^{-1} (the tissue-specific range depends on its values of material parameters); for excessive strains the value of Q extends beyond 1 and ln(1-Q) is not defined.

$$W_{iso} = \frac{C}{2}\left(\overline{I_1} - 3\right) \tag{7b}$$

$$W_{aniso} = \frac{c_1}{2c_2} \sum_{i=4,6} \left\{ \exp\left[c_2 \left(\overline{I_i} - 1\right)^2 \right] - 1 \right\}, \tag{7c}$$

where $\overline{I_i}$ are modified invariants of right Cauchy-Green deformation tensor; the 4th and 6th invariants incorporate the direction vectors of the two families of fibres[3].

- Alternatively, the strain energy density function can be expressed as a sum of volumetric and deviatoric parts. For example, a general polynomial formula for the deviatoric part of the strain energy function [13] can be used in the following form:

$$W_{dev} = \sum_{i=1}^{3} a_i \left(\overline{I_1} - 3\right)^i + \sum_{j=1}^{3} b_j \left(\overline{I_2} - 3\right)^j + \sum_{k=2}^{6} c_k \left(\overline{I_4} - 1\right)^k + \sum_{l=2}^{6} d_l \left(\overline{I_5} - 1\right)^l$$
$$+ \sum_{m=2}^{6} e_m \left(\overline{I_6} - 1\right)^m + \sum_{n=2}^{6} f_n \left(\overline{I_7} - 1\right)^n + \sum_{o=2}^{6} g_o \left(\overline{I_8} - \varsigma\right)^o \tag{8}$$

Here a_i, b_j, c_k, d_l, e_m, f_n, g_o are material parameters and ς is a specific constant related to the directions of fibers.

5. Identification of parameters from experimental data

Alternatively to the usual least square method applied with calculated and measured stress values, an energy-based nonlinear function f_w may also be chosen (from the mathematical point of view both approaches are equivalent):

$$f_w = \sum_{i=1}^{n} \left(\psi_i - W_i\right)^2 , \tag{9}$$

where ψ_i is the strain energy for i-th data point[4] predicted by the constitutive model and

$$W_i = \int_0^{E_{11}^i} S_{11}^i dE_{11}^i + \int_0^{E_{22}^i} S_{22}^i dE_{22}^i \tag{10}$$

is the strain energy computed from experimental data.

Transformation of experimental data to mathematical model using this energy-based approach is shown in the following example. A numerical integration is used for Eq. (10) in the following form[4]:

$$W = \sum_{j=1}^{2} \sum_{i=1}^{n} \frac{S_{jj}^i + S_{jj}^{i-1}}{2} \left(E_{jj}^i - E_{jj}^{i-1}\right) \tag{11}$$

The best fit of the material model to experimental data is achieved if function f_w achieves its minimum.

Strain energy density function W is calculated from experimental data of three types of tests:

---

[3]In all of the above formulas, C and c_i are material parameters.

[4] n = number of experimental data points.

- two uniaxial tension tests with constrained transversal deformation (Figure 4 - curves 2, 3),

- equibiaxial tension test (Figure 4 - curve 1).

Using the off-line image analysis (the used software Tibixus was produced by P. Skacel), Cauchy stresses and principal stretch ratios in two orthogonal directions are obtained. These data are then expressed in the form of conjugated tensors, i.e. as 2nd Piola-Kirchhoff stress tensor and Green-Lagrange strain tensor. The parameters $C,\ c_1,\ c_2,\ c_3$ are then obtained by means of the standard nonlinear Levenberg-Marquardt algorithm for multivariate nonlinear regression by minimizing the strain-energy function. In physiological range of loading, the best-fit parameters were obtained by using logarithmic model for the strain-energy function (Eq. 6). The shape of the strain energy density function is presented in figure 5. When the parameters of the strain energy function have been identified, the stress components can be obtained as derivatives of W with respect to the corresponding strain components (Eq. 1):

$$S_{11} = \frac{\partial W}{\partial E_{11}} = \frac{C\left(c_1 E_{11} + c_3 E_{22}\right)}{1 - \left(\frac{1}{2} c_1 E_{11}^2 + c_3 E_{11} E_{22} + \frac{1}{2} c_2 E_{22}^2\right)} \tag{12a}$$

$$S_{22} = \frac{\partial W}{\partial E_{22}} = \frac{C\left(c_3 E_{11} + c_2 E_{22}\right)}{1 - \left(\frac{1}{2} c_1 E_{11}^2 + c_3 E_{11} E_{22} + \frac{1}{2} c_2 E_{22}^2\right)} \tag{12b}$$

Relations between principal Cauchy stresses σ_{ii} and 2nd Piola-Kirchoff stresses S_{ii} stresses are (under assumption of an incompressible material):

$$\sigma_{ii} = S_{ii} \cdot \lambda_i^2 \tag{13}$$

Comparison of experimental stress-strain data and curves calculated using Eqs. (12) and (13) are in figures 6, 7, 8:

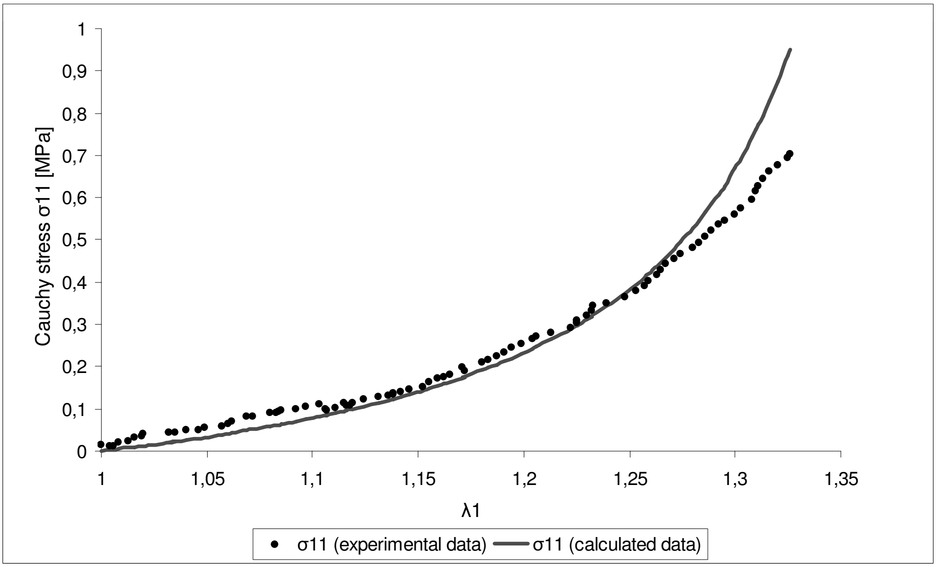

Figure 6. Tension test – uniaxial tension in "1" direction with constrained transversal contraction in „2“ direction

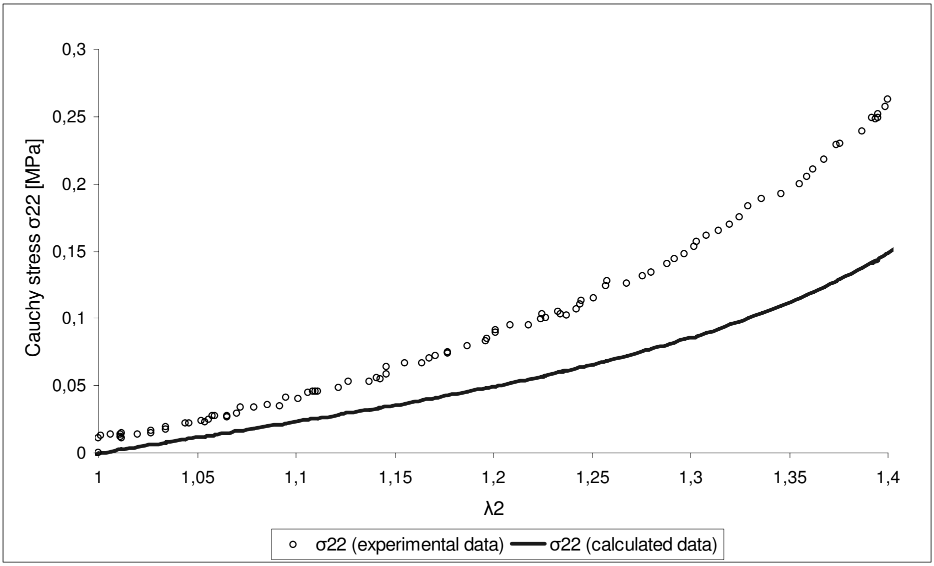

Figure 7. Tension test – uniaxial tension in "2" direction with constrained transversal contraction in „1“ direction

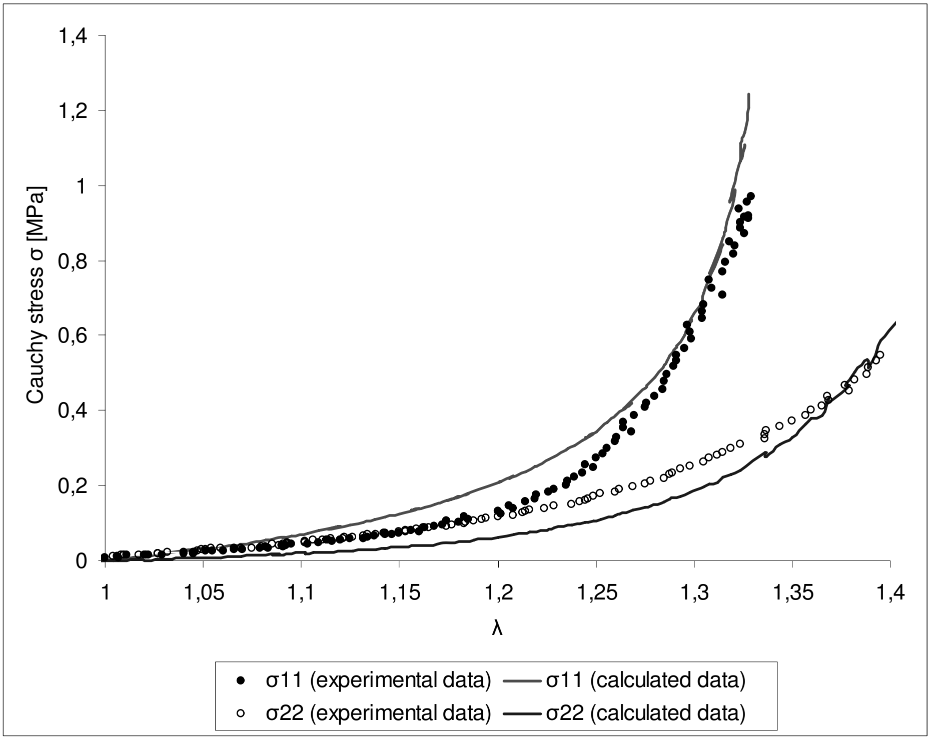

Figure 8. Results of equibiaxial tension test - experiment vs. model

6. Discussion

The results presented above show some interesting features. At the beginning, however, it should be mentioned that biaxial tests with constrained transversal deformation (figures 6 and 7) do not correspond to trajectories 2 and 3 in figure 4. As the transversal displacements are constrained only by the two or four narrow clamps (see figure 3), the transversal displacements of reference points in the central part of the specimen are non-zero, as well as transversal strain that is negative here. The exact ratio between transversal and longitudinal strains depends on the type and size of anisotropy and is determined by the material structure.

The presented material (porcine aortic wall) is much stiffer in direction "1" (longitudinal direction in the artery) than in direction "2" (circumferential). If loaded in direction "1", the material shows (in the central part of the specimen) negative transversal strains close to uniaxial stress conditions (curve 7 in figure 4) rather than to plane strain state (curve 2 in figure 4). Probably the low transversal stiffness enables the material large local deformation in the surroundings of clamps. Conversely, if loaded in direction "2", the high transversal stiffness constrains substantially the transversal strains and the test is much closer to the plain strain conditions (curve 3 in figure 4). To achieve plane strain conditions more preciously in these tests, it would be necessary to control the transversal movement of clamps by a feedback from strain values; this is not possible, because the strains are not evaluated on-line. The only realizable possibility is to load the specimen by a lower, but non-zero deformation rate also in the transversal direction. Fortunately, the credibility of the constitutive model identification is not limited by this fact; the real measured curve lies somewhere between uniaxial tension and biaxial tension under plain strain conditions (curves 2 and 7, or 3 and 8 in figure 4).

Comparison of the experimental results of uniaxial tension tests (with limited transversal deformation) for both directions shows that the material appears highly anisotropic. In direction "1", Cauchy stress of 0,675 MPa corresponds to stretch ratio 1.32 , while in direction "2" the stress is about four times lower (0,170 MPa at the same stretch ratio). In equibiaxial tension test, however, the stresses (at the same values of both of the stretch ratios) are 0,815 MPa and 0,300 MPa in directions "1" and "2", respectively; the size of anisotropy (i.e. the ratio of these stresses) is substantially lower here (about 2,7). Also this difference confirms that more types of tests, especially biaxial ones, are necessary for a reliable identification of parameters of constitutive models.

7. Conclusion

The present study deals with the equipment and methodology enabling us a credible identification of parameters of orthotropic hyperelastic constitutive equations for soft tissues of arterial wall. As the stress states in arterial wall are at least biaxial, these constitutive equations describe several general skew surfaces in 3D representation. Each of these surfaces should be covered by experimental points with a sufficient density, especially in the parts corresponding to the real "in vivo" strain states. Otherwise the results of computational modelling can be false similarly to those lying outside of the range of experimental data, e.g. in the case of uniaxial stress state.

References

[1] Y. C. Fung: Biomechanics, Mechanical Properties of Living Tissues, *Springer-Berlin* , (1993).

[2] J. D. Humphrey, R. K. Strumpf, F. C. P. Yin: Determination of a Constitutive Relation for Passive Myocardium: I. A New Functional Form, J., *Journal of Biomechanical Engineering* **112** (1990), 335.

[3] D. H. S. Lin, F. C. P. Yin: A Multiaxial Constitutive Law for Mammalian Left Ventricular Myocardium in Steady-State Barium Contracture or Tetanus, *Transactions of the ASME* **120** (1998), 505.

[4] J. D. Humphrey: Cardiovascular Solid Mechanics; Cells, Tissues and Organs. *Springer-Verlag New York*., (2002).

[5] M. Vajdak, J. Bursa: Experiment planning in evaluation of soft tissue mechanical characteristics, *Biomechanics of Man* (2002), Cejkovice, 286 – 288.

[6] Ch.A.J. Schulze-Bauer, Ch. Mörth, G.A. Holzapfel: Passive Biaxial Mechanics Response of Aged Human Iliac Arteries, *Journal of Biomechanical Engineering*, **125** (2003), 395-406.

[7] D.J. Patel, R.N.Vaishnav: The Rheology of Large Blood Vessels. Cardiovascular Fluid Dynamics **2**, *Academic Press, London and New York*, (1972).

[8] Y.C.Fung, K. Fronek, P. Patitucci: Pseudoelasticity of Arteries and the Choice of its Mathematical Expression. *Amer. Journal of Physiology* **237** (1979), H620-H631.

[9] W.W.v.Maltzahn, R.G.Warriyar, W.F.Keitzer: Experimental measurements of elastic properties of media and adventitia of bovine carotid arteries. *Journal of Biomechanics* **17** (1984), 839-847.

[10] C.J.Chuong and Y.C.Fung: Residual stress in arteries. In: Frontiers in Biomechanics, *Springer Verlag New York,* (1986).

[11] K.Takamizawa, K.Hayashi: Strain energy density function and uniform strain hypothesis for arterial mechanics. *Journal of Biomechanics* **20**, (1987), 7-17.

[12] G.A.Holzapfel,, T.C.Gasser, R.W.Ogden: A New Constitutive Framework for Arterial Wall Mechanics and a Comparative Study of Material Models, *Journal of Elasticity* **61**, (2000), 1-48.

[13] ANSYS User's Manual, Version 10.0, Theory, Chapter 4.7.5.

Medicine Meets Engineering
J. Hammer et al. (Eds.)
IOS Press, 2008

Fundamental Mechanisms of Fatigue and Fracture

Hans-Jürgen CHRIST[a,1]

[a] *Institut für Werkstofftechnik, Universität Siegen, Germany*

Abstract. A brief overview is given in this article on the main design philosophies and the resulting description concepts used for components which undergo monotonic and cyclic loading. Emphasis is put on a mechanistic approach avoiding a plain reproduction of empirical laws. After a short consideration of fracture as a result of monotonic loading using fracture mechanics basics, the phenomena taking place as a consequence of cyclic plasticity are introduced. The development of fatigue damage is treated by introducing the physical processes which (i) are responsible for microstructural changes, (ii) lead to crack initiation and (iii) determine crack propagation. From the current research topics within the area of metal fatigue, two aspects are dealt with in more detail because of their relevance to biomechanics. The first one is the growth behaviour of microstructural short cracks, which controls cyclic life of smooth parts at low stress amplitudes. The second issue addresses the question of the existence of a true fatigue limit and is of particular interest for components which must sustain a very high number of loading cycles (very high cycle fatigue).

Keywords. Fracture mechanics, fatigue design, crack propagation, VHCF

Introduction

Biomechanical parts are often made of metallic materials and used under monotonic and cyclic loading conditions. From a solely mechanical point of view, damage and failure develop in an identical manner as it is the case for engineering parts. Hence, the same basic mechanisms control damage evolution and the same design concepts should be applied, in order to avoid intolerable failure.

This article tries to shed light on the fundamental mechanisms which are taking place during mechanical loading of metallic materials and which are responsible for the evolution of damage leading potentially to failure. The corresponding design concepts are introduced and critically discussed with respect to the range and limits of applicability. The first chapter deals with monotonic loading conditions and shows that the suitable design rule depends strongly on the ductility of the material and the presence of flaws. Cyclic loading conditions lead to fatigue and are much more susceptible to failure in engineering practice. In chapter two examples are given illustrating the sequence of processes (i) cyclic hardening/softening and saturation, (ii) strain localization and crack initiation and (iii) crack propagation and fracture. Two current research issues are briefly introduced in chapter 3. The particular and to some extent hardly predictable propagation behaviour of microstructurally short fatigue cracks is illus-

[1] Corresponding Author: Prof. Dr.-Ing. Hans-Jürgen Christ, Institut für Werkstofftechnik, Universität Siegen, D-57068 Siegen; hans-juergen.christ@uni-siegen.de

trated and the question is addressed, whether from the physical point of view a true fatigue limit exists.

1. Monotonic Loading

From an engineering viewpoint, loading conditions are not considered to be critical, if mainly monotonic static or quasi-static loading prevails in combination with ambient temperature. The available armamentarium developed during centuries in mechanical engineering and materials science provides reliable and robust design concepts and rules.

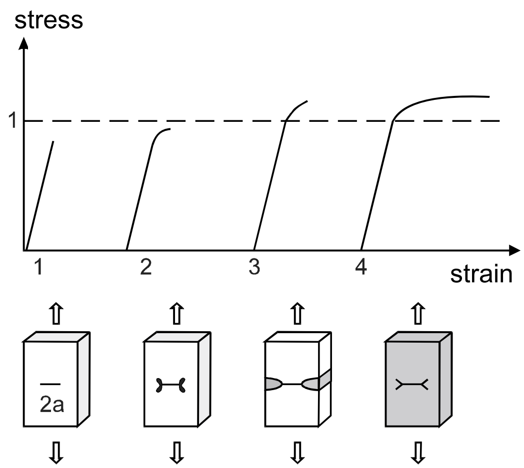

Figure 1. Schematic representation of stress-strain curves of materials of different ductility and their respective response to a centre crack of length *2a* (after [1])

In Figure 1 four different stress-strain curves of tensile loading are plotted for a specimen geometry containing a centre crack of length *2a*. The ductility of the materials increases from curve 1 through curve 4. The size of the corresponding plastic zone ahead of the crack tip expands with the ductility and stretches across the entire cross section in case 4. As a consequence of the high ductility in this case, the presence of the crack does not affect the loading capacity. A respective part can be constructed on the basis of the ultimate tensile strength R_m or more conservatively the yield strength $R_{p0,2}$ from tensile tests performed on crack-free samples. Case 1 is the classical case for the application of linear elastic fracture mechanics. The brittle behaviour of the material leads to fracture before appreciable plastic deformation develops. In order to avoid failure, the stress intensity factor K_I, which describes the stress field around the crack tip (see Figure 2) must not reach or exceed the critical stress intensity factor K_{Ic} (often also called fracture toughness), which must be determined experimentally. Small-scale yielding as shown in case 2 is typical of high-strength metallic materials. The linear elastic fracture mechanic (LEFM) approach can also be used in this case, however a simple expansion has to be taken into account using the sum of the crack length and the radius of the plastic zone instead of the plain crack length.

A large size of the plastic zone (case 3) violates the assumptions of LEFM and hence elastic-plastic mechanics must be employed. Instead of K_I more complicated loading parameters have been introduced in the literature, the most prominent are probably the *J*-integral or the crack tip opening displacement (*CTOD*). The load capacity is reached at the corresponding critical value of the respective parameter.

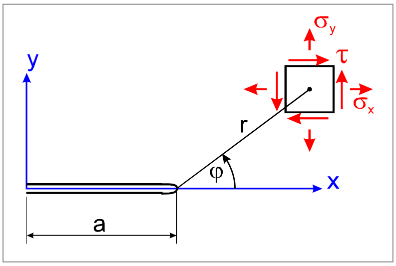

$$\sigma_x = \frac{K_I}{\sqrt{2\pi r}} \cos\frac{\varphi}{2}(1 - \sin\frac{\varphi}{2}\sin\frac{3\varphi}{2})$$

$$\sigma_y = \frac{K_I}{\sqrt{2\pi r}} \cos\frac{\varphi}{2}(1 + \sin\frac{\varphi}{2}\sin\frac{3\varphi}{2})$$

$$\tau = \tau_{xy} = \frac{K_I}{\sqrt{2\pi r}} \cos\frac{\varphi}{2}\sin\frac{\varphi}{2}\cos\frac{3\varphi}{2}$$

$$K_I = \sigma\sqrt{\pi a}\, Y_I\left(\frac{a}{w}\right)$$

Figure 2. Near crack tip stress field and stress intensity factor in LEFB

The application of the stress intensity factor for design purposes means that this parameter is assumed to dominate the onset or continuation of crack advance in a material. As seen in Figure 2, K_I is a measure of the intensity of the near-tip stress field under linear elastic conditions. The equations describing this stress field are approximate, asymptotic solutions which deviate from the full elasticity solutions, which include higher order terms, *e.g.* the so-called *T*-term. This deviation increases with increasing distance to the crack tip.

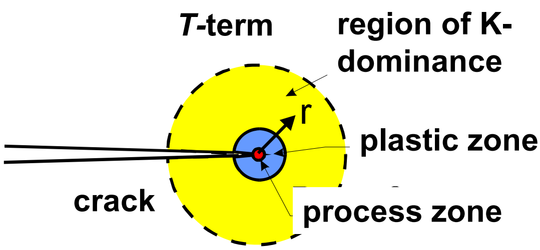

Figure 3. The various zones around a crack tip which may dominate crack advance

Consequently, the region of *K*-dominance is limited by an outer radius (Figure 3). Furthermore, the calculated stress singularity at the crack tip is not realistic. In ductile solids, the material at the crack tip yields when the near-tip stress exceeds the flow strength and the linear elastic solution loses its validity within the plastic zone. Even if the crack tip plastic deformation zone is very small, *e.g.* in the case of a brittle ceramics, a zone of failure processes, often referred to as process zone, limits the region of *K*-dominance towards the crack tip. Despite all the restrictions mentioned above, the *K* concept is widely and successfully applied to determine the loading capacity of flaw-containing components of high-strength.

2. Cyclic Loading

More than 90 pct of the failure cases in mechanical engineering, which are a consequence of mechanical loading, result from fatigue [2]. Repeatedly acting loads can cause sudden and unexpected failure, even if the maximum stress never reached the macroscopic yield strength $R_{p0,2}$. Fatigue damage develops evolutionary and is macroscopically often not accompanied by a shape change, which would announce the fracture. Figure 4 shows the main stages of damage evolution during the fatigue process.

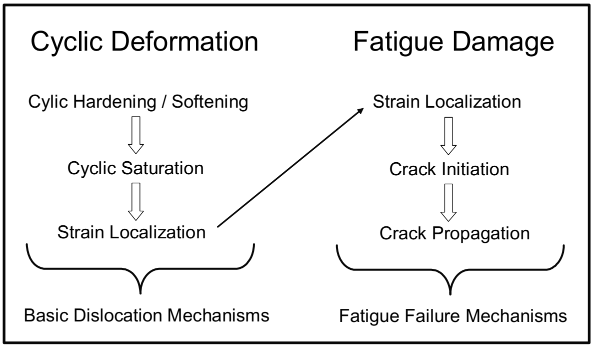

Figure 4. Main stages of fatigue damage evolution [3]

Metallic engineering materials are usually either annealed or thermomechanically pretreated before applied as components in service. Cyclic plastic deformation results in an increase or decrease of strength (cyclic hardening or softening) and reach often after this transient process a stage of cyclic saturation. This stage is characterized by the observation that the stress-strain response is stabilized, *i.e.* the strain amplitude is constant in tests at a constant stress amplitude and *vice versa*. This means from a microstructural viewpoint that a constant dislocation arrangement establishes. *In-situ* observations by means of transmission electron microscopy (TEM) have documented that the permanence of the dislocation arrangement in cyclic saturation results from a highly dynamic equilibrium of dislocation annihilation and production [4]. The type of dislocation structure formed depends mainly on the slip character of the dislocations in the material. If dislocations are restricted in glide to their slip plane (planar slip), planar arrangements form, whereas the ability of cross slip enables the dislocations to leave the slip plane (wavy slip) and to form three-dimensional geometric arrangements. Furthermore, the type of dislocation arrangement is controlled by the loading amplitude. Low plastic strain amplitudes can be accomplished by means of single slip, *i.e.* only one slip system is activated, while higher amplitudes require multiple slip.

Figure 5 depicts four TEM micrographs showing different dislocation arrangements which are typical of metallic materials of wavy dislocation slip character. Single slip leads to the formation of dislocation bundles or veins (Figure 5a) at low plastic strain amplitudes. If the amplitude is increased slightly, so-called persistent slip bands (PSB) can form with the bundle/vein matrix (Figure 5b). Plastic deformation is highly concentrated in the PSB leading to the formation of slip lines where they reach the surface. The resulting protrusions consist of extrusions and intrusions and can act as crack initiation sites. A further increase in plastic strain amplitude activates an additional slip system. The mutual interaction of the dislocations from two slip systems can lead to the formation of a labyrinth dislocation arrangement (Figure 5c). At high plastic strain amplitudes, dislocation cells prevail (Figure 5d). The cell walls are characterized by a high dislocation density, whereas the cell interior is dislocation-poor.

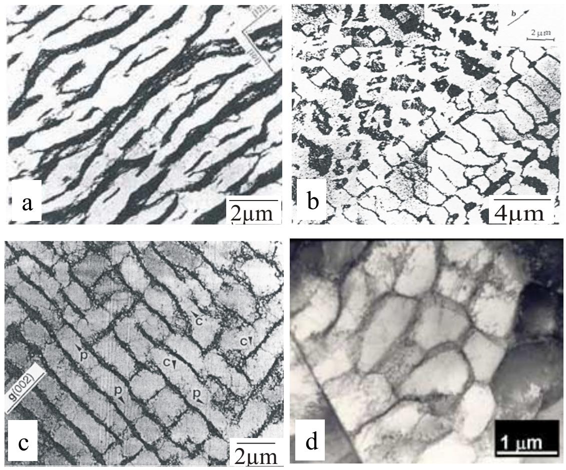

Figure 5. Typical dislocation arrangements of wavy-type materials. The plastic strain amplitude increases from a) through d): a) bundle/vein structure, b) persistent slip bands embedded in a matrix structure, c) labyrinth structure and d) cell structure

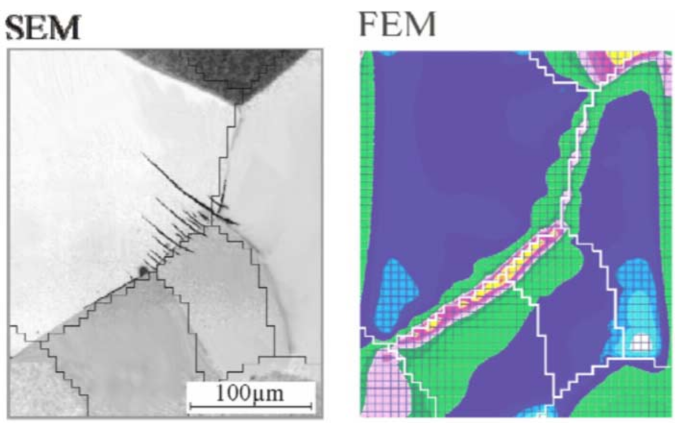

Figure 6. Comparison of a SEM micrograph showing cracks formed at a grain boundary with the calculated distribution of the stresses arising from elastic anisotropy

As indicated in Figure 4, crack initiation is a consequence of a strain localization in the case of a material free of internal and surface defects. Besides the PSBs mentioned above, any kind of local differences in mechanical properties may lead to stress concentrations, particularly at interfaces, and hence can give rise to the formation of cracks. An example is shown in Figure 6 which compares a micrograph taken in a scanning electron microscope (SEM) with a corresponding visualization of the result of a finite-element method (FEM) calculation [5]. The calculation considers the experimentally determined grain orientations and the grain shapes and takes into account that the beta titanium alloy LCB studied exhibits an elastic anisotropy. Since the elastic stiffness depends on the crystallographic orientation, compatibility stresses result at the grain boundaries and add to the externally applied stresses. The grain boundaries with the highest calculated total stress are most susceptible to crack initiation and show indeed microcracks in the SEM micrograph. It should be noted that in engineering materials often inclusions, large precipitates or pores act as crack initiation sites.

The stage of crack initiation is followed by stable fatigue crack growth (see Figure 4). The so-called *damage tolerant approach*, which is often used in the aircraft industry, ignores the stages of crack initiation and short crack propagation and assumes that a long crack exists from the beginning. The fatigue life is calculated on the basis of a crack propagation law assessing the number of loading cycles which grow a fatigue crack from a known or estimated starting length to a final length, at which the crack becomes instable. The crack growth rate da/dN, *i.e.* the slope of the curve of the crack length a versus the number of cycles N is mostly expressed as a function of the range of the stress intensity factor ΔK. The basis for this type of formulation is the well-known Paris' law Eq. (1) [6], which does not have a physical foundation but is fulfilled by many materials.

$$\frac{\mathrm{d}a}{\mathrm{d}N} = \mathrm{C}\,\Delta K^{\mathrm{m}} \tag{1}$$

C and m are material constants, which must be determined experimentally.

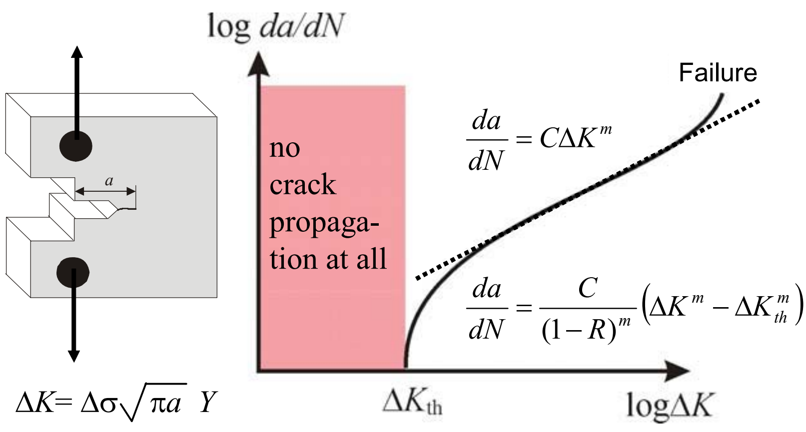

Figure 7. Typical specimen geometry used for crack growth measurements and corresponding representation of the fatigue crack propagation rate versus the stress intensity factor range

Figure 7 shows the typical course of a crack growth curve. The fatigue threshold ΔK_{th} defines the lower limit of crack propagation and is often incorporated in the Paris' law in order to describe also the first part of the curve.

The Paris' law and its extensions holds true for long crack propagation only. Usually the size of the plastic zone ahead of the crack tip of long cracks comprises several grains and the crack advance is no longer affected by the crystallographic orientations (stage II crack propagation). Often this type of crack advance is connected with the formation of striations and the striation spacing correlates nicely with the crack growth per corresponding loading cycle. In the literature, almost 100 models exist that try to explain in which way striations are formed. The two best established models are probably the "basting planting" model of Laird [7], which addresses ductile materials, and the "alternating slip model" of Neumann [8], which was verified for single crystals under symmetrical loading of two slip systems. It is important to note that not all engineering materials form striations during stage II crack propagation. Striations are barely visible in high-strength and cold-worked alloys and often the fracture surface is damaged as a consequence of sliding contact of both surfaces during the compressive part of the loading cycle.

Figure 8 shows the fracture surface of an austenitic steel (X12CrNi-17-7). Clearly, the crack initiation site can be identified at the surface. The area of fatigue crack propagation differs strongly from the final rupture area and is characterized by the presence of striations. The transition to rupture takes place, when the crack has become so long that the maximum stress of the last cycle in combination with the crack length leads to a stress intensity factor which reaches the critical stress intensity factor.

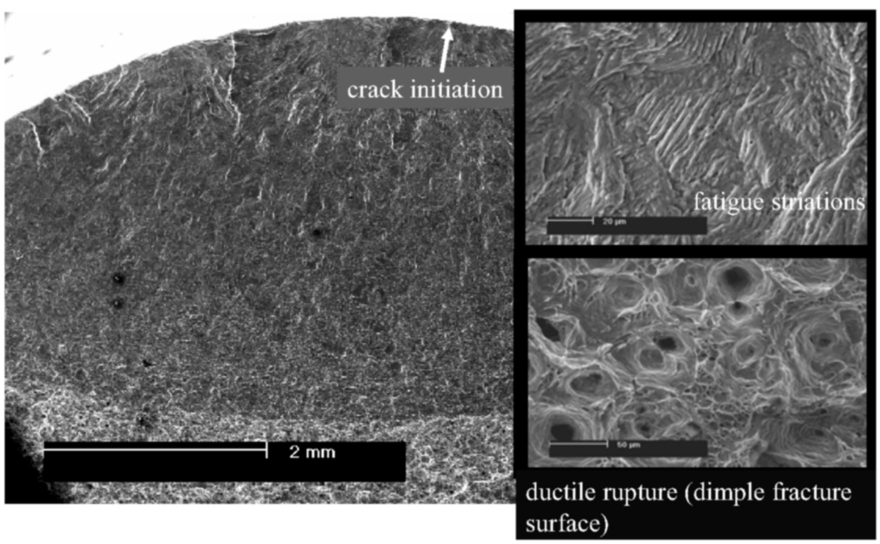

Figure 8. Fracture surface of an austenitic stainless steel (X12CrNi-17-7) showing crack initiation at the surface, fatigue crack propagation (striations) and ductile rupture (dimples)

3. Current Research Issues

Despite the long tradition of fatigue research in mechanical engineering and materials science, the development of new materials and the increasing demand of an economical but also ecological use of resources and materials triggers consistently new research fields within the topic fatigue. Two rather new aspects are briefly introduced here because of their direct biomechanical significance.

3.1 Short Fatigue Crack Behaviour

It has been emphasized above that a simple description of fatigue crack propagation, *e.g.* by means of the Paris' law, holds only true, if the assumptions of the LEFM are at least approximately fulfilled. The samples used in corresponding tests (see Figure 7) contain long cracks which were generated by cyclic loading at notches before the actual experiment. In many practical applications, however, components are free of notches or flaws and the surface is smooth (or even polished). Hence, the later fatal crack is naturally formed and grows during a large part of fatigue life (up to 90 pct) at a length which is in the same order as the size of microstructural features of the material, *e.g.* the grain size. These microstructurally short cracks can grow faster than long cracks at the same ΔK value and can even grow at ΔK values below the threshold for long crack propagation ΔK_{th} (Figure 7).

The growth behaviour of short cracks is very complex since it is strongly affected by the interaction of the crack with microstructural obstacles [9]. Grain and phase boundaries act as such obstacles since they impede the penetration of the plastic deformation ahead of the crack tip into the adjacent grain or second-phase particle. A life prediction requires a mechanism-based simulation of the relevant processes and must strongly consider the microstructure of the material. Figure 9 gives an example.

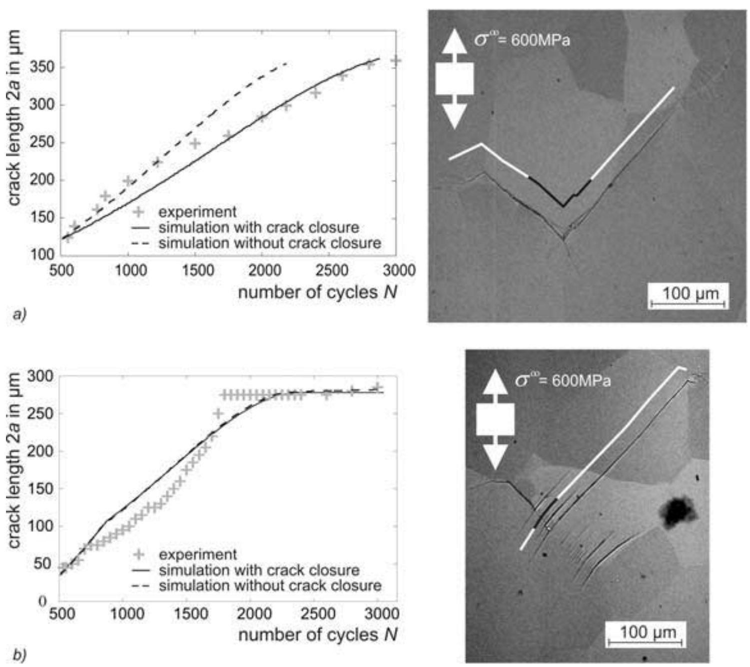

Figure 9. Comparison of the experimentally determined short fatigue crack growth behaviour of a single-phase titanium alloy (LCB) with the results of a numerical simulation, which is based on a finite-boundary-element method taking the interaction of the spreading slip band with the adjacent grain boundary into account

The two short cracks depicted in Figure 9 were observed in a single-phase beta titanium alloy (LCB) and were monitored regarding their growth. The surrounding microstructure was analysed with respect to the grain orientations and the grain boundary characters. By means of a simulation model, which uses the finite-boundary-element technique, the crack tip slide displacement (CTSD) was calculated as a consequence of the interaction of the slip band in front of the crack tip with the adjacent grain boundary. The crack advance per cycle was assumed to be proportional to the range of CTSD. Figure 9 documents an excellent agreement of the test results with the predictions, if the effect that the crack is closed during a part of the cycle (crack closure effect) is taken into account. See ref. [10,11] for more details.

Mechanism-based models provide an insight into the relevant processes and allow a prediction of cyclic life. Moreover, simulation runs can be performed in artificial microstructures with systematically varied stereological parameters. Figure 10 shows the results of crack growth simulations in simulated duplex (two-phase) microstructures, which were generated by a Voronoi-algorithm, in order to determine the influence of the arrangement of the two phases. For this purpose, a crack was placed in a microstructure representing a certain set of parameters and subjected to a calculation that reproduces cyclic loading conditions. Also, the experimentally obtained yield stresses were assigned to the phases. Figure 10 shows the results of a number of such simulations. Here the relative lifetime of the respective microstructures is shown with the corresponding geometrical parameters. Per definition the end of lifetime was reached, when the crack was 300μm long. The varied parameters are the grain size *D*, the fraction of clusters *r* and the contiguity *C*, according to the values noted at the abscissa. It turned out that a higher grain size leads to shorter fatigue life, as expected, and that a value of r_γ=0 (which means that the γ phase serves as the matrix phase) is beneficial for lifetime, as well as a contiguity of about 0.5 for both phases [12,13]. Regardless the details of this study, the example shows that simulation provides a useful tool for the identification of fatigue-resistant microstructure.

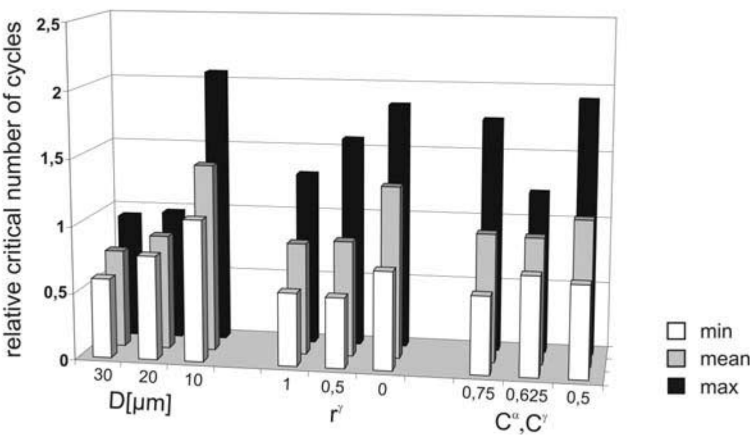

Figure 10. The dependence of lifetime on microstructural parameters. Displayed are the results of ten simulations for each value, respectively (90 simulations in total). White is the minimal occurring lifetime, black the maximum and grey the mean value. The results are related to the mean lifetime obtained from the 30 simulations of each group varying one parameter, which yields the relative critical number of cycles.

3.2 Existence of Fatigue Limit

The so-called *total life approach* is the classical approach to fatigue design and probably still the one used most. In this concept, the number of cycles necessary to induce fatigue failure in initially uncracked and smooth laboratory specimens is determined under constant amplitude. The resulting fatigue life comprises the stages crack initiation and crack propagation until failure without separating these stages. Under high-cycle fatigue conditions, *i.e.* at low stress amplitudes, design concepts usually assume that a fatigue limit (endurance limit) exists. If the stress amplitude is smaller than the fatigue limit, fatigue life of the material is infinite.

The availability of new testing systems which can perform cyclic loading of samples and components at high frequencies has triggered investigations on the fatigue mechanisms in the so-called very high cycle fatigue (VHCF) regime at numbers of cycles far beyond 10^6 (up to 10^{10}). Figure 11 shows schematically, how a S-N-plot may look like, if the range of the number of the cycles to failure is extended to very high values [14].

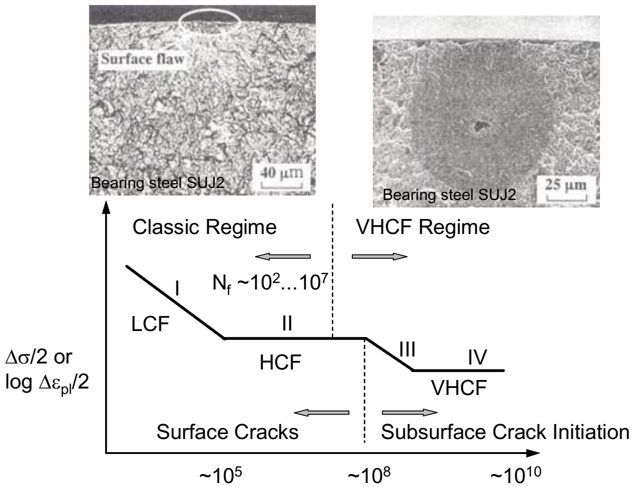

Figure 11. S-N-curve extended to very high numbers of loading cycles for a high-strength steel containing inclusions

Figure 11 refers to a material that contains inclusions such as oxide, carbides, sulfides or nitrides. Typically steels belong to this class of materials. The high-cycle fatigue (HCF) behaviour is determined by a fatigue limit often applied to parts for a fatigue endurable design (stage II in Figure 11). The observation of a further decrease of the tolerable stress amplitude means that parts which undergo high numbers of loading cycles (such as springs, railway axes, stents, valves,...), must be designed more conservatively. The decrease of the fatigue strength is connected to a change in the crack initiation site from the surface to the interior.

Conclusions

The behaviour of engineering materials and components under monotonic and cyclic loading conditions were dealt with from a mechanistic and microstructural point of view. The main conclusions are:

- The limits for static loading can safely be assessed on the basis of experimental data from tensile tests for ductile materials and by means of established concepts from linear elastic and elastic plastic fracture mechanics.
- Cyclic loading conditions are much more dangerous as compared to monotonic loading, since damage accumulates and may lead to unexpected failure as a result of fatigue of materials.
- The damage evolution process of fatigue comprises local cyclic deformation, crack initiation, crack propagation and fracture. The respective life fractions depend mainly on the loading conditions, the surface condition and the mechanical properties of the material.
- The stage of propagation of microstructurally short cracks can determine up to 90 pct of total fatigue life. Continuum mechanics is not adequate to describe the crack growth rate. Rather a mechanistic and microstructure-related approach is necessary.
- In the VHCF regime, the endurable stress amplitude decreases further with increasing number of loading cycles. In the case of materials containing inclusions (*e.g.* steels), this phenomenon is connected to a shift of the crack initiation site from the surface to the interior of the material.

Acknowledgement — Part of the results reported in this article was taken from Ph.D. theses carried out in the research group of the author. Most of these studies were third-party funded. The author thanks in particular *Deutsche Forschungsgemeinschaft* for continuous financial support.

References

[1] H. Blumenauer, G. Pusch, *Technische Bruchmechanik*, Deutscher Verlag für die Grundstoffindustrie, Leipzig, 1993.
[2] S. Suresh, *Fatigue of Materials,* 2nd Edition, Cambridge University Press, Cambridge, U.K., 1998.
[3] H. Mugrabi, Dislocations in fatigue, in: *Dislocation and Properties of Real Materials*, Book No. 323, 244-261, The Institute of Metals, London, 1985.
[4] J. Lepinoux, L. P. Kubin, In situ TEM observations of the cyclic dislocation behaviour in persistent slip bands of copper single crystals, *Philosophical Magazine A* **51** (1985), 675-696.
[5] U. Krupp, W. Floer, J. Lei, Y. M. Hu, H.-J. Christ, A. Schick and C.-P. Fritzen, Mechanisms of short-fatigue-crack initiation and propagation in a beta titanium alloy, *Philosophical Magazine A* **10** (2002), 3321-3332.
[6] P. C. Paris, M. P. Gomez and W. E. Anderson, A rational analytic theory in Engineering, *TheTrend in Engineering* **13** (1961), 9-14.
[7] C. Laird, The influence of metallurgical structure on the mechanisms of fatigue crack propagation, in: *Fatigue Crack Propagation*, ASTP-STP 415, 131-168, The American Society for Testing and Materials, Philadelphia, USA, 1967.
[8] P. Neumann, Coarse slip model of fatigue, *Acta Metallurgica* **17** (1969), 1219-1225.
[9] S. Pearson, Initiation and fatigue crack growth in aluminum alloys and the subsequent propagation of very short cracks, *Engineering Fracture Mechanics* **7** (1975), 235-247.
[10] B. Künkler, A. Schick, C.-P. Fritzen, W. Floer, U. Krupp and H.-J. Christ, Simulation of microstructurally controlled short crack propagation, *Steel Research* **74** (2003), 514-518.

[11] A. Schick, H.-J. Christ, W. Floer, C.-P. Fritzen and U. Krupp, Experimentelle Charakterisierung und zweidimensionale Simulation der mikrostrukturbestimmten Ermüdungsrissausbreitung in einer Beta-Titanlegierung, *Materialwissenschaft und Werkstofftechnik* **33** (2002), 244-251.
[12] O. Düber, B. Künkler, U. Krupp, H.-J. Christ and C.-P. Fritzen, Experimental characterization and two-dimensional simulation of short-crack propagation in an austenitic-ferritic duplex steel, *Intern. Journal of Fatigue* **28** (2006), 983-992.
[13] H.-J. Christ, O. Düber, W. Floer, C.-P. Fritzen, U. Krupp, B. Künkler and A. Schick, Microstructural effects on short fatigue crack propagation and their modelling, in: *Fracture of Nano and Engineering Materials and Structures*, Proceedings of the 16th European Conference of Fracture, ECF-16, Alexandroupolis, Greece, on CD-ROM.
[14] H. Mughrabi, Specific features and mechanisms of fatigue in the ultrahigh-cycle regime, *Intern. Journal of Fatigue* **28** (2006), 1501-1508.

Medicine Meets Engineering
J. Hammer et al. (Eds.)
IOS Press, 2008

How do anisotropy and age affect fatigue and damage in cancellous bone?

Sebastian DENDORFER [a,1], Hans J. MAIER [b] and Joachim HAMMER [a]
[a] *Laboratory for Materials Science, University of Applied Sciences Regensburg, Germany*
[b] *Institute for Materials Science, University of Paderborn, Germany*

Abstract. The fatigue behaviour of materials is of particular interest for the failure prediction of materials and structures exposed to cyclic loading. For trabecular bone structures only a few sets of lifetime data have been reported in the literature and structural measures are commonly not considered. The influence of load contributions not aligned with the main physiological axis remains unclear. Furthermore age effects on the fatigue behaviour are not well described. In the present study, different groups of human vertebral cancellous bone were exposed to cyclic compression. The inital modulus and therefore lifetimes were found to be highly dependent on age. The decrease in both with increasing age was much more pronounced in specimens which were not aligned with the main physiological axis. This implies that old bone is much more sensitive to (cyclic) failure loads in general but particularly to loads which are not coincident with the physiological main axis.

Keywords. Bone mechanics, fatigue, fracture, damage mechanism, mechanical properties, cancellous bone, age

1. Introduction

There is an increased risk of bone fractures with age [10]. Age affects the biomechanical and morphological properties of bone. Peak bone mass and strength were found to be highest at an age of 20 to 30 years and bone mass and strength on average to be higher in men than women [14]. The compressive strength of human femoral cancellous bone revealed an decrease by 8.5 per cent each decade [11]. For both sexes an extreme decline in vertebral bone strength during ageing could be observed. Whereas men show a certain compensatory increase in bone size with age, no cross sectional adaptation could be found for women [14]. The architecture of cancellous bone structures does also change with age. Women show, especially at ages older than 50 years (menopause), a higher tendency for the perforation of horizontal (normal to the main physiological axis) struts of the trabeculae network [13] [14]. Trabecular number was found to be reduced in females, whereas in males, strut thickness was reduced [15]. Despite these structural changes overall vertebral cancellous bone density was found to be equal for both sexes and compressive stress appeared to be independent of gender [7].

[1]Corresponding Author: Sebastian Dendorfer, University of Applied Sciences Regensburg, Galgensbergstrasse 30, 93049 Regensburg, Germany; E-mail: sdendorfer@lwm-regensburg.de

Bone as a living material has the ability to remodel and therefore repair microdamage which may be induced due to cyclic or isolated loadings. Cyclic loading is known to induce microdamage and may result in stress or fragility fractures [19][2]. Therefore microdamage can also be found in-vivo. The microcrack density was shown to increase exponentially with age in human femoral cortical bone [18]. Despite this increase, longer fatigue life in cortical bone could be associated with higher initial crack density when modulus variability was taken into account [20]. Fatigue life in cortical bone decreased exponentially with age, and old bone exhibited a different evolution of damage in terms of modulus degradation than younger bone [6]. The fatigue behaviour for cancellous bone has only been investigated with respect to the main physiological axis [12][4] and age effects are not reported.
However, despite the knowledge of structural changes, increased microdamage in elderly bone and numerous data on the fatigue behaviour of cortical bone still quite a few issues on the behaviour of cancellous bone under cyclic load exposure remain unsolved. One aspect which has not been reported on yet is in which manner age and therefore increased (inital) microdamage and anisotropy affect the fatigue properties of cancellous bone. Therefore, in this study fatigue data for cancellous bone specimens with varying orientation (load axis to physiological bone axis) were analysed with respect to donor age and its effect on the macroscopic (continuum) deformation behaviour was investigated.

2. Material & Methods

Human vertebral cancellous bone specimens from eight donors (46 - 80 years, mean 61±11 years, 7 male, 1 female) were extracted in three different orientations with respect to the physiological bone axis. The adjusted angles were 0, 45 and 90 (angular) degree and refer to the main whole bone axis (comp. Figure 3). Specimen preparation followed a recently published protocol [5]. The resulting specimens' cross section was cylindrical with a diameter of 11.2 mm and a height of 15 mm. In total 42 specimens were loaded in cyclic compression with a triangular wave form between zero and a defined peak. Therefore a negative mean stress was acting. The applied load was normalized with the inital (secant) modulus (E_0) of each specimen, which was analysed prior to fatigue testing using preloading cycles with only a small peak load (-1 to -5 N). This normalization is a standard procedure in mechanical testing of foam structures in order to reduce the scatter of the results [9]. Failure was defined with a ten percent reduction in secant modulus. The deformation behaviour was analysed on the specimen level in terms of permanent (residual) and total (accumulated residual and elastic) strains. The evolution of damage was analysed using a scalar damage variable (E_{sec}/E_0) which relates the secant modulus of each cycle to the inital modulus. Furthermore lifetime curves were established which relate the applied load (σ/E_0) to the number of cycles. Age effects were analysed on the established relationships and the inital modulus.

3. Results

The initial secant modulus of the specimens was found to be highly dependent on donor age (Figure 3). For all specimen groups the modulus decreased with increasing age. This

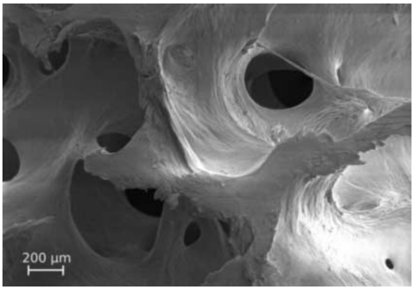

Figure 1. Human vertebral cancellous bone, male 46 years, main axis in horizontal direction.

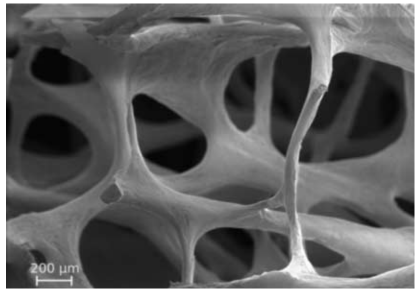

Figure 2. Human vertebral cancellous bone, male 80 years, main axis in horizontal direction.

holds with the exception of the specimens from the 46 year old male donor of the 0° group, which showed a slightly weaker mechanical performance than the overall trend, as well as one specimen from a 72 year old male donor whose value was exceptionally high. In both cases, the bone samples did not show any (macroscopic) conspicuous features.

The relationship between the decline of the initial secant modulus and the donor's age are represented most suitably as quadratic and cubic polynomials (thus exponential relationships provide good correlations). While the principle change appears to be similar concerning the different groups, the relative decrease of the modulus appears to be more pronounced in the 45° and 90° groups compared to the 0° group. In these off-axis groups mean modulus drops within 20 years ($60 - 80$ years) by more than 70 percent from (mean) approx. 180 MPa and 160 MPa to 50 MPa and 20 MPa, respectively, whereas the group aligned with the physiological axis revealed a decrease of 25 percent from approx. 440 MPa to 330 MPa.

The characteristic cyclic deformation behaviour showed no remarkable change with increasing age. All specimens followed the stages of deformation described earlier in fatigue of cancellous bone with an increasing residual deformation, decreasing secant modulus and increasing hysteresis loops during cyclic deformation. Damage evolution, defined as a decrease in secant modulus, did also not appear to be different with increasing donor age. Figure 4 shows the evolution of this scalar damage variable as a function of the percentage of total fatigue lifetime for four 45° specimens from two 61 year old and two 80 year old specimens. Damage increases rapidly within a small percentage of lifetime, this transient is followed by a lowered, constant damage rate which increases at approx. 75 to 85 % of the total lifetime indicating macroscopic failure. Similar results can be obtained for the other specimens/groups.

Neither maximum strains at failure nor accumulated residual strains revealed a significant influence of donor age on the results. Specimens with different donor ages showed no tendencies in higher of lower (integral) deformations at failure. Likewise, no influence of donor age on the tendency of earlier or later failure could be observed once initial stiffness was taken into account. Age showed no influence on the propability distribution along the lifetime curves (Figure 5). The other groups behaved similar to the 45° group already shown.

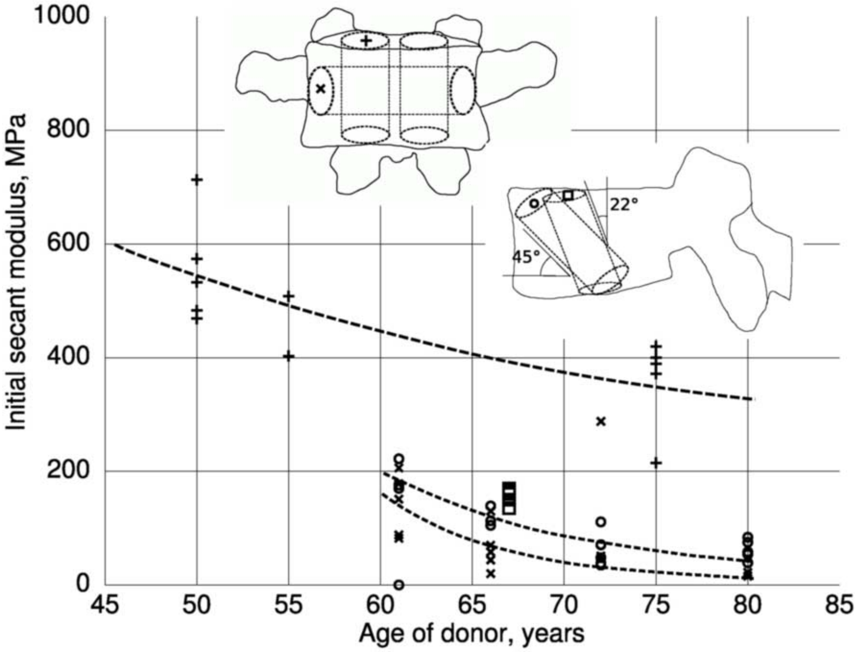

Figure 3. Initial (undamaged) secant modulus as a function of donor age for different specimen groups. The groups differed in their coring direction with respect to the physiological axis.

4. Discussion

The data of the cyclic deformation experiments was analysed with respect to donor age in order to reveal the influence of age on the fatigue properties of cancellous bone. The initial secant modulus of the specimens was found to be highly dependent on donor age. The modulus decrease was much more pronounced in the off-axis groups, this increasing mechanical anisotropy indicates also an increased degree of structural anisotropy with age, findings that correspond with data from [16], who showed that there is relative conservation of stiffness in the axial direction compared with the transverse direction.

Initial stiffness is used as a normalisation factor in fatigue analysis of cancellous bone [1,12] and therefore the corresponding relationships are directly related to its magnitude. Consequently, fatigue lifetime is also highly dependent on age and decreases more pronouncedly in the off-axis orientations. This implies that old bone is much more sensitive to (cyclic) failure loads in general but particularly to loads which are not coincident with the physiological main axis. Therefore, for instance the right implant anchorage (which may result in unphysiological local stress) is much more important in older bone. Also changes in the physiological load flow through a change in habitual tasks increase the risk of fatigue fractures for elderly people. Furthermore, these findings suggest that the integrally measured value for bone strength in current routine clinical

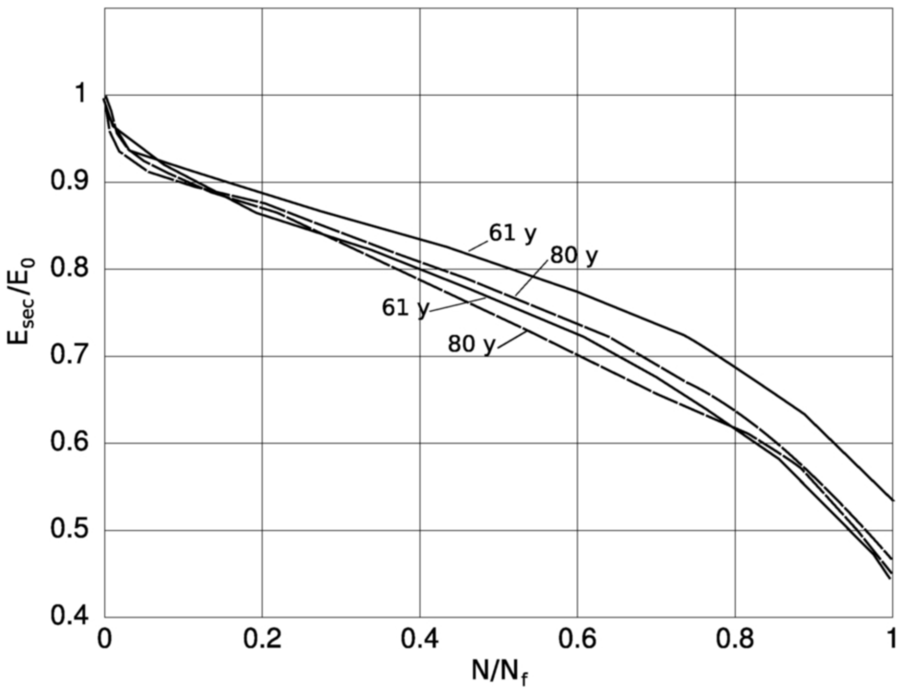

Figure 4. Evolution of damage in terms of a decreasing secant modulus as a function of the percentage of fatigue life. The numbers refer to the age of the donors. The lifetimes of the plotted specimens (45 degree group) ranged between 1,600 and 11,000 cycles.

practice, BMD [8], may be of decreased predective value concerning older bone as the structural anisotropy becomes increasingly important.

While for human cortical bone modulus degradation profiles were found to be different regarding younger and older bones [6], the data in this study did not reveal an effect of age on damage evolution. Additionally, age did not show any further influence on lifetime curves and deformations at failure once initial stiffness has been included. As old bone is known to have reduced quality e.g. in terms of increased microdamage [18], one could expect older bones to reveal a tendency for reduced lifetimes. At least in the range of the data presented there is no evidence for this, once initial stiffness is included. There may be different explanations for these findings. Firstly, initial stiffness is a highly sensitive parameter of tissue quality, which has also explanatory power for cyclic loadings; secondly, initial (micro-)damage may not be critical for fatigue failure; and thirdly, the range of donor age is too limited to reveal significant results. [17] found for bovine cortical bone that bone fails by extensive propagation of a few cracks, not the proliferation and coalescence of microcracks, and therefore initial microdamage is not a significant factor in fatigue failure, which may also be true for cancellous bone. Additional microdamage quantification and analysis is needed to confirm this assumption. It has been suggested that damage rates increase with age for cortical bone [3]. Whether

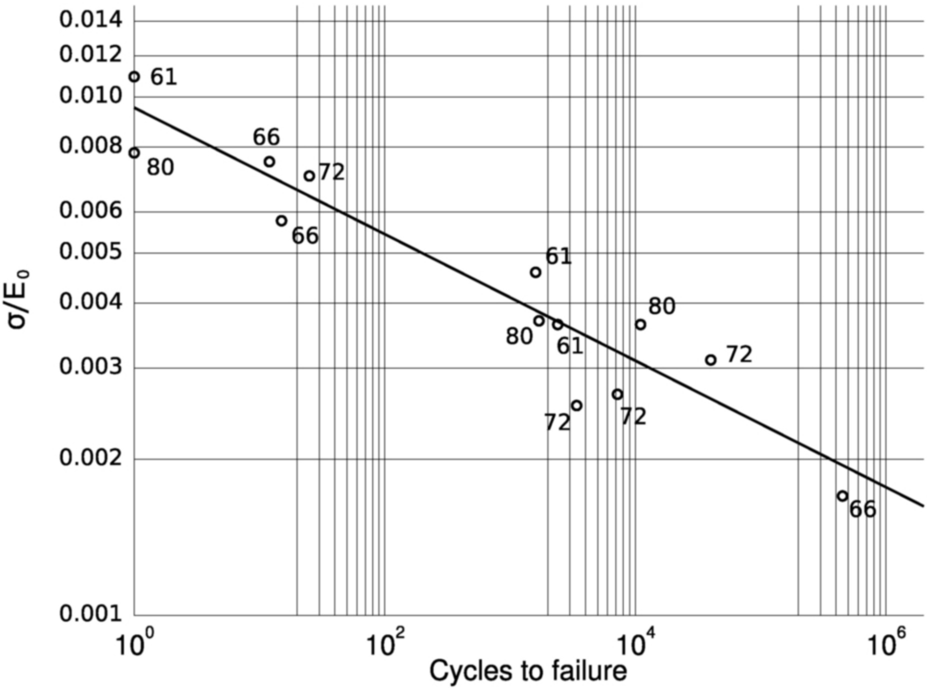

Figure 5. Lifetime (S-N) curve for the 45° group. The loads are normalised by the mean initial modulus. The numbers refer to the age of the donor.

this is also true for cancellous bone could not be proved with this study due to the limited amount of data.

The deformation mechanism for static failure is reported to depend on the cancellous bone density and therefore age. At lower density values elastic buckling dominates, whereas at higher density levels a lowered slenderness ratio of the trabeculae causes failure by progressive microfracturing [21,9]. While these findings hold for static loadings, cyclic loadings much below the static failure values did not yield in these critical deformations and may therefore not so strongly depend on the slenderness ratio, which could explain the similarity of the deformation behaviour.

Even if the age range of the donors is limited in this study, it represents the age-group, where bone quality becomes an important issue. The limited number of data points does not allow for an exact determination of the relationships between initial modulus and age, but nevertheless the trends can be shown and are valid.

Concluding, initial modulus and therefore lifetimes were found to be highly dependent on age. The decrease in both with increasing age was much more pronounced in specimens which were not aligned with the main physiological axis.

References

[1] S. M. Bowman, X. E. Guo, D. W. Cheng, T. M. Keaveny, L. J. Gibson, W. C. Hayes, and T. A. McMahon. Creep contributes to the fatigue behavior of bovine trabecular bone. *J Biomech Eng*, 120(5):647–654, 1998.

[2] D. B. Burr, M. R. Forwood, D. P. Fyhrie, R. B. Martin, M. B. Schaffler, and C. H. Turner. Bone microdamage and skeletal fragility in osteoporotic and stress fractures. *J Bone Miner Res*, 12(1):6–15, 1997.

[3] John R Cotton, Keith Winwood, Peter Zioupos, and Mark Taylor. Damage rate is a predictor of fatigue life and creep strain rate in tensile fatigue of human cortical bone samples. *J Biomech Eng*, 127(2):213–219, 2005.

[4] S. Dendorfer, H. J. Maier, and J. Hammer. Deformation behaviour of bovine cancellous bone. *Technol Health Care*, 14(6):549–556, 2006.

[5] S. Dendorfer, H. J. Maier, and J. Hammer. Anisotropy of the fatigue behaviour of cancellous bone. *Journal of Biomechanics*, in press.

[6] T. Diab, S. Sit, D. Kim, J. Rho, and D. Vashishth. Age-dependent fatigue behaviour of human cortical bone. *Eur J Morphol*, 42(1-2):53–59, 2005.

[7] E. N. Ebbesen, J. S. Thomsen, H. Beck-Nielsen, H. J. Nepper-Rasmussen, and L. Mosekilde. Age- and gender-related differences in vertebral bone mass, density, and strength. *J Bone Miner Res*, 14(8):1394–1403, 1999.

[8] Alan W Friedman. Important determinants of bone strength: beyond bone mineral density. *J Clin Rheumatol*, 12(2):70–77, 2006.

[9] L. J. Gibson and M. F. Ashby. Cellular solids: structure & properties. *Cambridge University Press, Cambridge*, 2nd, 1997.

[10] J. A. Kanis, O. Johnell, A. Oden, F. Borgstroem, N. Zethraeus, C. De Laet, and B. Jonsson. The risk and burden of vertebral fractures in sweden. *Osteoporos Int*, 15(1):20–26, 2004.

[11] R. W. McCalden, J. A. McGeough, and C. M. Court-Brown. Age-related changes in the compressive strength of cancellous bone. the relative importance of changes in density and trabecular architecture. *J Bone Joint Surg Am*, 79(3):421–427, 1997.

[12] T. L. Moore and L. J. Gibson. Fatigue of bovine trabecular bone. *J Biomech Eng*, 125(6):761–768, 2003.

[13] L. Mosekilde. Sex differences in age-related loss of vertebral trabecular bone mass and structure–biomechanical consequences. *Bone*, 10(6):425–432, 1989.

[14] L. Mosekilde. Age-related changes in bone mass, structure, and strength–effects of loading. *Z Rheumatol*, 59 Suppl 1:1–9, 2000.

[15] M. G. Mullender, S. D. Tan, L. Vico, C. Alexandre, and J. Klein-Nulend. Differences in osteocyte density and bone histomorphometry between men and women and between healthy and osteoporotic subjects. *Calcif Tissue Int*, 77(5):291–296, 2005.

[16] P. H. Nicholson, X. G. Cheng, G. Lowet, S. Boonen, M. W. Davie, J. Dequeker, and G. Van der Perre. Structural and material mechanical properties of human vertebral cancellous bone. *Med Eng Phys*, 19(8):729–737, 1997.

[17] F. J. O'Brien, D. Taylor, and T. C. Lee. Microcrack accumulation at different intervals during fatigue testing of compact bone. *J Biomech*, 36(7):973–980, 2003.

[18] M. B. Schaffler, K. Choi, and C. Milgrom. Aging and matrix microdamage accumulation in human compact bone. *Bone*, 17(6):521–525, 1995.

[19] Rebecca A Snyder, Michael C Koester, and Warren R Dunn. Epidemiology of stress fractures. *Clin Sports Med*, 25(1):37–52, viii, 2006.

[20] O. S. Sobelman, J. C. Gibeling, S. M. Stover, S. J. Hazelwood, O. C. Yeh, D. R. Shelton, and R. B. Martin. Do microcracks decrease or increase fatigue resistance in cortical bone? *J Biomech*, 37(9):1295–1303, 2004.

[21] P. R. Townsend, R. M. Rose, and E. L. Radin. Buckling studies of single human trabeculae. *J Biomech*, 8(3-4):199–201, 1975.

Medicine Meets Engineering
J. Hammer et al. (Eds.)
IOS Press, 2008

Wear analysis and finishing of bioceramic implant surfaces

Berend DENKENA [a], Martin REICHSTEIN [a], Marijke VAN DER MEER [a,1], Sven OSTERMEIER [b], Christof. HURSCHLER [b]

[a] *Institute of Production Engineering and Machine Tools, Leibniz Universität Hannover, Germany*

[b] *Laboratory for Biomechanics and Biomaterials, Orthopaedic Department, Medical School of Hannover, Germany*

Abstract. A primary cause for revision operations of joint replacements is the implant loosening, due to immune reactions resulting from the agglomeration of polyethylene wear debris. Motivated by the successful application of bioceramic materials in hip joint prostheses, a trend towards the development of hard implant materials has occurred. Nonetheless in the area of total knee arthroplasty (TKA), modern efforts have still utilized polyethylene as the tibial-inlay joint component. The use of bioceramic hard-hard-pairings for total knee arthroplasty has been prevented by the complex kinematics and geometries required. Ceramics cannot cope with non-uniform loads, which suggests the need for new designs appropriate to the material. Furthermore, biomechanical requirements should be considered. A rolling-gliding wear simulator, which reproduces the movements and stresses of the knee joint on specimens of simplified geometry, has therefore been developed. High-precision machining processes for free formed bioceramic surfaces, with suitable grinding and polishing tools which adjust to constantly changing contact conditions, are essential. The goal is to put automated finishing in one clamping with five simultaneous controlled axes into practice. The developed manufacturing technologies will allow the advantageous bioceramic materials to be applied and accepted for more complex joint replacements such as knee prostheses.

Keywords. Rolling-gliding test station, gravimetrical wear detection, machining

Introduction

Currently about 80,000 knee joints are endoprosthetically treated in Germany per year. The overall complication rate lies at about 26%. Causes for revisions are diverse, such as infections, wear or breakage, but the late implant loosening is considered a major cause [1]. PE-wear debris concentration in the joint is thought to be responsible for the loss of the anchorage of the implant components. These fragments can activate bone decomposing osteoclasts via immunological reactions [2]. Classical material pairing is up to today the usage of cobalt-chrome-alloys combined with polyethylene (CoCr-PE). Also titanium-PE is utilized for allergic patients. Presently wear reducing bioceramic pairings find application in the field of total hip arthroplasty (THA) [3]. However for

[1]Corresponding Author: Marijke van der Meer, Institute of Production Engineering and Machine Tools, An der Universität 2, 30823 Garbsen, Germany; E-mail: meer@ifw.uni-hannover.de

complex joint replacements like knee prostheses this could not yet be realized due to high requirements for implant quality [4].

Ceramics react sensitively to loading peaks and tensile stress. In hip implants, the ball and socket build congruent surfaces. Therefore the stresses can be distributed area-measured, whereby high loads can be avoided. In a knee joint a too congruent design of the implant components would equal a limitation of mobility. So a compromise between necessary conformity of the gliding partners and the essential flexibility has to be found. Here on the one hand the load compatible prosthesis design based on biomechanical wear analysis is to develop under consideration of biomechanical and material conditions. On the other hand a machining process to finish complex bioceramic surfaces rational with high accuracy is required. One of the market leaders of implant manufacturers expresses the demand for new manufacturing methods: “As (...) new production methods are being developed, we anticipate excellent acceptance and growth of the ceramic total knee replacement market.”[5].

The reduction of wear has been sought by the application of DLC-coatings [6] or high-grade hard materials like zirconium or aluminium oxide. Also new materials like oxinium [7] and ceramics with mixed oxides are created [8, 5]. Additionally these materials purpose the prevention of foreign body responses, because no particles of conventional metallic components can emerge. All approaches have in common; that still a combination with PE is state of the art and a chain is only as strong as its weakest link.

1. Biomechanical Requirements

In totally bioceramic implants without elastic deformable PE-inlays, the „artificial cartilage“, possess a modified load situation. For example a punctiform respectively linear load is distributed on a smaller circular or ellipsoid area. Consequently the occurring stress increases. Such loadings can hardly be avoided in hard-hard-pairings with complex geometry. To analyse the wear of these pairings under this special conditions a novel rolling-gliding-test station has been composed (Fig. 1).

Figure 1: rolling-gliding test station

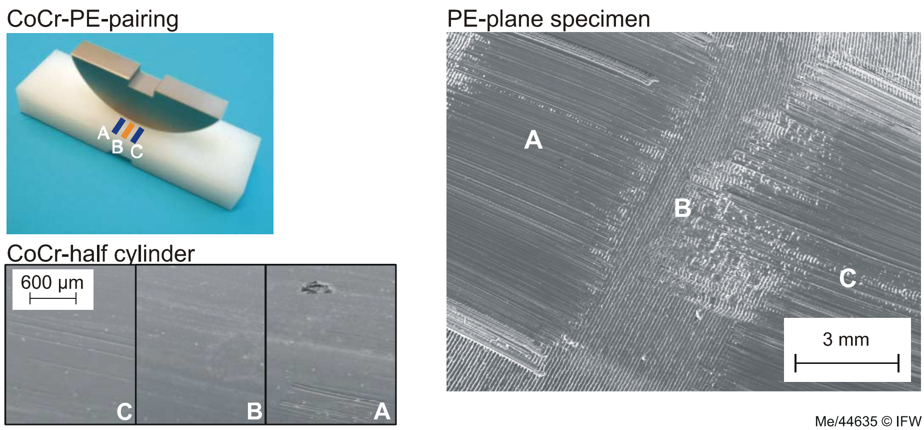

Figure 2: CoCr-PE after three million cycles

During the simulation of standardized knee joint analogous movements and loadings the test station enables to analyse the wear behaviour of different tribologic pairings with the help of simplified test components [9]. The test station is conceived to execute different movement phases.

Via the translation of the plane specimen of 15 x 100 x 30 mm³ a rotation of the half cylinder here with 32 mm radius and 10 mm thickness starts. Pure rolling is executed between both specimens (area B). In the two neighbouring phases (areas A and C) a combined rolling-gliding is performed by means of adjustable stop units. The undertaken examinations took place at body temperature in a standardized on calf serum based synovial fluid (ASTM F1715). The accrued wear was detected gravimetrically after different cycle quantities up to three million cycles. The generated wear marks were analysed qualitatively with scanning electron microscopy and additionally the depth of these marks were measured tactile.

To establish the new test method and to have a comparison with a conventional implant material pairing first of all half cylinders made up of cobalt-chrome (CoCr) were tested against ultrahigh molecular weight polyethylene (UHMW-PE). For the example-pairing, which is shown in figure 2, a wear of 8 mg was determined after three million movement cycles. This corresponds with a wear volume of 8.5 mm³ considering a density of 0.94 g/cm³. The appearance of the wear marks on the PE-part is characterized by a nearly undamaged region in the pure rolling area (area B). Two zones with plastic deformations labelled occur in the bordering combined rolling-gliding areas (areas A and C). On the CoCr-half cylinder no significant wear could be observed, but it developed macroscopically visible scratches.

Results of the examination of a ceramic-ceramic pairing are exemplarily shown in figure 3. After three million cycles the wear of the plane specimen amounts 2.80 mg and 2.39 mg for the ceramic half cylinder. This means a collective volumetric wear of 1.18 mm³, which was a reduction of wear by a factor of 7.2.

The wear marks occurring via the test of the ceramic-ceramic-pairing differ significantly from the observed marks with the conventional CoCr-PE-pairing. The ceramic half cylinder generates flattened areas in the changeover sector of movement phases due to the non-portable rotation point of the test station. At the plane ceramic specimen three different zones arise, which can be explained with the roll up of the edges of the flattened half cylinder (Fig. 3).

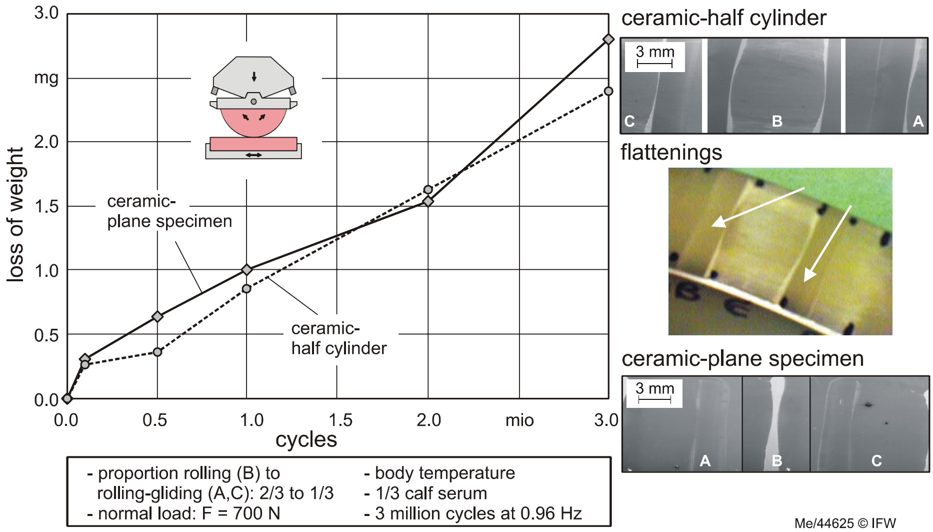

Figure 3: ceramic-ceramic wear development

On the basis of the measured maximum depth of the wear marks (Fig. 4), it is verified that the wear of the hard-hard-pairing is still smaller under these tightened terms compared with usual interfacial test methods, like pin-on-disc, ring-on-disc or hip simulator tests. And it has to be mentioned that scratches on CoCr-part can act as cutting edges on the PE specimen.

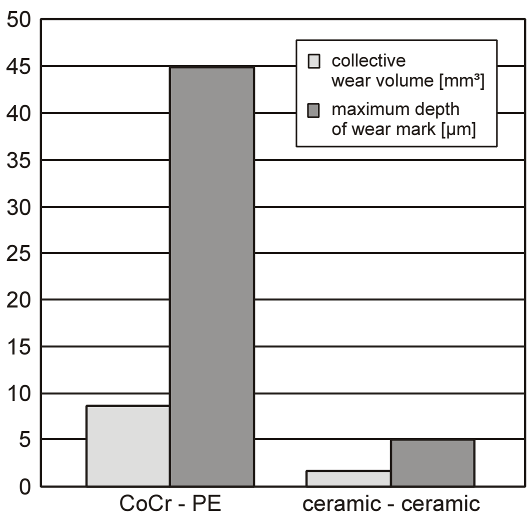

Figure 4: wear comparison after 3 million cycles

It has to be stated, that besides the noncircular behaviour the flattening of the ceramic half cylinder could lead to an undesirable increase of wear with a rising amount of movement cycles. For this reason it is suggestive to concept the radii differences during the design of the implant components as small as possible. The congruency has to be designed as high as the biomechanical requirements allow. The rolling-gliding test station will be adapted to movements with soft transition, which are more like those occurring in endoprosthetic treated knees.

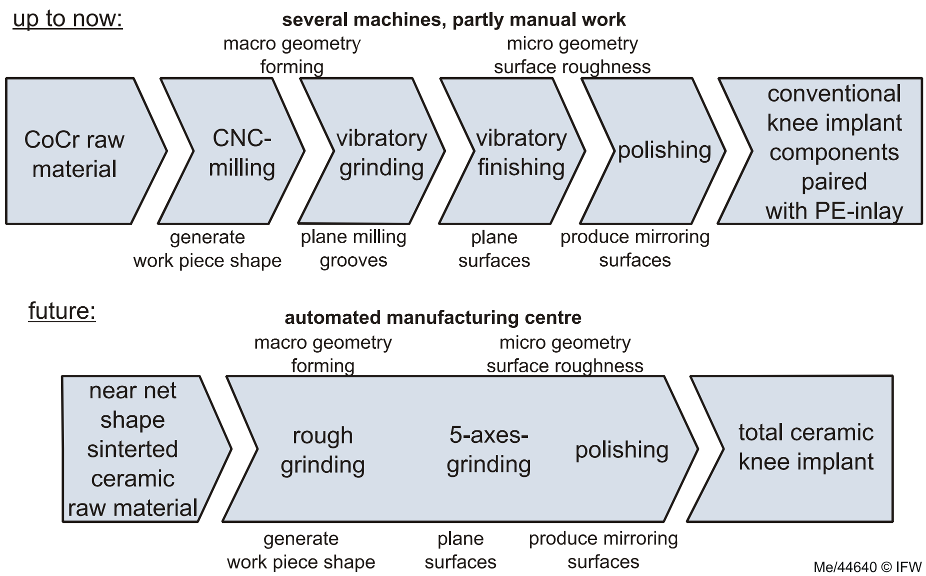

Figure 5: processing strategy

2. Finishing

Ceramics are featured by the ability to withstand great compressive stresses, yet they break in a brittle manner at relatively small tensile loadings, and thus exhibit very low fracture toughness. Dependent on the fault state range and according to the fineness of the microstructure the strength properties are very scattered. Thus the finishing of ceramic components has a considerable influence on the durability. It is very important to realise a finishing process with high accuracy. By means of the development of a complete machining in one clamping on one machine tool, this is intended to put into practise (Fig. 5). Targeted is to machine the macro geometry of the near net shape sintered and pre-ground bioceramic component with high-precision via grinding with five simultaneous controlled axes. Subsequent a polishing process with very small constant removal rate has to be realised. Only the roughness peaks generated by the grinding process will be levelled without changing the generated shape of the part.

Due to their bond geometry in combination with their adjustable orientation towards the work piece, in particular toric tools, depicted in figure 6, are appropriate to adapt to complex geometries. Orthogonal to the work piece big convex radii can be machined – likewise small concave radii are machinable with a defined contact angle of the toric tool. Furthermore with variable contact angle it is possible to carry out an alignment towards the constantly changing contact conditions. Through this a constant material removal is ensured, which is necessary to achieve high shape accuracy.

In this context electroplated toric diamond grinding tools were examined under varying parameters. To analyse the effects of the tool geometry on the surface generation different bond radii with defined contact angle, feed and cutting speed were used. Plane bioceramic wok pieces were machined with differing path distance.

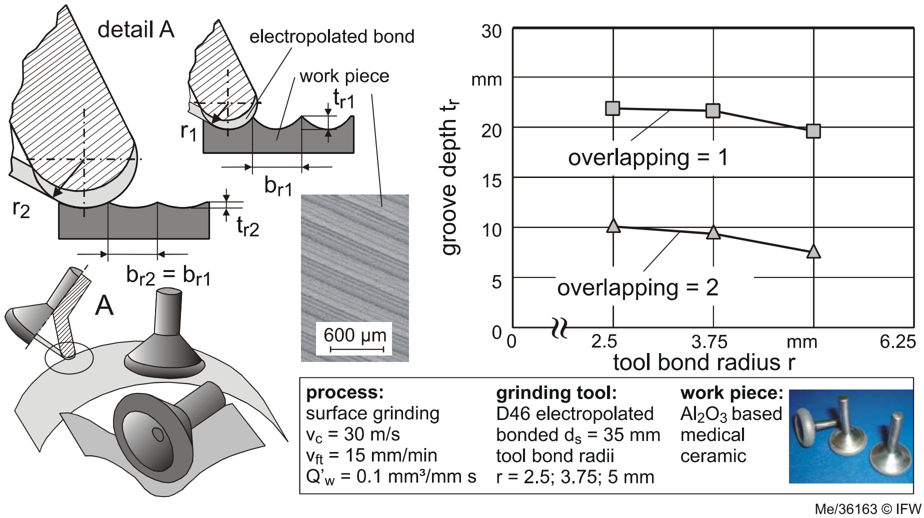

Figure 6: grinding with toric tools

These examinations confirm the theoretical conditions (Fig. 6 top left): the groove depth t_r decreases with increasing tool bond radius r at constant path distance b_r. Additionally the experimental achieved diagram clarifies, that with an larger overlapping the produced groove depth can be reduced. A minimized groove depth is essential to reduce the effort for the polishing process. Concerning the design of the grinding tool a compromise is needed. Bigger tool bond radii enhance the surface quality, but at the same time these radii are limited by the component contour, namely the smallest concave radius, which has to be produced [10].

To put the multi-axes grinding with simultaneous tool paths into practise, firstly ruled geometries were reproduced. Besides the generated surface properties here the achievable shape accuracy was of interest. The toric tools were applied with of foregoing examinations defined process parameters.

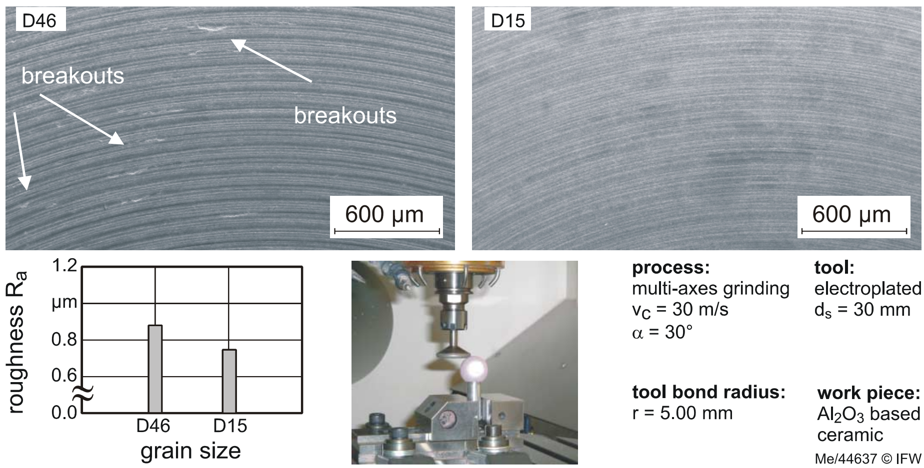

Figure 7: ground multi-curved surfaces

Figure 8: multi-axes grinding of a free form bioceramic implant segment

The measured form deviations of machined balls were in the range of micrometers, minimum 1.6 µm and maximum 11.2 µm [11, 12]. In figure 7 a closer look on the surface formation is given for a tool with a bond radius of 5 mm. Left with the grain size of 46 microns and right with 15 microns. In the diagram one sees confirmed, that the miniaturization of the grinding grain affects the surface quality positive. The SEM-pictures clarify these measured roughness values. On the left side breakouts can be discovered whereas on the right a smoother surface is shown.

Grinding process development is always connected to an appropriate conditioning method. A dressing spindle was therefore integrated in the machine tool (Figure 8, top left). It enables to ensure the sharpness of the grinding layer and to reproduce the grinding tool profile via contour-controlled tool paths.

Summary and perspective

With the rolling-gliding test station implant material pairings of varying geometry can be analyzed under adjustable load and rotation angle. The gravimetrical wear is detected and affects of sliding velocity or -direction are taken into account. This simulator will be expanded for the testing of multi-curved geometries. It is intended to analyze in as far production tolerances or deviations can be permitted with regard to durability and wear behaviour, so that the boundary conditions for the machining processes can be derived.

With the workings concerning the process development suitable adaptable grinding tools are available. These are suitable to machine complex bioceramic surfaces with the acquired process parameters with a shape accuracy of about 3 µm and a surface roughness R_a below 0.1 µm. The basic for a machining of free from implant components under constant material removal conditions is therewith given (Fig. 8). Also first polishing examinations on free form knee implant segments have been undertaken. In the next step these processes will be adjusted to each other.

Acknowledgement

The investigations described in this paper were undertaken with support of the German Research Foundation (DFG) within the collaborative research center SFB 599 "Sustainable Bioresorbable and Permanent Implants of Metallic and Ceramic Materials". Researchers of different professions work together in this work scope to develop forward-looking concepts for the design and production of metallic and ceramic implants.

References

[1] Annual Report 2005 Swedish knee arthroplasty register founded 1975, Lund university Hospital, Dept. of Orthopedics
[2] Willert, H.G. et al: Implant materials for hip endoprostheses: old proofs and new trends. Arch Orthop Trauma Surg, 114, S. 61-67, 1995
[3] Kawanabe, K.: Effect of femoral head on clinical results in cemented total hip Arthroplasty: old versus current alumina. Journal of Orthopaedic Science, 10, S. 378-384, 2005
[4] Plitz, W.: Knee endoprosthesis: selection and requirements of materials. Der Orthopäde, 29(8), S.727-731, 2000
[5] Kuntz, M.: Future ceramic strategies. In: 10. BIOLOX®-Symposium 2005, Session 6. New Applications for Ceramics, S.201-206, 2005
[6] DLC verbessert Verträglichkeit von Transplantaten. Pressetext über DLC-Beschichtungen an Implantaten. URL: http://www.pressetext.at/, 11.04.2006
[7] Gelenkersatz aus neuem Material auch für Allergiker. URL: http://www.smithnephew.at/, 11.04.2006
[8] Voigtsberger, B. et al: Biokompatible nanodispers verstärkte Dispersionskeramiken für die Gelenkendoprothetik. Hrsg. Hermsdorfer Institut für Technische Keramik, Hermsdorf, 30.06.2004
[9] Ostermeier, S.; Denkena, B.; Reichstein, M.; van der Meer, M.; Stukenborg-Colsman, C.; Hurschler, C.: Verschleißprüfung von vereinfachten Knieprothesenkomponenten unter simulierter Roll-Gleitbewegung. Biomateralien 6(3), S. 242, 2005
[10] Denkena, B.; Becker, J. C.; van der Meer, M.: Fertigung zukunftsfähiger Implantate – Automatisierte Freiformflächenbearbeitung verschleißarmer Keramikimplantate am Beispiel Kniegelenk. wt Werkstattstechnik online 2004_06, Jahrgang 94, Springer-VDI-Verlag, Düsseldorf, S. 284-288, 2004
[11] Stukenborg-Colsman, C.; Ostermeier, S.; Buhrmester, O.; Wirth, C. J.: Dynamische In-vitro-Messung des retropatellaren Drucks nach alloplastischem Kniegelenksersatz, Der Orthopäde, 32(4), S. 319-322, 2003
[12] Denkena, B.; Hurschler, C.; Stukenborg-Colsman, C.; van der Meer, M.; Ostermeier, S.: Teilprojekt D4 "Automatisierte Freiformflächenbearbeitung und Prüfung verschleißarmer Keramikimplantate". In: Kolloquium, Sonderforschungsbereich Biomedizintechnik, 4.-5.11.2005, Universität Hannover, S. 65-67, 2005

Medicine Meets Engineering
J. Hammer et al. (Eds.)
IOS Press, 2008

Mechanical Problems in Human Hearing

Albrecht EIBER
Institute of Engineering and Computational Mechanics, University of Stuttgart
Pfaffenwaldring 9, 70550 Stuttgart, Germany
E-mail: eiber@itm.uni-stuttgart.de

Abstract. A description of the hearing process is given using three-dimensional mechanical models. By means of simulation, normal, pathological and reconstructed situations can be investigated. The development of new concepts and prototypes as well as the optimization and the way of insertion of passive and active implants is facilitated by carrying out virtual tests. Mechanical models of spatial structures of the middle ear and its adjacent regions are established by applying multibody systems and finite element modeling approach. In particular, the nonlinear behavior of the elements is taken into account. For the determination of parameters such as coupling parameters in reconstructed ears, measurements using Laser Doppler Vibrometry (LDV) were carried out. The governing differential equations of motion allow the investigation of transient and steady state behavior by time integration and frequency domain methods. Optimization methods can be applied for determination of design parameters such as coupling stiffness and damping, the characteristics of actuator, the position of attachment and direction of actuation. Mechanical models enable non-invasive interpretation of dynamical behavior based on measurements such as LDV from umbo or multifrequency tympanometry. It is shown: The transfer behavior is depending on static pressures in the ear canal, tympanic cavity or cochlea. For reconstructed ears, the coupling conditions are governing the sound transfer substantially. Due to restricted coupling forces, the excitation of inner ear is limited and the sound transfer is distorted. Other sources of distortion are nonlinear coupling mechanisms. In reconstructions with active implants, the actuator excites the microphone whereby feedback effects may occur.

Keywords. mechanical models, middle ear, sound transfer, reconstructed middle ear

Introduction

Hearing is a highly dynamical process of displacements of elements in the middle and inner ear due to forces that originate from time-variant pressure fields and actuators. They are transmitted through the middle ear by levers, rods and ossicles. In a micro scale, the contact forces between two bodies and the local elastic or plastic deformations are of interest whereas the spatial motions of the ossicles play an important role for the sound transfer. Various profiles of the exciting forces such as stationary, transient, low or high intensity can be distinguished leading to different classes of response.

For a reconstructed middle ear, the sound transfer characteristics depend essentially on the mechanical behavior of the coupling between passive or active implant with the ossicular chain.

Static pressure variations [1-4] or preloads from middle ear prostheses and scar tissue displace the ossicles. This changes stiffness and damping of the visco-elastic elements, which directly modifies the dynamical properties of middle ear. Consequently, the hearing impression is influenced by a shift of frequency sensitivity, changed loudness and distorted transfer.

Important questions are therefore, how to get a full compensation of hearing loss without distortion or ringing in the transfer.

1. Problems and Methods

To study the mechanical behavior of hearing system, both experimental and computational investigations have to be made in combination based on real and theoretical models.

Modeling is a very difficult task, which strongly depend on the particular problem or question at hand. First, the complex reality is reduced considering only sections of it and neglecting all effects that are not of interest. The resulting system under consideration is further abstracted by applying different modeling approaches and describing different levels of simplification. Based on these quantitative models, simulations can be conducted to get a prognosis of the behavior in the future.

In order to draw a conclusion from such simulations to the complex reality, various errors are inherent within the modeling process: due to the reduction step, due to the abstraction step, due to the numerical algorithms and computations as well as due to the reverted interpretation of computational model and of reduced system to reality.

The results from theoretical investigations are always related to the used particular model, they are only effectual within the validity of the model. This means in particular, the model has to be assigned to the specific task at hand and obviously, modeling is an iterative process.

Theoretical or mathematical models are often based on electrical analogies but mechanical problems should be described on the base of mechanical laws to get a direct interpretation of its parameters. Well-developed tools like the Multibody Systems or the Finite Element approach are available for the computerized establishing of the models of complex spatial systems and their belonging equations of motion. In Figure 1 a typical Multibody System model is shown with its rigid bodies malleus, incus and stapes. The ear drum, the air in the outer ear canal and the fluid of the inner ear are modeled as lumped mass points or bodies. The ligaments and muscles tensor tympani and musc. stapedius are described as visco-elastic elements with an active part. The model has 77 degrees of freedom and the important generalized coordinates are indicated in the figure.

Several categories of problems can be grouped during the investigations: firstly, due to anatomy dealing with the geometrical representation of the elements; secondly, due to function or processes considering physical effects and thirdly due to mathematical reasons dealing with several forms of descriptions like linear or nonlinear systems. All of these aspects are interconnected and coupled, thus they have to be regarded altogether.
After establishing a model and generating the governing equations, the parameters have to be determined or at least estimated. This is a difficult task and the accuracy of

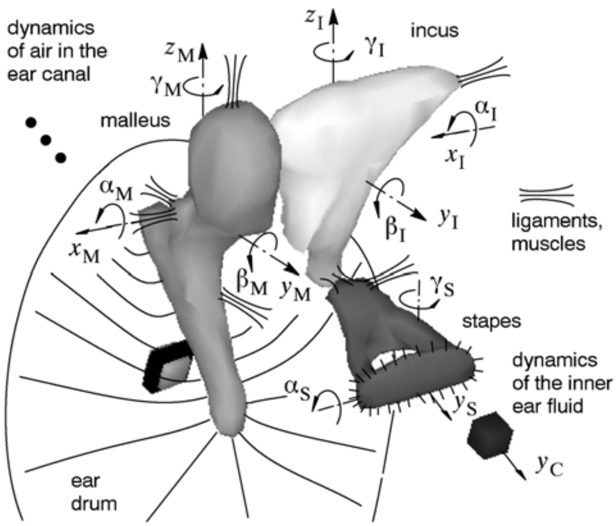

Figure 1. Multibody System model of the middle ear and its adjacent structures

determining the parameters must be in accordance to the chosen model. Usually, averaged values are taken because the parameters of the hearing organ are time variant and show inter- or intra-individual different behavior. Specific measurements on living or cadaveric subjects can be made but also clinical data from hearing test or tympanometry can be evaluated. Laser Vibrometry is a powerful tool to pick up displacements or velocities of particular points of the ossicular chain without contact.

1.1. Middle Ear

1.1.1. Ear Drum

Due to its different mechanical behavior, the pars flaccida and the pars tensa have to be distinguished. Both have a spatial formed shape and there is a fluid/solid interaction at both sides to the ear canal and to the tympanic cavity. The drum is composed of several layers reinforced with fibers. It can be considered as an anisotropic, inhomogeneous material. Nonlinear effects must be regarded due to nonlinear constitutive laws of material but also due to large kinematical displacements.

1.1.2. Ossicles

The geometrical shape of the ossicles and the contact points of ligaments and joints are important entities for the mechanical models [5, 6]. Due to the inhomogeneous material with its anisotropic behavior, the mass and distribution of it has to be measured [7, 9].

During normal sound transfer, their elastic deformations are small in comparison to that of the ligaments and joints hence they are often considered as rigid bodies.

1.1.3. Ligaments

It is very difficult to acquire the length and the cross sections as well as the inner structure of ligaments. Moreover, the mechanical characteristics at different locations within a ligament are not known in detail and considerable differences can be seen between the different types of ligaments. Thus, for realistic models the mechanical behavior of ligaments is described by simplified force laws even in the seemingly detailed FEM analysis.

For very small deformations, they are considered as visco-elastic elements described by 6-dimensional force laws accounting for deformation and their time derivatives in a linear relation.

For larger deformations the relation of deformation respectively velocities and the forces become highly nonlinear [10]. Such deformations may occur due to sound events with high intensity but also in case of static preload leading to a working position different from the natural one. Static preloads of the ossicular chain originates from pressure differences in the cavities, scar tissues or from inserted prostheses cause local static forces which governs the dynamical process of sound transfer essentially.

1.1.4. Joints

Similar to ligaments, the joints are considered as visco-elastic elements described by 6-dimensional force laws accounting for deformation and their time derivatives in a linear relation as long as the deformations are small.

For larger deformations, nonlinear behavior must be regarded in particular for investigations in the higher frequency range.

Due to the complex shape, additional kinematical constraints may appear which impede motions in particular directions. In particular, this effect appears very pronounced in the incudo-malleolar joint.

1.2. Inner Ear

Caused by the motion of stapes there is a solid/fluid interaction on its footplate. Due to the annular ring, the stapes is able to move perpendicular to its footplate and to tilt around its short and long axis. The translation produces a global volume displacement, whereas rocking cause only local displacements in the perilymph fluid. In classical hearing theory, only the global volume displacement is considered as resulting in a hearing sensation. Measurements recently made, give evidence that rocking motions evoke an inner ear response, too [11]. Therefore, the spatial motion of the stapes footplate has to be taken into account for calculating the dynamic pressure fluctuations in the inner ear fluid. Static pressure changes may be caused e.g. by posture variations or cranial pressure alterations.

1.3. Modeling Techniques

In engineering approved program packages based on different modeling procedures and approaches are available. Besides the particular focus of investigations, an appropriate choice pays also attention to the computational costs, the effort for acquisition and determination of geometrical and material data, the accuracy of that data, the effects under consideration and the demanded accuracy of results.

Finite Element Method (FEM) is effectively used for calculation of local stress and small deformation; the models have plenty of degrees of freedom and need detailed data for geometry and material.

Boundary Elements (BEM) are suitable for transition of sound between different media.

Multibody Systems are widely used for dynamical problems and for large spatial motions. Nonlinear behavior of elements is elegant to implement and the models are of low degrees of freedom.

2. Parameters

The determination of parameters is a difficult problem because living subjects show a time dependent behavior and there are significant intra- and inter-individual differences. Moreover, the access to the objects is very restricted even in the lab and particularly under living conditions.

Additionally to observations from the clinical practice, specific measurements in the lab are used for the estimation of parameter sets suitable to the specific model under consideration. Besides of parameter identification procedures, mostly an adaptation of parameters is carried out by comparing the observations with simulation results.

2.1. Measurements

The hearing organ may be excited in a more natural way by acoustical sources like loudspeakers or mechanically by specific shakers [12] or active middle ear implants.

For the response, usually Laser Doppler Vibrometry is used to pick up without any contact either displacements or velocities of the particular points of elements. From these signals, transfer functions between the excitation and the response at and particular points can be calculated. To reconstruct the dynamical behavior of the system, the transfer functions between particular points, e.g. umbo and stapes may be of interest as well as the dynamical behavior of the coupling between an implant and ossicles as sketched in Figure 2 and 3. Applying of scanning vibrometry facilitate the reconstruction of the spatial motions and the animation of the modes.

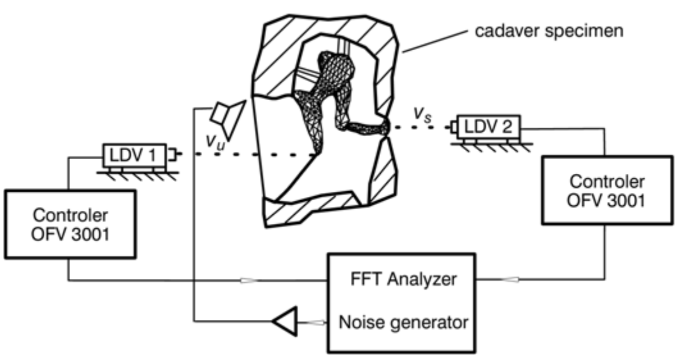

Figure 2. Setup for measuring transfer functions

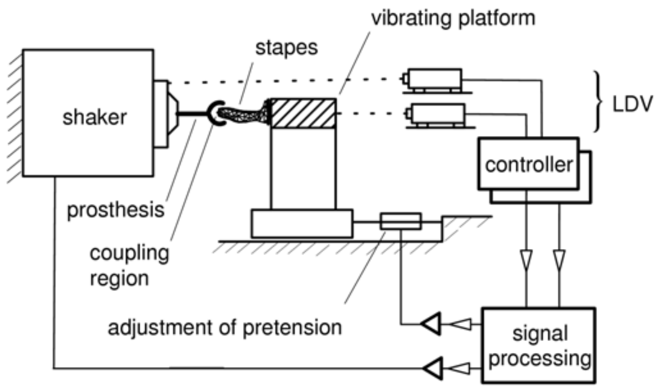

Figure 3. Setup for measuring coupling conditions

Other measurements of the response are the subjective hearing impression or the derivation of potential of nerves [11].

2.2. Local Multifrequency Tympanometry

To study the influence of static preloads the Multifrequency Tympanometry is a very powerful procedure. Precise information can be found by plotting the relation between distinct points of the ossicular chain leading to so called Local Multifrequency Diagrams LMFT [13]. Preloads may come from static pressure differences between outer ear canal, middle ear cavity or inner ear, scar tissues or prestressed implants. The method offers a good insight into the nonlinear behavior and allows the estimation of nonlinear force laws.

3. Simulations

3.1. Spatial Motions of ossicles

Simulations show that the ossicles in the middle ear carry out a three-dimensional motion. The specific form of the actual motion is strongly dependent on the frequency. In the higher frequency range the ossicular chain vibrates quite different from the classically known rotation around the axis between the lig. mall. ant. and lig. inc. post. resulting in distinct rocking motions of the stapes [14].

For a natural ear and a reconstruction with a partial ossicle replacement prosthesis (PORP) replacing the missing incus the spatial motion of stapes is shown in Figure 4. A pronounced rocking is obvious in the higher frequency range particularly in the reconstructed case.

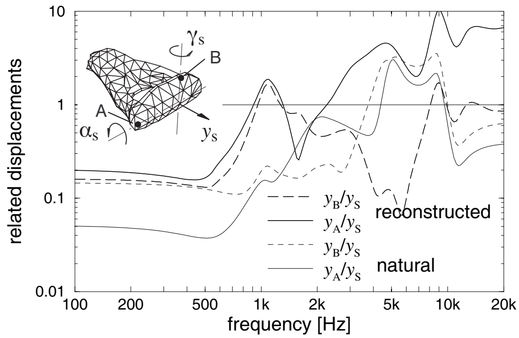

Figure 4. Rocking of stapes in a natural and a reconstructed middle ear: displacements of vertices A and B related to the piston motion y_s

3.2. Coupling

Crucial points of coupling an implant are the points of attachment and the force law of coupling characterized by the stiffness, damping and its nonlinearity.

Stiffness and damping are depending on size, intermediate crafts and on the gap between ossicles [15, 16]. Depending on the design principle of connection like crimping, clamping, or pushing together or gluing, the coupling shows a more or less nonlinear behavior. It is mainly governed by the applied preload, which consequently plays an important role in sound transfer.

Commonly used active implants are driven by piezo-elements or electromagnetic coils. They act on an ossicle via a rod pushed towards it. This static preload can be regulated by the surgeon using an adjustment screw. Due to the nonlinear behavior of the ossicular chain and the force law of coupling the preload governs the capacity of implant and the sound transfer. It may also cause ringing due to the feed back of the excitation to the microphone [17]. A general guideline for the adjustment travel of the screw is given in [18] regardless the individual stiffness of the middle ear. The static adjustment influences the sound transfer of the dynamical system essentially. Therefore, mechanical characteristics of the entire system have to be regarded for the investigation of hearing, the description of the motion of stapes, the distortion in the sound transfer and the risk of ringing.

3.3. Nonlinear effects

Investigations of the dynamical behavior of a given system start mostly with a linear description. To study particular effects like distorted sound transfer, attenuation for excitation with high intensities or transfer characteristics depending on static preload, a nonlinear description is necessary [10]. In Figure 5 the load-deflection characteristic of several elements of the middle ear are sketched.

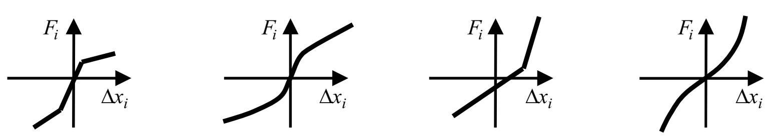

Figure 5. Nonlinear characteristics of middle ear elements

After a luxation of the incudo-stapedial joint, its characteristic is very different for push and pull direction as shown in Figure 6. This leads to a distorted sound transfer. Additionally to the basic frequency f_0 of excitation higher harmonics f_k appear in the stapes motion

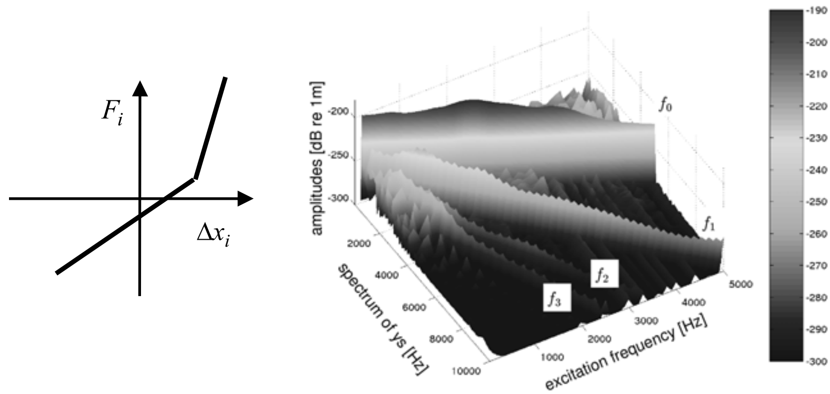

$$y_s(t)=\hat{y}_{s0}\sin(f_0+\varphi_0)+\sum_{k=1}^{\infty}\hat{y}_{sk}\sin(k\,f_0+\varphi_k)$$

Figure 6. Distorted sound transfer due to nonlinear coupling of stapes and incus. Stapes motion contain higher harmonics of excitation frequency

3.4. Feedback

Driving the ossicular chain actively at the incus, not only the stapes is excited but also the malleus and the ear drum [17]. The radiated sound may cause ringing by feedback as illustrated in Figure 7.

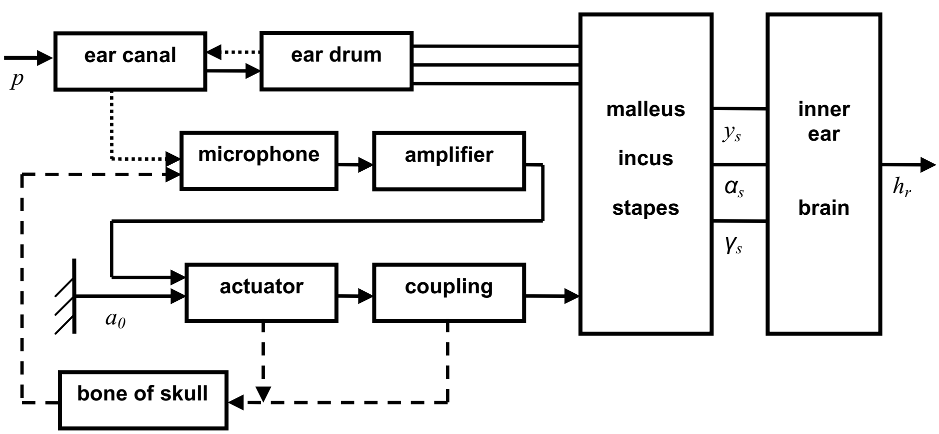

Figure 7. Schematic representation of sound transfer with feedback loops

A strongly amplified excitation is necessary to compensate an inner ear hearing loss or e.g. a reduced mobility of stapes due to an otosclerotic annular ring. Because of the distinct nonlinearity of the annular ring, particularly in case of high static pretension the transfer from actuator to stapes shows a higher attenuation than that from actuator to malleus as shown in Figure 8 when the actuator is pressed against the incus denoted by adjustment travel a_0.

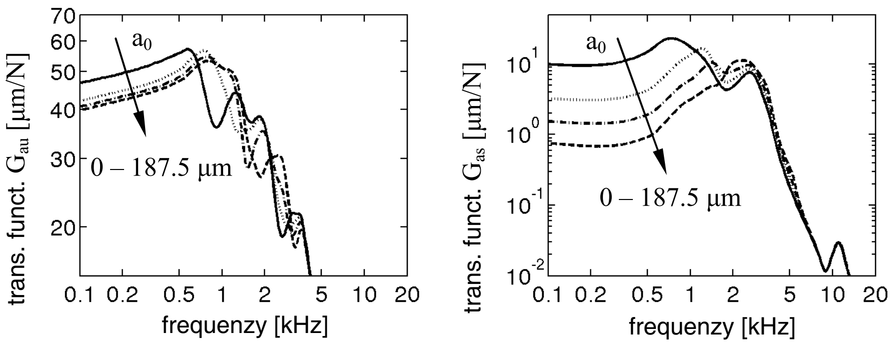

Figure 8. Transfer functions from actuator at incus to the umbo (left) and to the stapes piston motion (right) for different adjustment travel a_0 of the actuator

Simulations show in agreement to the measurements, that the static adjustment a_0. of the actuator influences the amplitude of stapes and the amplitude of umbo depending on the stiffness of the chain. For these investigations, first the working position of the ossicular chain due to the static adjustment was calculated and the sound transfer was simulated using a model linearized with respect to this working position.

The amplitude of stapes determines the hearing impression *hr* whereas the motion of umbo leads to a sound radiation into the outer ear canal. It can be used for the detection of contact during surgery [18] but it may cause a feedback of excitation.

Due to the nonlinear behavior of the ligaments, in particular of the stiffening annular ring, the ossicular chain becomes immobile with increasing static adjustment. A linear increasing adjustment travel cause a shift of the natural frequencies to higher values and a nonlinear drop in stapes amplitude can be seen in the lower frequency range up to 3 kHz. For the umbo motion, this effect is not so distinct because the ear drum has as wider range of mobility than the annular ring.

Consequently, the gain margin $GM = G_{stab} / G_{comp}$ as the ratio of the highest maximal stable amplification G_{stab} and the amplification G_{comp} as desired for a full compensation of hearing loss is limited and ringing occur if GM is below one, Figure 9. An increased static adjustment travel leads to a better coupling indeed, but causes a reduced gain margin with a higher risk of ringing.

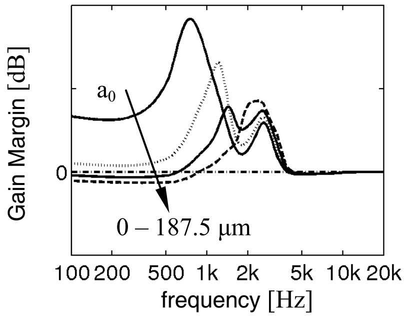

Figure 9. Gain margin for increasing adjustment travel of active implant

In the coupling region, it may occur that pushing the driving rod against the incus (forward motion) has a higher stiffness than the retraction. This nonlinear coupling cause a distorted motion of the stapes containing the frequency of excitation and higher harmonics of it as illustrated in Figure 6.

3.5. Optimization

For a good reconstruction several criteria of optimization have to be regarded leading to a multicriteria optimization problem. This can be achieved only by considering the entire system.

In order to the design an active or passive implant, generalized or averaged data of the anatomical structure and their mechanical characteristics are taken into account. A problem is the wide spectrum of different manners of insertion and different design of coupling. Thus, a strong demand for the final realization is to have a "robust" design insensitive against changes in the parameters of the system. This is very essential because biological structures undergo alterations due to time.

As an example for optimization of coupling the attachment of a PORP to the ear drum and malleus handle is considered. Taking its position, the size of intermediate layer and the stiffness of it as design variables and considering the difference between the natural and the reconstructed transfer together with the loudness as cost function, a multicritera optimization [19] leads to an improved design of coupling as shown in Figure 10.

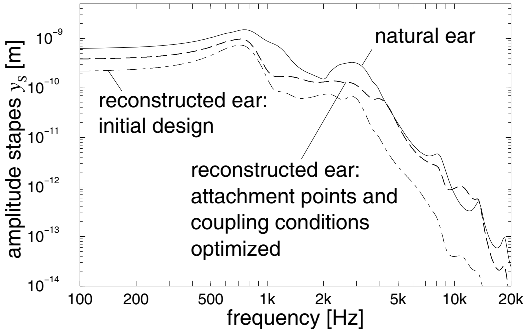

Figure 10. Improved design of coupling a PORP achieved by multicritera optimization

4. Conclusions

The main part of the hearing process is concerned with mechanics and therefore, a mechanical description should be used. The Multibody system approach combined with Finite Elements deliver suitable models adequate to most of the stated problems. Depending of it, nonlinear or linearized models are used to simulate natural, pathological or reconstructed situations. Such investigations are focused on the understanding and description of hearing itself, the interpretation of measurements for diagnosis and the development and improvement of diagnostical procedures.

An important field is the development and the optimization of known and new concepts of reconstructions with passive and active implants. Here, the coupling of implants with the ossicles is important for the sound transfer.

Optimal coupling depend on the design of the coupling region, the mechanical properties of the implant itself as well as on the dynamical behavior of the ossicular chain. Optimization criteria may be good sound transfer, low distortion and no ringing. The realization must be “robust”, i.e. not sensitive against changes in the parameters of the system. This is very essential because biological structures undergo alterations due to time, particularly the given prestress of ligaments and static pressure may change.

Acknowledgements

Parts of these investigations were financed by the German Research Council (DFG).

References

[1] K. B. Hüttenbrink, The mechanics of the middle ear at static air pressures, *Acta otolaryngol* **451** (1988), 1-35.

[2] J. J. Dirckx and W. Decraemer, Area change and volume displacement of the human tympanic membrane under static pressure, *Hearing Research* **62** (1992), 99-104.

[3] O. Densert, A. Ivarsson and K. Pedersen, The influence of perilymphatic pressure on the displacement of the tympanic membrane, *Acta otolaryngo* **84** (1977), 220-226.

[4] M. Gaihede and J. Kabel, The normal Pressure-Volume Relationship of the Middle Ear System and its biological Variation. In J. Rosowski and S. Merchant (eds.), *The function and mechanics of normal diseased and reconstructed middle ears*, Kugler Publications, The Hague, 2000, 59-70.

[5] J. Lang, *Klinische Anatomie des Ohres,* Springer, Wien and New York, 1992.

[6] I. Kirikae, *The Structure and Funktion of the Middle Ear*, The Tokyo University Press, Tokyo, 1960.

[7] C. Weistenhöfer, *Funktionale Analyse des menschlichen Mittelohres durch dreidimensionale Messung und Modellierung*, GCA-Verlag, Herdecke, 2002.

[8] M. Bornitz, T. Zahnert, H.-J. Hardtke and K.-B. Hüttenbrink, Identification of Parameters for the Middle Ear Model, *Audiology and Neuro-Otology* **4** (1999), 163-169.

[9] S. Puria, J. H. Sim, J. Tuck-Lee and C. Steele, Middle ear Morphology from Cadaveric Temporal Bone Micro-CT Imaging. In A. Huber and A. Eiber (eds.), *Middle Ear Mechanics in Research and Otology,* World Scientific, Singapore, 2007, 259-268.

[10] A. Eiber and C. Breuninger, Nonlinear Properties of the Middle Ear, Some Influences on Hearing and Diagnosis. In K. Gyo, H. Wada, N. Hato and T. Koike (eds.), *Middle Ear Mechanics in Research and Otology,* World Scientific, Singapore, 2004, 19-26.

[11] D. Sequeira, C. Breuninger, A. Eiber and A. Huber, The Effects of Complex Stapes Motion on the Response of the Cochlea in Guinea Pigs. In A. Huber and A. Eiber (eds.), *Middle Ear Mechanics in Research and Otology,* World Scientific, Singapore, 2007, 130-135.

[12] A. Eiber and C. Breuninger, Mechanical Excitation of Complex Stapes Motion in Guinea Pigs. In A. Huber and A. Eiber (eds.), *Middle Ear Mechanics in Research and Otology,* World Scientific, Singapore, 2007, 123-129.

[13] A. Eiber, H.-G. Freitag and T. Hocke, On the relationship between multifrequency patterns and the dynamic behavior of the middle ear. In J. J. Rosowski and S. N. Merchant (eds.), *The function and mechanics of normal diseased and reconstructed middle ear,* Kugler Publications, The Hague, 2000, 157-166.
[14] H.-G. Freitag, *Zur Dynamik von Mittelohrprothesen,* Shaker Verlag, Aachen, 2004.
[15] T. Zahnert, M. Bornitz and K.-B. Hüttenbrink, Calculations and Experiments on the influence of Prosthesis coupling to the Middle Ear Transfer Function. In K. Gyo, H. Wada, N. Hato and T. Koike (eds.), *Middle Ear Mechanics in Research and Otology*, World Scientific, Singapore, 2004, 83-90.
[16] A. Eiber, H.-G. Freitag, G. Schimanski and H.-P. Zenner, On the Coupling of Prostheses to the Middle Ear Structure and its Influence on Sound Transfer. In J. J. Rosowski and S. Merchant (eds.), *The function and mechanics of normal diseased and reconstructed middle ears*, Kugler Publications, The Hague, 2000, 297-308.
[17] A. Eiber, C. Breuninger, J. Rodriguez, H. P. Zenner and M. Maassen, On the Optimal Coupling of an Implantable Hearing Aid – Measurements and Simulations. In A. Huber and A. Eiber (eds.), *Middle Ear Mechanics in Research and Otology,* World Scientific, Singapore, 2007, 246 – 252.
[18] B. Waldmann, H. Maier and R. Leuwer, Indicator for Efficient Coupling of the Otologics MET™ Ossicular Stimulator. In K. Gyo, H. Wada, N. Hato and T. Koike (eds.), *Middle Ear Mechanics in Research and Otology,* World Scientific, Singapore, 2004, 377-383.
[19] A. Eiber, H.-G. Freitag and C. Breuninger, Virtual Reconstruction of Impaired Hearing. In W. Schiehlen and M. Valasek (eds), *Virtual Nonlinear Multibody Systems*, Kluwer, Dordrecht, 2003, 427 - 435.

Medicine Meets Engineering
J. Hammer et al. (Eds.)
IOS Press, 2008

T-Peel Test for the Analysis of Articular Cartilage Integration

**Englert, C; **Greiner, G; *Berner, A; **Hammer, J*
** University Medical Centre Regensburg, Bavaria, Germany*
*** University of Applied Science Regensburg, Bavaria, Germany*

Introduction: A central aim of current research is to determine the molecular mechanisms of articular cartilage repair. One major issue of articular cartilage repair is the achievable mechanical strength which has been correlated with the collagen metabolism, deposition and collagen cross-linking [1-3]. Current *in vitro* techniques, leading to cartilage integration used a shear test to failure [4-6]. Another well established in vitro method to investigate articular cartilage integration is the insert-ring push out model which is mainly utilized investigating the integration of tissue engineered cartilage to native cartilage [7-11]. Finite element modeling illustrates at least for the shear test to failure that the contact area is not homogeneously loaded [12]. For the mechanical analysis of articular cartilage integration in regard to its inhomogeneous integration a higher mechanical resolution method is needed.

Furthermore the shear test to failure as well as the ring-insert model lacks a comparison to in situ trauma situation, where ruptured or fractured articular cartilage surfaces are opposed after surgical reduction. Considering all these a T-peel test has been introduced in literature [13] but never been experimentally performed. This project deals with the establishment of a T-peel test as a topographical sensitive tool in mechanical analysis of T-peel data and its potential to investigate articular cartilage *in vitro* integration in comparison to articular cartilage rupture strength.

Methods.

From the patello femoral groove of calf knees (Figure 1 A) osteochondral fragments were cut (Figure 1 B) and dissected into defined slices (600 µm) of articular cartilage by a sledge microtome (Figure 1 C). The preparation of these articular cartilage blocks to final and accurate specimen geometry is performed from the upper volume. These slices were cut to final specimen geometry (defined for all experiments: 12 mm x 2.4 mm x 0.6 mm). In order to minimize geometrical effects on the results obtained, one end of the planar section subjected for peeling strength analysis was cut to approximately half of the specimen length (i.e. 6 mm, Figure 1 D). During the entire preparation procedure the cartilage was kept moist by continuously rinsing or in a bath of physiologic salt solution, to avoid drying of the tissue and therewith necrosis.

For mechanical analysis the specimen was clamped into fixings of the test rig (Hegewald & Peschke). The accuracy of the load cell was better than 0.1 N. Peeling progress, i.e. crack propagation, was continuously recorded by a linear variable differential transformer (LVDT) with a resolution of 0.01 mm. All preliminary tests reported in this work were performed in laboratory air. At a later state it is planned to use a PBS bath in order to avoid tissue drying during mechanical analysis.

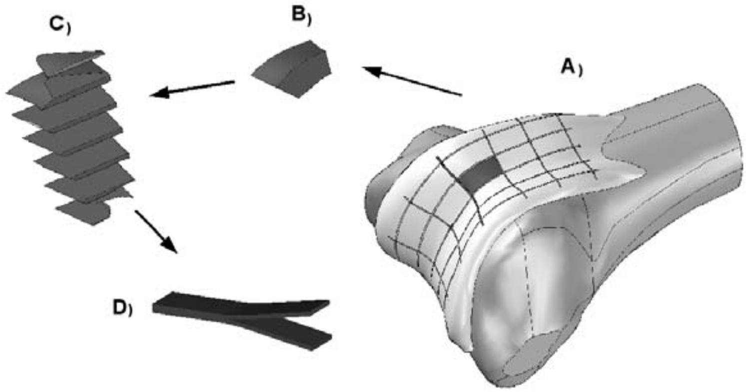

Figure 1: Preparation steps from the patello femoral groove of a calf knee to a defined articular cartilage block, fitting to the T Peel configuration.

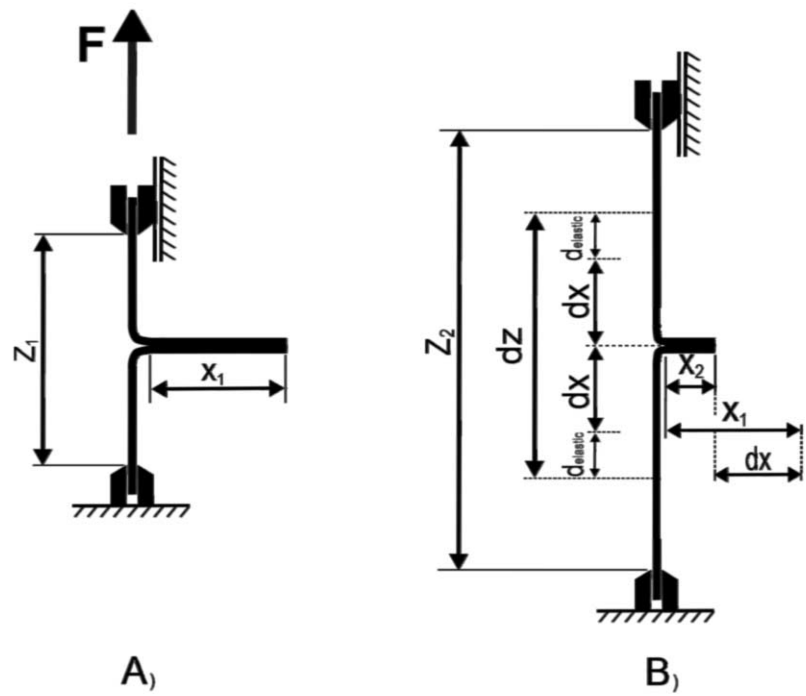

Figure 2: T-peeling of a cartilage block, schematic: Initial configuration prior to peeling, A) and after peeling by a peeling distance dz, B). Peeling of the articular cartilage block results in superimposed elastic (d_e) and plastic (d_x) deformation contributions.

Peeling was performed until total rupture of the cartilage blocks. The recorded load versus peeling distance data were analyzed in terms of the initial stiffness of the laps, load threshold for onset of peeling and peeling force normalized per incremental line segment as a function of peeling length.

At a later state it is planned to restrict peeling of the cartilage blocks to a length of approximately 4 mm leaving a small section undamaged (x_2 = 1 mm, Figure 2). For subsequent integration this peeled section can be precisely realigned and placed in a cultivation chamber with optional superimposition of defined compressive stresses in order to stimulate and support integration mechanisms (Figure 3). After cultivation the integrative repair of the articular cartilage can be analyzed by a repeated T-peeling of the cartilage block. The success of the integrative repair can be directly compared to the peeling strength assessed by the initial T-peel test of the cartilage block. Additional important information about influences of the initial trauma is of interest. By comparison of the peeling strength values of the initial cartilage to the scar tissue after integration, direct access and comparison to the repair potential of integration media can be obtained. Furthermore, by peeling the initially undeformed segment x_2 in the second peeling experiment (i.e. remaining unfractured end segment after first peeling) other effects such as aging or inflammation can be determined.

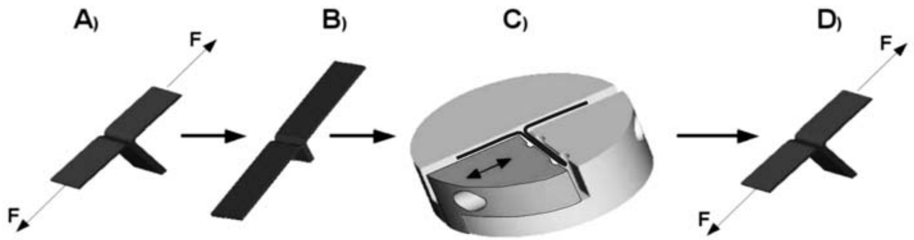

Figure 3: Articular cartilage integration process, schematic: T-peeling, A) until x_2, compare Figure 2, B); realignment of peeled surfaces with optional compressive forces, C) and re-peeling of the integrated section, D).

Results.

Preliminary T-Peel experiments were performed on 39 articular cartilage blocks (second and third slice) harvested from two calf knees. In immature articular cartilage vessels occurring in the depth zone can substantially reduce mechanical properties. Preliminary T-peel experiments were affected by residual vessels in the cartilage block, harvested from the deep zone. The fracture propagation within the cartilage block during T-peel revealed early failure. The rupture line was attracted by the vessel and propagated out of the defined peeling plane in the middle of the block leading to undefined boundary conditions. Therefore, only homogeneous cartilage blocks from the upper zone were used (second and third slice in Figure 1 C). Thus, during peeling failure propagation was focused into the middle section of the blocks and similar boundary conditions on both laps of each specimen and also among the different sample blocks were guaranteed.

Representative results in terms of best, minor and mean load vs. peeling length curves are given in Figure 4. Instantaneously after mechanical loading, small non-linear transient contributions due to influences of the specimen fixings are obvious. After this initial transient all curves exhibit linear elastic deformation, characterized by constant dFT/dST. It should be noted that the scatter in elastic behavior among all 39 specimens investigated is almost negligible and represented by Figure 4. At an individual threshold in peeling force increasing influences of superimposed viscoelastic effects lead to non-linear deformation until the peeling load approaches a more or less constant value. In this section indications for the onset of peeling are visible by oscillations in the recorded data. The failure progresses in longitudinal direction by first local de-cohesions of the tissue along the gap orientated normal to the axis of crack propagation. Fracture stabilizes and additional loading is required until further incremental propagation of the fracture line is induced. In this region, peeling progresses until total rupture in similar to ideal plastic deformation, i.e. without any work hardening or softening contributions. Tissue damage is related to the horizontal sections of the load vs. peeling length diagram. During these initial steps of crack propagation, the generation of additional fracture requires additional (small) loads until the combination of applied load (stress) and induced stress concentrations exceed the local rupture strength of the tissue.

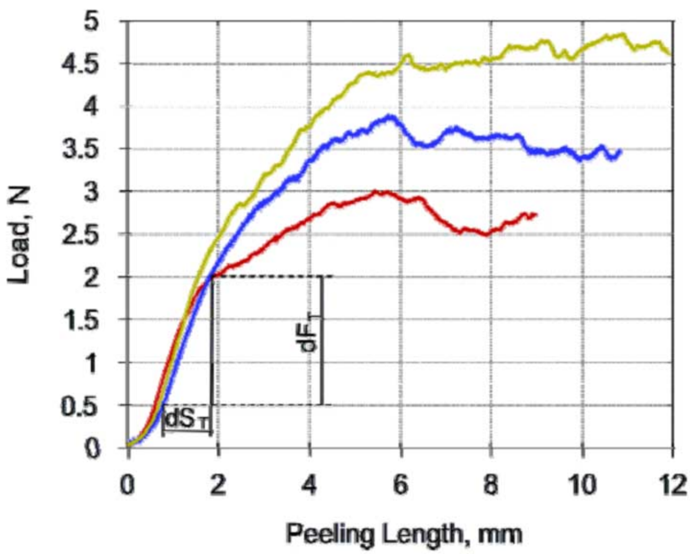

Figure 4: Typical load versus displacement curves obtained from T-peel testing. The curves represent best, mean and worst strength of 39 individual articular cartilage specimens.

It should be noted that the recorded peeling lengths dz represent not only the increase in new de-bonded “free length” dx, but also include elastic deformation contributions $d_{elastic}$ according to $dz = 2\ (dx + d_{elastic})$. Increases in peeling thus continuously provide additional “free length” which reacts with enhanced elastic deformation. Therefore the quantitative peeling length is not strictly linear correlated to the initial specimen length. Higher (local) peeling strength is directly related to increases in elastic deformation of the tissue laps already orientated in loading direction.

Discussion.

The preliminary results illustrate that the T-peel model is feasible to investigate the strength of articular cartilage by peeling. In comparison to established models, e.g. the push-out ring test and the single lap shear experiment; T-peeling should provide direct and comparable access to the strength of tissues prior and after integration. In conventional shear experiments the two laps for integration are cut from neighboring sections of the cartilage. Therefore, the areas subjected for bonding are ideally smooth due to microtome cutting. For integration the exact repositioning of both strips is not sufficiently precise. Thus, it cannot be guaranteed that exactly the opposing local areas of the initial cartilage can be readjusted. The adhesive strength resulting from the overlapping area and the detected load at failure (shear test to failure model) or the detected work until failure (push out model) lack a detailed analysis of the integration site. Furthermore, the investigated overlapping area definitely cannot be assumed as fully integrated. The integration of articular cartilage wound surfaces seems to result in multiple local adhesion points of the opposing surfaces. These sections are loaded in the shear test to failure from the periphery to the center while the adhesion points confluent in its mechanical stability. Integration success may thus be affected by bridging areas which were not directly overlapping in the native tissue prior to preparation.

Native tissue strength and failure of cartilage samples is usually analyzed under normally acting stresses. Fracture is therefore related to the comparatively small cross section of the sample strips. In comparison, mechanical strength of integrated tissues is investigated under shear forces acting in a large area of overlapping tissue and the measured fracture load (stress) and the corresponding displacement can only be regarded as integral mean information of the entire overlapping (bonded) area. Local sections of excellent integration are superimposed by regions where only reduced bridging has developed during the integration treatment cannot be differentiated and the cartilage repair potential of different integration conditions is only characterized the average strength of the overlapping area. This strong dependency on size effects limits the transferability of the experimental results. Also comparison of these results to native tissue strength must not be performed, due to the basically different mechanical loading conditions (normally applied stresses vs. shear stresses). Although, for strictly elastic deformation, the mechanical behavior analyzed in both types of experiments can be expressed by elastic constants according to Hooke´s law, i.e. in the case of normally acting forces by the Young´s modulus according to $\sigma = E\ \varepsilon$, and for elastic shear deformation by the Shear modulus $\tau = G\ \gamma$ [14,15]. Knowing one of these elastic constants and measuring the Poisson´s ratio ν the second elastic constant can be calculated using $G = E/2(1+\nu)$. Unfortunately, the determination of ν for articular cartilage has not been yet performed successfully and thus, the transformation of elastic shear deformation to deformation under normally acting stresses is impossible. Additionally, the integration area of the shear specimens shows double material thickness. This local "reinforcement" generally affects the measured stiffness data of the bonded/integrated section. A detailed separation of the measured integral LVDT-signal between elastic tensile deformation resulting from the strips of the single lap specimen and the elastic shear deformation of the overlapping area with double material thickness is not possible.

During T-peel testing the material in the peeling area is continuously "scanned" by the fracture line running progressing in this plane and thus provides higher local resolution as the peeling strength has only integral information contributions due to the line length and not to a comparatively "large" area like in the single lap configuration.

To compare native tissue strength to developed scar tissue strength this experiment refers closer to the clinical practice where fractured tissue surfaces are originally realigned for integrative repair. Sharp microtome cut surfaces, used for the shear test rather refer to the clinical well known mosaic plastic [17]. Therapeutic interventions such as steroid hormone stimulation of the cell metabolism to enhance integrative repair as well as inflammatory responses due to the impact of trauma with the expression of cytokines can be better judged to the mechanical parameters [5,16]. The comparison of tissue strength at rupture load to scar strength at rupture load will show a percentage range of gained integrity after integrative repair.

Although, the T-peel test provides clear advantages over the classical in vitro experiments concerning the interpretation of to recorded material data, a number of limitations have to be considered and need to be clarified. These are as follows:

It must be guaranteed that the peeling results after integration i.e. strength values corresponding to defined peeling lengths can be directly compared to the measured data of initial state peeling. Therefore, a suitable marker system is necessary to identify the local peeling length positions.

The measured strength data usually determined as normally orientated stress in the actual peeling section may be affected by superimposed shear contributions induced by misalignment of the unpeeled end segment of the cartilage slice, Figure5.

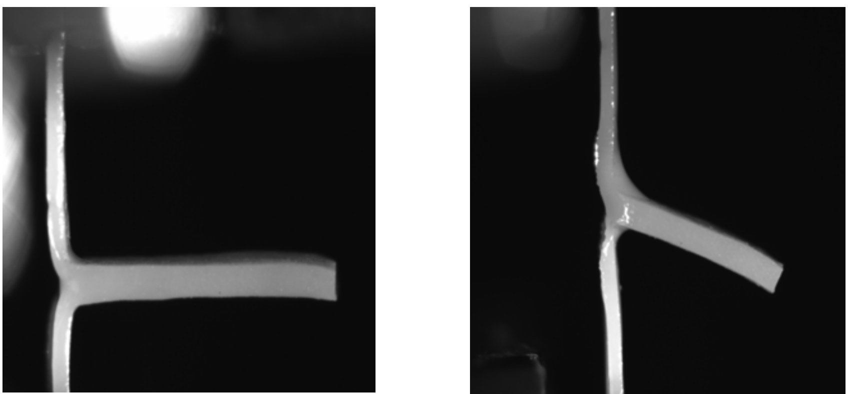

A) B)

Figure 5: Cartilage during peeling: Normal stress in the peeling plane and homogeneous crack propagation A) and shear stress contributions in crack propagation plane and local reduction in cross section of peeled strips B).

With respect to the discussed aspects requiring further experimental improvement T-peel testing can enable the comparison of native mechanical cartilage properties to integrated tissue. By precise realigning of the opposing articular cartilage strips obtained from the peeled cartilage block and subsequent cultivation the integrative repair capability can be quantified in terms of a repeated, second T-peel test and directly compared to the initial tissue strength (rupture load per length). A higher mechanical resolution is assessable to obtain more insights in the in homogeneous bonding of integrated articular cartilage wounds.

References

[1] Ahsan T, Lottman LM, Harwood F, Amiel D, Sah RL: Integrative cartilage repair: inhibition by beta-aminopropionitrile. J Orthop Res 1999, 17: 850-857.

[2] DiMicco MA, Sah RL: Integrative cartilage repair: adhesive strength is correlated with collagen deposition. J Orthop Res 2001, 19: 1105-1112.

[3] DiMicco MA, Waters SN, Akeson WH, Sah RL: Integrative articular cartilage repair: dependence on developmental stage and collagen metabolism. Osteoarthritis Cartilage 2002, 10: 218-225.

[4] Englert C, McGowan KB, Klein TJ, Giurea A, Schumacher BL, Sah RL: Inhibition of integrative cartilage repair by proteoglycan 4 in synovial fluid. Arthritis Rheum 2005, 52: 1091-1099.

[5] Englert C, Blunk T, Fierlbeck J, Kaiser J, Stosiek W, Angele P et al.: Steroid hormones strongly support articular cartilage integration in the absence of interleukin-1ß. Arthritis Rheum 2006, 54: 3890-3897.

[6] Reindel ES, Ayroso AM, Chen AC, Chun DM, Schinagl RM, Sah RL: Integrative repair of articular cartilage in vitro: adhesive strength of the interface region. J Orthop Res 1995, 13: 751-760.

[7] Hunter CJ, Levenston ME: Maturation and integration of tissue-engineered cartilages within an in vitro defect repair model. Tissue Eng 2004, 10: 736-746.

[8] Moretti M, Wendt D, Schaefer D, Jakob M, Hunziker EB, Heberer M et al.: Structural characterization and reliable biomechanical assessment of integrative cartilage repair. J Biomech 2005, 38: 1846-1854.

[9] Obradovic B, Martin I, Padera RF, Treppo S, Freed LE, Vunjak-Novakovic G: Integration of engineered cartilage. Journal of Orthopaedic Research 2001, 19: 1089-1097.

[10] Tognana E, Chen F, Padera RF, Leddy HA, Christensen SE, Guilak F et al.: Adjacent tissues (cartilage, bone) affect the functional integration of engineered calf cartilage in vitro. Osteoarthritis Cartilage 2005, 13: 129-138.

[11] Zhang Z, McCaffery JM, Spencer RG, Francomano CA: Growth and integration of neocartilage with native cartilage in vitro. J Orthop Res 2005, 23: 433-439.

[12] Fierlbeck J, Englert C, Reuben RL, Hammer J: Biomechanical properties of articular cartilage as a standard for integrated tissue interfaces. Technol Health Care 2006, 14: 445-451.

[13] Ahsan T, Sah RL: Biomechanics of integrative cartilage repair. Osteoarthritis Cartilage 1999, 7: 29-40

[14] Hayes WC, Mockros LF: Viscoelastic properties of human articular cartilage. J Appl Physiol 1971, 31: 562-568.

[15] Hayes WC, Keer LM, Herrmann G, Mockros LF: A mathematical analysis for indentation tests of articular cartilage. J Biomech 1972, 5: 541-551.

[16] DiMicco MA, Patwari P, Siparsky PN, Kumar S, Pratta MA, Lark MW et al.: Mechanisms and kinetics of glycosaminoglycan release following in vitro cartilage injury. Arthritis Rheum 2004, 50: 840-848.

[17] Hangody L, Feczko P, Bartha L, Bodo G, Kish G: Mosaicplasty for the treatment of articular defects of the knee and ankle. Clin Orthop 2001, S328-S336.

Medicine Meets Engineering
J. Hammer et al. (Eds.)
IOS Press, 2008

A pilot study for evaluation of bond strength of orthodontic brackets to enamel using a new impact test machine

R.E. HENDRY[1], T.GILGRASS[1], L. CHUNG[1], R. MacPHERSON[2], T.H.J. YANG[2], R.L. REUBEN[2†]

[1] *University of Edinburgh, Postgraduate Dental Institute, Edinburgh, UK.*
[2] *Heriot-Watt University, School of Engineering and Physical Sciences, Edinburgh, UK.*

Abstract. We report an *in-vitro* pilot study to assess the ability of a new impact test machine to evaluate bond strength of orthodontic brackets to tooth enamel. A total of 37 extracted premolar teeth were bonded with APC Plus MBT Victory orthodontic brackets. Bond strength was tested using a new pendulum-based instrumented impact test machine. The maximum stress, the impact energy and interaction time required to debond the brackets were recorded. Of the total tested, 9 samples were successfully debonded with no obvious damage to the tooth surface although 28 samples fractured through the enamel and dentine. There was a statistically significant difference between the maximum stress required to debond the bracket and that required to fracture the tooth, a higher stress being required to debond the bracket. Significantly less stress was required to fracture older teeth. The high incidence of tooth fracture suggests a need to modify the impact test protocol. The lack of a simulated periodontal ligament, which is present clinically and acts as a shock absorber, may have contributed to the high failure rate, although the striking position of the pendulum also needs to be considered.

Keywords. Orthodontics, dental adhesive, brackets, bond strength

Introduction

Orthodontics is the dental specialty that is concerned with the development of the dentition and occlusion and with the diagnosis and treatment of occlusal anomalies. Orthodontic treatment uses bonded attachments on teeth (Figure 1) and an adequate bond is paramount for the success of orthodontic fixed appliance treatment. As well as providing the means of transfer of load to the teeth from springs and wires, the adhesive attaching the bracket to the tooth enamel needs to have a high enough bond strength to withstand a wide range of masticatory and external forces. However, it is equally important that the bond can be broken on completion of treatment, with no damage to the enamel. The development of dental adhesives has progressed significantly and many different adhesives are now available for orthodontic application.

Figure 1: Orthodontic Fixed Appliance

[†] Corresponding author: Professor R.L.Reuben, Heriot-Watt University, School of Engineering and Physical Sciences, Edinburgh, EH14 4AS, United Kingdom, R.L.Reuben@hw.ac.uk.

Despite the large volume of publications on bond strength testing, there is neither consensus on bond strength values nor a standard protocol for bond strength testing in orthodontics. The majority of previous bond strength testing has used a slow build up of force to debond using a machine like a tensile tester. However, accidental debonds during orthodontic treatment are more likely to occur under a short impact force, for example during mastication, and it is of interest to know the resistance of the adhesive to this type of impulse.

This study aims to develop a method of measuring the fracture energy for an adhesive bond, rather than a load at failure, which is likely to depend very much on the rate of application of the load. This method of impact testing was deemed to be more clinically relevant for the debonding process.

There are many factors that might affect bond strength and some which are of interest to this study are identified here. Linklater and Gordon [1] carried out *in vitro* experiments to show that the bond strength is not uniform across all teeth. Canine and premolar teeth exhibited significantly higher bond strengths and lower probabilities of failure than incisors. A later study by the same authors [2] on *in vivo* measurements confirmed that the bond survival of the brackets is not uniform for all teeth, and found that the mandibular and posterior teeth had higher failures rates than maxillary and anterior teeth. Knoll *et al* [3] agreed with Linklater *et al*, suggesting that the lower values of bond strength for molar teeth may relate to non-uniform resin adhesive thickness due to adaptation of the bracket and the presence of buccal grooves. Hobson *et al* [4] made similar observations and concluded that the same tooth type needs to be used for meaningful comparison of any mechanical measurements.

The quality of the bonded surface was identified as another factor that may affect bond strength. Whittaker *et al* [5] have shown, for newly-erupted teeth, that the gingival third to half of the crown is often covered with an amorphous follicle and has a surface enamel rod pattern that is more divergent than older teeth, making less rods available for bonding hence reducing the bond strength. The structure of the surface zone of enamel differs from its deeper layers. There can be great variation in the microscopic structure between teeth within surface enamel alone and the pattern and number of enamel prisms can vary. Some teeth may have a prismless outer enamel layer, persisting to a greater depth and more commonly seen in posterior teeth and this is considered to produce an inferior etch pattern.

To produce a strong enough bond between the orthodontic adhesive and the tooth, the tooth surface is etched and primed prior to bonding. In addition to the inherent natural features of a tooth surface that might affect the bond quality, etch patterns induced by acid application to the tooth surface have been found to affect the bond strength significantly. Mattick and Hobson [6] have examined the etch pattern produced on the orthodontic bonding surfaces of a range of different tooth types. The extent to which an ideal etch was achieved diminished towards the distal end of each arch with first molars showing <2% coverage and incisors showing > 90% coverage with an ideal etch pattern. It was suggested that the difference in etched enamel morphology affected the composite bond strength and consequently the survival rate of bonded orthodontic brackets. These results may partially explain the higher failure rates of teeth bonded in the buccal segments observed by Linklater and Gordon [2]. Hobson *et al* investigated the relationship between acid etch quality and bond strength/survival. Both *ex vivo* bond strength and *in vivo* bond failure rates were assessed in relation to etch quality. There was no significant difference in etch quality between left and right sides or upper and lower arches. There was, however, a significant difference between specific teeth. The greatest amount of type A etch pattern (well developed 'conventional' etch pattern, Galil and Wright [7]) was found on the lower incisors but this only covered 5% of the bonding surface, whilst the majority of the surface area was occupied by a poorer quality etch pattern. *Ex vivo* bond strengths recorded varied from 6.5 MPa (upper first molar) to 13.1 MPa (lower first molar) concluding that an ideal etch is not essential in order to produce a strong bond. *In vivo* investigation, however, showed a statistically significant relationship between the areas occupied by ideal etch type and the length of survival of the bond, i.e. the better the quality, the better the bond.

Ideally the etching process should provide selective dissolution of surface enamel prism cores or peripheries resulting in micro porosities that resin can flow into prior to polymerization. This results in a mechanical bond with the enamel. Reynolds [8] reported that acid etching also changed the enamel surface from a low energy hydrophobic surface to a high energy hydrophilic surface, increasing the surface tension and allowing improved wettability thus enhancing the resin penetration and improving the mechanical bond. Several different types of etching solutions, concentrations and modes of application have been used historically.

Traditionally, orthophosphoric acid has been used to increase the bond strength between composite resin and enamel, first proposed by Buonocore [9]. Further developments introduced the use of phosphoric acid in varying concentrations. Wang *et al* [10] investigated *in vitro* bond strengths with different concentrations of phosphoric acid and found that concentrations between 10 and 30% applied for 15 seconds produced adequate bond strengths. The most popular conventional acid etch used for the purpose of orthodontic bonding is phosphoric acid of 37% concentration. Gardner and Hobson [11] compared the acid etch patterns achieved with 37% phosphoric acid and 2.5% nitric acid applied for different times, 15, 30 or 60 seconds. Results showed that phosphoric acid produced a better quality etch pattern than nitric acid. With phosphoric acid, the amount of good quality etch was time-specific with 15 seconds being less effective. However, there was no significant difference between 30 and 60 seconds. The findings support the use of 37% phosphoric acid with an optimum application time of 30 seconds.

A concern with the conventional separate etch and prime technique is the risk of tooth surface contamination between the steps. To attempt to cope with this risk of contamination, self-etching primer systems (SEP) have been introduced. This system integrates the etching and priming steps into one. Bond strength testing of the new generation SEPs has produced variable results. The majority of *in vitro* tests have shown bond strengths produced with SEPs to be acceptable if not better than conventional etch and prime technique.

Materials

Patients' consent was sought for obtaining the premolar specimens. The specimens consisted of 37 sound premolar teeth stored in thymol solution prior to testing. Selected teeth had intact buccal enamel with no caries or restorations present. The roots of the teeth were removed using a high-speed hand-piece and diamond bur under a constant stream of water spray. The crowns were embedded in heat cured acrylic and cured for 20 minutes in water at 45°C at a pressure of 2 bars. The specimens were then turned down to a 10mm diameter cylinder with the bracket at the centre of rotation in order to fit into the mounting jig in a specially modified impact test machine. The specimens were polished using a fluoride-free pumice, then etched and primed using Transbond Plus self-etching primer. The self-etching primer combines 22% phosphoric acid enamel etchant and a primer of unfilled resin within a single 'lollipop' system. This was applied to the surface enamel using a brush, agitating the surface for 3-5 seconds to allow sufficient fresh primer to react. Oil-free compressed air was used to evaporate residual solvent for 2-3 seconds following application. The premolars were then bonded onto MBT Victory APC Plus orthodontic brackets precoated with APC plus adhesive. A stainless steel MBT Victory bracket precoated with composite resin adhesive was bonded to each sample by a single operator. The adhesive was then cured for 10 seconds using a Light Emitting Diode (LED) curing light, applied for 5 seconds mesial and distal to the bracket. Following bonding, the samples were stored in distilled water for 24 hours at 37°C and thereafter the specimens were subjected to mechanical impact testing.

Figure 2: A tooth specimen bonded with a bracket partially embedded in acrylic

Experimental Test Rig

The partially embedded tooth specimen (Figure 2) mounted in a cylindrical acrylic section of diameter 10mm, was designed to be clamped within one end of a rotating arm in a modified impact test machine (Figure 3). The arm was able to pivot around a pin but was restrained from doing so by a compression load cell connected to a base plate made from an aluminium alloy. The occlusal tie-wing was aligned to the edge of the pendulum at the point where it would strike. The pendulum was released from a consistent fixed height of 30cm in relation to the specimen, thus striking the occlusal tie-wings of the bracket at a speed of around 2.5ms^{-1}. The resulting impact was recorded by the force sensor (Honeywell FS series), located at the other end of the rotating arm. The data from the force sensor was recorded at a rate of 40ksamples/second using a data acquisition system consisting of a PC with a National Instruments NI-6024E card running under Labview.

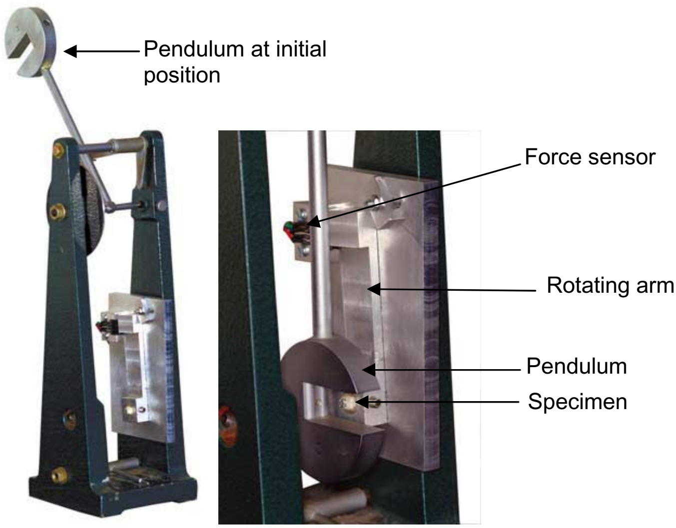

Figure 3: Impact tester

Experimental Results

Figure 4 shows a typical force-time record after applying a running average of eight sample points. As can be seen, the resolution after this degree of averaging is sufficient to allow the peak force, the interaction time and the impulse (area under force-time graph) to be determined.

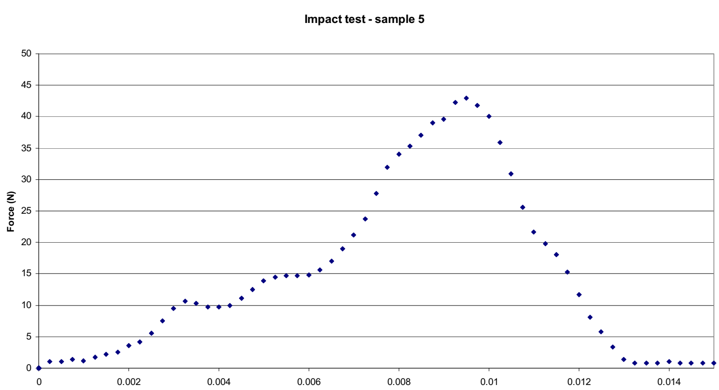

I

Figure 4: Typical force-time record during impact

In the initial group of 20 samples tested, 6 brackets were successfully debonded on impact and, in the remainder, the tooth fractured. The teeth that were used in this initial group had been extracted more than 6 months prior to testing and it was thought that this may have an effect on the quality of the enamel chemistry. Therefore, a second group was tested, using only teeth extracted within 6 months of the tests, with identical brackets and the same test protocol. Of this batch of specimens, consisting of 17 samples, only 3 brackets debonded successfully the tooth again fracturing in the remainder. Figures 5 to 10 summarise all of the data (both batches) separately for cases where the bracket debonded (left) and cases where the tooth broke (right).

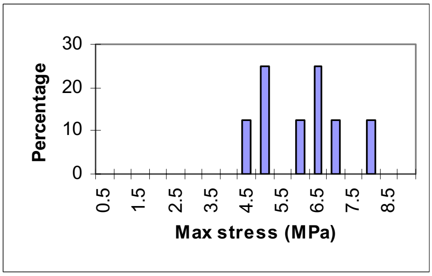

Figure 5: Maximum stresses for debonding brackets

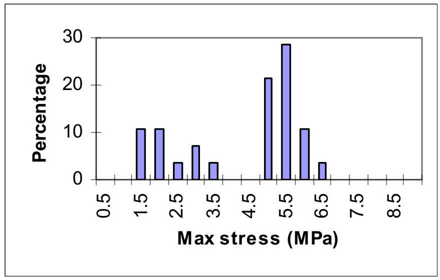

Figure 6: Maximum stresses for tooth breakage

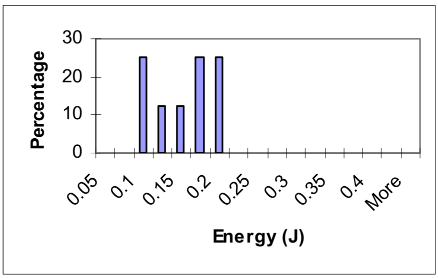

Figure 7: Energy for debonding brackets

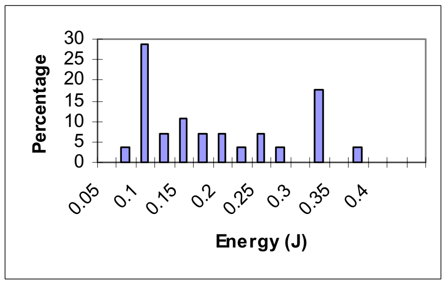

Figure 8: Energy for tooth breakage

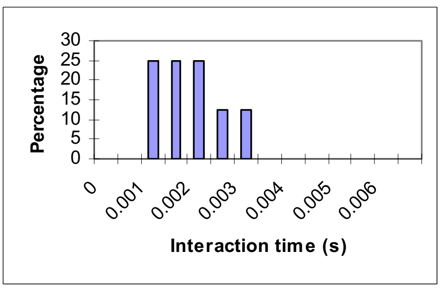

Figure 9: Interaction time for debonding brackets

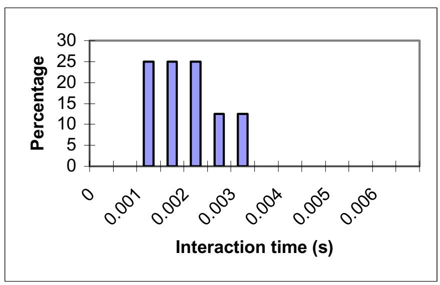

Figure 10: Interaction time for tooth breakage

The maximum stresses were simply determined from the maximum force in the force-time graph divided by the area of the bond pad, and is hence a shear stress. If it is assumed that the speed of the pendulum remains constant throughout the interaction time, the energy required to break the bond (or tooth) can be determined from:

$$E = v_s \int_0^{t_i} F(t) \cdot dt \qquad (1)$$

With the mass of indenter used, this assumption is marginal [12] so that the energies quoted in Figures 7 and 8 are somewhat over-estimated. The interaction time was quite simply determined from the time that the load cell was recording a non-zero force.

The site of bond failure was morphologically analysed under a stereo optical microscope to provide information on the quality of the bond between the bracket and adhesive, and between the adhesive and the enamel. The bond was qualitatively graded using the Adhesive Remnant Index (ARI) of Artun and Bergland [13] which describes the amount of adhesive left on the tooth surface. The ARI criteria used in this study are consistent with other published data on bond strength studies [14-16] and are as follows: score 0 = no adhesive left on the tooth; score 1 = less than half of the adhesive left on the tooth; score 2 = more than half of the adhesive left on the tooth; score 3 = all adhesive left on the tooth, with distinct impression of the bracket mesh. The ARI was recorded for the 9 samples which debonded successfully without tooth fracture and were between 0 and 3 with an average value of 1.33, Figure 11.

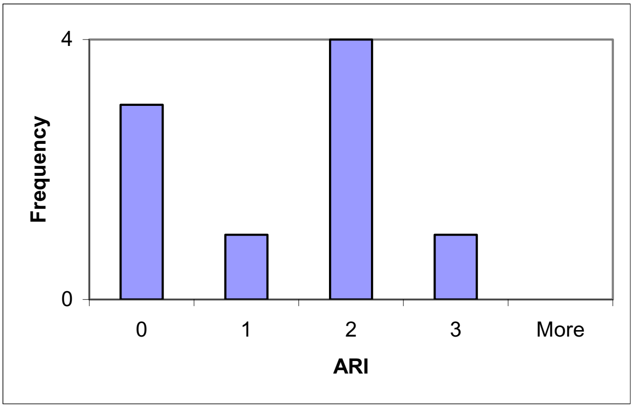

Figure 11: Adhesive Remnant Index (ARI) values for specimens with brackets successfully debonded

Because of the relatively small number of samples, ANOVA analyses were carried out (at the 5% level) to assess whether there were any statistically significant differences between the results for the two groups of specimens i.e. the ones where the brackets were debonded successfully and those where the tooth broke. The analyses showed significant differences of maximum stress between the 2 groups of specimens (p=0.006). However, no significant difference was found either in impact energy (p=0.27) or interaction time (p=0.66) between the two groups.

It was also of interest to find if the newer teeth had behaved significantly differently than the older ones when they broke. Splitting the tooth breakage data into two groups revealed that the older teeth fractured at significantly lower stresses than the newer ones (Figures 12 and 13), and the older teeth showed also a significantly lower impact energy. There was no significant difference in interaction times between the old and new teeth which broke.

Finally, although the data are very thin, it is worth noting that brackets which debonded from the newer teeth did not require significantly different impact energy, although, contrary to what might be expected, it required a significantly greater maximum force to debond brackets from the older teeth.

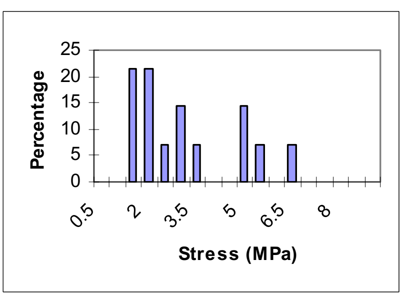

Figure 12: Maximum stresses for debonding brackets with breakage – batch 1 (older teeth)

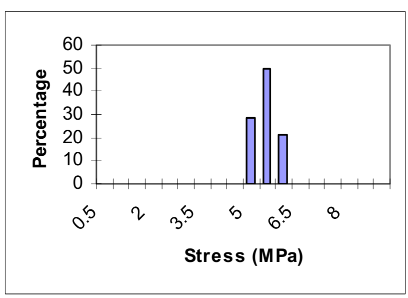

Figure 13: Maximum stresses for debonding brackets with breakage – batch 2 (newer teeth)

Discussion

Eliades and Brantley [17] have written critically on orthodontic bond strength assessment protocols, calling into question the clinical relevance of some of the published studies, and addressing such issues as tooth selection, storage and preparation, bonding, testing and data analysis and presentation. Whereas it is difficult to see firm conclusions and/or recommendations from this review, the authors raise a number of issues which can conveniently be applied to the present study.

Premolar teeth were selected for the present study and it appears [17] that this is not uncommon practice due to the facility of their collection, although crown contour variations are perhaps more than in other types of teeth. Hobson *et al* [18] have measured bond strengths to surface enamel for a total of 240 extracted teeth divided into 12 tooth types (of which four were premolars, four were incisors, two were canines and two were molars). They found a significant difference between tooth types, although they did not note any significant differences between premolars and other tooth types. They also noted that ARI was influenced by tooth type in a statistically significant way. Although the mode of testing (peel at 1mm/min) was not the same as used in the present work, it is worth noting that average bond strengths (between 8.1 and 12.7MPa) and average ARIs (between 0.4 and 0.9) for premolars are rather different to those found in the present work.

Eliades and Brantley state that time of storage (beyond 20 minutes) does not appear to affect bond strength to enamel, although they recognise that the storage medium may have an effect, particularly citing formalin as increasing bond strength over samples stored in saline, whereas saline storage softens enamel more than does storage in water. As pointed out earlier, there is little direct evidence that the time of storage of the teeth has affected the bond strength in the present work, and this would be consistent with the reviewed literature. It is, however, reasonably clear that the teeth which had been stored for longer fractured more easily, although this may have more to do with degradation of the (more organic) dentine than of the (less organic) enamel. For brackets where the bond strength was tested, the variability in the maximum stress, the impact energy and the ARI seem similar, although the number of observations (nine) is somewhat lower than one would like in order to assess if this variability is due to; variability in tooth geometry or surface quality, variability in the quality of the individual bond (which we have sought to standardise by using a single operator and procedure), or the reproducibility of the test conditions. A means of improving the yield of the experiments is required in order to move forward on this aspect.

Eliades and Brantley [17] and Fox et al [19] have identified considerable variation (not to mention confusion) in the way in which debonding forces are applied in bond strength testing. Part of this inconsistency arises out of a lack of clarity in what the purpose of the testing is and is fuelled to an extent by the observation that the function of brackets is to transmit both forces and moments to teeth, which they do by a combination of tensile and shearing loads transmitted by the adhesive. Fox *et al*, in reviewing 66 papers on bond strength testing categorise loading methods in terms of the direction of the applied force, identifying a predominance amongst investigators for shear loading (44 of 66 investigations), i.e. parallel to the tooth, with most of the rest (16 of 66) using tensile loading (normal to the tooth surface). Most significantly, all of the above investigations use a test machine (Instron or similar) with a relatively slow crosshead speed. Whereas a speed of 0.5 mm/min seems to be preferred [17], Klocke and Kahl-Neike [20] have carried out shear tests at speeds of between 0.1mm/min and 5mm/min and have found no significant differences in the shear strength.

Middleton et al [21] have calculated stresses in the adhesive / wire mesh layer in an orthodontic bracket subjected to a plucking force (normal to the tooth) such as might be applied by a “lift-off de-bracketing instrument” and have found maximum and minimum principal stresses to be in the region of 0.8 and -0.2 MPa, respectively, whereas those in the enamel are somewhat higher. Middleton *et al* also point out that the relevant failure mode is brittle fracture, citing the fracture mechanics approach of Lin and Douglas [22]. In contrast to strength testing, fracture mechanics testing is either carried out using impact forces or using test machines where a pre-existing crack has been introduced. The fact that *in vivo* debonding is likely to occur under impact loading [17] would tend to suggest that an impact test where a fracture mechanics parameter (a measure of toughness, as opposed to a measure of strength) is measured would therefore seem to be a more appropriate way of proceeding. There is a developing literature on fracture mechanics testing for adhesives, albeit mostly currently applied to engineering applications of adhesives [23, 24]. Clearly, such tests cannot be reproduced *in vivo* and there is a need to relate impact energies to plucking strengths in a scientifically consistent way in order that *in vitro* findings can be compared with the *in vivo* situation. The present authors have developed an instrumented de-bracketing tool, similar to one reported by Brosh *et al* [25], which they aim to use to obtain comparative *in vivo* and *in vitro* data which can then be related to impact data in a series of co-ordinated tests.

Conclusions

This pilot study has shown that it is practicable to assess bracket bond quality using impact energy, from which can be derived a fracture mechanics parameter (toughness) which can be used to assess bond quality rather than the inevitability inconsistent approach of using a nominal strength (measured force divided by cross-sectional area).

There is a clear need to improve the yield of the experiments (to prevent tooth fracture during testing), which the authors propose to achieve by using a compliant anchor for the tooth (a simulated peridontal ligament) and by controlling more carefully the striking point of the impactor.

In order to be able to compare *in vitro* bond quality with *in vivo* bond quality, parallel pluck tests will need to be carried out using an instrumented de-bracketing tool with a controlled "squeeze rate" (equivalent of crosshead speed), coupled with a fracture mechanics analysis of the results in the light of the impact tests.

The above results show that older teeth fracture more easily so that, in principle, the yield should be improved by using teeth more quickly following extraction. Also, keeping samples hydrated at all times, except during bonding, will help to reduce the effects of desiccation. The first group of samples had been allowed to dry during milling down of the acrylic which may have contributed to their brittleness. The second group of samples did not require milling as they were constructed from new moulds of the correct size.

References

[1] Linklater, R. A. and Gordon, P. H., An ex vivo study to investigate bond strengths of different tooth types. J Orthod, 2001. 28(1): p. 59-65.
[2] Linklater, R. A. and Gordon, P. H., Bond failure patterns in vivo. Am J Orthod Dentofacial Orthop, 2003. 123(5): p. 534-9.
[3] Knoll, M., Gwinnett, A. J., and Wolff, M. S., Shear strength of brackets bonded to anterior and posterior teeth. Am J Orthod, 1986. 89(6): p. 476-9.
[4] Hobson, R. S., Ledvinka, J., and Meechan, J. G., The effect of moisture and blood contamination on bond strength of a new orthodontic bonding material. Am J Orthod Dentofacial Orthop, 2001. 120(1): p. 54-7.
[5] Whittaker, D. K., Structural variations in the surface zone of human tooth enamel observed by scanning electron microscopy. Arch Oral Biol, 1982. 27(5): p. 383-92.
[6] Mattick, C. R. and Hobson, R. S., A comparative micro-topographic study of the buccal enamel of different tooth types. J Orthod, 2000. 27(2): p. 143-8.
[7] Galil, K. A. and Wright, G. Z. Acid etching patterns on buccal surfaces of permanent teeth, Pediatr. Dent, 1979. 1(4): p. 230-234
[8] Reynolds, I.R., A review of direct orthodontic bonding. Br. J. Orthod, 1975. 2: p. 171-178.
[9] Buonocore, M. G., A simple method of increasing the adhesion of acrylic filling materials to enamel surfaces. J Dent Res, 1955. 34(6): p. 849-53.
[10] Wang, W. N., Yeh, C. L., Fang, B. D., Sun, K. T., and Arvystas, M. G., Effect of H3PO4 concentration on bond strength. Angle Orthod, 1994. 64(5): p. 377-82.
[11] Gardner, A. and Hobson, R., Variations in acid-etch patterns with different acids and etch times. Am J Orthod Dentofacial Orthop, 2001. 120(1): p. 64-7.
[12] BS EN ISO 179-2: 1999, Plastics - Determination of Charpy impact properties - Part 2 Instrumented impact test, BSI, London.
[13] Artun, J. and Bergland, S., Clinical trials with crystal growth conditioning as an alternative to acid-etch enamel pretreatment. Am J Orthod, 1984. 85(4): p. 333-40.
[14] Hirani, S. and Sherriff, M., Bonding characteristics of a self-etching primer and precoated brackets: an in vitro study. Eur J Orthod, 2006. 28(4): p. 400-4.

[15] Schaneveldt, S. and Foley, T. F., Bond strength comparison of moisture-insensitive primers. Am J Orthod Dentofacial Orthop, 2002. 122(3): p. 267-73.

[16] Zeppieri, I. L., Chung, C. H., and Mante, F. K., Effect of saliva on shear bond strength of an orthodontic adhesive used with moisture-insensitive and self-etching primers. Am J Orthod Dentofacial Orthop, 2003. 124(4): p. 414-9.

[17] Eliades, T. and Brantley, W.A., The inappropriateness of conventional orthodontic bond strength assessment protocols. Eur J Orthod, 2000. 22: p. 13-23.

[18] Hobson, R.S., McCabe, J.F. and Hogg, S.D., Bond strength to surface enamel for different tooth types. Dent Mater, 2001. 17: p. 184-9.

[19] Fox, N.A., McCabe, J.F. and Buckley, J., A critique of bond strength testing in orthodontics. Brit J Orthod, 1994. 21: p. 33-43.

[20] Klocke, A. and Kahl-Niecke, B., Influence of cross-head speed in orthodontic bond strength testing. Dent Mater, 2005. 21: p.139-144.

[21] Middleton, J., Hübsch, P., Kralj, B., Knox, J. and Jones, M.L., Numerical investigation of fixed orthodontic brackets. Proc. Instn. Mech. Engrs., 2000. H214: p. 311-323.

[22] Lin, C.-P. and Douglas, W.H. Failure mechanism at the human dentine-resin interface: a fracture mechanics approach. J Biomechanics, 1994. 27: p. 1037-1047.

[23] Kihara, K., Hiroaki, I., Yamabe, H. and Sugibayashi, T., A study and evaluation of the shear strength of adhesive layers subjected to impact loads. Int J Adhesion and Adhesives, 2003. 23: p. 253-259.

[24] Fernlund, G., Stress analysis of bonded lap joints using fracture mechanics and energy balance. Int J Adhesion and Adhesives, 2006, doi:101016/j.ijadhadh.2006.10.005.

[25] Brosh, T., Kaufman, A., Balabanovsky, A. and Vardimon, A.D., In vivo debonding strength and enamel damage in two orthodontic debonding methods. J Biomechanics, 2005. 38: p. 1107-1113.

Medicine Meets Engineering
J. Hammer et al. (Eds.)
IOS Press, 2008

Dynamic measurement of intraocular pressure using a mechanical model of the human eye

M. HIEN [a,1], T.H.J. YANG [a], R.L. REUBEN [a] and R.W. ELSE [b]
[a] *Heriot-Watt University, School of Engineering and Physical Sciences, Edinburgh, UK*
[b] *University of Edinburgh, Veterinary Pathology Unit, Easter Bush, Roslin, UK*

Abstract. Heightened intraocular pressure (IOP) is not always indicative of glaucoma, but is an important risk factor for the progression of certain types of eye damage not obviously felt by the sufferer. A number of measurement systems have been devised in the past to measure the IOP by applying force or pressure to the cornea, but past studies have shown that the cornea thickness and its curvature have a significant effect on measurements which may ultimately lead to clinical misdiagnosis. A cyclic strain controlled dynamic probing measurement system has been developed using an indenter of diameter 3.06 mm operating at actuation frequencies of between 0.1 Hz and 4 Hz and displacements up to 1 mm. The cyclic strain is actuated by a linear stage with a load cell and indenter coupled in series. The load cell records the resultant cyclic force where the dynamic modulus is expressed as amplitude ratio and phase lag. The mechanical eye model consists of a silicone membrane that can be varied in thickness and it is distended hydraulically to simulate a range of IOP. A pressure sensor measures the dynamic IOP within the system which will be compared against the dynamic modulus. The relationship between the mechanical properties and the physical properties of the membrane will be established in order to develop a probe which can be used clinically taking into account the effects of corneal stiffness and hydraulic behaviour of the eye. The preliminary study reported here a significant increase in amplitude ratio and mean ratio with increasing the frequency similar to the behaviour found in biological materials and gelatin.

Keywords. Dynamic Measurement, Intra Ocular Pressure IOP, Central Cornea Thickness CCT

Introduction

The healthy eye maintains an almost constant intraocular pressure (IOP) at approximately 2.1 kPa by continually forming a watery fluid (the aqueous humour) which surrounds the iris in two cavities, known as the anterior and posterior chambers. These chambers are essentially bounded by the cornea and the lens, the latter of which sits

[1]Corresponding Author: Heriot-Watt University, School of Engineering and Physical Sciences, Edinburgh, UK; E-mail: mrh6@hw.ac.uk.

on the main cavity of the eyeball which is filled with a gel known as the vitreous humour. The aqueous humour is produced in corrugated membranous structures (the ciliary processes) and leaves the anterior chamber primarily through two pathways (Schlemm's canal and the uveoscleral pathway) which act essentially as pressure control valves [1]. The IOP retains the rigid shape of the eye and maintains the appropriate distances between cornea, lens and retina [1]. Excessive IOP is not the same as glaucoma, but can contribute to damage asymptomatically and is often caused by failure of fluid outflow [2,3,4]. This failure of the outflow can lead to degeneration of the retina and can ultimately cause blindness [5,6,7,8,9] so that IOP measurements are routine procedures at every eye clinic. A number of different methods have been developed to measure IOP the most important of which in current use is Goldmann applanation tonometry, considered as the gold standard [6]. This method is based on the Imbert Fick law (Eq.1) which is an applanation principle that determines the IOP by flattening the cornea and calculating the pressure as the ratio between applied force and applanated area. This law is valid under ideal conditions which include an infinitely thin cornea and a dry surface with perfect elasticity [1,10,11].

$$IOP = \frac{F_c}{A} \tag{1}$$

Although this method is in clinical use and well established with a correction for an average central cornea thickness (CCT) of 500 μm and a uniform corneal architecture, the IOP may be over- or under-estimated if there are large deviations from this norm [5, 12]. There is therefore some scope to develop methods of measurement which can isolate corneal characteristics from IOP characteristics. The central principle of the current work is that treating the cornea as an elastic (or even visco-elastic) membrane, supported on a hydraulic cushion and probing the assembly with a dynamic displacement should allow the effects of IOP and corneal stiffness to be examined separately, perhaps using different probe frequency ranges. An additional benefit is that dynamic probing of the IOP may allow the efficiency of the drainage of the aqueous humour to be probed directly in a way that is not currently possible.

1. Materials and Methods

1.1. Mechanical Model of the Human Eye

The current simulation is rather crude and is aimed only at varying the membrane stiffness and the pressure in the aqueous humour (Fig.1). For this experiment a piece of silicone membrane of thickness 100 μm representing the cornea is suspended over a well, machined into a Poly(methyl methacrylate) (PMMA) cube which can be filled with liquid through a borehole using a syringe and which, in due course can be used to offer various flow resistances to drain. A ring held down with set-screws is used to seal the membrane to the cube. The chamber pressure P_{inst} is measured with a pressure sensor P_{sensor} and, once the chamber pressure has been set, the connection between the syringe and the chamber is closed to ensure constant chamber volume.

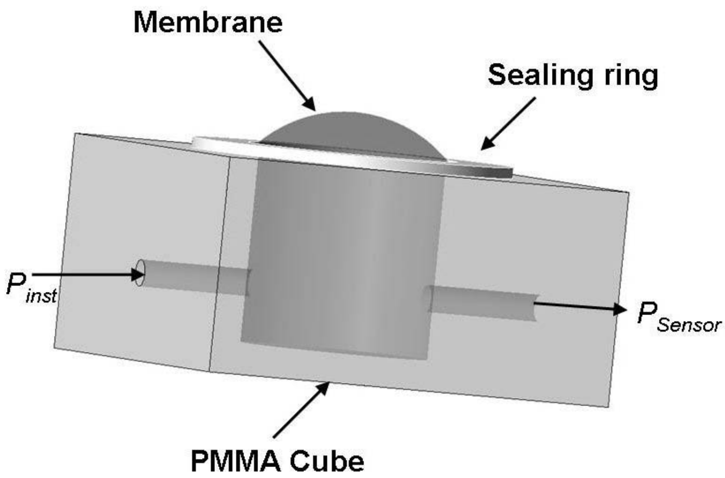

Figure 1. Mechanical model of the Eyeball

1.2. Sensors and Transducers

All sensors and transducers were delivered with technical specifications, but these were calibrated for data like linearity, repeatability and stability under the conditions pertaining to the experimental rig repeating each measurement point ten times. A Measurement Capability (Type one) study was used to investigate the repeatability, accuracy and short time capability for each sensor, and the capability indices c_g and c_{gk} which define the measurement system error [13] determined as follows:

$$c_g = \frac{1.5 \cdot T}{6 \cdot s_g} \leq 1.33 \tag{2}$$

$$c_{gk} = \frac{0.1 \cdot T\,|x_m - \overline{x}_g|}{6 \cdot s_g} \leq 1.33 \tag{3}$$

where T = range of the allowed tolerance; s_g = standard deviation; x_m= calibration standard value; $\overline{x}_g$= mean of all measured values

New tonometry methods are subject ISO standards, ISO 8612:2001, and ISO 15004:1997, which together specify the minimum requirements for tonometers intended for routine clinical use in the estimation of IOP. The standard requires an accuracy within ± 0.67 kPa [10].

Pressure sensor

For the investigation of IOP in this work a pressure sensor (RS Type 286-658) with a pressure range of 0 - 34.47 kPa was used. To calibrate the pressure transducer, the sensor was loaded with a column of distilled water giving a static head according to Eq. 4.

$$P_{Watercolumn} = \rho_{Water} \cdot g \cdot h_{Watercolumn} \tag{4}$$

According to the technical specification, the sensor has a full scale output (FSO) of 50 mV with a sensitivity of 10 mV/psi. The null offset is between -1.5 and +1.5. Figure 2 shows the calibration data obtained and, as can be seen, the curve is smooth with no evidence of hysteresis on increasing and decreasing the column height. The best-fit straight line y = 9.9218x with an R^2 value very close to unity proves the linearity of this sensor. With $c_g = 2.91$ and $c_{gk} = 2.64$ for a tolerance of ± 0.35 mV this corresponds to an accuracy of ± 0.24 kPa which complies with the ISO standard.

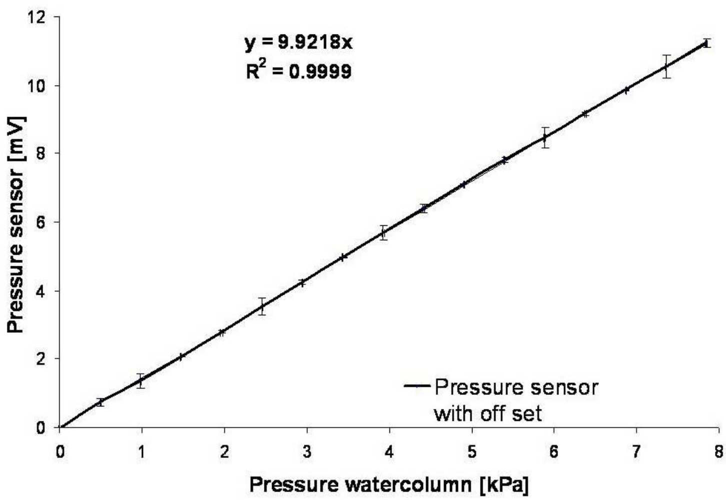

Figure 2. Calibration of the pressure sensor

Force Sensore

The test rig was equipped with a low range isometric force sensor, UF1 from LCM Systems. The sensor has a full scale range (FSO) of 25 g and an output sensitivity of 4 mV/V, with an indicative accuracy of $\pm 3\%$ FSO and repeatability of 1% FSO. The force sensor was calibrated using dead weight loading and the resulting curve is shown in Figure 3 giving a gradient of 1.329 as a calibration factor from grammes force to mV. Using the Goldman standard diameter of 3.06 mm for applanation along with the Imbert Fick Law (Equ.1) the force accuracy can be re-stated in terms of a pressure. With $c_g = 1.77$ and $c_{gk} = 1.68$ for a tolerance of $\pm$ *0.5 mV* this corresponds to an accuracy of $\pm$ 0.376 g$\equiv$ $\pm$ 0.5 kPa again complying with the ISO standard.

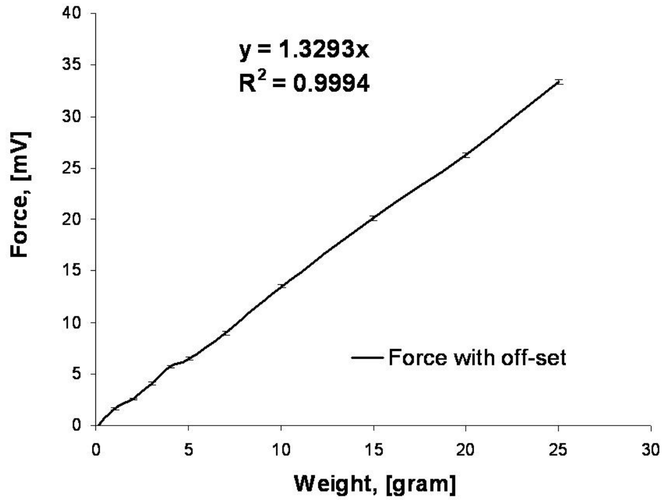

Figure 3. Calibration of the load cell

Proximity Probe with Translation Stage VT-80

The reciprocating movement was achieved using a translation stage, Type VT-80 from Micos, and the real time values of the displacement were measured with a Bentley Nevada 3300 XL 11mm Proximity Transducer System. The calibration of the proximity probe with an Incremental Scale Factor (ISF) of 4.297 was within the specification of the datasheet (Fig.4), and the standard deviation is under 1% of ISF. The repeatability for the bidirectional movement of the translation stage amounts . Therefore the proximity probe must be ten times better. With the capability indices $c_g = 1.33$ and $c_{gk} = 1.59$ for a tolerance of $\pm$ 0.065V $\equiv \pm$ 15 μm the measurement capability is achieved.

1.3. Methods

The simplest viscous model which might represent the membrane (cornea) - reservoir (aqueous humour) model of the eye is a Maxwell element (Fig.5) in which the aqueous humour has the properties of a damper with dynamic viscosity and the cornea behaves like a spring with an elastic modulus E.

The principle of this stage of the experiment is to apply an oscillatory displacement to the membrane over a range of frequency and to measure the resulting force, comparing the observed variation in phase lag and amplitude ratio with frequency to that predicted by a Maxwell element (Fig.9). Varying the reservoir pressure should, in principle, only affect the damping component, and separation of the spring and damping characteristics may permit separate observation of the IOP, the outflow characteristics of the anterior and posteriors chambers, and the corneal properties.

A range of control conditions were chosen to give frequencies varying from a fraction of one Hz to a few Hz, with a range of modulation amplitudes and mean values. These conditions were chosen on the basis of earlier experience [14] on the sensitive range for biological tissues and tissue mimics. For these preliminary experiments the reservoir

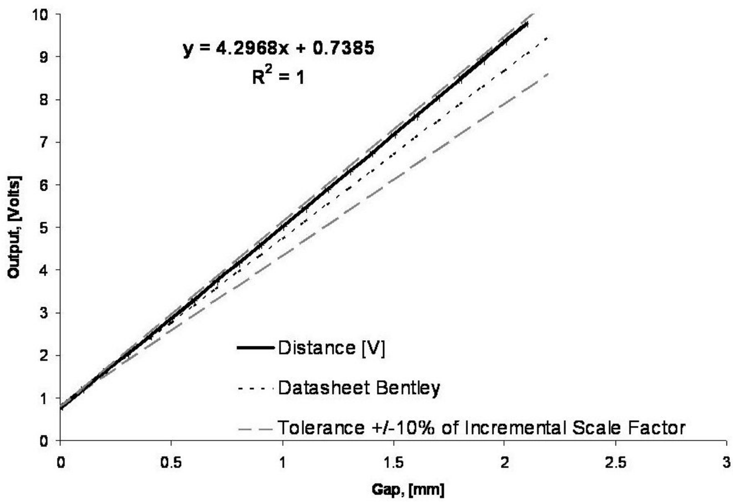

Figure 4. Calibration of proximity probe

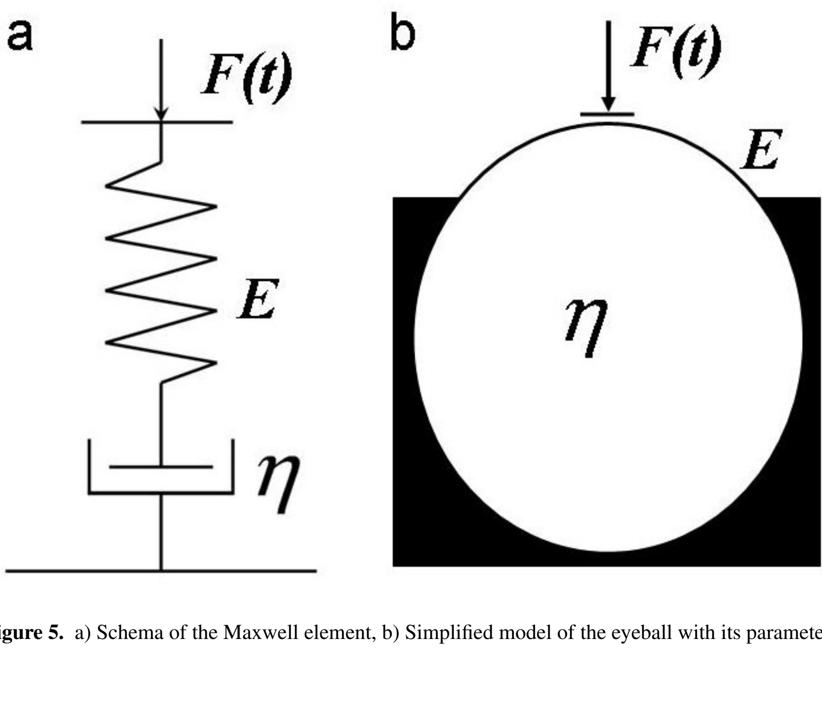

Figure 5. a) Schema of the Maxwell element, b) Simplified model of the eyeball with its parameters

initial pressure was set at 2 kPa (about 16mmHg, equivalent to an average human IOP) with the applanation contactor just touching the surface of the membrane with no force (Fig.6). A pre-strain of between 0.1 mm and 1.0 mm was set by moving the translation stage against the silicone surface to use the whole area of the contactor. The contactor is then reciprocated for 20 cycles and the displacement, pressure and load measured simultaneously using a National Instruments PCI-6024E card.

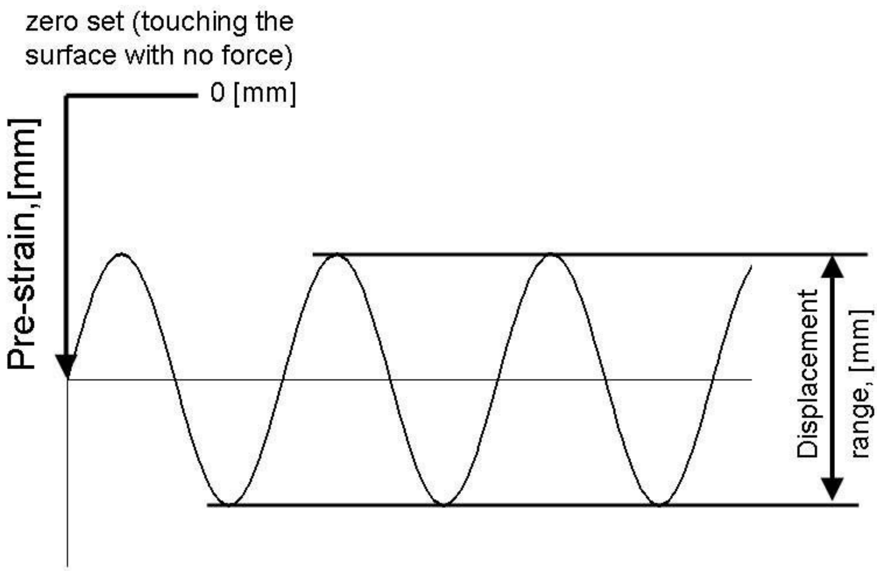

Figure 6. Definitions of pre-strain and displacement

2. Results

The raw waveforms were signal averaged over the 20 cycles and the first Fourier coefficients determined in order to establish the mean value, phase and amplitude of the force and the displacement. Figure 7 shows the amplitude and mean ratios (system stiffness) as a function of frequency for each of the pre-strain and displacement range values. It appears that the main factor influencing system stiffness is the pre-strain, larger pre-strains giving an expected increase in the general level of stiffness and also giving a greater positive slope with frequency.

Figure 8 shows the phase difference of force relative to displacement as a function of actuation frequency, again over the range of pre-strain and displacement range chosen. Whereas the absolute values of phase difference are rather small, there does appear to be a significant decrease with increasing frequency. The effect of the other input variables (displacement range and pre-strain) is not discernible in the range studied here.

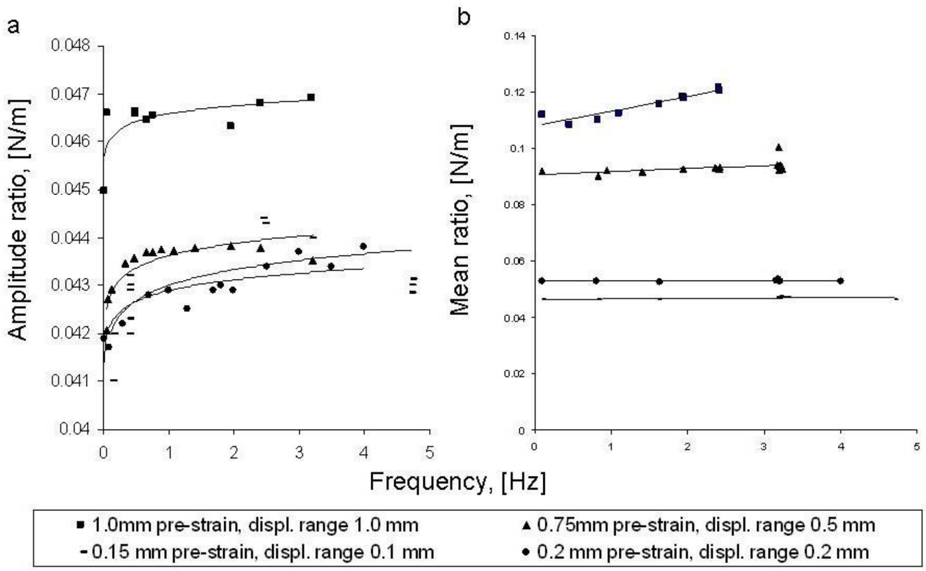

Figure 7. Amplitude ratio and mean ratio of force to displacement as a function of frequency.

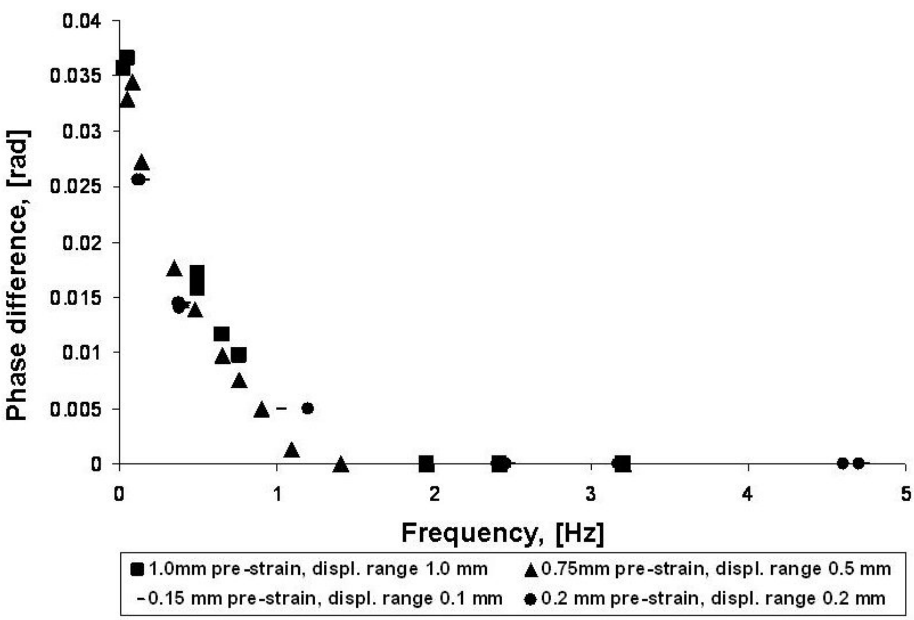

Figure 8. Phase difference as a function of frequency

3. Discussion

The behaviour of a Maxwell Model under dynamic strain can be determined by solving its constitutive equation:

$$\dot{\sigma} + \left(\frac{E}{\eta}\right)\sigma = E\dot{\varepsilon} \tag{5}$$

For an oscillatory input condition:

$$\varepsilon = \varepsilon_0 + \varepsilon_1 \exp i\omega t \tag{6}$$

a quasi-stationary state is set up (once transients have decayed) for the stress:

$$\sigma = \sigma_o = \sigma_1 \exp i\left(\omega t + \delta\right) \tag{7}$$

Where the phase lag is given by:

$$\tan\delta = \frac{\omega_0}{\omega} \tag{8}$$

And the amplitude ratio by:

$$|E^*| = E\frac{\omega/\omega_0}{\sqrt{\left(\omega/\omega_0\right)^2 + 1}} \tag{9}$$

where

$$\omega_0 = \frac{E}{\eta} \tag{10}$$

Since the stress relaxes eventually to zero at times which are large in comparison with ω_0 for the Maxwell Model, it is not a suitable model for describing the ratio of mean values. However, the amplitude ratio for the Maxwell Model generally shows a growth-to-a-limit shape with frequency, the limiting value of E being approached at values of frequency which are large compared with ω_0. The phase angle decreases with frequency, approaching zero at frequencies much large than ω_0. The relatively modest growth of amplitude ratio of force:displacement and the significant increase for all measurements in phaseleg with decreasing frequency shows that the reachable frequency range is adequate for this model.

4. Conclusion

The measurements so far have shown that the mechanical simulation has some dynamic characteristics.
Whereas the Maxwell Model seems to be suitable for describing the behaviour of the amplitude and the phase with frequency, it is unsuitable for describing the mean ratio.
Further measurements with the existing configuration are required in order to arrive at a suitable model and test range before introducing additional aspects such as variation in pressure, variation in membrane thickness and/or material and variation in reservoir drainage conductance.

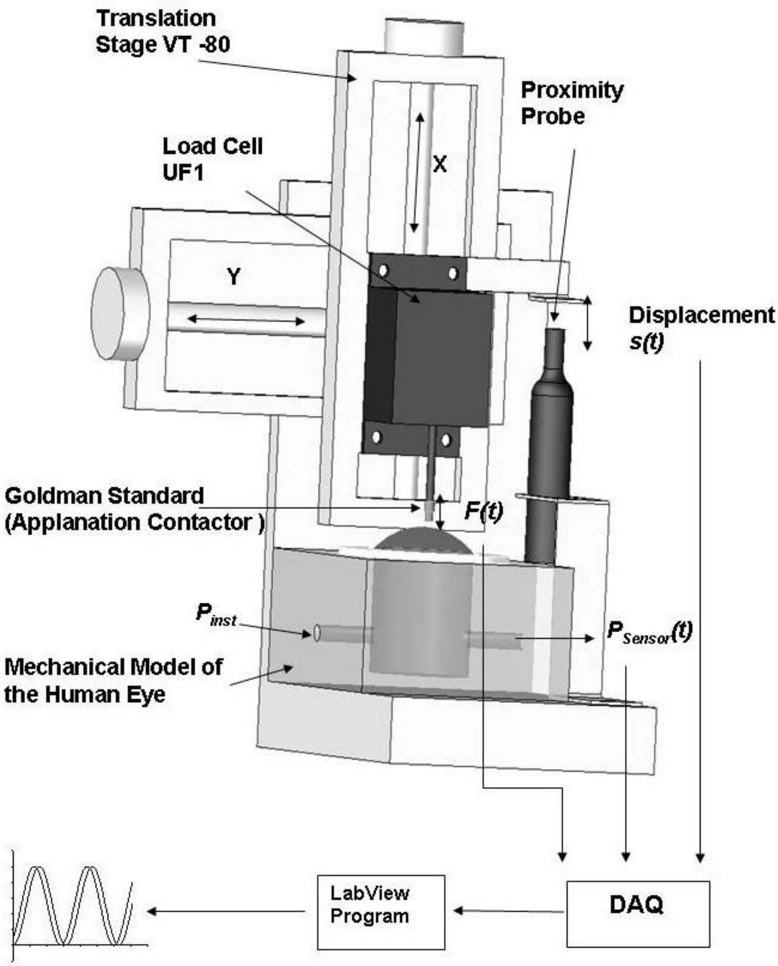

Figure 9. Design of the dynamic measurement system

References

[1] Midelfart A., Wigers A.: "Clinical comparison of the ProTon and Tono-Pen tonometers with the Goldmann applanation tonometer", British Journal of Ophthalmology, 1994, **78**, 895-898.

[2] Glaucoma Laser Trial Research Group: "The Glaucoma Laser Trial (GLT) and Glaucoma Laser Trial Follow-up Study: '7. Results'", Am J Ophthalmol, 1995, **120** , 718-731.

[3] Jay J.L., Allan D.: "The benefit of early trabeculectomy versus conventional management in primary open-angle glaucoma relative to severity of disease", *Eye*, 1989, **3**, 528-535.

[4] Migdal C., Gregory W., Hitching R.L.: "Financial outcome after early surgery compared with laser and medicine in open-angle glaucoma", *Ophthalmology*, 1994, **101**, 1651-57.

[5] Archana B.,Browning A., Shah S., Hamilton R., Dinesh D. and Harminder S.: "Effect of Corneal Thickness on Intraocular Pressure Measurements with the Pneumotonometer, Goldmann Applanation Tonometer, and Tono-Pen", *Investigative Ophthalmology and Visual Science*, May 2002, **43**, 1389-92.

[6] Banobre A., Alvarez T.L., Fechtner R.D. ,Greene R.J., Thomas G.A., Levi O., Ciampa N.:"Measurement of Intraocular Pressure in Pig's Eyes Using a New Tonometer Prototype", 2005, *IEEE*, 260-261.

[7] The International Bank for Reconstruction and Development/the World Bank: "World Development Report 1993", Oxford *Oxford University*,1993

[8] Quigley H.A.:"Number of people with glaucoma worldwide.", *Br J Ophthalmol*, 1996, **80**, 389-93

[9] Dongqi H., Zeqin R.: "A biomathematical model for pressure-dependent lamina cribrosa behavior", *, Journal of Biomechanics*, 1999, **32** , 579-584

[10] Halberg P.: "Applanation resonance tonometry for intraocular pressure measurement", Dissertation, Umea, 2006,

[11] Hallberg P., Lindt'en C.,Lindahl O.A.,Baecklund T.,Eklund A.: "Applanation resonance tonometry for intraocular pressure in humans", *Physiol. Meas.* , 2006, **25**, 1053-1065

[12] Ku J.Y.F., Danesh-Meyer H.V., Craig J.P., Gamble G.D. and McGhee C.N.J.: "Comparison of intraocular pressure measured by Pascal dynamic contour tonometry and Goldmann applanation tonometry", Eye,2006, **20** (2), 191-198.

[13] Dietrich E. , Schulze A.: "Richtlinien zur Beurteilung von Messsystemen und Prozessen, Abnahme von Fertigungseinrichtungen (mit Originalrichtlinien von Ford, General Motors und Daimler-Benz)",Carl Hanser Verlag München Wien (1998)

[14] Yang T.H.J., Leung S.K.W., Reuben R.L., Habib F.K., McNeill S.A., Schneider A., McBride G., Stevens R.: "Structure-property relationships for assessing tissue quality to aid diagnosis of prostate disease.", Journal of Biomechanics, 2006. **39(Sup 1)**: p. S395 (Abstract no.6661)

Medicine Meets Engineering
J. Hammer et al. (Eds.)
IOS Press, 2008

Micro-engineered remote palpation device for assessing tissue compliance

M. HIEN [a,1], T.H.J. YANG [a] S.K.W. LEUNG [b] R.L. REUBEN [a] F.K. HABIB [b] S.A. MCNEILL [c] A. SCHNEIDER [d] G. MCBRIDE [d] R. STEVENS [d] R.W. ELSE [e]

[a] *Heriot-Watt University, School of Engineering and Physical Sciences, Edinburgh, UK.*
[b] *University of Edinburgh, Prostate Research Group, Edinburgh, UK.*
[c] *Western General Hospital, Department of Urology, Edinburgh, UK.*
[d] *Rutherford Appleton Laboratory, CCLRC, Didcot, UK.*
[e] *University of Edinburgh, Veterinary Pathology Unit, Easter Bush, Roslin, UK.*

Abstract. This paper concerns the operation of the actuator for a prototype micro-engineered mechanical palpation device for deployment via a cystoscope to measure the dynamic mechanical properties of the prostate gland *in vivo*. The sub-assembly consists of a 400×200 μm silicon (Si) piston manufactured using deep reactive ion etching (DRIE) housed within an anodically bonded glass-Si-glass sandwiched housing. The micro-channel on the Si layer was formed by powder blasting and contains the micro-piston with one end pointing to the side of the housing and the other facing a *via* hole leading to a capillary tube. The opening on the side of the housing was sealed by a 5 μm thick silicone membrane which acts to retain the micro-piston and act as a return spring. A 320 μm diameter capillary forms the connection between the micro-channel and a micro-syringe which is operated by a programmable syringe pump to produce a reciprocating action. A pressure sensor is connected along the capillary tube to measure the dynamic pressure within the system. The micro-piston has already been used, separately actuated to measure the dynamic mechanical properties of known viscoelastic materials and prostate tissue. The purpose of the present work is to assess the functionality of the actuator assembly.

Keywords. dynamic measurement, micro device, prostate

Introduction

Earlier work in this area [1] has developed and refined techniques which allow measurement of dynamic modulus of human tissue *in vitro* and has established a method for assessing the histological characteristics of excised prostate tissue [2]. Work is progressing [3, 4] on the relationship between "tissue quality" and mechanical properties *in vitro* in order that a detailed specification of a trans-urethral device capable of making clinically significant measurements can be arrived at. The key diagnostic outcome in relation

[1]Corresponding Author: Heriot-Watt University, School of Engineering and Physical Sciences, Edinburgh, UK; E-mail: mrh6@hw.ac.uk.

to prostate is to establish a means of using trans-urethral mechanical probing to assess the degree to which the gland is affected by Benign Prostatic Hyperplasia (BPH) and/or prostate cancer (PCa). Simultaneously, the components of a micro-engineered probe for measuring dynamic modulus *in vivo* have been developed, using a working specification based on the $invitro$ measurements.

The micro device will be actuated hydraulically *via* a syringe pump which is programmable and reciprocates the syringe plunger at a frequency of a few Hertz, pushing the working fluid to an actuator assembly *via* a very small flexible tube. Combined with an appropriate delivery device, such as a urological cystoscope, the device is designed to be used in minimally invasive examinations of prostate glands so that the peri-urethral prostate can be probed at a number of different points, building up a map of visco-elastic properties. The measurement of the mechanical properties will be achieved by applying a dynamic displacement, and measuring the resulting dynamic force, the ratio being used to determine the dynamic modulus, which can be described by the amplitude ratio (|E*|) and the phase difference (tanδ) between the sinusoidal waveforms of the displacement and the resulting force from the tested tissue [1].

1. Materials and Methods

1.1. Micro device

The micro device and its fabrication has been described in detail elsewhere [5, 6]. A micro channel, etched in to silicon, is sandwiched between two Pyrex glass layers. First, one 200 μm thick Pyrex wafer was anodically bonded to a 450 μm thick silicon wafer. Then, the silicon was patterned with an etch-resist (AZ9260) prior to Deep Reactive Ion Etching (DRIE) of the channels right through the silicon, with the Pyrex glass acting as an etch stop. Next, the Pyrex was patterned with SBX photoresist on a mask aligner to pattern 300 μm diameter *via* holes in the correct relation to the micro channels from the back side of the silicon. Subsequently, conical *via* holes, to be used as recesses to mount a capillary tube for the hydraulic actuation of the piston and to provide a port for an optical fibre were created by powder blasting. Finally, the second Pyrex layer was anodically bonded to the silicon wafer to close the top of the channel. Individual circular chips of varying external diameter, the smallest being 1.5 mm, were cut out from the sandwich structures by powder blasting and DRIE so that the microchannel is open on one side of the chip (Fig.1) [6]. The micro piston, which reciprocates along the micro channel, is 200 μm wide, 400 μm high and up to a few millimetres long. The pistons were produced by DRIE through-etching using a few micron thick SiO_2 layer as etch stop with the structures supported by a backing wafer (Fig.1) [6]. Once installed in the channel, there is a clearance of around 25 μm on either side of the piston. To return the piston during actuation, an almost mechanically transparent silicone membrane is used. For the fabrication of the membranes, liquid uncured silicone was spin coated onto silicon wafers down to a thickness of 5 μm. The wafer was then patterned and etched to give a ring and piston tip still bonded to the silicone (Fig. 2) such that the suspended membrane diameter was 1 mm . The piston was then attached to the mounting tip using adhesive (Fig.1).

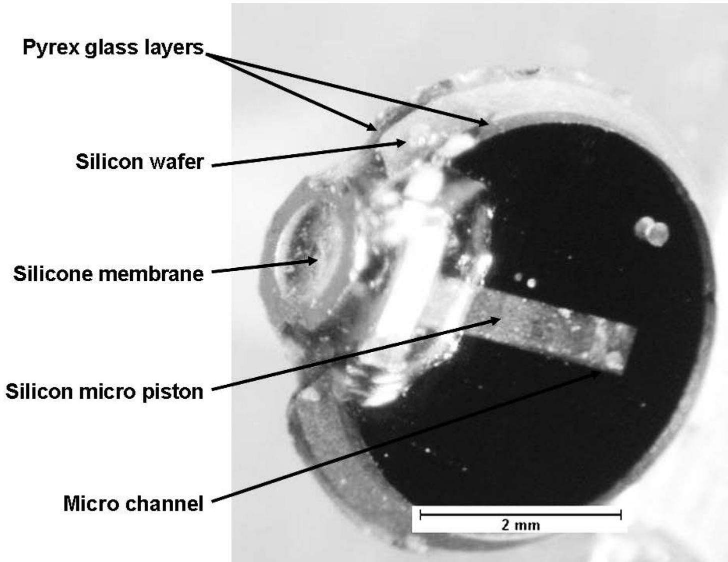

Figure 1. Manufactured micro device

Figure 2. Silicone diaphragm with silicon mounting ring and silicon piston tip.

1.2. LVDT Displacement Transducer with syringe pump

In a full prototype assembly, the reciprocating movement will be provided from a syringe pump, KD Scientific (Type KDS 200), although manual actuation of a syringe was used in the current work. To obtain the real time values of the displacement, an LVDT displacement transducer from RDP Group (Type D2/200A) was used. The calibration of the proximity probe with an Incremental Scale Factor (ISF) of 0.2674 was within the specification of the data sheet (Fig.3). The standard deviation is under 1% of ISF. The repeatability for the bidirectional movement of the syringe pump is not given. However, the LVDT displacement transducer is capable within $\pm 30\ \mu$m .

1.3. Pressure sensor

For the investigation of the actuator behaviour, a pressure gauge from RS (Type gauge 286-658) with a pressure range of 0-5 psi (0-34.474 kPa) was used. To calibrate the pressure transducer, the sensor was compared with the differential pressure from a column of distilled water (Equ. 1).

$$P_{Watercolumn} = \rho_{Water} \cdot g \cdot h_{Watercolumn} \tag{1}$$

According to the technical specification, the sensor had a full scale output (FSO) of 50 mV with a sensitivity of 10 mV/psi. The null offset was between -1.5 and +1.5. Figure 4 shows the pressure sensor calibration which can be seen to be sensibly linear with an R^2 value very close to unity and no observable hysteresis for increasing and decreasing the static head of water.

1.4. Methods

The syringe pump offers two syringe mounting positions of which one was used to attach the LVDT transducer in order to measure the displacement. The pressure sensor was mounted between the micro device and the syringe pump to measure the pressure bearing on the micro piston and consequently on the membrane. For *in vivo* use, the membrane contacts the surface of the tissue and the piston acts to profile the membrane and also carries an optical encoder so that its position can be measured through the other *via* hole (plugged in these experiments) using an optical fibre.
For a visco-elastic tissue, which behaves like a combination of springs and dampers, the force (measurable in this case with a pressure) and displacement will be out of phase,

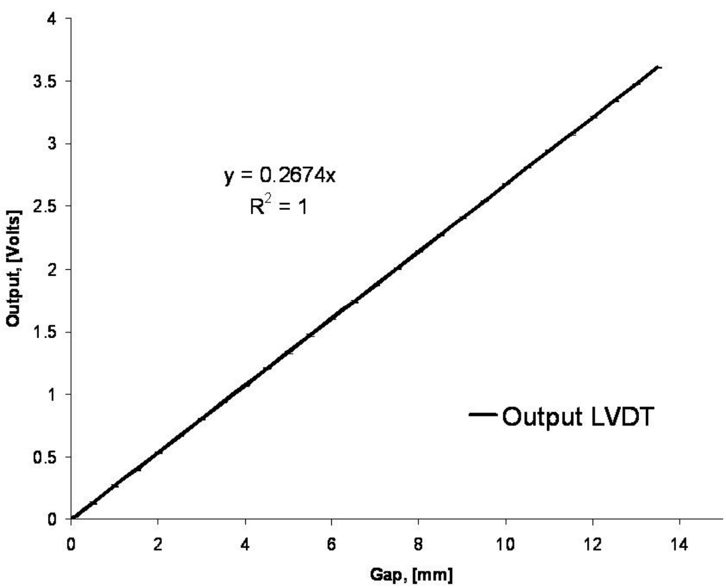

Figure 3. Calibration of the displacement transducer

and the phase lag and amplitude ratio between the force and the displacement will give the dynamic modulus.

However before carrying out any cyclic tests on the micro device, it is important to asses the force displacement relationships associated with deflection of the membrane and movement of the piston when there is no mechanical resistance being offered by a tissue to be probed. Furthermore it is important to find what pressures and working fluids will be appropriate for such a device.

The actuator assembly needs to be put together manually since it involve planar micro-fabrication in two orthogonal planes, for the membrane and for the channel plate. Assembly involves the insertion of the piston, already attached to the piston tip (and hence the membrane) and the adhesive bonding of the diaphragm mounting ring onto the channel plate. Finally, capillaries were attached to the fluid *via* holes and the remaining *via* hole was plugged with adhesive. Three sample assemblies were available for the current tests. The first experiments consisted of gradually increasing the pressure with ambient air during which it was found that two of the devices were leaky. The third device was tested three times using air until it, too, developed a leak. All of the leaking devices were then lightly pressurised using distilled water, and the leaks located and sealed by local application of the same silicone formulation as used for the membranes. A set of experiments were then performed on the third device (the one which had been tested in air), this time using water as the working fluid.

2. Results

For the experiments with ambient air, the pressure was raised incrementally up to 2.76 kPa (Figure 5) and the piston movement assessed by video images taken through a

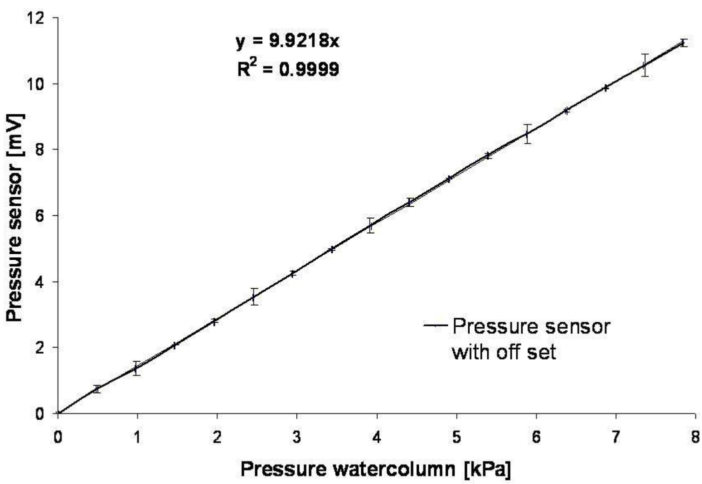

Figure 4. Calibration of the pressure sensor

stereo-optical microscope (Figure 6). As can be seen from Figure 5, beyond a threshold pressure of about 500 Pa, a relatively linear region of deflection vs pressure ensues, where the susbsequent pressurisation sequences seem to be relatively reproducible. The slope of the linear region (around 7×10^4 Pa/mm) corresponds reasonably well to those measured by Yang et al directly on membranes of 5 μm thickness pressurised under a white light interferometer. In this case, a membrane stiffness of around 2×10^4 Pa/mm was measured for 0.8 and 1 mm diameter membranes, and 6×10^4 Pa/mm for 2 mm diameter membranes. The different in stiffness here is attributed to a possibly stiffer edge fixity, and also the reduction in suspended area brought about by the area bonded onto the piston. It is anticipated that the initial threshold corresponds to the force required to move the piston in the channel against the friction and jamming resistive forces.

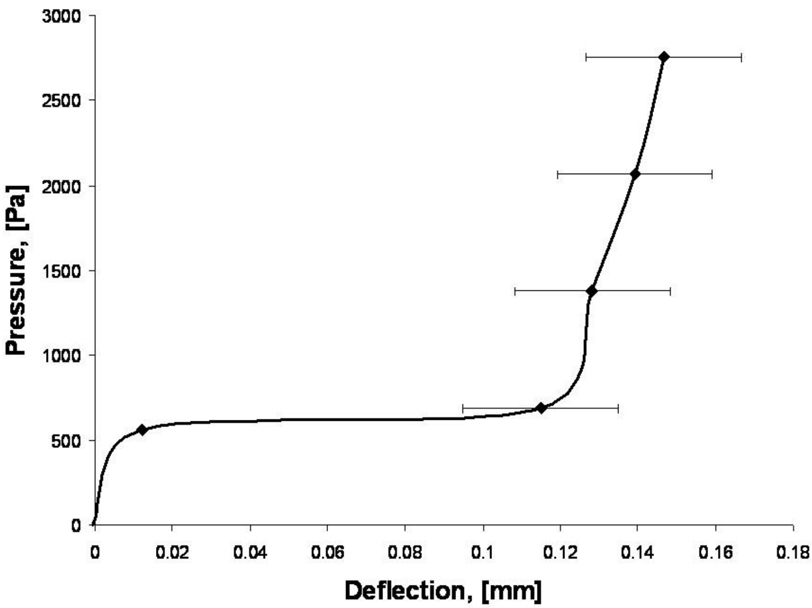

Figure 5. Pressure-deflection relationship for Device No.3 using ambient air

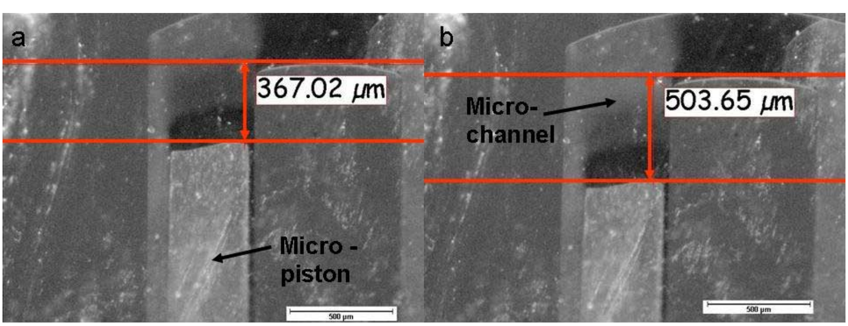

Figure 6. a) Piston initial offset with 0 psi applied; b) Piston displacement with 0.4 psi applied

The experiments on the repaired membrane with distilled water are summarised in Figure 7 which shows the stiffness of the linear region to be around 8×10^4 Pa/mm, a little higher than in the air tests and this is confirmed with membrane deflection measusrements which agree with the piston position measurements. However, in these tests, the absolute value of pressure for a given piston displacement is much higher, indicating that there must have been some kind of mechanical slack in the system prior to repair, which has now been taken up. When the piston is drawn back by applying suction to the capillary, it appears that this mechanical slack is reinstated, and far larger deflections are again obtained for a given applied pressure, although the slope of the linear portion is again similar, at around 9×10^4 Pa/mm.

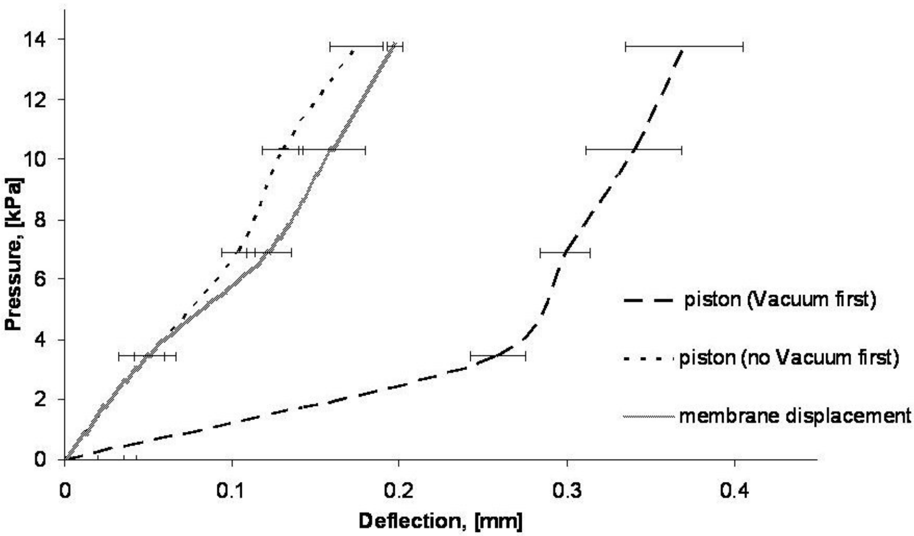

Figure 7. Pressure-deflection relationship for Device No.3 after repair using water

3. Conclusion

On first pressurising the device using air, there appears to be a threshold pressure required to move the piston against the stiction resistance, after which the membrane behaves mechanically in approximately the way expected from earlier measurements using direct pressurisation. This initial movement gives an initially low effective stiffness, so is not entirely accounted for by friction forces, but indicates some mechanical slack where the membrane elastic stiffness is not the only operating factor, and this seems to be associated with lateral movement of the piston in the channel (Fig. 8).

Pressurising with distilled water on the repaired membrane shows only a slight increase in stiffness in the linear region, which is explained by additional reinforcement of the membrane brought about by the repair (Figure 9), but shows a drastic increase in pressure for a given displacement, which can be reduced somewhat by applying suction to

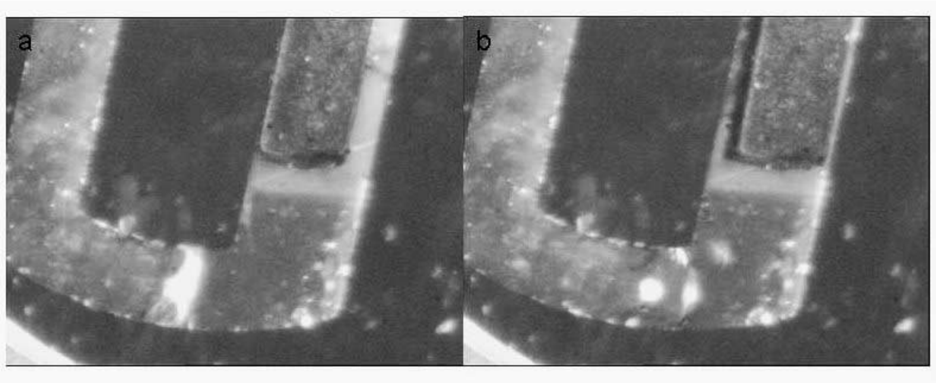

Figure 8. Fishtailing of piston as pressure is first applied using air a) at 0 Pa b) between 0 and 500 Pa

the device before pressurising. The different behaviour when water is used and the reinstatement of some of the initial behaviour used suction, further supports the notion that piston lateral movements and friction/cohesions are important in the design of such small devices.

The implications of these observations for the design of micro-actuators for medical use are yet to be fully understood, but it is clear that the piston shape and clearance and the nature of the working fluid will have a significant effect on the idling behaviour.

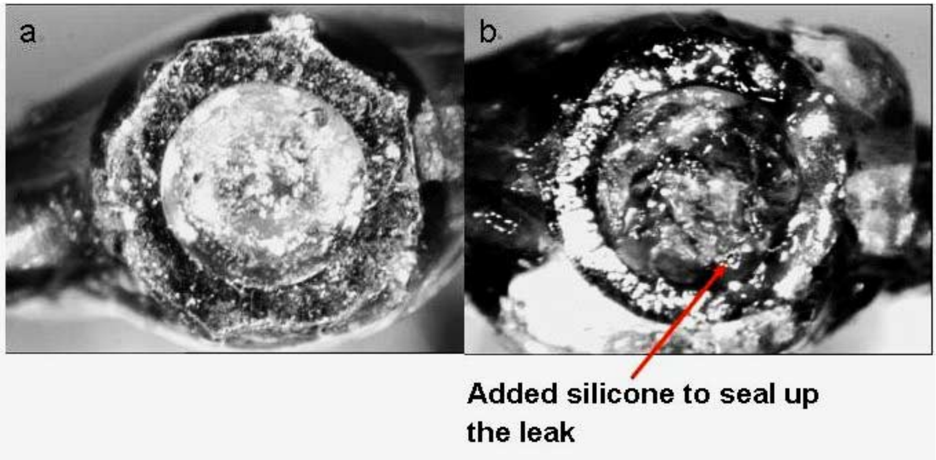

Figure 9. a) Shows membrane before failure; b) Shows membrane sealed with silicone

References

[1] Lakshmanan V., Yang T. H. J., Reuben R. L., Hammer J., Else R. M.: "Multi-scale Techniques of Measuring the Dynamic Properties of Soft Biological Tissue", Technology and Healthcare, **13**, 2006, 1-13.

[2] Phipps S., Habib F. K., McNeill S. A.: "Quantitative Morphometric Analysis of Resected Prostatic Tissue Specimens using Immunohistocemical Staining and Colour Image Analysis" (accepted for publication). BJU Int, 2004, **94(6)**: p. 919-21.

[3] Leung, S. K. W., Phipps S., Yang T. H. J., Reuben R. L., Habib F. K. and McNeill S. A.: "Morphometric analysis of the prostate demonstrates the importance of the loco-regional morphology to the mechanical characteristics of the gland." European Urology Supplements, 2006, **5(2)**: p. 121.

[4] Yang T. H. J., Leung S. K. W., Reuben R. L., Habib F. K., McNeill S.A., Schneider A., McBride G., Stevens R.: "Structure-property relationships for assessing tissue quality to aid diagnosis of prostate disease." Journal of Biomechanics, 2006, **39(Sup 1)**: p. S395 (Abstract no.6661).

[5] Schneider A., Yang T. H. J., Reuben R. L., Stevens R., McNeill S. A.: "Microstereolithography for microdevice packaging in biomedical applications - a Urology Catheter for minimal invasive endoscopy", ASME Conference: European Micro and Nano Systems, Paris. Oct 2004.

[6] Schneider A., Malik A., Djakov V., Yang T. H. J., Reuben R. L.: "Optimisation of Si DRIE for perfect high sidewalls of microchannels and movable micropistons in hydraulic actuated device with silicone membrane for restoring piston position", ASME Conference: European Micro and Nano Systems, Paris. Oct 2004.

Medicine Meets Engineering
J. Hammer et al. (Eds.)
IOS Press, 2008

Modeling and Simulation of an Intelligent ER Force Element for Rehabilitation of Human Hands

Ahmad HOSSEINI-SIANAKI [a,1] and Mohammad NIKKHOO [b]
[a] *Islamic Azad University, Central Tehran Branch, Tehran, Iran*
[b] *Iran University of Science and Technology, Tehran, Iran*

Abstract. Improving the process of designing modern tools and devices for rehabilitation of both muscular and neural disabilities requires such intelligent systems that together with organizing intensive therapy could have an effective role in returning some of the patient's abilities and encourage them to complete the course of the training in order to get back to normal daily life. In this paper, first properties and laws governing the behavior of the electro-rheological fluid (ERF) as a smart material are briefly described. Then the principles of designing a two-degree-of-freedom intelligent damping system based on an electro-rheological fluid for the application in rehabilitation of human hands are explained. This mechanism provides the capability to create a virtual environment in which the training can be intelligently manipulated on the basis of body's feedback system. Also it can encourage the patient to continue with the therapy. Modeling and simulation of the electro-rheological (ER) force element is presented and results are compared with the available experimental data obtained, by other researchers, from a prototype system with relatively similar geometry but for other applications. Very good agreement is being noted between the theoretical model and the experimental data for different test configurations.

Keywords. Intelligent force element, Electro-rheological fluid, Hand rehabilitation, Modeling

Introduction

Generally, disorders resulting from brain strokes are the most common reasons for muscular and neural disabilities which cause various limitations of the body's motions. Treatment methods, in more than 70 per cents of these disabilities, are inclined towards non-surgical techniques and are designed on the bases of physiotherapy principles. However, this means, in order to get back to normal daily life, these patients will require timely and persistent rehabilitation to recover the function ability impaired by the stroke.

Physiotherapy methods are usually divided into two forms. First, is the active treatment which means using the patient's on abilities in the treatment. Second is the passive treatment, meaning the use of devices or aid persons in the course of the therapy. Results of research works during the last twenty years demonstrate that the

[1] Corresponding Author: Islamic Azad University, Central Tehran Branch, Sanat Sq., Shahrak Quods, Tehran, Iran; E-mail: a_hoseini@iauctb.ac.ir

active treatment method is more effective than the passive one and thus the need to design and develop novel devices suitable for this purpose [1]. Improvements in the process of designing modern tools and devices as well as rehabilitation methods for the aforementioned disabilities require such intelligent systems that together with organizing intensive therapy could have an effective role in returning some of the patient's abilities and encourage them to complete the course of the training.

One of these advances is the development of virtual reality systems that can, in many ways, help the process of rehabilitation of different parts of the body [2]. Virtual Reality (VR) or Virtual Environment (VE) is a comparatively new technology using interactive simulations which aim to convince the user that he/she is in an artificial but realistic virtual world. The first generation of this technology consists mainly of vision based systems that are worn as headgears by the patient. This system, in practice, plays an important role towards encouraging the patient through the course of rehabilitation [2]. However, the vision based system only partially meets the intentions of researchers in this field. What will really be more useful, as part of virtual reality technology, is the creation of force feedbacks and hence making the system to work intelligently. Gradual changes and intelligent loading during exercises, use of the body's own feedback, creating virtual environment with force responses to encourage the patients to continue with the exercises and also designing master-slave systems especially in the case of post-stroke patients are factors that must be considered in the design of intelligent rehabilitation devices [3]. In response to this need, much research works have been carried out in recent years which by introducing automatic and semi-automatic robotic systems meet the aforementioned expectations [4]. The most important factor in guaranteeing the efficiency of such systems is their control system design in which the use of non-delay controllers and complete conformity with the body's neural systems are very important. Therefore, by introducing smart materials such as electro-rheological fluids and its many applications in mechanical engineering in recent years [5], one can expect the advent of new generation of such systems.

Considering the aforementioned cases, in this paper it is envisaged that, by modeling and simulation, foundations are provided for the design of an intelligent force element based on electro-rheological fluid as part of a smart rehabilitation system for human hands.

1. Electro-rheological Fluid Properties

Electro-rheological fluids are one of the smart materials that when subjected to an electric current, they instantly turn into a gel-like solid and when the current is removed, they revert to the liquid state. The change in the state can occur in 0.0001 to 0.001 second. These fluids are a mixture of fine semi-conducting polymer particles (usually micron sized) suspended in a non-conducting oil. In a schematic form, the physical change that ensues when an electric filed is applied across the fluid is shown in Figure 1.

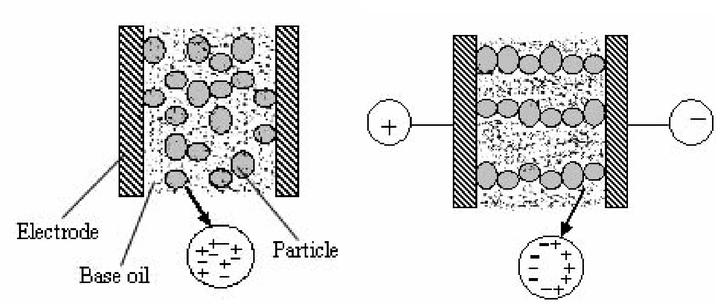

(a) (b)

Figure 1. Simple model of particles chaining between electrodes
(a) Without electric field, (b) With electric field

The strength of the formed chains, depending on the system in which the fluid is used, explains the smartness of the system [6,7and 8]. On the application of the electric field, the fluid practically show a non-Newtonian behavior which can be explained by the Bingham plastic model shown in Eq.1.

$$\tau = \tau_y + \mu\dot{\gamma} \tag{1}$$

Where τ is total shear stress, τ_y is electric field induced yield stress which in the static and dynamic states are given by Eqs.2 and 3 respectively. Also μ is given by Eq.4.

$$\tau_{y,Static} = C_s(E - E_{ref}) \tag{2}$$

$$\tau_{y,Dynamic} = C_d E^2 \tag{3}$$

$$\mu = \mu_0 - C_v E^2 \tag{4}$$

All symbols are as described in the nomenclatures at the end of the paper.

2. ER Force Element Model

The rehabilitation system, in its simplest form, consists of a glove with five cylinder-piston elements. Each element, in practice, is a two-degree-of-freedom mechanism which connects the finger tips to the palm. Figure 2 presents a schematic diagram of this glove system.

Figure 2. A schematic picture of the rehabilitation system

Each element comprises a piston that is designed to move inside a sealed cylinder filled with the electro-rheological fluid. As shown in Figure 3, the piston is designed to have multiple slots along its surface that in fact serves as valves. Therefore, by applying the appropriate level of electric filed across the channel between the piston and the cylinder, using the electro-rheological fluid properties, the required force for the movement of the piston within the cylinder is finely controlled. In other words, the stiffness of each element can be controlled by the fluid flow rate inside the channel.

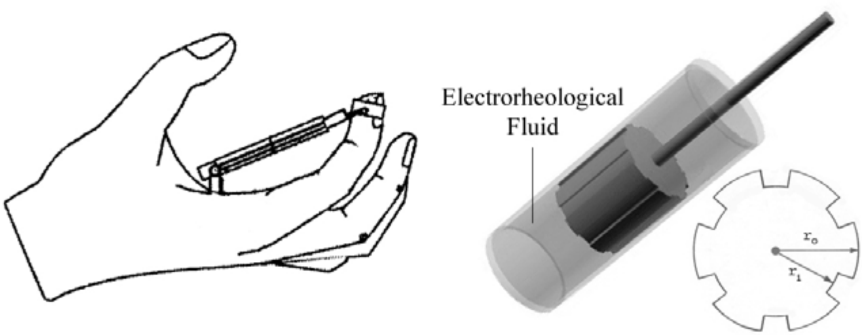

Figure 3. The rehabilitation system and piston- cylinder arrangement

In order to design the system, first, mathematical relations which describe the resistive element must be derived. In modeling the system the most important problem, in practice, is to find the function which governs the amount of the element resistive force based on the applied voltage across the system, the characteristic parameters of the fluid, geometrical and motion specifications of the piston-cylinder mechanism.

As it was noted, the force due to the shear stress of the fluid is a function of the applied electric field. According to Gauss's theorem, the created electric field can be determined from Eq.5.

$$\oint \vec{E} \cdot d\vec{A} = \frac{q}{\varepsilon_0} \Rightarrow E = \frac{q}{2\pi\varepsilon_0 rL}\vec{e}_r \qquad (5)$$

Similarly, the voltage may be obtained from Eq.6.

$$V = \int_{r_i}^{r_o} \left(\frac{q}{2\pi\varepsilon_0 r L} \right) \vec{e}_r \cdot d\vec{r} = \left(\frac{q}{2\pi\varepsilon_0 L} \right) \ln \left(\frac{r_o}{r_i} \right) \tag{6}$$

Hence the relationship between the applied voltage and the created electric filed may be given by Eq.7.

$$E = \left(\frac{V}{\ln(\frac{r_o}{r_i})} \right) \frac{1}{r} \tag{7}$$

The element resistive force is the sum of the forces due to shear stress, pressure and friction. The frictional force can be neglected when compared to the other two forces and thus Eq.8.

$$F_R \approx F_\tau + F_p \tag{8}$$

By expanding the governing equations, the static resistive force for a channel is given by Eq.9.

$$F_{R,Static} = \left(\tau_s(r_o) A_1(r_o) + \tau_s(r_i) A_1(r_i) + 2 \int_{r_i}^{r_o} \tau_s(r) dA_2 \right) \tag{9}$$

Where, A_1 and dA_2 are defined according to Eqs.10 and 11.

$$A_1(r) = r\theta L \tag{10}$$

$$dA_2 = Ldr \tag{11}$$

Hence, the equation for the static resistive force of one channel, considering the aforementioned relations and Eq.2 may be given as a function of the applied voltage in Eq.12.

$$F_{R,Static} = C_s L \left((2 + \frac{2\theta}{\ln(\frac{r_o}{r_i})}) V - (2(r_o - r_i) + \theta(r_o + r_i)) E_{ref} \right) \tag{12}$$

In the dynamic state, the system will have velocity and acceleration. In this situation, as in the static state, the overall relation may be given by Eq.13.

$$F_{R,Dynamic} = \left(\tau_d(r_o)A_1(r_o) + \tau_d(r_i)A_1(r_i) + 2\int_{r_i}^{r_o} \tau_d(r)dA_2 \right) \tag{13}$$

By considering the equilibrium of the governing force and calculating the resistive forces due to shear stress, using Eqs.3 and 4, Eq.14 can be obtained.

$$F_{\tau,Dynamic} = L[(C_d - C_v \frac{v}{\Delta r})(\frac{\theta}{r_o} + \frac{\theta}{r_i} + \frac{2}{r_i} - \frac{2}{r_o})\frac{V^2}{(\ln(\frac{r_o}{r_i}))^2} + \mu_0 v(2 + \theta(\frac{r_o + r_i}{r_o - r_i}))] \tag{14}$$

Also, the fluid pressure forces, calculated from the pressure gradient in the channels, may be obtained by Eq.15 in which A_3 is the wetted surface by the fluid and is given by Eq.16.

$$F_{P,Dynamic} = \Delta P A_3 = -\frac{dp}{dx} L A_3 \tag{15}$$

$$A_3 = \pi r_o^2 - \frac{N\theta}{2}\left(r_o^2 - r_i^2\right) \tag{16}$$

Therefore, the overall relation for the force exerted on one channel is as Eq.17.

$$F_{R,Dynamic} = L(\frac{\pi r_o^2}{\frac{\theta}{2}(r_o^2 - r_i^2)})[(C_d - C_v \frac{v}{r_o - r_i})(\frac{\theta}{r_o} + \frac{\theta}{r_i} + \frac{2}{r_i} - \frac{2}{r_o})\frac{V^2}{(\ln(\frac{r_o}{r_i}))^2} \tag{17}$$
$$+ \mu_0 v(2 + \theta(\frac{r_o + r_i}{r_o - r_i}))] - \rho La(\pi r_o^2 - 3\theta(r_o^2 - r_i^2))$$

3. ER Force Element Simulation

For the proposed design, the cylinder geometric parameters are chosen to correspond to the human hand anthropometry and a piston having six channels has been suggested. The electro-rheological fluid constant parameters are based on a fluid developed by the ER Fluid Development Ltd. codenamed ERF354S. Using the derived equations and constant parameters governing the system, a model for the system has been simulated by employing a computer software package. Results of the force-voltage (static state) and force-voltage-velocity (dynamic state with constant acceleration) are shown in Figures 4 and 5 respectively.

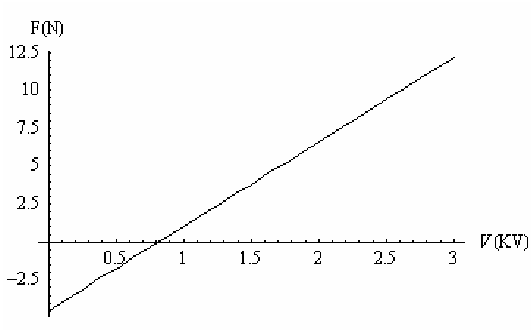

Figure 4. Variation of Force with Voltage for static state

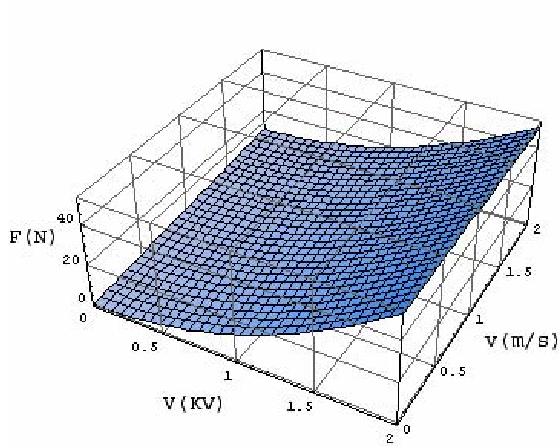

Figure 5. Variation of Force-Voltage-speed for dynamic state

According to the Eqs.12 and 17, the relationship between force and voltage in the rehabilitation force element is linear in the static case and parabolic in the dynamic case. It is important that in static case, the formula is only valid for fields greater than E_{ref}. Also this simulation shows that the reaction force in the dynamic state is almost independent of the velocity imposed by the user. This is due to the fact that the velocity contribution in the reaction force is much smaller than the effect of the voltage related term. A similar parametric simulation revealed the same behavior for the acceleration. These findings can simplify as well as increase the reliability of the control procedure for the novel rehabilitation system.

4. Comparison of Results with Experimental Data

In order to evaluate the proposed model and simulation, results are compared with the available experimental data [9] carried out on a prototype system having similar specifications but different scale and number of channels.

Here, the constant parameters for the experimental prototype system are entered in the model and results are compared with the measured data. Figure 4 depicts the variation of displacement with time for a voltage of 2kV and four different constant pressure forces. As it can be seen very good agreements have been achieved, especially at lower pressure forces. This figure and similar results strongly support the validity of the proposed model.

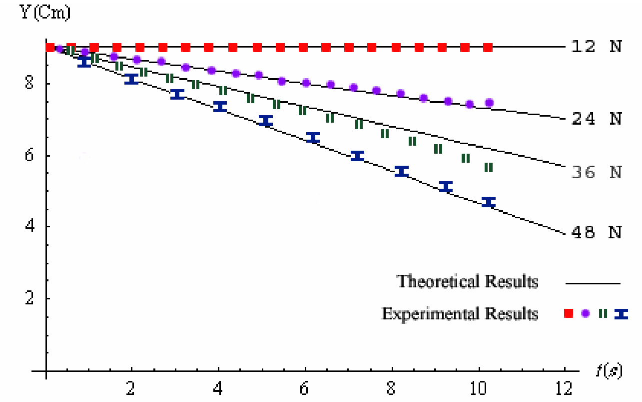

Figure 6. Comparison of theoretical and experimental results for 4 constant forces

5. Conclusions

First, properties and laws governing the behavior of the electro-rheological fluid as a smart material are briefly described. Principles of designing a two-degree-of-freedom intelligent damping system based on an electro-rheological fluid for the application in rehabilitation of human hands are then explained. This mechanism provides the capability to create a virtual environment in which the training can be intelligently manipulated on the basis of body's feedback system. Also it can encourage the patient to continue with the therapy.

Modeling and simulation of the ER force element is presented and results are compared with the available experimental data obtained, by other researchers, from a prototype system with relatively similar geometry but for other applications. Very good agreement is being noted between the theoretical model and the experimental data for different test configurations.

Future works will be devoted to the overall design of components for the rehabilitation system. Moreover, the critical research points will be the optimization of the control system for this novel rehabilitation force element based on the body’s own feedback.

Nomenclatures

a	Acceleration (m/s^2)
C_d	ERF dynamic constant parameter (0.00025 $Pa.m^2/KV^2$)
C_s	ERF static constant parameter (2.77 Pa.m/KV)
C_v	ERF zero volt constant parameter (1.98×10^{-8} $Pa.s.m^2/KV^2$)
e_r	The unit vector in radial direction
E	Electric field strength (V/m)
E_{ref}	ERF reference electric filed strength (1090 KV/m)

F_R	Resistive force (N)
F_τ	Forces due to shear stress (N)
F_p	Forces due to pressure (N)
L	Length of the channels (m)
N	Number of channels
q	Electric charge (C)
r	Average radius of the piston (m)
r_i	Inner radius of the piston (m)
r_o	Outer radius of the piston (m)
V	Voltage (v)
v	Velocity (m/s)
ε_0	Electrical permittivity of free space (8.9×10^{-12} $C^2/N.m^2$)
ρ	Density (kg/m^3)
μ	Dynamic viscosity ($N.s/m^2$)
μ_0	Zero field viscosity (0.125 $N.s/m^2$)
θ	Angular width of the channel (rad)
τ	Shear stress (Pa)
τ_y	Yield stress (Pa)
$\dot{\gamma}$	Shear rate (1/s)

References

[1] Adams J.C., Hamblen D.J, August 2001, "Outline of Orthopedics", Churchill Livingstone Publisher, 13th edition.

[2] Burdea G., Popescu V. et al., 2000,"Virtual reality-based orthopedic telerehabilitation" ,IEEE Transactions on rehabilitation engineering, Vol. 8, No. 3.

[3] Aisen M.L., Krebs H.I., Hogan N. and McDowell F., Apr.1997, "The effect of robot-assisted therapy and rehabilitative training on motor recovery following stroke", Arch. Neurol. J., Vol. 54, pp. 443–446.

[4] Kawsaki H., Ito S. et al., 2004 ," Hand rehabilitation support system based on self-motion-control", IEEE Transactions on rehabilitation engineering.

[5] Hosseini-Sianaki A. and Bullough, W.A., 2003, “Engineering applications of a smart fluid", Proc. of the 11th Annual (International) Mechanical Engineering Conference, Mashhad, Iran, pp.113-119.

[6] Taylor P.M., Hosseini-Sianaki A. and Varley C.J., 1996, "Surface feedback for virtual environment systems using electrorheological fluids," Int. J. of Modern Physics B, Vol. 10, No. 23 & 24, pp. 3011-3018.

[7] Taylor P.M., Pollet D.M. and Hosseini-Sianaki A., 1998, "Advances in electrorheological fluid based tactile array", Displays J., Vol. 18, No. 3 (Elsevier Publishers), pp. 135-141.

[8] Hosseini-Sianaki A. and Nikkhoo M., 2006, “Haptic devices for telesurgery”, Proc. Mechanical Engineering conf. Azad University, Shahr-e-Ray, Tehran, Iran.

[9] Bar-Cohen Y. and et al., March 2001, "Virtual reality robotic telesurgery simulations using MEMICA haptic system", 8th Int. Symp. on Smart Structures and Materials, , Newport, USA.

Medicine Meets Engineering
J. Hammer et al. (Eds.)
IOS Press, 2008

Biomechanical analysis of fracture healing in guinea-pigs

Richard KDOLSKY[1], Roland REIHSNER[2], and Rudolf BEER[2]

[1] *Department of Traumatology, University of Vienna Medical School, Austria*
[2] *Institute of Strength of Material, University of Technology, Vienna*

Abstract. To validate the hypothesis that healing of fractures can be accelerated by oral administered L-arginine a guinea-pig model was chosen. A diaphyseal defect fracture was established in the right femur of each of the 32 small animals and stabilized. According to randomization groups the oral administration was realized (2 or 4 weeks medication / solvent). The following biomechanical variables were measured after 4 weeeks in 32 right femora and the corresponding uninjured left femora. The measurement for the healed femur was individually compared with that of the uninjured femur in each animal; bending, force (necessary for refracture) and energy (necessary for refracture). To apply the bending moment in a measurable and reproducible way each end of the femur was secured using a special device. For each femur a strain/momentum graph of the measurements and the essential parameters were drawn (stiffness, end of the linear range, and failure-point). The bending moment was always applied with the same loading rate.
The following three variables were used for the biomechanical evaluation; bending stiffness, force until failure and energy necessary for refracture. The bending stiffness reached 73% by the control group and 88% by the 4-week treatment group. The force necessary for refracture was 52% in the control compared with 65% in the 4-week treatment group. The energy necessary for refracture was 36% in the control compared with 73% in the group treated for 4 weeks.
The 2 week treatment group showed no statistical significant differences to the control, but the femora from the 4 week treatment group required statistically significant higher energy for refracture than the femora from the control.

Key-words. Small animals, Long bones, Fracture healing, Point of failure, Bending, Force, Energy

Introduction

The hypothesis was to validate that healing of femoral fractures can be accelerated by oral administration of nutrition supplementation on the basis of a nitric oxide precursor [1]. A guinea-pig model was chosen because guinea pigs have been established as a good model for studies on experimental diaphyseal defects of long bones using intramedullary stabilization [2]. The choice of guinea-pig - femora led to the necessitity to develop a mechanical evaluation suitable for these very small long bones.

Biomechanics

To examine the biomechanical material properties of long thin specimens “pure bending”, is usually used in calibration tests. Experimentally only strain can be measured. The stress and strain distribution is given by the following equations:

$$\sigma = \frac{M}{J}.y \tag{1}$$

$$\varepsilon = \frac{M}{E.J}.y \tag{2}$$

M ….. loading moment
y …… distance from the “neutral axis” (stress $\sigma = 0$; strain $\varepsilon = 0$)
J …… momentum of inertia (based on the “neutral axis”)
E …… Young´s modulus of the material

Pre-conditions for the applicability of these equations are:

1. The measurement of the cross-section must be small compared with the length of the specimen.
2. There must be no sudden change in the dimensions of the cross-section.
3. If the axis of the specimen is not straight, the measures of the cross-section must be small compared with the curvature of the axis.
4. The material properties should be recordable fairly well using Young`s modulus.

These requirements are more or less fulfilled for long small bones, especially if the comparison is to be made between specimens having the same geometry and texture which is the case in this study.

Because of the described difficulty of biomechanically testing small bones like the femora of guinea pigs, we constructed a special apparatus that can register bending and stiffness of bones simultaneously. This enabled both measurements to be recorded while all bones were loaded until refracture (Fig. 1 and 2).

In biological materials stress strain relations consist of three parts in the graph: linear range followed by a non-linear range and finally the point of failure. The four pre-conditions for applicability of the equations that are listed above are only fulfilled when a more or less linear range can be detected [3]. The tangent of the angle is then a measurement of the Stiffness (E.J) up to the point M*. The non-linear range can be

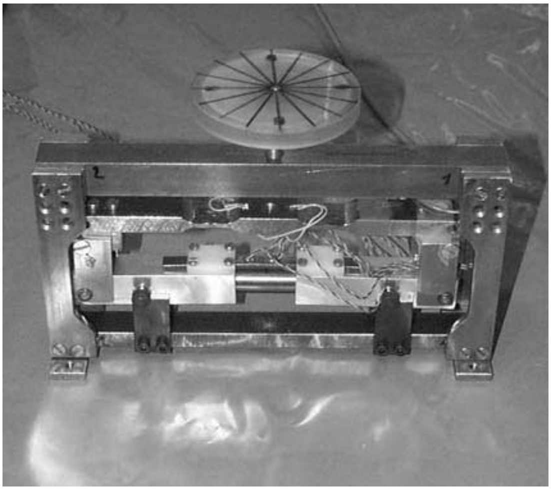

Figure 1: photograph of the mechanical apparatus showing the method used (four point bending test) to distinguish between the mechanical properties of the femora compared

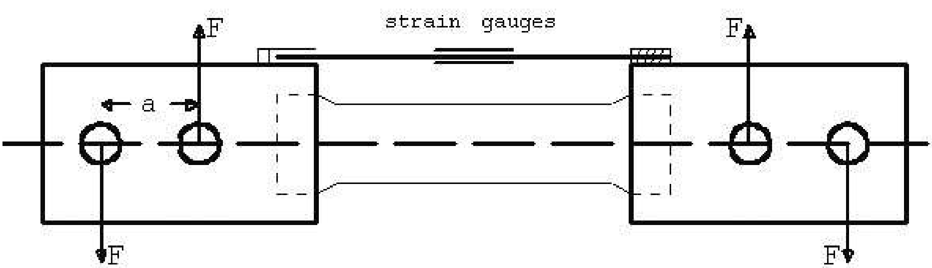

Figure 2: sketch of the mechanical apparatus showing the method used (four point bending test) to distinguish between the mechanical properties of the femora compared

inferred from the range M* to M_{max} which is the point of final failure (complete disruption).

$$tg\alpha = \frac{d\varepsilon}{dM} = \frac{y_{max}}{E.J} \tag{3}$$

For each femur a strain/momentum graph of the measurements the essential parameters were drawn: with y_{max} as value at the end of the linear rangeof the graph we may write: the slope tgα of the graphs is a measure of the stiffness of the femora. The parameters $M_{e,max}$ and $\varepsilon_{e,max}$ indicate the end of the linear range and M_f the failure-point. These parameters were collected for each femur group for successive statistical interpretation. Due to the rheological properties of bone the bending moment was always applied with the same loading rate.

In this study geometrical parameters such as the exact position of the neutral axis, and the value of the momentum of inertia are not needed because the aim of the study was to compare healing of diaphyseal defects in treated femora with that in untreated femora and each injured femur was individually compared with the uninjured femora of the same animal. In this case the dimensionless ratio of the following equation is appropriate for measuring the influence of treatment on the healing process:

$$\frac{d\varepsilon}{dM} \Big/ \frac{d\varepsilon_R}{dM} = tg\alpha \big/ tg\alpha_R = E \big/ E_R \qquad (4)$$

Materials and Methods

Animals

Male, adult (>300g) guinea-pigs (Charles River, Sulzfeld, Germany), each with a stabilized intramedullar bone defect, were allocated at random to three groups to receive the following treatments at a dose of 100 mg/kg per day given orally by pipette; group A (control, n=16), 0.9% NaCl (Mayrhofer, Linz, Austria), group B (n=17), L-arginine for 4 weeks and group C (n=15), L-arginine for 2 weeks. Treatment was blinded. Animals were kept one to a cage and identified by fibre-tip pen markings and cage number. They were fed on pellets (Ssniff, Soest, Germany) and given free access to water. The study was reviewed by the institutional board, approved by the Ministry of Science under the provisions of the Austrian and European law (GZ 66.009/202) and was carried out in accordance with Good Laboratory Practice (GLP).

Manipulation of bone defects

All guinea-pigs underwent general anaesthesia (sedation by atropin 0.05mg/kg i.m, and anaesthesia by 150 mg/kg ketamine i.m. and 5 mg/kg xylazine i.m) [4]. To ensure the correct length of the limb, a 1.4-mm K-wire was implanted, under sterile conditions, into the right femur intramedullary through a small incision in the proximal third of the shaft. To produce a diaphyseal bone and periosteal defect, the skin on the lateral side of the femur was incised and a fracture of 7 mm in length made in the proximal to middle third of the prestabilized femur shaft with a scalpel saw. The wound was then closed. On average, the procedure took about 15 minutes.

The animals were weighed before and on the 7^{th}, 23^{rd} and 14^{th} day after the fracture procedure, and after death. They were killed on the twenty-ninth and thirtieth day after fracture by injection of an overdose of vetanarcol (Pentobarbital, Richter, Wels, Austria). Both femora of each animal were removed and x-rayed after explantation of the intramedullary K wire.

Measurement of biomechanical variables

The following biomechanical variables were measured in 32 healed femora and the corresponding uninjured femora. The measurement for the healed femur was individually compared with that of the uninjured femur in each animal; bending, force (necessary for refracture) and energy (necessary for refracture). To apply the bending moment in a measurable and reproducible way each end of the femur was secured using a special device. For each femur a strain/momentum graph of the measurements and the essential parameters were drawn (stiffness, end of the linear range, and failure-point). The bending moment was always applied with the same loading rate.

Statistical analysis

For analysis of the mechanical measurement in each of the three groups, the pooled absolute measurements of the mechanical variables, bending, elongation, force and energy are reported as median, standard deviation, and standard mean error. Fisher's Exact test (SAS software - SAS Institute, Cary, NC, USA) was used for evaluation. A p-value of < 0.05 was considered to indicate statistical significance.

Results*:*

Biomechanical analysis (n=32)

The biomechanical measurements were recorded and analyzed by a strain/momentum graph. The right injured femur of each animal was compared with the corresponding left uninjured femur and all measurements obtained from the injured femur were calculated as a percentage of the uninjured femur. The following three variables were used for the biomechanical evaluation; bending stiffness, force until failure and energy necessary for refracture. The bending stiffness reached by the control group was 73%, by the 4-week treatment group, 88%, and by the 2-week treatment group 77%. The force necessary for refracture was 52% in the control group compared with 65% in the 4-week treatment group and 53% in the 2-week treatment group. The energy necessary for refracture was 36% in the control group compared with 73% in the group treated for 4 weeks and 39% in the group treated for 2 weeks.

The femora from the 4 week treatment group required statistically significant higher energy for refracture than the femora from the control.

Even though the other results show no statistically significant differences a clear trend can be seen on examination of the individual graphs (Figure 3).

Examination of the individual graphs:

The curves obtained for all left uninjured femora regardless of whether the specimens were from the treated or untreated groups typically showed a curve geometry with a linear gradient up to the point of failure. Typical curves obtained for specimens of right injured femora from the untreated group showed a similar linear gradient up to the point of failure. After the failure point interrupted successive creep occurs similar to a Bingham-Hinge. In contrast typical curves obtained for specimens of the right injured femora from the treatment groups showed lower almost linear gradients from the outset whereby usually a higher point of failure was reached than that for the untreated injured right femora (Figure 3).

Biomechanical analysis of unbroken femora:

The values obtained for the treatment groups B and C were compared with the control group A. No significant differences were found between the groups using Student's t test.

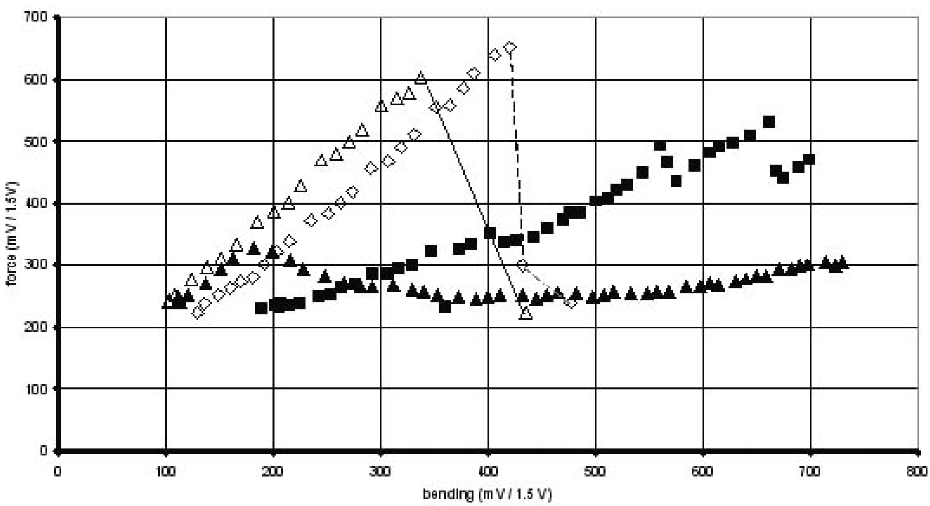

Figure 3: Example showing typical mechanical testing graphs. Specimen from untreated guinea pig (No. 2) indicated by triangles, from 4-week treated guinea pig (No. 1) indicated by squares (white left uninjured femur, black right injured femur).

Discussion

A special apparatus that can register bending and stiffness of long bones simultaneously was to be constructed for the biomechanical evaluation of the stability achieved after fracture healing in these small animals. Due to the small stiffness of the parallel measurement device its contribution to the measurement of the stiffness of the femora can be neglected. This enabled both measurements to be recorded while all bones were loaded until refracture. The mechanical testing gave significant differences regarding the energy (necessary for failure) between the 4 weeks treatment and the control group. The differences between these groups regarding force (up to failure) and elongation missed only by margin the statistical significance ($0{,}066 > p > 0{,}05$). In almost all parameters a trend towards improving mechanical properties were seen in both treatment groups which got clearer after 4 weeks of oral administered L-arginine.

The initial slop of the strain-momentum graphs served as a measure of the bending-stiffness in the elastic range. The range after the elastic range until failure indicated some more differences between the groups, however, these ranges overlapped to some degree due to the remarkable scattering. The mechanical measurements did not show a statistically significant distinction between the different groups of femora. Nevertheless, the results of the mechanical tests, from which the energy necessary for refracture is the most interesting for further clinical research, showed a positive trend in the group which received L-arginine for 4 weeks. Surprisingly, some of the injured femora in both treatment groups reached higher values than those reached in the corresponding uninjured femora.

References:

[1] Furchgott RF, Zawadzki JV. The obligatory role of the endothelium in the relaxation of artifical smooth muscle by acetylcholine. Nature 1980; 288: 373 - 376.

[2] Passl R, Müller CH, Zielinski CC, Eibl MM. A model of experimental post-traumatic osteomyelitis in guinea pigs. J Trauma 1984; 24: 323 - 326.

[3] Kobayashi AS. Handbook on Experimental Mechanics. VCH – Publisher, 1993

[4] Küpper W. In: Gabrisch and Zwart (eds) Krankheiten der Heimtiere, Narkose und chirurgische Eingriffe bei Kaninchen und Nagetieren. 2nd ed. Hannover: Schuter´sche Verlagsanstalt und Druckerei, 1990: 57-73.

Medicine Meets Engineering
J. Hammer et al. (Eds.)
IOS Press, 2008

The Behaviour of Fatigue-Induced Microdamage in Compact Bone Samples from Control and Ovariectomised Sheep

Oran D. KENNEDY[a,b 1], Orlaith BRENNAN[a,b], Peter MAUER[a,b], Fergal J. O'BRIEN[a,b], Susan M. RACKARD[c], David TAYLOR[a], T. Clive LEE[a,b]

[a]*Trinity College Dublin, Trinity Centre for Bioengineering, Ireland.*
[b]*Royal College of Surgeons in Ireland, Department of Anatomy, Ireland.*
[c]*University College Dublin, School of Agriculture, Food Science and Veterinary Medicine, Ireland.*

Abstract. This study investigates the effect of microdamage on bone quality in osteoporosis using an ovariectomised (OVX) sheep model of osteoporosis. Thirty-four sheep were divided into an OVX group (n=16) and a control group (n=18). Fluorochromes were administered intravenously at 3 monthly intervals after surgery to label bone turnover. After sacrifice, beams were removed from the metatarsal and tested in three-point bending. Following failure, microcracks were identified and quantified in terms of region, location and interaction with osteons.

Number of cycles to failure (Nf) was lower in the OVX group relative to controls by approximately 7%. Crack density (CrDn) was higher in the OVX group compared to controls. CrDn was 2.5 and 3.5 times greater in the compressive region compared to tensile in control and OVX bone respectively. Combined results from both groups showed that 91% of cracks remained in interstitial bone, approximately 8% of cracks penetrated unlabelled osteons and less than 1% penetrated into labelled osteons. All cases of labelled osteon penetration occurred in controls. Crack surface density (CrSDn), was 25% higher in the control group compared to OVX.

It is known that crack behaviour on meeting microstructural features such as osteons will depend on crack length. We have shown that osteon age also affects crack propagation. Long cracks penetrated unlabelled osteons but not labelled ones. Some cracks in the control group did penetrate labelled osteons. This may be due the fact that control bone is more highly mineralized. CrSDn was increased by 25% in the control group compared to OVX. Further study of these fracture mechanisms will help determine the effect of microdamage on bone quality and how this contributes to bone fragility.

Keywords. Bone quality, osteoporosis, compact bone, microcracks

1. Introduction

Osteoporosis is a skeletal disorder characterized by reduced bone strength predisposing a person to an increased risk of fractures. The most recent European data puts the cost of this disease to the economy at €17.1 billion annually [1]. In clinical practice, dual

[1]Corresponding Author: Oran Kennedy, Trinity Centre for Bioengineering, Trinity College Dublin, Dublin 2, Ireland; Email: okennedy@rcsi.ie.

energy X-ray absorptiometry (DEXA) scanning is widely used for measuring bone mineral density (BMD) levels and is the current gold standard for diagnosing and monitoring osteoporosis. BMD is calculated as the mass of mineral per unit area and is normally quoted as ‘areal density’ this is a 2-D measurement of a 3-D property and as such it is thought to be a limiting factor for this technique. Currently, there is no accurate clinical measure of overall bone strength, however it is known that strength depends on bone quantity and bone quality. Bone quality is defined by at least four factors: (1) the rate of bone turnover; (2) architecture/geometry of the bone; (3) properties of the collagen/mineral matrix; (4) microdamage accumulation [2].
It has been shown that microdamage accumulates in athletes and military recruits who experience increased rates and magnitudes of loading[3,4]. It has also been proposed that microdamage plays a role in regulating the bone remodelling process, however, the precise link between the two remains unclear. The balance between damage and repair is an important one and can be upset by increased damage creation or deficient repair. An imbalance in remodelling may cause microdamage to accumulate in the elderly [5-7] and could contribute to osteoporotic fractures. Microcracks have been observed in bone *in vitro* due to fatigue loading. They can be classified as either individual cracks which are approximately 100-300μm in length, or diffuse damage which consists of a collection of small cracks which are between 2-10μm long and are oriented roughly along the direction of loading [8]. It has been shown in many studies that the majority of microcracks are found in the interstitial bone[9-11]. Interstitial bone tends to have a higher microdamage burden because it is comparatively older than the surrounding bone. Also, the degree of mineralisation in interstitial bone is normally relatively high, which allows microcracks to propagate easily. Histological measurements of microcracks have shown that when viewed along the longitudinal axis of the bone cracks are significantly longer than when they are viewed transversely in the bone [12]. This is intuitively correct as the cracks in any material will preferentially travel along the path of least resistance with the ‘grain’ of the material.
However, there is still much that remains unknown about microdamage such as how its behaviour changes in areas of high bone turnover and also how microcracks behave in bone which has undergone long term treatment with anti-resorptive drugs. The specific aims of this study were 1) to measure the fatigue life of control and OVX compact bone samples and 2) to quantify resultant microdamage in terms of location and interaction with the surrounding microstructure.

2. Materials and Methods

2.1 Animal model

Thirty-four aged skeletally mature sheep (5-9 years) were randomly divided into an ovariectomised group (OVX; n=16) and a control group (n=18). Animals in the OVX group underwent ovariectomy at the beginning of month 0 in order to simulate post-menopausal osteoporosis. Animals in both groups received an intravenous injection of a fluorochrome bone marker at that time and then at 3 monthly intervals until sacrifice after one year. Different fluorochrome markers were used at each time-point so that bone turnover at 5 different intervals during the experiment could be assessed. The details of fluorochromes used, the dosage, and administration schedule are shown in Table 1. All animals were sacrificed at 12 months post OVX. All experimental procedures were carried out under Irish government license.

Table 1. Details of fluorochromes, dosages and administration schedules used during experimental period.

Fluorochrome	Specification	Month	Dosage [mg/kg]
Oxytetracycline	75965	0 (Nov'03)	50
Alizarin Complexone	12765-5	3 (Feb'03)	25
Calcein	CO875	6 (May'03)	10
Xylenol Orange	95615	9 (Aug'04)	90
Calcein Blue	M1255	12 (Nov'04)	30

2.2 Sample preparation and fatigue testing

Rectangular beams were removed from the anterior quadrant of the right metatarsal using a diamond saw (Accutom-50, Struers, Ballerup, Denmark). The final dimensions (2 x 2 x 36 mm) were attained using a slow speed grinding wheel (DP10, Struers, Ballerup, Denmark). Specimens were fatigue loaded in three-point bending on a pneumatic testing machine (MTS Tytron 250, USA). The testing rig used had a span of 30mm giving a span/depth ratio for these tests of 15 which complies with recommended standards. Loading was applied such that compression would be induced on the endosteal surface and tension on the periosteal surface. Specimens were fatigued at a stress range of 110 MPa with a frequency of 3 Hz and were tested to outright failure.

2.3 Histological analysis

Following failure, specimens were stained *en bloc* with basic fuchsin. Transverse histological sections with a thickness of ~200μm were cut with a diamond saw adjacent to the failure surface ensuring to avoid the main failure crack. Sections were then ground down using silicon carbide paper to a thickness of 100μm and were mounted on a standard glass slide. Sections were examined at 4X magnification to measure bone area (Olympus IX51, Hamburg, Germany) and then were examined using epifluorescence microscopy at 10X magnification to identify microdamage. The measurement area was divided at the midpoint into two regions; compressive and tensile. Linear microcracks were identified using standard criteria. Microdamage was classified in terms of region (compressive Vs tensile) location (interstitial Vs osteonal) and any interaction between microdamage and local microstructural features, specifically fluorochrome labeled osteons, was recorded. Crack density (CrDn) and crack surface density (CrSDn) were also calculated.

3. Results

The number of cycles to failure was 7% lower in the OVX group compared to the controls. This difference was not significant due to the relatively large amount of scatter in the data. These data are shown on an S/N curve in Figure 1. The bending modulus was also reduced in the OVX group compared with controls, 17.65 ±2.11 and 20.37 ±7.93 GPa, respectively.

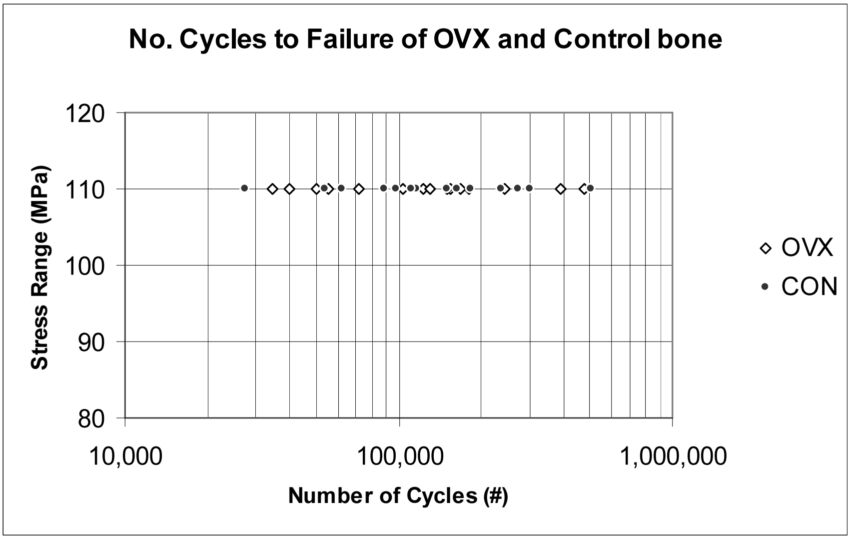

Figure 1. S/N curve from fatigue tests of control and OVX bone samples at a stress range of 110MPa.

CrDn was increased in the OVX group compared to controls, this difference was not significant, however, it can be explained by the high level of scatter in the fatigue data. When region (compressive Vs tensile) was considered, CrDn was 3.5 and 2.5 times greater in compressive compared to tensile areas in OVX and controls respectively ($p < 0.05$). These data are illustrated in Figure 2.

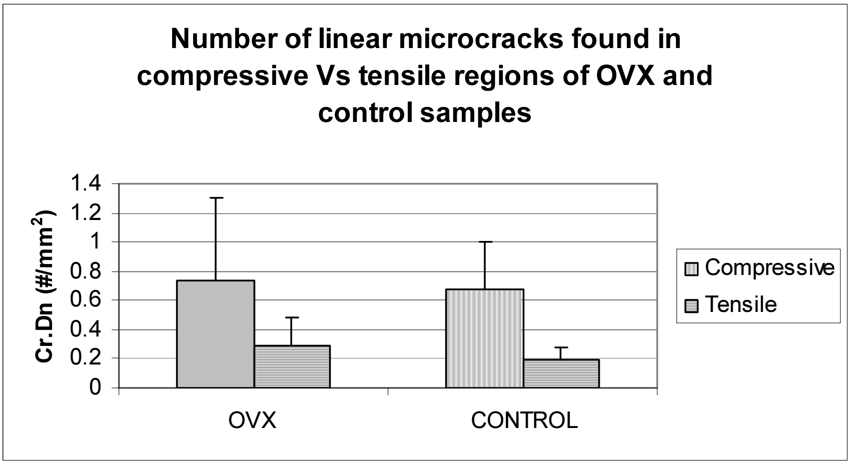

Figure 2. CrDn in compressive Vs tensile regions of OVX and control bone samples.

CrSDn was increased by approximately 25% in the control group compared the OVX ($p<0.05$). These data are illustrated in Figure 3.

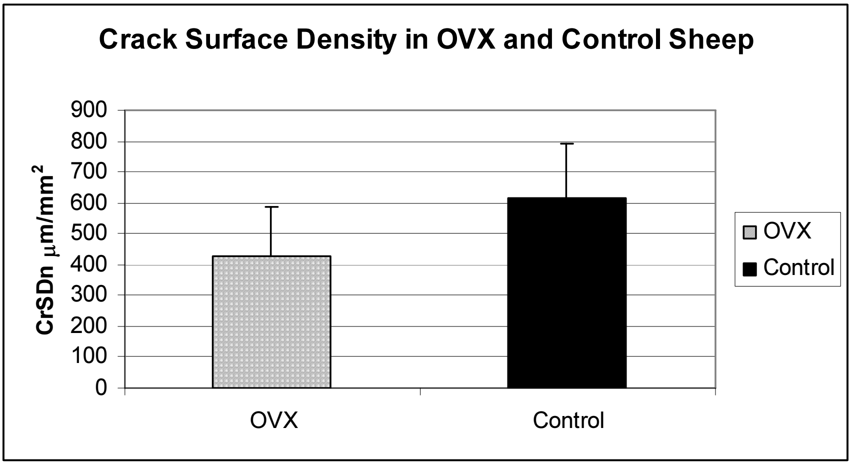

Figure 3. Crack surface density from control and OVX and bone samples.

Pooled results from both groups (control and OVX) showed that 91% of microcracks remained in interstitial bone, 8% penetrated through the cement-line of old (unlabelled) osteons and about 1% penetrated into new (labelled) osteons. These data are illustrated in Figure 4. Interestingly, all cases of new osteon penetration were in control samples. Figure 5 shows two long microcracks which have propagated through and area of interstitial bone but have arrested at a new (labelled) osteon.

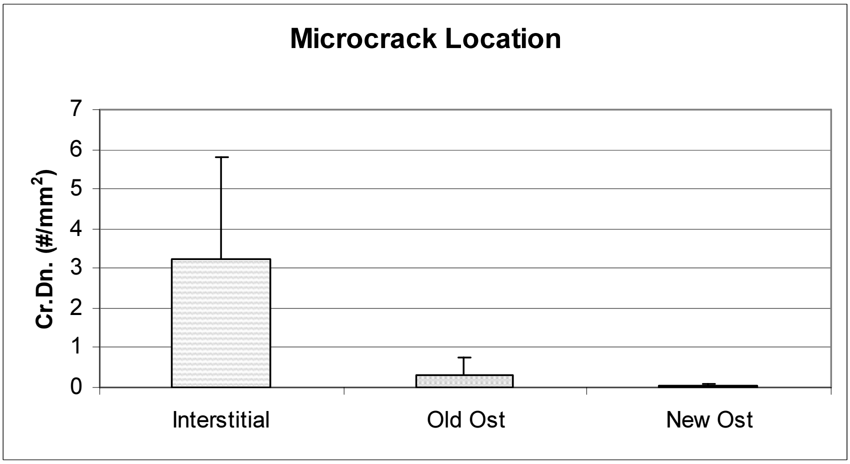

Figure 4. Pooled data from OVX and control groups of microcrack location. Cracks were classified as interstitial, penetrating old (unlabelled) osteons or penetrating new (labelled) osteons.

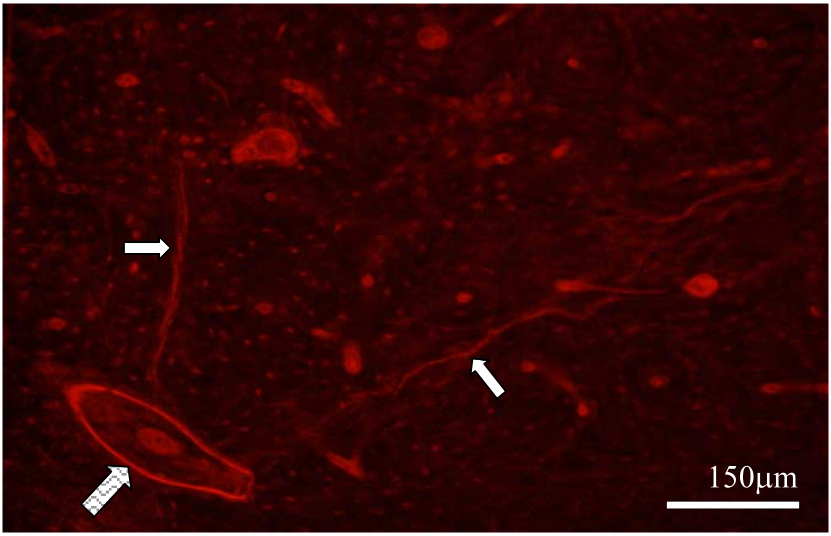

Figure 5. Two microcracks which have propagated through interstitial bone and have arrested at a new (labelled) osteon.

4. Discussion

Understanding the aetiology and pathophysiology of osteoporosis is becoming increasingly important as the worlds elderly population continues to grow. Although bone strength and fracture risk are clinically assessed by measuring BMD the mechanical properties of bone are in fact determined not only by bone mass but also by bone quality [2]. One important parameter of bone quality is microcrack accumulation. The objective of this study was to investigate the effect of osteoporosis on bone quality. Specifically we measured the fatigue life of control and OVX compact bone samples and quantified resultant microdamage in terms of region, location and interaction with osteons.

While considerable scatter was present in the fatigue data, the number of cycles to failure (Nf) was 7% lower in the OVX group compared to controls. This difference was not statistically significant due to the scatter in the data, however, our values compared well to the literature. The modulus of bending was also lower in the OVX group compared to the control (17.65 ±2.11 and 20.37 ±7.93 GPa, respectively). Other authors have reported a modulus of bending value of 18.9 ±2.2 from sheep metatarsus samples of similar dimensions [13].

CrDn was higher in the OVX group compared to controls, but the difference was not significant. However, if we assume that our samples behave like fibre reinforced composites (with newly formed osteons acting as fibres) then these data agree with the theory for crack behaviour in fibre reinforced composites. This theory states that in a composite material with a large number of fibres, cracks will tend to initiate easily but find it difficult to grow. Conversely, in a composite with a small number of fibres, cracks will not initiate as readily but those ones that do form will tend to find it easier to grow.

More microdamage was present on the compressive region compared with the tensile region in both groups. This finding agrees with the idea that damage is self-limiting in regions of tension but not compression [14,15].
It is known that the behaviour of microcracks depends on crack length, in other words, the energy that the crack has [16]. In other studies from the same laboratory a microstructural barrier effect in bone was described whereby short cracks (~100μm in length) tended to stop at osteons, longer cracks (up to 300μm) tended to deflect around the osteon and cracks over 300μm were found to penetrate into the osteon [16,17]. In this study, most microcracks were found in interstitial bone Some long cracks penetrated old (unlabelled) osteons, which can be explained because the crack has sufficient energy and the osteon is sufficiently old (and thus mineralised) to cause penetration. However, cracks of a similar size did not penetrate labelled (newer) osteons suggesting that the status of the osteon contributes to whether the osteon is penetrated or not. A small number of new (labelled) osteons were penetrated. All of these were found in the control group. This can be explained by noting that CrSDn in the control group was significantly higher than the OVX.

5. Conclusion

This study shows that fatigue-induced microcrack behaviour depends not only on the crack properties, but also on the properties of any microstructural features which it may meet during propagation.

Acknowledgements

We are grateful for the funding provided by the Higher Education Authority under the Programme for Third Level Institute Cycle 3. This work was also partially funded by the Health Research Board in Ireland under Grant No: RP/2004/229. The authors would also like to acknowledge technical support from Amir Al-Munajjed and Peter O'Reilly and help with animal handling from staff at veterinary college in UCD and Lyons Estate.

References

1. Klibanski A BT, Blair SN, Boden SD, Dickersin K, Gifford DR, Glasse L, Goldring SR, Hruska K, Johnson SR, McCauley LK, Russell WE (2001) Osteoporosis prevention, diagnosis, and therapy. Jama 285(6):785-95.
2. Burr DB (2004) Bone quality: understanding what matters. J Musculoskelet Neuronal Interact 4(2):184-6.
3. Meurman KO, Elfving S (1980) Stress fracture in soldiers: a multifocal bone disorder. A comparative radiological and scintigraphic study. Radiology 134(2):483-7.
4. Daffner RH, Pavlov H (1992) Stress fractures: current concepts. AJR Am J Roentgenol 159(2):245-52.
5. Schaffler MB, Choi K, Milgrom C (1995) Aging and matrix microdamage accumulation in human compact bone. Bone 17(6):521-25.

6. Norman TL, Wang Z (1997) Microdamage of human cortical bone: incidence and morphology in long bones. Bone 20(4):375-9.
7. Zioupos P (2001) Ageing human bone: factors affecting its biomechanical properties and the role of collagen. J Biomater Appl 15(3):187-229.
8. O'Brien FJ, Taylor D, Dickson GR, et al. (2000) Visualisation of three-dimensional microcracks in compact bone. J Anat 197 Pt 3:413-20.
9. Frost HM (1960) Presence of microscopic cracks in vivo in bone. Bull Henry Ford Hospital 8:27-35.
10. Burr DB, Turner CH, Naick P, et al. (1998) Does microdamage accumulation affect the mechanical properties of bone? J. Biomech. 31(4):337-45.
11. Lee TC, Myers ER, Hayes WC (1998) Fluorescence-aided detection of microdamage in compact bone. J Anat 193 (Pt 2):179-84.
12. O'Brien FJ, Taylor D, Lee TC (2003) Microcrack accumulation at different intervals during fatigue testing of compact bone. J. Biomech. 36(7):973-80.
13. Currey JD (1988) The effect of porosity and mineral content on the Young's modulus of elasticity of compact bone. J. Biomech. 21(2):131-9.
14. Carter DR, Hayes WC (1977) Compact bone fatigue damage--I. Residual strength and stiffness. J. Biomech. 10(5-6):325-37.
15. Griffin LV, Gibeling JC, Martin RB, et al. (1997) Model of flexural fatigue damage accumulation for cortical bone. Journal of Orthopaedic Research 15(4):607-14.
16. O'Brien FJ, Taylor D, Clive Lee T (2005) The effect of bone microstructure on the initiation and growth of microcracks. J. Orthop. Res. 23(2):475-80.
17. Mohsin S, O'Brien FJ, Lee TC (2006) Microcracks in compact bone: a three-dimensional view. J Anat 209(1):119-24.

Medicine Meets Engineering
J. Hammer et al. (Eds.)
IOS Press, 2008

Using robotic systems in order to determine biomechanical properties of soft tissues

Kunkel ME [1], Moral A, Westphal R, Rode D, Rilk M, Wahl FM
Institute for Robotics and Process Control
Technical University of Braunschweig, Germany

Abstract. Biomechanical properties of soft tissue are important not only during computer simulation for medical training but also for systems where tissue deformation must be estimated in real-time, for example, Robot Assisted Surgery. The purpose of this paper is to describe some biomechanical tests consisting in the measurement of contact forces and deformations in tissue phantoms and porcine soft tissues (liver, brain, stomach and intestine). During the measurements two different procedures were applied. First, we have used a 5DOF micromanipulator instrumented with a spherical probe and a 6-axis force/torque ATI sensor. In the second procedure instead of the micromanipulator a Stäubli RX60 robot was used to apply the force over the samples. During this last test a high noise-signal relationship was detected and in order to improve the accuracy of the experiments some results were obtained using a Stäubli TX40 robot. Major accuracy in research in the field of soft tissue could be reached using standard procedures. Robotic systems allow precise movements to carry on biomechanical tests, and also permit a wide range of tasks to be implemented.

Keywords. Soft tissue, indentation test, tissue phantom, robotic systems.

Introduction

An extensive literature on biomechanics [1-6] demonstrates that to determine tissue parameters of soft tissue is not a trivial task. Soft tissues have very low resistance to deformation in their physiological rest state and even careful handling of then can cause them to deform and change the perceived initial length. Therefore, tissue deformation is a complex matter and still subject of much research. The tissue modeling is considered complex also because of the nonhomogeneous, anisotropic, non-linear, and elastic viscous behavior of the biological tissue [1]. There are also discrepancies between material properties obtained from different approaches or test geometry. As a result, a material property measured or calculated with a certain method may not be suitable to others. Major accuracy in researches in the field of soft tissue should be reached using standard procedures.

[1] Corresponding author: Institute for Robotics and Process Control, Technical University of Braunschweig, Germany. E-mail address: eku@rob.cs.tu-bs.de (Maria Elizete Kunkel).

In the study of deformation of biological tissues, flexible plastic tissue phantoms should be used for modeling and validation because of the high level of control and repeatability that they offer during experiments. The inhomogeneous nature of soft tissues makes such experiments and validation infeasible. Ideally, the material of the phantoms should mimic human tissue. Despite that phantom just simplify the general structure of the soft tissues; they are very good to test if a specific methodology can capture the mechanical behaviour of a material. For example, if a mechanical test can differentiate materials with different elasticities through different deformation curves.

There are a number of approaches to obtain material properties of biological tissues [1]. Normally, mechanical tests are used and a variety of techniques are found in the literature to measure tissue properties, these include tensile, compression, torsion and indentation tests. Different organs require different techniques and each type of measurement has advantages and limitations. Some devices work just under limited conditions. For example, some methods do not work easily with small tissues, since it is difficult to produce regular shaped specimens. There are several commercial mechanical test machines for biological tissues, but their high cost and poor flexibility make then not suitable.

Robotic systems allow precise movements and a wide range of tasks, permitting several biomechanical tests to be implemented. Measure material properties of soft tissues using those systems demand some efforts. First, it is necessary to choose a mechanical test suitable with the material to be analyzed. Once the type of mechanical test is defined, we need to estimate adequate parameters to perform the tests. These parameters include the dimension of the specimen, loading rate, displacement rate, and size of the probe, among others.

The objective of this work is to describe the actuation of a microindenter manipulator and a robotic system, that are used to measure forces and deformations during mechanical experiments on tissue phantoms and porcine soft tissues (liver, brain, stomach and intestine mucosa). The issues of the parameters to be used in such systems are examined. Indentation tests were preferred, once they are commonly used to measure nondestructively the mechanical properties of soft tissues [2-6]. Other advantages to perform indentation tests is that it is unnecessary to prepare regularly shaped specimens, we just need to consider a model, where a thin layer of tissue is supported on a flat and rigid substrate [4].

In this study we have used as the experimental material tissue phantoms (whose mechanical characteristics look like soft tissue) and porcine soft tissues. Using homogeneous phantoms allow us to obtain comparable results during different tests. Porcine liver, brain, stomach and intestine tissue mechanical properties have been well-characterized in vitro [2, 3, 5 and 6] and can been used as reference values. Therefore, using these materials we can conclude the precision of our results.

The knowledge of biomechanical properties of soft tissues is a prerequisite to the development of surgical simulators, surgeon-training systems and also for systems where tissue deformation must be estimated in real-time such as reality-based model for robot surgery. We have particular interest in the development of an experimental methodology for future assesses in the determination of material properties (as elastic module and Poison's ratio) of soft tissues from nasal cavities. These parameters will be used for modeling and simulation of the nasal structures for Robot Assisted Endonasal Surgery.

Material and Methods

Experimental setup

In this part we describe the micromanipulator and the robotic systems that were used to perform the indentation tests. The microindenter was designed and developed at the Technical University of Braunschweig, Germany. The 5-DOF manipulator consists of a shaft with a cylindrical flat-ended probe, a handle, a 6-axis force/torque sensor ATI Nano 43SI-36-0.5 (Schunk GmbH & Co. KG, Lauffen/Neckar, Germany) that records force responses until 36 N and an electronic caliper that records the deformation as small as 1 µm. Monitoring is performed by custom software that records forces and displacements. We have used three interchangeable probe heads (diameters of 2 mm, 4 mm and 6 mm) for our tests. The equipment is shown in Figure 1. The microindenter is fixed onto a rigid horizontal support. The manually action on the handle moves the cylinder shaft instrumented with the force sensor vertically, allowing the indenter tip to exert forces onto an object under of it, allowing the flexibility of choosing the loading rate and the depth of the indentation.

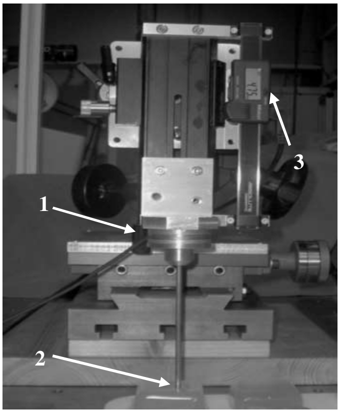

Figure 1. The manipulator: the 6-axis force sensor (1), the indenter probe (2) and the electronic caliper (3).

Two robots for general purpose (RX60 and TX40, Stäubli, Germany) were also used. These are 6-DOF manipulators, with only revolute joints, a repeatability of ±0.02 mm and protection class IP 65. The robots have being assembled between the flat-ended cylindrical probe and the end-effector, the 6-axis, the force/torque sensor ATI, already described. The Table 1 shows the main differences between both robots.

Stäubli Robots Specifications	RX60	TX40
Reach at Wrist	665 mm	515 mm
Nominal Load Capacity	2.5 kg	1.7 kg
Maximum Load Capacity	10 kg	2.3 kg

Table 1. Technical specifications of the Stäubli robots TX40 and RX60 used in the experimental set up.

Figure 2 shows the Stäubli TX40 robotic system used for indentation tests.

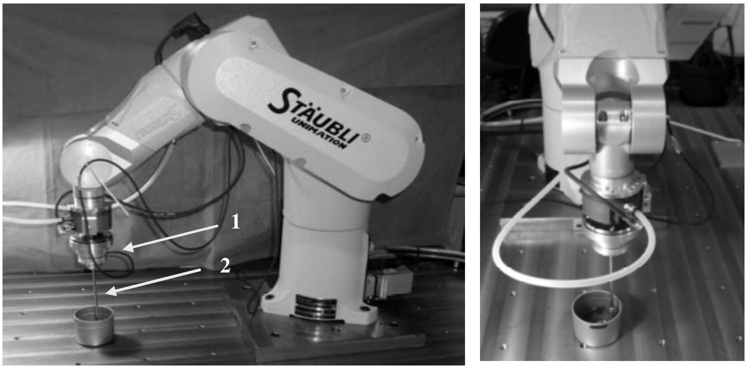

Figure 2. The Stäubli TX40 robotic system: the 6-axis force sensor (1) and the indenter probe (2).

Sample preparation

In this part we describe two different materials used during mechanical tests, tissue phantoms and porcine soft tissue.

There are several materials that can be used as tissue phantoms. After the search about a suitable material to produce the soft tissue phantoms, we have chosen polyvinyl chloride (PVC) mixed with a phthalate ester (liquid plasticizer) (M-F Manufacturing, TX). As a building material, PVC is cheap and easy to assemble. The other advantage of this product is the possibility to produce elastic phantoms with different values of flexibility (elastic modulus) just by varying the proportion of plasticizer added to the PVC. There are two kinds of basic products, the “Regular Liquid Plastic”, and the “Super Soft Liquid Plastic”, both are already pre-mixed PVC with liquid plasticizer in different proportions, but it is possible to combine the “Regular Liquid Plastic” with the liquid plasticizer to make plastics into a softer or tougher material respectively.

This material for tissue phantom was used with success to produce homogeneous soft tissue phantoms with elastic modulus known and to measure deformations applied into phantoms during needle-tissue interaction [7]. It is possible to obtain phantoms with elastic modulus ranging from 0,01MPa (approximately to the breast tissue) to well over 0,1MPa, a range that covers many of the body’s soft elastic tissues [1].

We have produced homogeneous phantoms with two different elasticity and isotropic and linear behavior,. To produce soft tissue phantom we have used the “Regular Liquid Plastic” product. The liquid was heated and stirred gradually, as far as the final product becomes viscous and mobile, when the liquid reached clear consistency it was poured into a mould and allowed to cool to room temperature. To produce super soft phantom, more flexible then the first, we have used the “Super Soft Liquid Plastic” product using the same procedure described above. By compression tests, the elastic moduli of the tissues phantoms were calculated. The values of the elastic moduli obtained were 0,147 MPa for the soft and 0,065 MPa for the super soft tissue phantom.

Porcine tissues (fresh liver, brain, stomach and intestine) were obtained from a local abattoir (Figure 3). The tissues were sectioned into flat slabs for measurement in vitro. Uniform specimens thicknesses were accomplished using a surgical scalpel. The tissues were used within 4 hours post mortem.

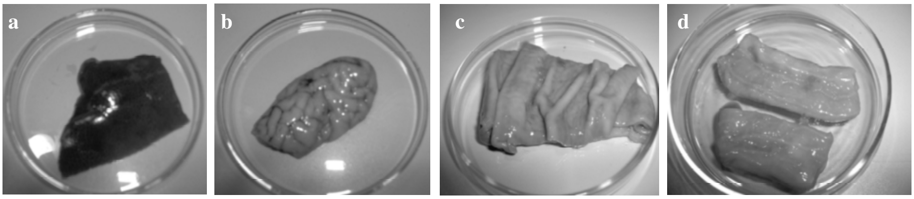

Figure 3. Porcine tissues used in indentation tests: liver (a), brain (b), stomach (c) and intestine (d).

Indentation testing

To test the feasibility of our approach, mechanical deformations were performed on phantoms and porcine soft tissues. The procedure for indentation tests in vitro here described was used with the micro manipulator and with the robotic system, and was repeated for all the samples. The indenter probe was first driven to touch the surface of the tissue layer with a very small preload of 0.02 N. No preconditioning was performed before each trial. The force value was offset-adjusted, so that its reading was approximately zero N when no force was applied. The probe follows perpendicular to the underlying sample surface to press it into the samples, which lies upon a horizontal platform, as shown in Figure 4.

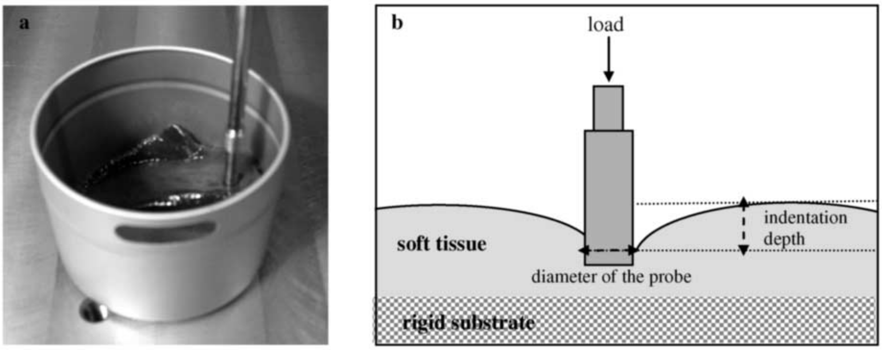

Figure 4. In vitro indentation of porcine liver tissue (a) and schematic of the indentation experiment including rigid, flat-ended cylindrical indentor and soft tissue layer bonded with rigid flat substrate (b).

We have assumed the displacement of the indentor to be the deformation of the soft tissue layer. The maximum indentation displacement was controlled and limited to within approximately 50 percent of the initial thickness of the samples. In the relaxation tests the indenting depth was applied followed by a specific time for displacement hold.

Results

In this section are described the tests using the force/torque sensor ATI with different robots, and the set of data from indentation experiments.

Before deciding the robot system to be used for indentation tests, measurements of the forces without contact with tissues or phantoms were registered, when the robots were turned on but no movements were performed. The goal of this procedure was to verify the behavior of the force/torque sensor when mounted in both robotic systems.

Figure 5 shows that the biggest range of variation is found in the force sensor mounted at RX60. This is due to RX60 posses a bigger structure, which produces bigger vibrations that affect the forces measured. Although, for other applications this variation could be considered small enough to be depreciated, in our case, this can be considered an off-set that overlaps smaller forces of interest. Therefore, we have discarded the option of using RX60 and used TX40 for the tests.

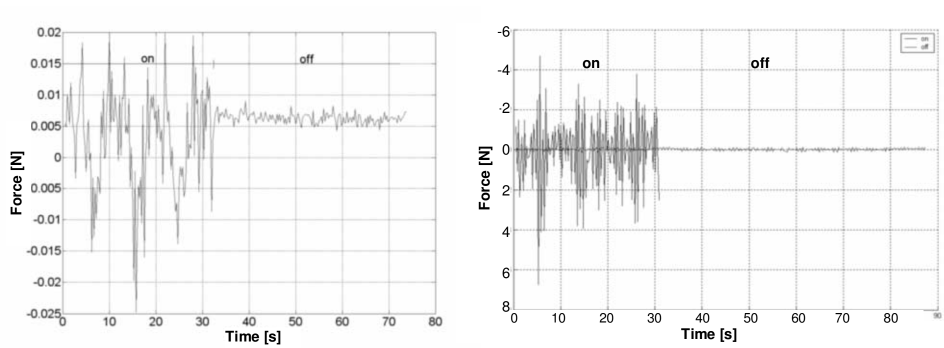

Figure 5. Forces vs. Time measured with the Force/Torque sensor ATI mounted on TX40 (left) and RX60 (right) Stäubli robots during two different states of the robot (on-off).

The result of the hysteresis, holding history, and poking experiments on tissue phantoms carried out with the micromanipulator and the robotic system are described in the Figures 6-8 and the same indentation procedures with porcine soft tissues are show in the Figures 9-11.

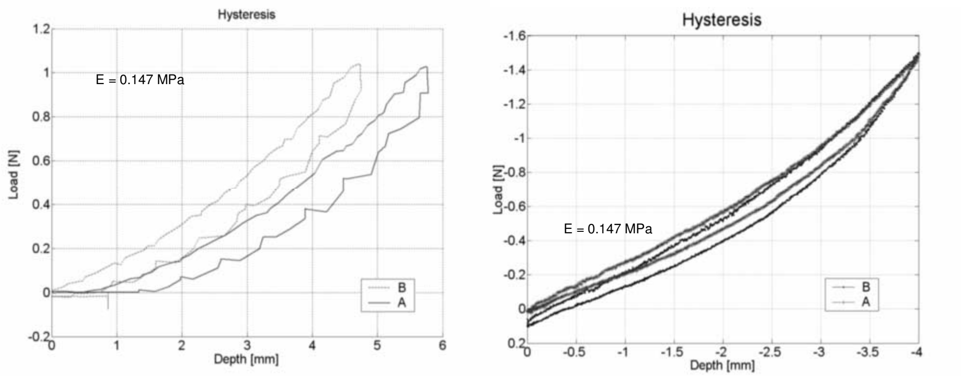

Figure 6. Representative hysteresis curves obtained for indentation of soft tissue phantom carried out with the micromanipulator (Left) and with the Stäubli TX40 robot (Right). Two cycles were recorded at different points of the same sample using a 4 mm diameter indenter and a loading rate of 0.2 mm/s.

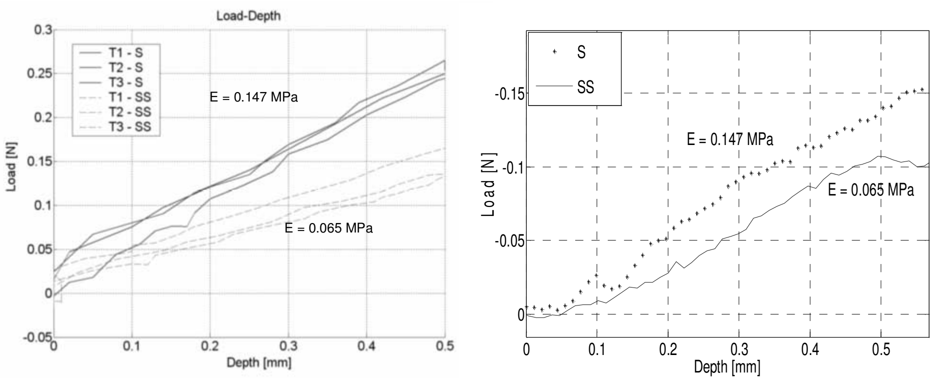

Figure 7. Representative load-depth curves obtained for indentation of tissue phantom, soft(S) and super soft(SS), carried out with the micromanipulator (superimposed data from three trials for each sample, left) and with the Stäubli TX40 robot (mean data for each sample, right). The tests were performed for short displacement using a 4 mm diameter indenter. The load rate was intended to stay constant for the manual trials (±0.1mm/s).

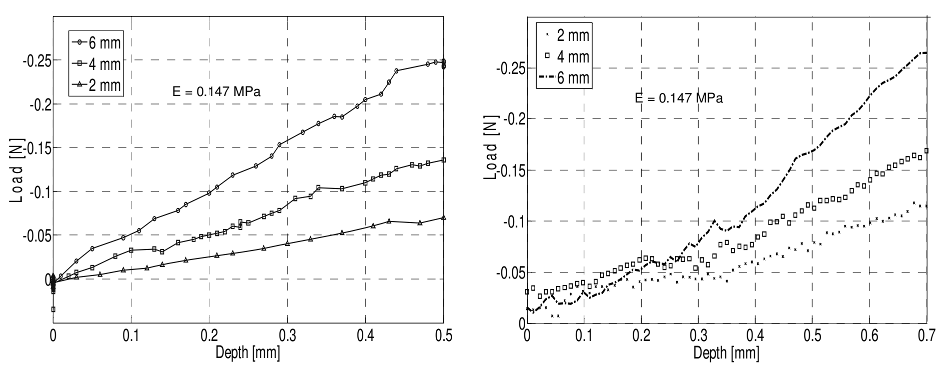

Figure 8. Representative load-depth curves obtained for indentation of soft tissue phantom using different-sized indenter (2, 4, 6 mm diameter). Test carried out with the micromanipulator (Left) and with the Stäubli TX40 robot (Right). The tests were performed for short displacement using a 4 mm diameter indenter.

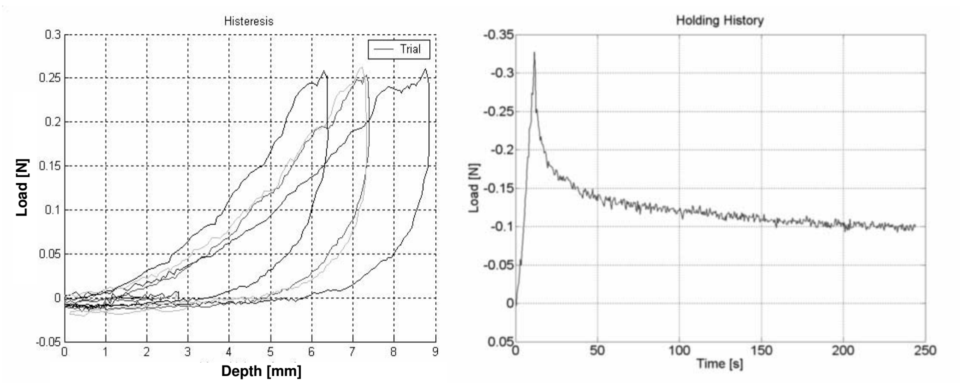

Figure 9. Representative hysteresis curve obtained for indentation of porcine brain tissue carried out with the micromanipulator(Left). Representative load-relaxation curve (holding history) obtained for indentation of porcine brain tissue carried out with the Stäubli TX40 robot(Right). The tests were performed using a 4 mm diameter indenter

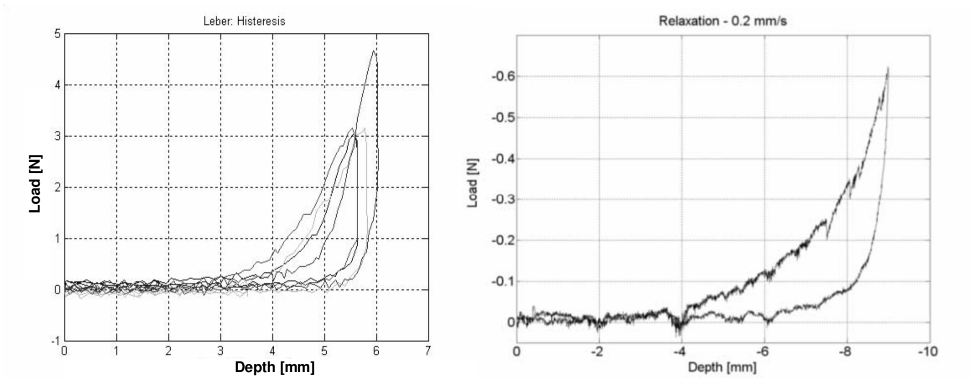

Figure 10. Representative hysteresis curves obtained for indentation of porcine liver tissue carried out with the micromanipulator(Left) and with the Stäubli TX40

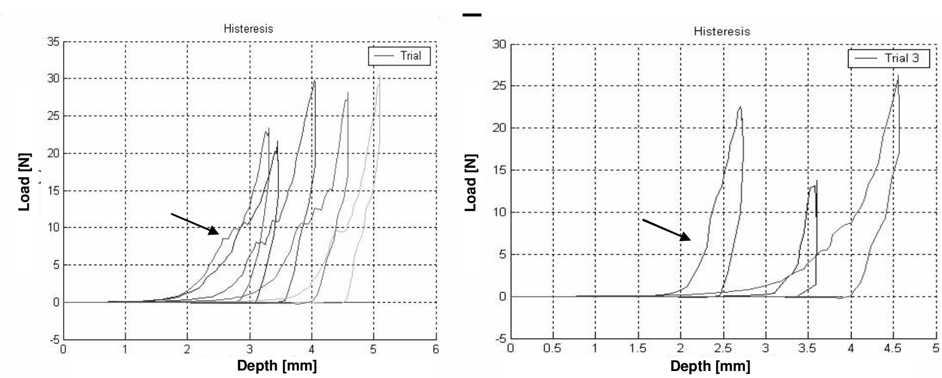

Figure 11. Representative hysteresis curves obtained for indentation of porcine stomach mucosal tissue (Left) and intestine mucosal tissue(Right) carried out with the micromanipulator. The arrows show the first variation of the curves.

Discussion and Conclusions

In our paper, we have presented a series of mechanical experiments performed in order to compare different indentation tests (hysteresis, load-depth and load-relaxation) using different types of samples with a manual and a robotic system.

The results of the indentation response obtained from phantoms using both experimental set ups are comparable. Agreement between hysteresis and load-depth curves shows that with our robot system, not only different tissue phantoms could be differentiated for short and large deformation (Figure 6-7) but also the indentation responses for different probes could be good represented (Figure 8). This achievement is very important in our research, since we are looking for a method to test several kinds of tissues, with different properties, using small range of variation in force and displacements and also changing the size of the tool.

Typical nonlinear and viscoelastic mechanical response of soft tissues are shown in Figures 9-11. The indentation tests with porcine tissues shown very satisfactory results for brain tissue (Figure 9), whose load relaxation curve for 250 s obtained with the robotic system can be directly compared with recently published measurements of fresh brain properties in vivo [3]. After indentation tests with porcine liver tissue, only the histeresis curve of manual indentation showed comparable results with the literature [7]. The discrepancy in the results obtained using the robot TX40 can be attributed to a very low loading rate adopted in this test. In this case displacements as small as 0.01 mm could be verified, but these too small steps produced an undesirable change on the speed of the probe, whose consequences are some degree in the load-indentation response presented in the liver tissue shown in Figure 10 (right). The results of Indentation tests using manual procedures on porcine mucosa (Figure 11) are comparable with previous indentation measurements in porcine stomach and intestine in vivo and in vitro [6]. These last tests with mucosa have not been performed with the robotic system, but at this point, we can suggest that following our procedure satisfactory results could be obtained. The most risky factor when indenting very thin tissue layer, as such as mucosa, is the possibility of causing damage to the force/torque sensor due to eminent contact of the probe on hard materials that support the sample. Future tests are necessary to limit this risk.

These preliminary results have show that using a robot system to carry out mechanical tests offer the advantage of setting parameters such as loading rate and displacement more precisely that one can do using a manually droved system. On the other hand, a disadvantage presented in robotic systems is the noise due to mechanical vibrations (Figure 5). This, in our case was solved by changing the type of robot, but when this option is not possible, the use of filters can be other solution.

Through this paper we have established the necessary basis and experience to work with robotic systems in order to obtain the biomechanical properties of soft tissues. From this moment, indentation tests will be performed for nasal tissues (mucosa and cartilage) characterization.

References

[1] FUNG, YC: Biomechanics. Mechanical Properties of Living Tissues. Springer-Verlag, New York. 2nd ed., 1993.

[2] MILLER K: Biomechanics of soft tissues. Med Sci Monit, 2000;6(1):158-167.

[3] MILLER K, Chinkei K, Orssengo G, Bednarz P. Mechanical properties of brain tissue in-vivo: experiment and computer simulation. Journal of Biomechanics 33(2000)1369-1376.

[4] JIN H, Lewis JK. Determination of Poisson ratio of articular cartilage by indentation using different-sized indenters. Transactions of the ASME. 126.(2004)138-145.

[5] HU T: Reality-based soft tissue Probing: Experiments and computational model for application to minimally invasive surgery: Doctor Thesis: Drexel University. 2006.

[6] BROUWER I, Ustin J, Bentley L, Sherman A, Dhruv N, Tendick F. Measuring In Vivo Animal Soft Tissue Properties for Haptic Modeling in Surgical Simulation. Medicine Meets Virtual Reality 69(2001)69-74.

[7] DIMAIO SP: Modelling, simulation and planning of needle motion in soft tissue. Doctor Thesis. University of British Columbia, 2003.

Medicine Meets Engineering
J. Hammer et al. (Eds.)
IOS Press, 2008

Assessing the quality of biological tissues using structure-property relationships: macro-scale tests on engineered phantoms

V. Lakshmanan [a], T.H.J. Yang [a], R.L. Reuben [a,], J. Hammer [b] and R.W. Else [c]*
[a] School of Engineering and Physical Sciences, Heriot-Watt University, Edinburgh, EHI4 4AS, UK
[b] Department of Mechanical Engineering, University of Applied Sciences, Regensburg, Regensburg, Germany
[c] Department of Veterinary Pathology, University of Edinburgh, Edinburgh, UK

Abstract: The overall aim of this work is to determine the quality of biological tissues based on the relationship between the dynamic mechanical properties and their histology. Two sets of rigs have been developed for dynamic mechanical measurement, one for micro-scale testing and the other for macro-scale testing. Preliminary results using the macro-scale measurement system only are reported here. This system uses strain-controlled cyclic probing actuated by a linear stepper motor operating at actuation frequencies between 0.5Hz and 20Hz. A 1mm diameter indenter probes the specimen up to a displacement of 0.2mm and a load cell measures the resultant cyclic force. A series of tissue mimics were prepared using various formulations of gelatin and safflower oil and preliminary tests carried out to determine a suitable range of experimental variables and to establish the repeatability of the tests. The dynamic mechanical properties are expressed as amplitude ratio, phase difference and mean ratios of stress and strain, and the behaviour of these measurands with actuation frequency, mean strain and strain amplitude was observed. Results consistent with the literature were found which form a foundation for measurements on collagen-lipid biological tissues.

KEYWORDS: Gelatin, elastic and viscous moduli, phantom tissue-mimic, structure-property relationship.

I. Introduction

The aim of this work is to develop a means of assessing the quality of biological tissue using mechanical measurement, a kind of instrumented palpation avoiding the need for subjective interpretation. Some earlier observations (e.g. [1]) have shown that dynamic probing at a frequency of a few Hz to a few tens of Hz might be an appropriate way of distinguishing between samples of biological materials of the same general type but with differing proportions of components which have distinct mechanical properties. The work presented here use techniques reported earlier [2] of which some results using the macro-scale experimental technique will be described here. A model biological system (animal connective tissue) has been chosen as it has two components, collagen and lipid, which are expected to have distinct mechanical properties. An engineered phantom material consisting of gelatin mixed with safflower oil, is also used, giving a two-component system (the gelatin corresponding to the collagen and the oil corresponding to the lipid) whose properties can be controlled by appropriate formulation.

Hall *et al* [3] have measured various strengths of gelatin and have found that Young's modulus (in kPa) is related to concentration (in g/l) by:

$$E_{gelatin} = 0.0034C^{0.29} \qquad (eq\text{-}1)$$

Furthermore Madsen *et al* [4] have shown that the introduction of safflower oil in dispersion in gelatin produces a series of heterogeneous formulations with a variation in elastic properties.

In this paper we report the commissioning of the macro-scale test rig and a set of calibration experiments where a single formulation is tested for repeatability and sensitivity to the various experimental parameters. Finally, the results of some systematic experiments on a range of formulations are reported with a view to assessing the extent to which the method can distinguish between formulations.

II. Experimental setup and methodology

The experimental protocol is based on carrying out a set of compressive probing operations on a range of mimic formulations. A modulated strain is applied to a standard sized specimen using an indenter, the primary experimental parameters being the mean value of the compressive strain and the amplitude and frequency of modulation. The resulting oscillatory force is measured and the dynamic elastic properties determined from the ration of mean values, the amplitude ratio and the phase lag between load and displacement.

Gelatin+oil standard tissue formulations		
Sample	Gel+oil Composition	Gel:Oil ratio
1	11.4g/100ml+30ml oil	0.38
2	15.4g/100ml+30ml oil	0.51
3	17.4g/100ml+30ml oil	0.58
4	11.4g/100ml+40ml oil	0.285
5	15.4g/100ml+40ml oil	0.385
6	17.4g/100ml+40ml oil	0.435
7	11.4g/100ml+50ml oil	0.228
8	15.4g/100ml+50ml oil	0.308
9	17.4g/100ml+50ml oil	0.348

Table 1: List of samples and their composition with corresponding gel:oil ratio.

The preparation of gel – safflower oil tissue mimics was based on work by Madsen *et al* [4] and the detailed formulation techniques are described in an earlier publication [2]. Each formulation was used to produce a batch of material which was then cut into samples of size 1cm × 1cm × 1cm. It is well established [5] that Young's modulus of gelatin can be varied from a few kPa to 10MPa by varying the gel strength and so a set of formulations (see Table 1) was used to vary the matrix modulus as well as the proportions of matrix and second phase (oil). Table 1 also shows, for each formulation, the gel:oil ratio (in g/ml) which will also be used as a measure of formulation strength. Once mixed, the samples were stored at room temperature for 20 hours prior to testing to ensure the completion of the collagen cross-linking. Figure 1 shows the experimental hardware, which consisted of an indenter driven by a linear stepper motor (Samtronic UBL1/2) towards the surface of the specimen, each step amounting to 0.03mm displacement of the indenter. The specimen is mounted on a load cell which measures the force while a proximity sensor measures the displacement of the indenter.

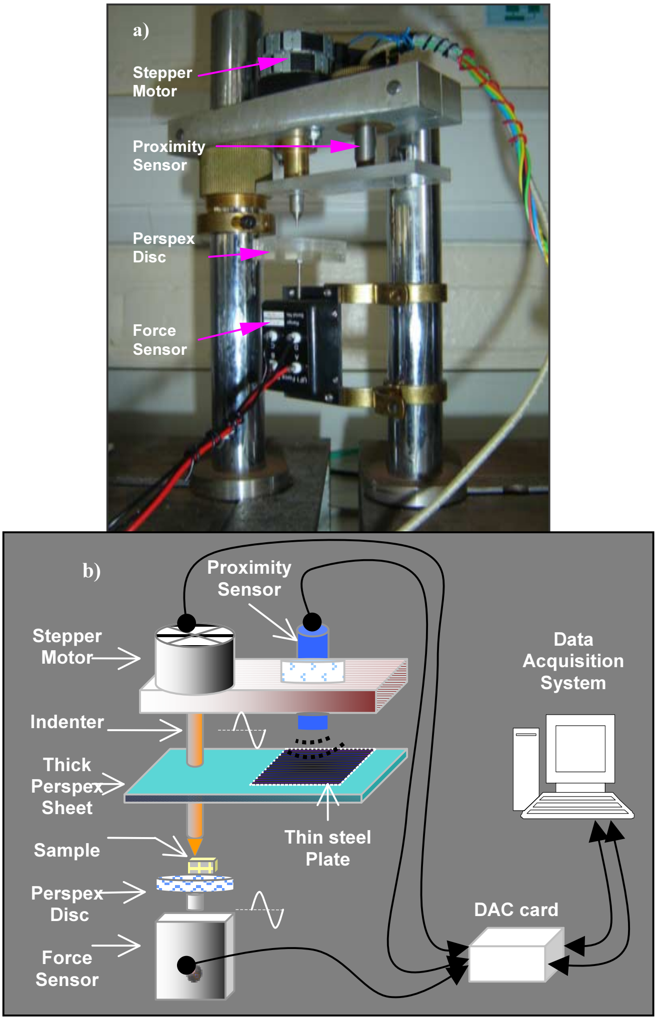

Figure-1: a) Image illustrating the experimental setup of macro-scale rig. b) Diagrammatic illustration of macro-scale experimental setup and data acquisition.

A specially designed control program generates and acquires the necessary signals simultaneously in real time. This control program was designed in LabWindows/CVI version 7.0 platform which incorporates Win32 API mode. The sequential algorithm enables much better interfacing, synchronization and buffer handling. This program has three modes of operation. The first mode performs the indentation by supplying the appropriate pulses to the linear stepper motor with given frequency and amplitude, while acquiring continuously. The second mode allows the indenter to be incremented or decremented in single steps with optional acquisition. The third mode is the automated version of the second mode where the indenter can be moved more than one step at a time and here the acquisition is automatic and mandatory. A typical experiment would start in the second mode where the indenter is actuated, step by step towards the sample. As it makes the first contact with the sample the force sensor output increases so that touch-down can be detected. After touch-down, the indenter can be taken to its desired pre-strain depth or mean and the operation changed to the first mode. The acquired data can be saved to ASCII files in which the displacement from the proximity sensor, the force from the force sensor and the direction control pulse to the motor are recorded at 1000 samples per second. When the experiment is stopped by pressing the stop button on the control panel, the operation is changed to mode three and the indenter is brought back to its original position. Figure 2 illustrates a typical record in the first control mode for the raw data of an indentation experiment at 1 Hz for a gelatin sample of concentration 17.4grams in 100ml of water with 30ml of dispersed safflower oil. The data were acquired by a NI 6024E DAC PCI card. The signal processing was done by Matlab programming. The unprocessed data acquired by the control program in ASCII format was fed to the signal processing program, where it was filtered, signal averaged and expressed as mean ratio, amplitude ratio and phase difference, all of stress relative to strain.

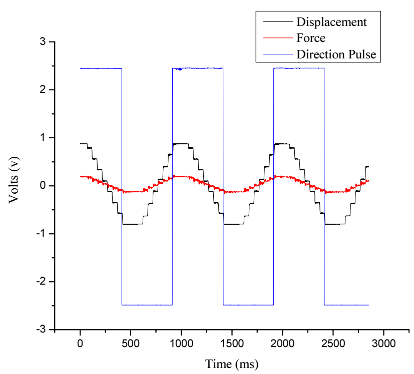

Figure 2: Typical experimental result.

When a material is subjected to a sinusoidal strain, the stress will also vary sinusoidally, but will lag behind the strain if the material has any time-dependent elastic properties (for a purely elastic material, the phase lag will be zero):

$$\varepsilon = \varepsilon_p + \varepsilon_0 e^{i\omega t} \quad \text{(eq-2)}$$

$$\sigma = \sigma_p + \sigma_0 e^{i(\omega t + \delta)} \quad \text{(eq-3)}$$

where, ε_p, σ_p are the pre-strain and resulting steady pre-stress, ε_0, σ_0 are the amplitudes of strain and stress and δ is the phase difference. The ratios of stress over strain are defined as follows: Amplitude Ratio (AR) = σ_0 / ε_0 and Mean Ratio (MR) $= \sigma_p / \varepsilon_p$.

The experimental procedure was carried out in three phases, the first two of which were exploratory tests carried out on the same formulation to assess repeatability and the effect of experimental variables. The third phase was systematic in that a single experimental protocol was applied to each of the nine formulations given in Table 1.

a. Calibration-I (effect of mean depth and ageing)

This calibration was performed on a single formulation (17.4grams gel with 30ml oil) with only the mean depth varied and therefore doubles as a repeatability test and to examine the effect of sample ageing. A set of four well separated mean depths were selected and the other variables (frequency and amplitude) were kept at 10 Hz and 30 microns, respectively. The chosen mean depths (after the touch-down) were 230 microns (M1), 390 microns (M2), 560 microns (M3) and 825 microns (M4).
Figure 3 shows the points on the surface where the tests were repeated and Table 2 gives the sequence in which each of the mean values was used at each point, points 1-4 being indented at all four mean depths without removing the indenter from the surface. Results from points 1-4 would show the effect of indenting the same points more than once albeit at a different depth, and the comparison of these points with points 5 to 8 would inform the experimental protocol. Points 9-12, being tested at a mean depth of M2 only, would give a measure of point-to-point repeatability. The set of 12 tests was repeated every day for four days in order to give an idea of the rate at which the sample mechanical properties might vary over the period of time required to make a systematic series of tests, the main concern being about drying of the samples in the laboratory atmosphere.

Points on sample	Type of test
1	M1+M2+M3+M4
2	M1+M2+M3+M4
3	M1+M2+M3+M4
4	M1+M2+M3+M4
5	M1
6	M2
7	M3
8	M4
9	M2
10	M2
11	M2
12	M2

Table 2: Sequence of mean depths for each of points 1-12 (Figure 3)

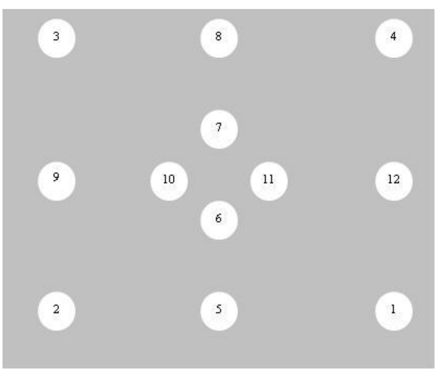

Figure 3: Test points 1-12 for Calibration I.

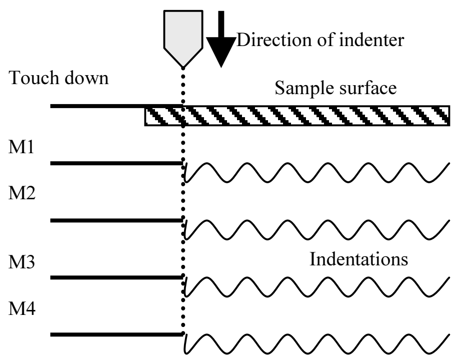

Figure 4: Diagrammatic illustration of tests for Calibration I.

b. Calibration-II (effect of frequency)

This calibration used the same formulation as Calibration I and only frequency was varied with the mean depth maintained at 390 microns (M2) and the amplitude at 30 microns. A total of 16 tests points was used (Figure 5) each at a different frequency (Table 3). The entire series of tests was carried out once on the Day of preparation and once again three days later.

Figure 5: Test points 1-16 for Calibration II.

Points on samples	Frequency
1	0.05
2	0.1
3	0.2
4	0.5
5	1
6	2
7	3
8	4
9	5
10	7
11	8
12	9
13	10
14	12
15	16
16	20

Table 3: Frequencies used at points 1-16 for Calibration II.

c. Systematic testing

The set of experimental variables in the macro-scale dynamic mechanical testing includes sample concentration, frequency, amplitude and mean depth (pre-strain). Because the samples contain a significant amount of water, it is recognized that the age of the sample (measured by number of days after formulation) is also significant. It was verified that the temperature does not change drastically in the laboratory over a period of four days and so this was not regarded as a significant variable. The systematic tests involved all nine formulations, each tested at four frequencies, two amplitudes and two mean depths on the first and fourth days after formulation. The frequencies used were 1, 4, 8 and 10 Hz, the amplitudes 30microns (A1) and 75microns (A2), and the mean depths 75microns (M1) and 330 microns (M2). Table 4 summarizes the protocol carried out on each of the nine formulations on Day 1 and Day 4 after formulation, giving a total of 288 tests.

Points on sample	Systematic tests-Variable combination
1	1hz+M1+A1
2	4hz+M1+A1
3	8hz+M1+A1
4	10hz+M1+A1
5	1hz+M1+A2
6	4hz+M1+A2
7	8hz+M1+A2
8	10hz+M1+A2
9	1hz+M2+A1
10	4hz+M2+A1
11	8hz+M2+A1
12	10hz+M2+A1
13	1hz+M2+A2
14	4hz+M2+A2
15	8hz+M2+A2
16	10hz+M2+A2

Table 4: Experimental protocol for each formulation (carried out on Days 1 and 4).

III. Results and analysis

a. Calibration I (mean depth and ageing)

Figures 6 and 7 summaries the results for Calibration 1, tests 1-4 where it appears that the mean value, as expected, has little effect on the amplitude ratio or the phase difference. It is, however, noticeable that, whereas there is little systematic change in either measure over the first three days, both the amplitude ratio and the phase are significantly higher on Day 4.

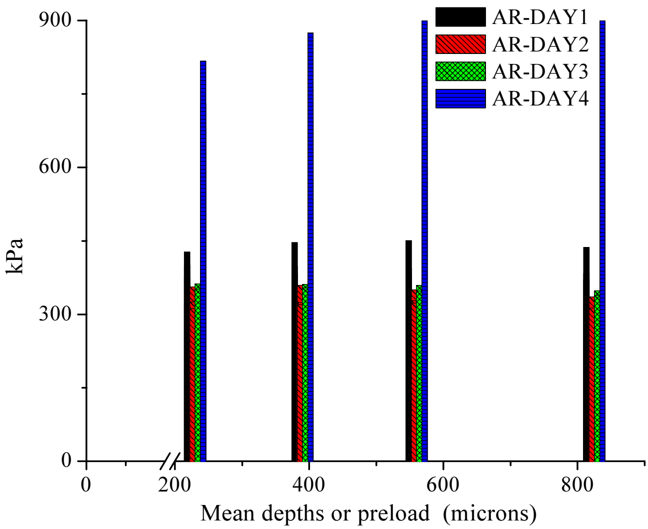

Figure 6: Calibration I, tests 1-4. Amplitude ratio for each mean value.

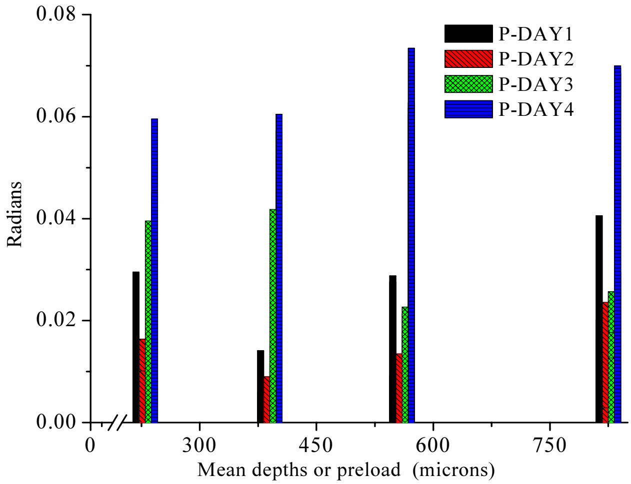

Figure 7: Calibration I, tests 1-4: phase lag for each mean value.

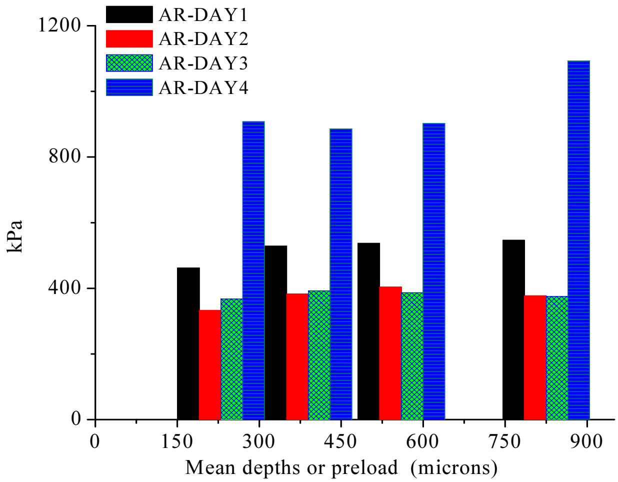

Figure 8: Calibration I, tests 5-8: amplitude ratio for each mean value.

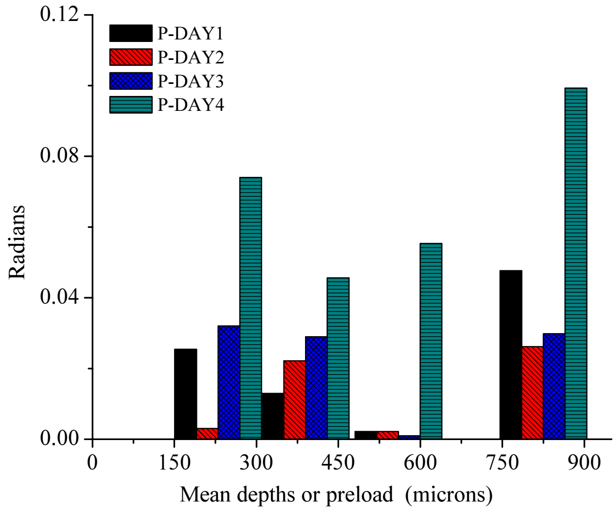

Figure 9: Calibration I, tests 5-8: phase lag for each mean value.

Similarly, Figure 8 and 9 confirm that there is no clear systematic effect of mean value on either amplitude ratio or phase, and confirm that there is a considerable increase in both on Day 4. Figure 10 (no variation in mean depth) shows the amplitude ratio values on a given day to be highly repeatable with a slight decrease in Days 2 and 3 followed by the sharp increase in Day 4. Finally, Figure 11 shows the phase values to be more variable than the amplitude ratio, but confirm the slight decrease in Days 2 and 3 followed by the marked increase on Day 4. The literature on ageing of gelatin (e.g. Hall et al [3] and Ferry, 1948, cited in [5]) would tend to suggest that any changes due to continued hardening processes are modest after the first 10-30 hours, and that any increases are steady. It is therefore likely that the increase from Day 3 to Day 4 is due to dehydration of the gel.

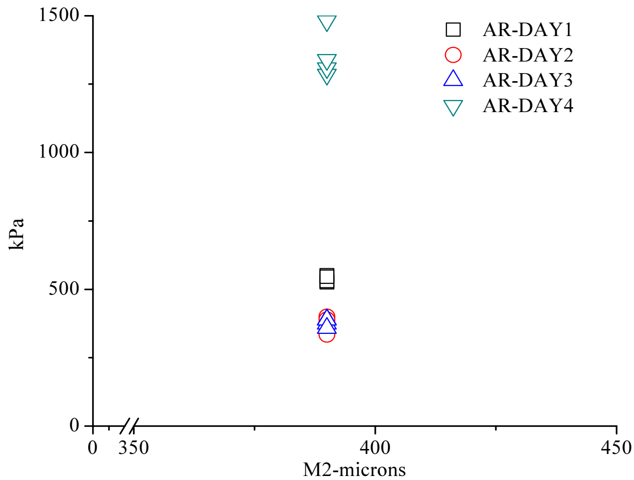

Figure 10: Calibration I, tests 9-12, amplitude ratio.

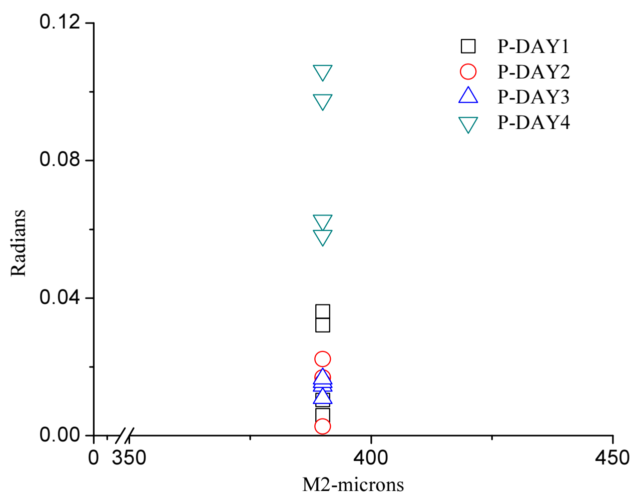

Figure 11: Calibration I, tests 9-12, phase lag.

b. Calibration II (effect of frequency)

The purpose of this calibration was to try to find a frequency range within which the gels displayed some interesting dynamic properties and so a wide range was chosen, the results being summarized in Figures 12-14 for the amplitude ratio, phase difference and mean ratio, respectively. Leaving aside the first two points in Figures 13 and 14, assumed to have been affected by the same equipment factors as the rest of the low frequency measurements, it seems that the phase lag exhibits a drop towards a frequency of around 8 Hz, followed by an increase between 8Hz and 20 Hz, with very little effect of ageing. The remaining two curves (mean ratio and amplitude ratio) are rather similar in shape, showing a very modest increase in the Day 1 results with frequency, along with a slightly more pronounced increase in the Day 4 results. Consistent with earlier observations, the Day 4 values at a given frequency are about a factor of two higher than those measured at Day 1.

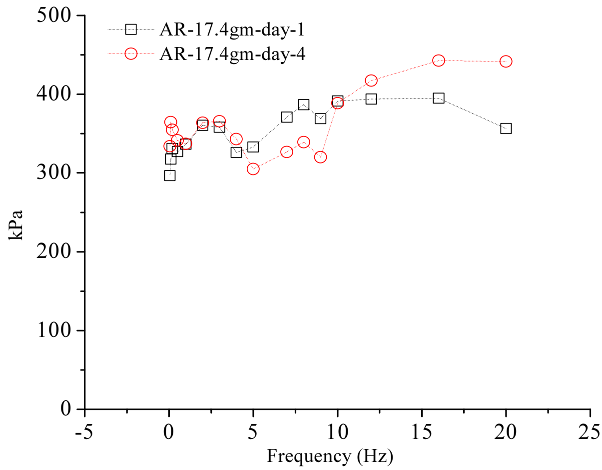

Figure 12: Calibration II; effect of frequency on amplitude ratio

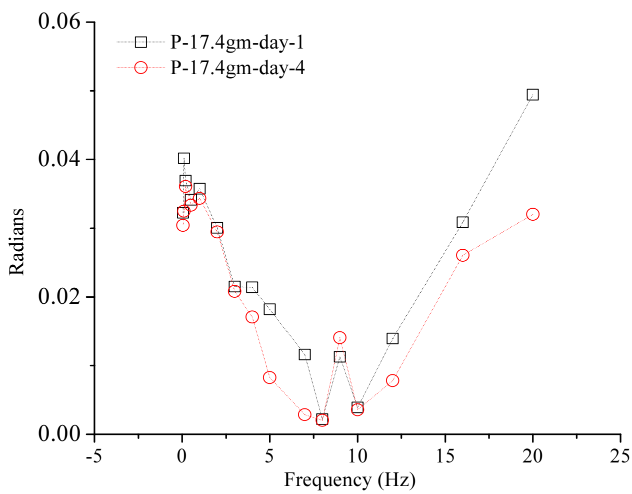

Figure 13: Calibration II; effect of frequency on phase lag

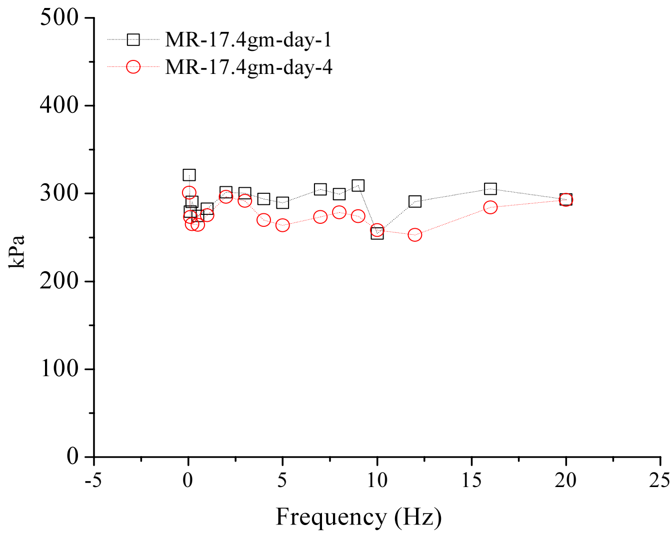

Figure 14: Calibration II; effect of frequency on Meanratio

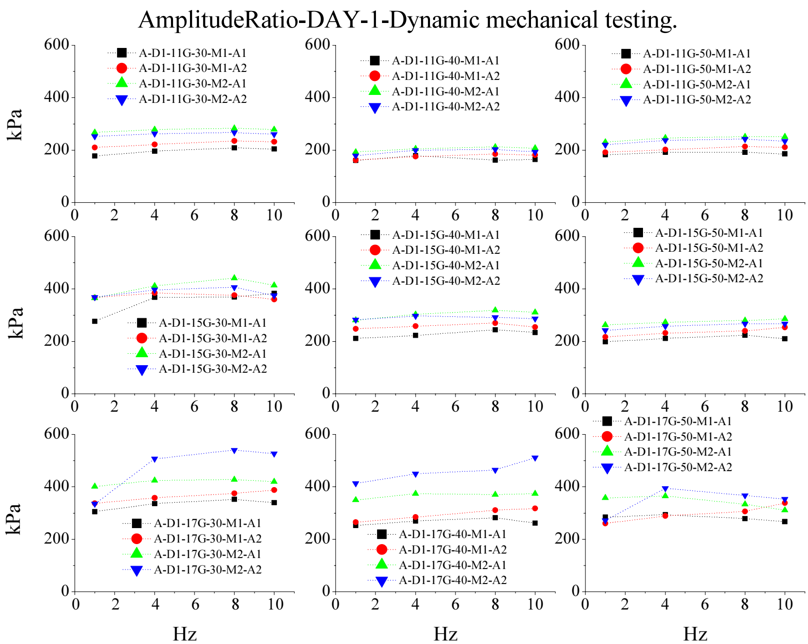

Figure 15: Systematic test results for amplitude ratio on Day 1

c. Systematic Testing

The systematic tests results are arranged in Figures 15 to 20 inclusive, as 3 × 3 sets of graphs in which the gel strength increases from top to bottom and the oil fraction

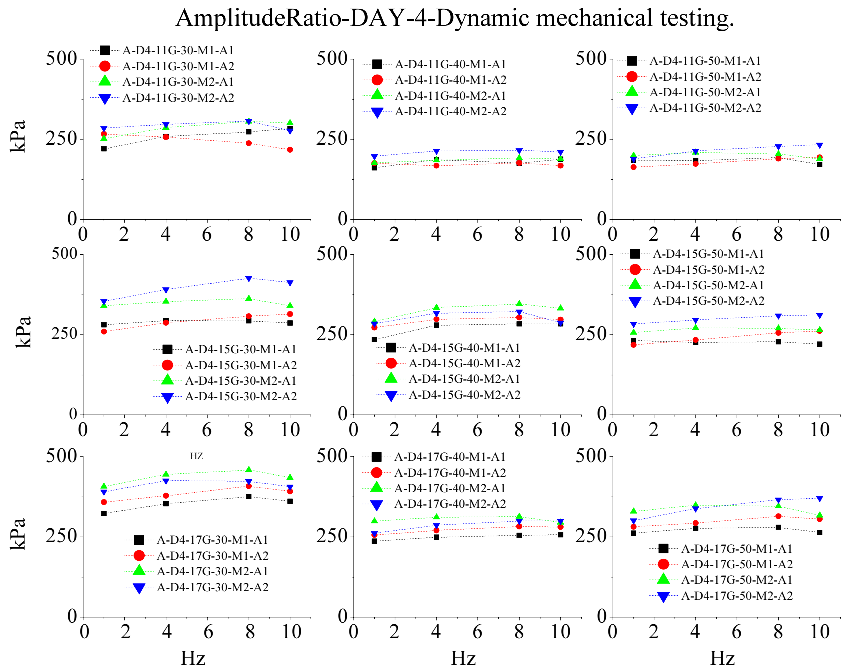

Figure 16: Systematic test results for amplitude ratio on Day 4

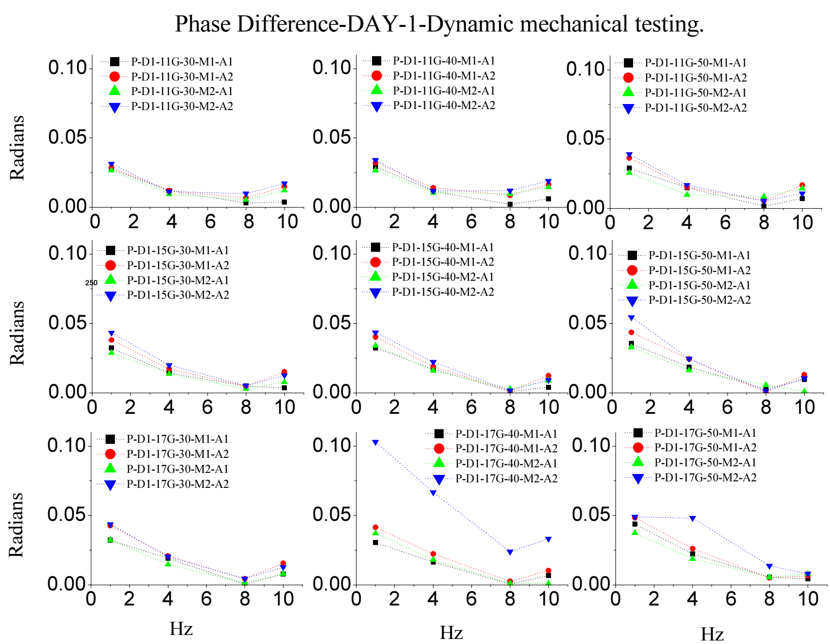

Figure 17: Systematic test results for phase difference on Day 1

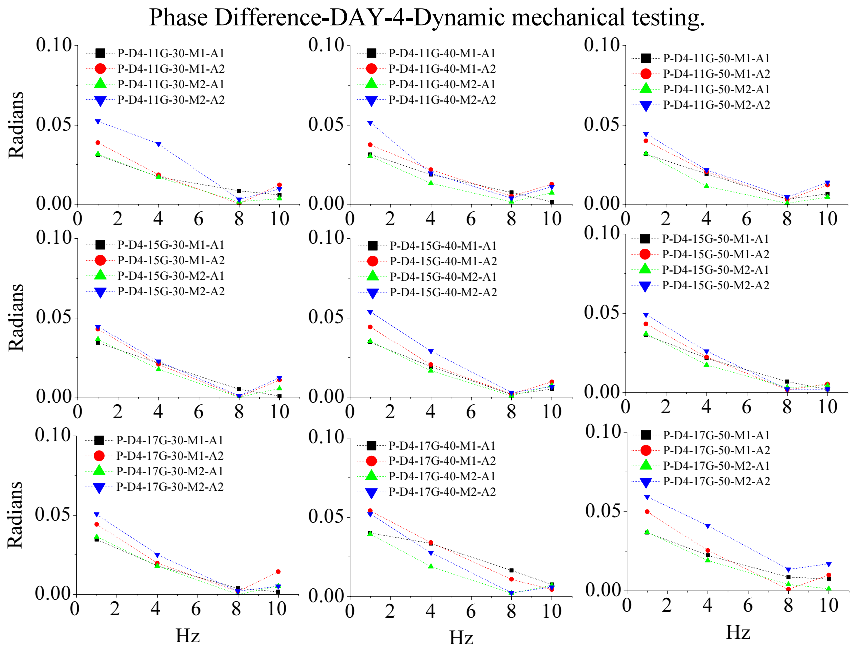

Figure 18: Systematic test results for phase difference on Day 4

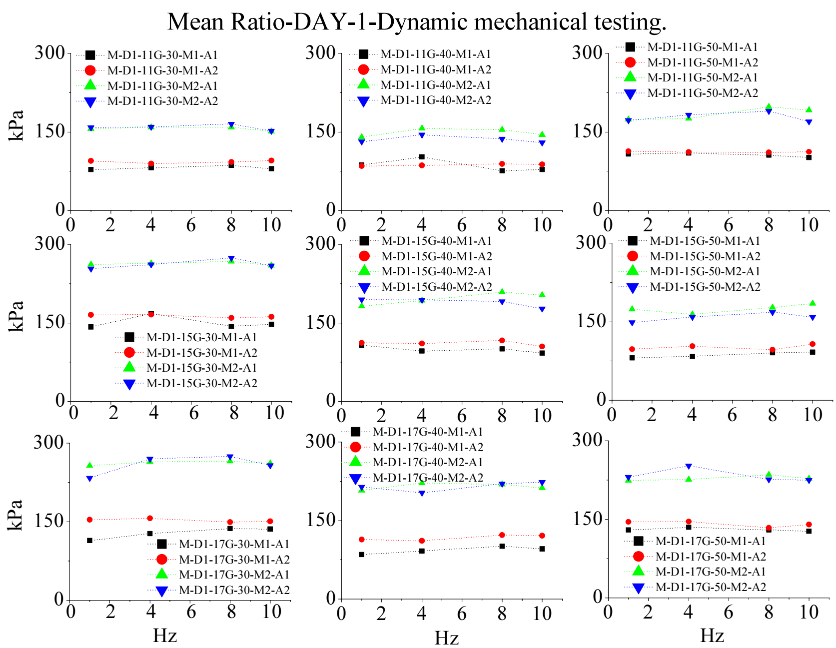

Figure 19: Systematic test results for mean ratio on Day 1

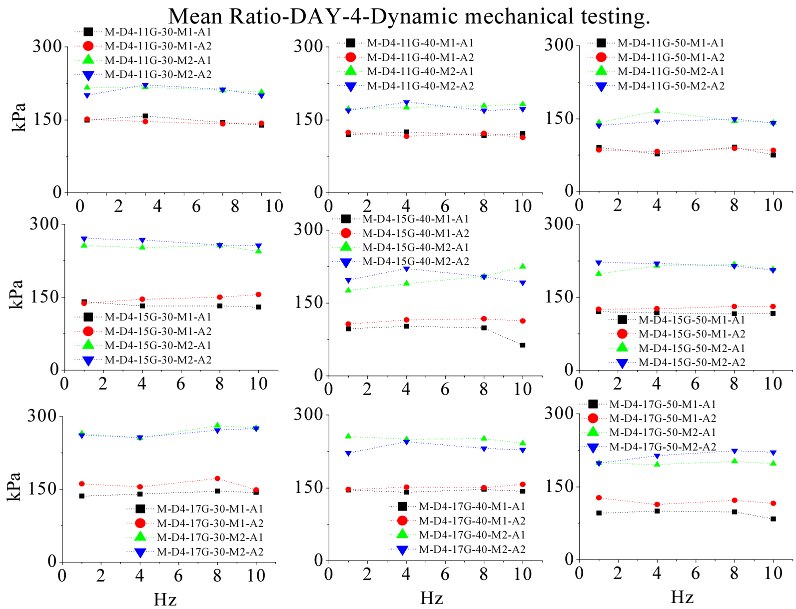

Figure 20: Systematic test results for mean ratio on Day 4

increases from left to right. Figures 15 and 16 summarizes the amplitude ratio data, Figures 17 and 18 the phase difference, and Figures 19 and 20 the mean ratio. A coding system is used to identify each set of points, the example of the top line in the top left graph in Figure 15, A D1 11G 30 M1 A1, being explained in Table 5.

A	Data feature, here amplitude ratio, similarly P for phase difference and M for mean ratio.
D1	Day on which the experiment was performed, here Day 1.
11G	Gel concentration in grammes per 100ml of de-ionized water.
30	Amount of oil in milliliters per 100ml of gel solution.
M1	Mean depth, here M1 (75 microns).
A1	Amplitude, here A1 (30 microns).

Table 5: Data coding system used in Figures 15-20

A few general observations are possible one the results as presented. Firstly, the amplitude ratios show a similar trend in both Day 1 and Day 4 data, the value generally changing only modestly, if at all with frequency, and higher oil fractions leading to a reduction in level, whereas higher gel strengths lead to an increase in level. The phase values, again irrespective of ageing, all tend to decrease with frequency, some increasing again between 8 and 10 Hz. Finally, the mean ratios show very similar behaviour to the amplitude ratios.

The matrices can be further understood in terms of the gel formulation by reference to Table 6, which shows the gel:oil ratio for each member of the 3 × 3 matrix.

Gel:oil ratio	Oil-30ml	Oil-40ml	Oil-50ml
Gel-11.4g/100ml	0.38	0.285	0.228
Gel-15.4g/100ml	0.51	0.385	0.308
Gel-17.4g/100ml	0.58	0.435	0.348

Table 6: Gel:oil ratio for matrix in Figures 15-20

As an example, Figure 21 shows the Day 1 amplitude ratio data plotted against gel:oil ratio, and it is clear that there is a systematic effect of this ratio and that it is stronger than the effect of frequency. The plots for Day 4 and for mean ratio show similar trends.

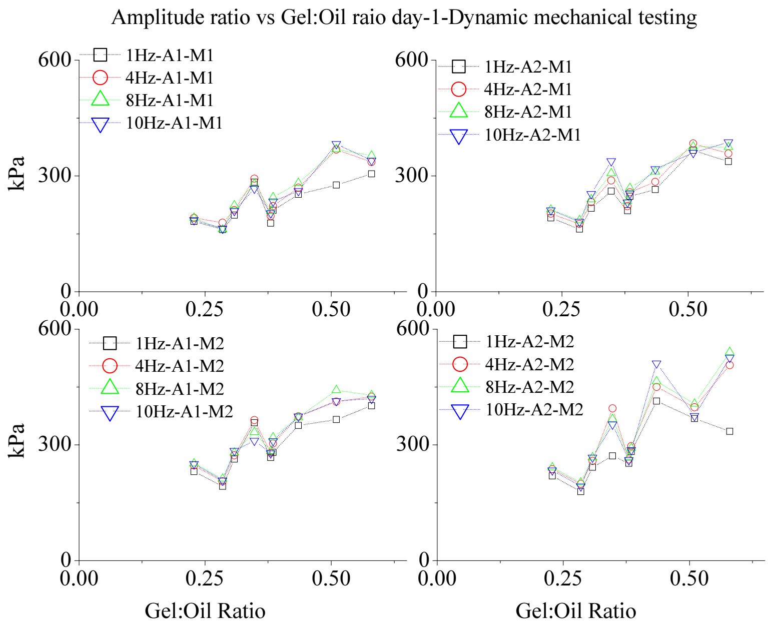

Figure 21: Effect of gel:oil ratio on amplitude ratio

By contrast, the effect of gel:oil on the phase lag is relatively modest as can be appreciated from Figure 22 which shows the best-fit straight line through the data points and the intercepts on the x- and y-axes can be used to highlight the effect of gel:oil ratio along with Table 6.

Average phase difference slope comparison day-1 and day-4-Dynamic mechanical testing

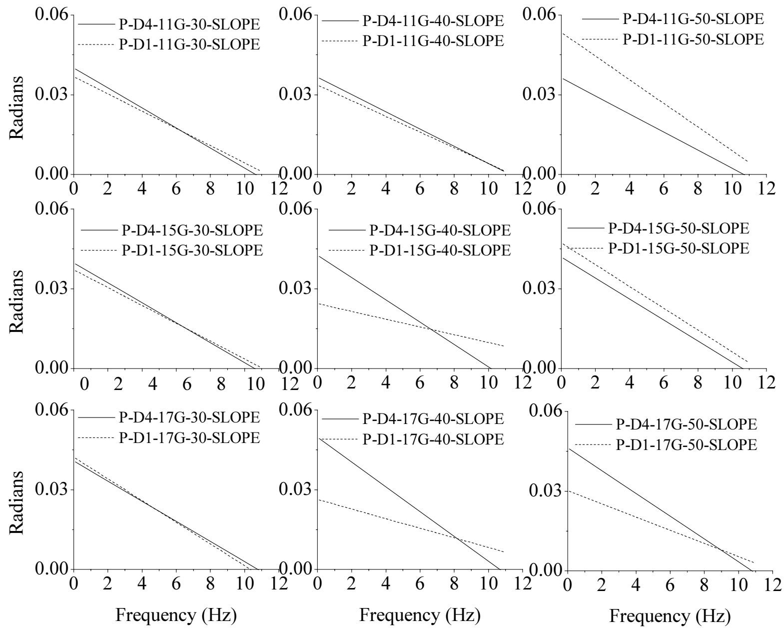

Figure 22: Simplified phase plots to highlight effect of gel:oil ratio

IV. Conclusions and future work

In terms of the general values of elastic modulus, the results are in broad agreement with published values of gelatin [3] and gelatin-based heterogeneous phantoms [4] but, tend to be slightly higher. This is probably attributable to the fact that the strain and stress have been assumed to be uniform in the sample. The dynamic values are, however, contrast with measurements made by Yang [6] on pure gelatin where the phase lag increased with frequency between 5 and 40 Hz and the amplitude ratio decreased very slightly over the same frequency range, but are more in accord with Yang's measurements on synthetic sponge material reinforced with gelatin. It can be concluded, therefore, that the mimic materials have some dynamic properties worthy of measurement in the frequency range tested, although it may be worthwhile to investigate lower frequencies if the rig limitations can be overcome.

The immediate future work will be to test biological samples consisting of varying proportions of collagen and lipid using the same protocol as reported here.

V. References

[1] S. Phipps, T.H.J. Yang, F.K. Habib, R.L. Reuben and S.A. McNeill. "Measurement of the mechanical characteristics of benign prostatic tissues: A novel method for assessing benign prostatic disease", Urology, 65(5) (2004), 1024–1028.

[2] V.Lakshmanan, T.H.J. Yang, R.L. Reuben, J. Hammer, R. Else. “Multi-scale Techniques of Measuring the Dynamic Properties of Soft Biological Tissue”, Technology and Healthcare, 13 (2006), 297-309.

[3] T.J. Hall, M. Bilgen, M.F. Insana and T.A. Krouskop. “Phantom Materials for Elastography”, IEEE Transactions on Ultrasonics, Ferroelectrics, and Frequency Control, 44(6) (1997), 1355–1365.

[4] E.L. Madsen, G.R. Frank, T.A. Krouskop, T. Varghese, F. Kallel and J. Ophir. “Tissue-mimicking oil-in-gelatin dispersions for use in heterogeneous elastography phantoms”, Ultrasonic Imaging, 25 (2003), 17–38.

[5] A.G. Ward and A. Courts. “The science and technology of gelatin”, Academic Press, London (1977).

[6] T.H.J. Yang. “Structure-property relationships in biological tissues”, PhD Thesis, Heriot-Watt University, 2007.

Medicine Meets Engineering
J. Hammer et al. (Eds.)
IOS Press, 2008

Imaging of Tissue Structures and Mechanical Analysis

Peter F. NIEDERER
Institute of Biomedical Engineering University of Zurich and Swiss Federal Institute of Technology Zurich Gloriastrasse 5 CH-8092 Zurich, Switzerland
niederer@biomed.ee.ethz.ch

Abstract. The anatomical structure of biological tissues and their mechanical function are closely related. Forces have a decisive influence on growth and remodeling of tissues; furthermore, intra- and extravascular transport processes are mostly controlled mechanically and the metabolism of many cells is influenced by flow-induced shear stresses. In order to facilitate a mechanical analysis of biological systems, the anatomical tissue structure has to be determined with the aid of 3D imaging methods. In particular, the anisotropic fibrous architecture of the organs involved along with appropriate constitutive relations have to be considered. Examples of structure-(mechanical) function relationships are discussed in an exemplary fashion for bone, the heart and the uterus. The behavior of biological structures under unphysiological loading situations, such as they may occur in accidents, is addressed.

Keywords: Biomechanics, Tissue Structure, Tissue Mechanics, Organ Dynamics

Introduction

All forms of life are exposed to mechanical loads throughout their existence. Besides field forces, in the first place due to gravity, there is a great variety of forces acting on the human body, animals or plants from contacts with the surrounding; in addition, numerous forces are generated in the course of physiological processes inside the different organs and tissues. As a consequence, the physiology and pathophysiology of biological systems have largely been adapted through evolution to mechanical interactions, such that anatomical structure and mechanical function are closely related. E.g., bones are structured such as to allow for body support, motion and protection of organs. The fiber architecture of the mammalian ventricles is optimized towards the ejection of blood upon stimulation. The cartilage layer in joints is organized such that large loads can be carried while friction is negligibly low. Many other examples can be found, not only in humans and animals, but also in plants.

Much effort in biomechanics is devoted to the analysis of organ and tissue structure as it relates to mechanical function. Both aspects, i.e., structure and mechanical function are of equal importance; the connection between the two is thereby provided by constitutive relations. The formulation of such relations is not straightforward at all; it depends on the possibility to perform force-deformation measurements on intact tissues and organs under physiological conditions which in turn requires imaging and mechanical analysis.

With respect to structure, a particular problem arises because a useful analysis requires a representation in 3-dimensional space. Classical histology, however, is mostly based on 2-D microscopy from which the derivation of a spatial tissue pattern is not an easy task. With the advent of novel imaging procedures which enable the non-destructive recording of tissue architecture, the internal structure of tissues, in particular their anisotropic character became more readily accessible. X-ray Computed Tomography (CT) and Magnetic Resonance Imaging (MRI) are the primary methods for this purpose although microscopic resolution is by far not reached thereby.

Regarding mechanical function, biological tissues can be characterized as composites consisting of numerous constituents that exhibit each a largely different nonlinear, viscoelastic and anisotropic behavior. As a rule, furthermore, biological tissues are fluid-filled such that they are mostly incompressible under physiological pressures. Because of arterial, venous and lymph flow, however, volumes are nevertheless not constant in time. Geometry is irregular. In view of all of these conditions, it is not astonishing that analytical procedures are limited to special cases where in part crude approximations are made. In general, a numerical approach is necessary.

In spite of the enormous complexity of biological tissues (or maybe in fact because of it), approximations based on continuum mechanics have proven to be useful for many tasks involving a mechanical analysis. For the numerical treatment of such problems, there exist basically three methods, viz., (i) finite difference methods, (ii) finite element techniques and (iii) particle-oriented approximations.

(i): The partial differential equations associated with continuum mechanics are discretized and differential quotients are replaced by difference quotients. Although many practical problems can well be solved in this fashion (finite difference methods are e.g. in widespread use in electric field theory), only sparse applications can be found in the biomechanics' literature.

(ii) The Finite Element (FE) technique is presently found to be the method of choice in biomechanics for the treatment of problems that are described in the form of continuum mechanical approximations. Examples will be shown in the following.

(iii) Particle-oriented methods [1] were originally developed in astrophysics from where they found their way first into fluid mechanics ("soft particle fluid dynamics"), now increasingly also into biomechanics, e.g., [2]. Such methods are particularly well suited for real-time applications, such as surgery simulators [3, 4], where the remeshing problem largely limits the use of finite difference or finite element schemes [5].

Continuum mechanics offer the advantage that covariant constitutive formulations can be found which are needed to treat problems where large deformations and displacements occur. A disadvantage in turn derives from the fact that the complex microscopic composition of biological tissues is mostly not reflected in continuum approximations. With increasing computational power and concurrently better knowledge of the constitutive properties of individual tissue components, however, it can be expected that formulations based on tissue composition (structured continua) will more and more be found.

A distinction is often made in biomechanics between "soft" and "hard" tissues. As a thumb rule, the Young's modulus (within the framework of a linear elastic simplification) for soft tissues covers a range of some 10 kPa up to several 100 kPa, while for hard tissues it is typically two orders of magnitude higher. While there are numerous kinds of soft tissues, hard tissue appears essentially in calcified form, in particular as bone. Thereby, the calcium is contained in hydroxyapatite crystals [Ca5 (PO4)3 OH] which are embedded in a collageneous matrix.

An important aspect of numerical modeling is related to model validation which includes an assessment of the sensitivity of the model with respect to the geometrical and constitutive parameters. For complex models which include many different parameters, a large number of simulations may be necessary in order to establish the reliability of the results. In case that a model exhibits an excessive dependence on the value of a particular parameter, simulations are only meaningful if the parameter in question can be determined with sufficient accuracy.

In what follows, three examples of tissues are demonstrated where a mechanical analysis was made after the anisotropic anatomical structure had been determined with imaging methods, viz., bone, the heart and the uterus. A short outlook is given into trauma-biomechanics which involves the analysis of the response of biological structures to unphysiological, possibly harmful loading situations.

1. Bone

The hard tissue of the human body is represented in the skeleton. On the one hand, bones support the body, facilitate motion and protect organs, on the other, they serve as a reservoir for calcium. Bone exists in various forms: Cortical bone makes up the shaft (diaphysis) of the long bones as well as the outer layer of other bones while trabecular or cancellous bone is located mostly in the medullary canal of long bones, particularly in regions close to joints (epiphysis and metaphysis) as well as in the spine and in bones whose primary task is not to support loads (e.g., skull, iliac crest). The metaphysis denotes the zone of growth between the dia- and epiphysis of young bones. The terms Haversian bone and woven bone, in turn, refer to the internal structure of the bone material. Haversian bone consists of cylindrically shaped osteons which along their longitudinal axis exhibit a canal (Haversian canal), whereas woven bone grows during growth and healing processes. For a more detailed description of bone, the reader is referred to the literature e.g., [6].

The ability to fulfill the supporting and stabilizing function of the human body adequately, i.e., the capacity to withstand mechanical loads and enable motion, is often denoted as "competence of bone" or associated with the term "bone quality" [7-9]. Typical incidents which are observed in case of insufficient competence or bone quality are a fracture of the femoral head, a fracture of the wrist or a collapse of a vertebra

(Figure 1). In the case shown, a cervical vertebra collapsed due to osteoporosis causing pain and spinal instability. As can be seen from the dates of the X-ray projections, such a collapse is a rather rapid, sudden process and does not necessarily extend over long periods of time; this is in contrast to degradation associated with loss of competence of the skeleton which may progress over years [10].

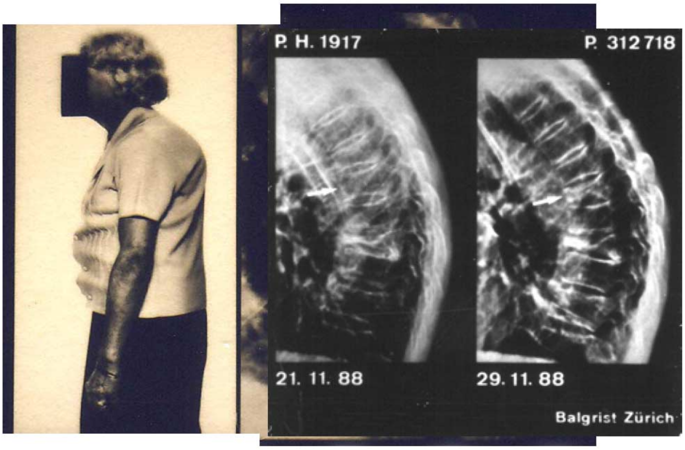

Figure 1. Collapse of a cervical vertebra in an elderly woman suffering from osteoporosis. Note the date of the two examinations (Courtesy: M. Dambacher, Balgrist Orthopedic University Hospital, Zurich).

The capacity of bone to support forces without damage is by definition a mechanical property and can accordingly be assessed on the basis of a mechanical analysis. To this end, the internal structure of load-bearing bones has to be known with an accuracy that allows to model among other the trabecular network. X-ray computed tomography is the method of choice for bone imaging, since bone is intransparent for ultrasound and MR signals from hard tissues cannot be recorded with present technology (the complement, i.e. the tissues surrounding bony structures however can, thereby allowing an imaging of hard tissues by highlighting locations without MR response). Limitations with respect to radioactive exposure limit the application of high-resolution CT in humans to peripheral bones (pQCT, peripheral quantitative computed tomography [11]).

Figure 2 exhibits a high resolution CT image of a wrist. The fact that deformations of mature load-bearing bones under physiological loading conditions (and beyond up to the yield limit) are small permits the application of a linear analysis. In case that a static situation is modeled, furthermore, viscoelastic effects can be neglected. Hooke' law is therefore adequate for such models. A large amount of degrees of freedom is however required, when an analysis based on Finite Elements is made (Figure 3).

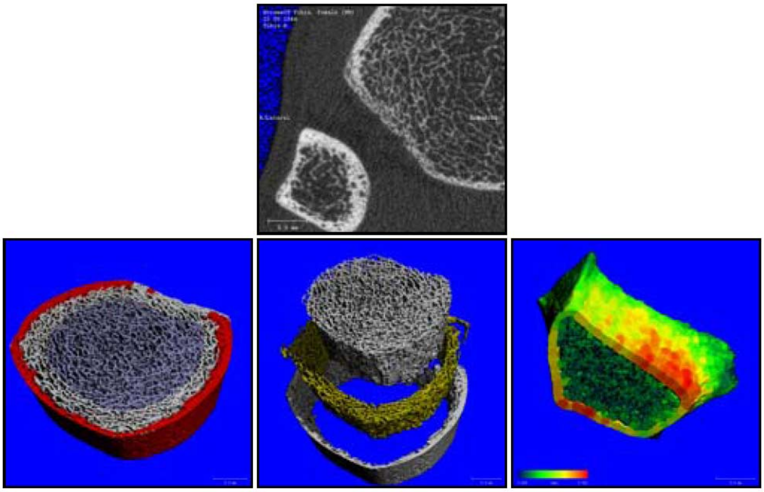

Figure 2. Peripheral Quantitative Computed Tomography (pQCT). The CT image including segmentation shows a human wrist with a spatial resolution of better than 100µm (Scanco Medical, Switzerland).

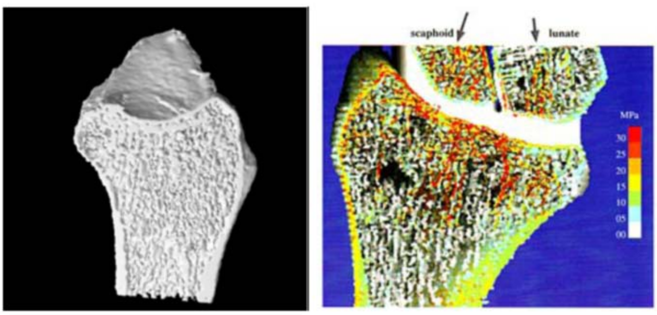

Figure 3. Finite Element (FE) analysis of human wrist. Von Mises stress (color-coded) was calculated under a hypothetical load on the hand due to a fall. Locations with increased fracture risk are highlighted in red.

Locations exhibiting excessive stresses in a load case mimicking a fall on the hand (a situation often leading to a Colles fracture) become clearly visible. In this highly dynamic situation viscoelastic contributions are however important, although nevertheless small. Within the framework of the ADOQ project (Advanced Detection of Bone Quality, [http://www.medes.fr/home_fr/applications_sante/osteoporose/adoq.html]) a large number of such analyses are being prepared in order to assess the relation between bone quality, mineral content and structure.

2. Heart

From a mechanical point of view, the mammalian heart is characterized by the interplay and cooperative action of four chambers, viz., the two atria and the two ventricles. Structure and function are in particular closely related in case of the two ventricles which have a common fibrous structure. This property lead several researchers in the past to seek special structural features associated with the architecture of the myocardium.

The left and right human ventricles are thick-walled and the internal structure of the ventricular walls has been described and interpreted in various forms in the literature [1215] supported the widely accepted concept that the human myocardium presents itself as a uniform continuous structure consisting of myocytes, connective tissue, blood vessels and interstitial fluid (Figure 4). The myocytes are multi-branched and organized in myocytic aggregates, which are interconnected among them longitudinally as well as laterally in various degrees of density and by a complex hierarchy of connective tissue. Although the global architecture of the healthy ventricles exhibits a well-organized structure, there are marked local and individual inhomogeneities throughout the ventricular wall. In addition, there are countless short gaps bridged by scarce branching between myocytes interspersed throughout the myocardium which facilitate relative movement between the myocardial aggregates throughout the heart cycle [16,17]. The size and orientation of these gaps are highly variable.

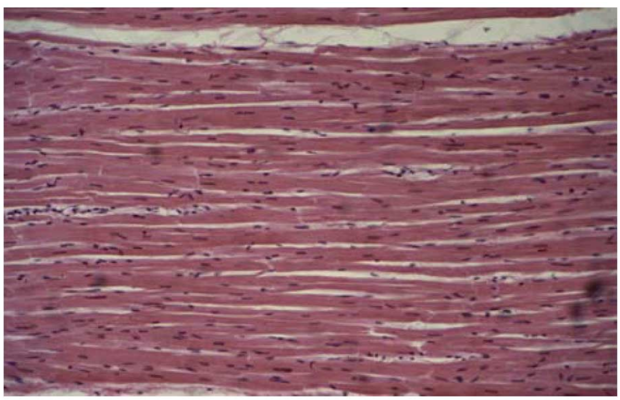

Figure 4. Healthy human myocardium (magnification 200). Note that a 2D section used for microscopic preparation is shown. Numerous out-of-plane branching connections were thereby destructed; the structure in fact extends in all three dimensions.

Both ventricles are subjected to large deformations during the cardiac cycle. According to biaxial tests performed by Smaill and Hunter [18] on thin myocardial sections from the left ventricle of dogs, the cardiac tissue can be stretched up to extensions of 15−25 percent in the direction of the myocytic aggregates and up to extensions of 60−80 percent in the perpendicular direction. The difference in the mechanical behavior of the heart between the two directions characterizes the anisotropy of the passive myocardium. While in the absence of active contractile forces during the diastolic filling process, the anisotropy is of a structural nature and its influence is of a secondary importance only [19,20], during systolic contraction, the anisotropy is prominent.

The myocytic aggregates in the ventricular wall are oriented such that the ejection of blood is optimally supported upon contraction. Nevertheless, the determination of fiber orientation in the beating heart is presently not (yet) possible with adequate spatial resolution. Excised hearts, in turn, are amenable to destructive analysis (peel-off technique [21]) or noninvasively to Magnetic Resonance Diffusion Tensor Imaging (MR-DTI [22]). Figure 5a exhibits the results of a peel-off analysis of a post mortem human and of MR-DTI imaging (Figure 5b) of an excised pig heart.

The large deformations which the heart undergoes during systolic contraction require the application of large deformation Finite Element methods. In addition, active contraction has to be included in the constitutive model. This can be achieved in a covariant fashion by adding time-dependent increasing stresses to the second Piola-Kirchhoff stress tensor (Figure 6 [23]). Diastolic filling, in turn, is largely governed by viscoelastic recoil which sets in after mitral vale opening in the still mechanically contracted, although physiologically relaxed myocardium. Deformation energy is thereby released causing the rapid filling phase during early diastole [24, 25].

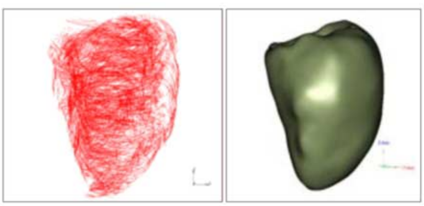

Figure 5a. Fiber architecture of a post mortem human heart obtained by peeling fiber strands (left) and epicardial surface (right).

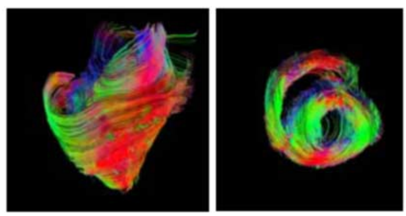

Figure 5b. Fiber architecture of an excised pig heart using MR Diffusion Tensor Imaging.

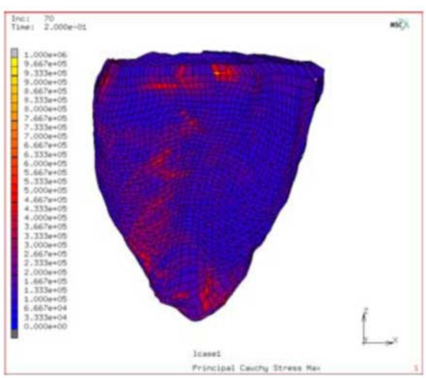

Figure 6. FE analysis of systole. By addition of stepwise increasing components to the Piola-Kirchhoff stress tensor, systolic contraction was modeled using the anisotropic fibrous structure shown in Figure 5a (left).

3. Uterus

The uterus is an organ with a number of particular properties. First, it undergoes a regular monthly cycle during the fertile years of the women. It builds up slowly and continuously in between menstruation periods and reduces its size rapidly during menstruation. Second, during pregnancy it serves as housing for the fetus and ascertains its healthy development.

A third function is performed by the uterus during delivery, when its muscular characteristics become prominent. Fourth, after the menopause, the uterus looses its function largely and develops itself into a gradually less compliant tissue. In view of these properties it is not astonishing that the uterus exhibits an extraordinary amount of biological variability throughout life (Figure 7). This may also be the reason why the fibrous architecture of the uterus along with its constitutive properties have been examined to a quite lesser degree than in other organs.

The fiber structure of the uterus has in fact been the subject of two quite different representations for many years. While according to Görttler [26] the uterus consists of two counterrunning systems of spirally shaped fibers, Wetzstein and Renn [27] described a more complex composition. In their studies, they found a spatial fibrous network without preferred direction in the middle layer of the uterine wall (stratum vasculare). The inner layer (stratum subvasculare), in turn, exhibited circularly oriented fibers, whereas the outer layer (stratum supravasculare) was arranged in four small tiers.

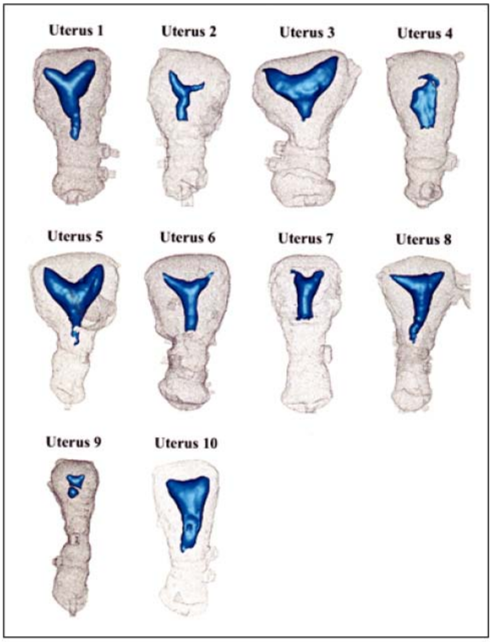

Figure 7. CT images of various excised human uteri. Note the enormous biological variability.

Recently, MR-DTI measurements allowed documenting the global fiber structure in the intact, excised uterus (Figure 8 [28]). While examining this picture, it has to be borne in mind, as mentioned in the introduction, that the investigations mentioned above (i.e., Görttler, Wetzstein and Renn) were derived from histology with microscopic resolution, while MR-DTI represents an approach on a macroscopic level. Little is furthermore documented in the literature with respect to the mechanical properties of the uterine tissue, all the more as these are subject to large variations likewise through the menstrual cycle as well as through life.

Endoscopic hysteroscopy is a procedure which is often performed in gynecology. As an initial step to facilitate an unimpeded vision in the intrauterine cavity, the latter is filled with saline under pressure such that it opens and enables the desired accessibility. This maneuver is denoted as hydrometra (Figure 9); typical pressures applied are around 20 kPa and the volume of saline delivered thereby amounts to several ml whereby this value exhibits a large individual variability.

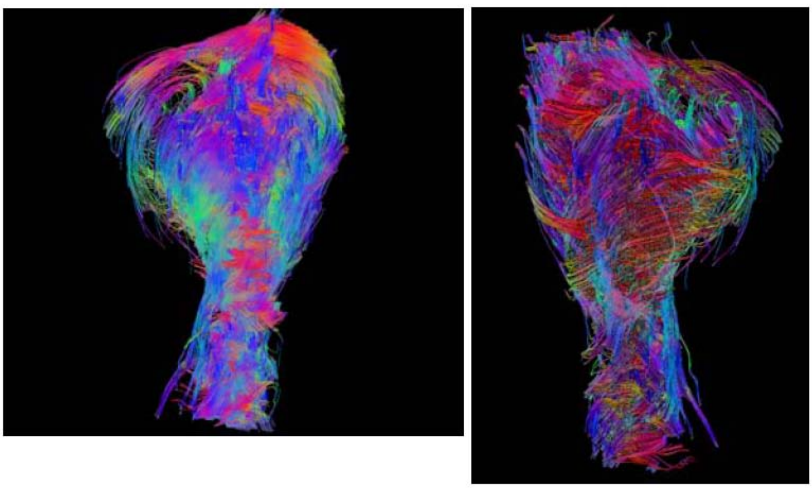

Figure 8. Fiber architecture of a human uterus determined by MR Diffusion Tensor Imaging.

The simulation of hysteroscopy is e.g. needed for virtual-reality based surgical simulators for demonstration and training purposes. For such an application, models running in real time are however required which allow virtual cutting, suturing, bleeding, etc. Given present computing capabilities, the numerical procedures described so far are not feasible. Radical simplification are necessary, e.g. in the form of mass-spring-damper combinations. Such models need calibration and validation, however, and to this end an accurate, off-line simulation by way of Finite Elements is useful.

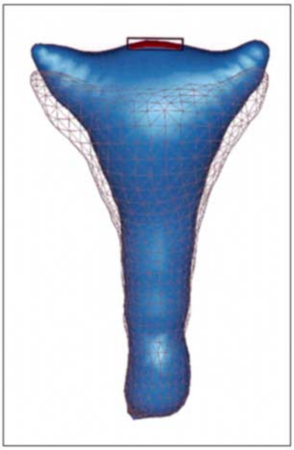

Figure 9. Mathematical model (FE) of hydrometra.

4. Structure and Accidental Loading

Trauma-biomechanics, i.e., the analysis, prevention and mitigation of accidents and injuries caused by accidental loading is an important discipline of biomechanics. Since experiments with living humans under mechanical exposure regimes which are prone to produce injuries are excluded, numerical simulation, among other, is of particular usefulness. From a structure-function related point of view, it is of interest to investigate how a biological structure behaves under the impact of forces which are unphysiological with respect to size and orientation, possibly beyond mechanical tolerance limits and which involve load cases for which it is not primarily adapted.

An example is seen in Figure 10. It represents a lateral impact on a pedestrian by an automobile with a speed of 10 m/sec. A major question which is analyzed with the aid of such a model is the relation between injury risk, impact speed, post-impact pedestrian trajectory, vehicle front geometry and deformability. This is an example where the problem of parameter sensitivity is particularly important. The real impact configuration is subjected to a high variability with respect to pedestrian characteristics, vehicle geometry, impact direction, etc., all of which has to be taken into account in the simulation. Even a small change of e.g. the body height of the impacted pedestrian can change the impact dynamics largely. Von Mises stresses, in turn, depend primarily on the internal local structure of the area contacted by the vehicle front. An accurate representation of the anatomical details including the constitutive properties of the tissues are decisive (Figure 11). A large number of simulations in the form of comprehensive parameter studies has to be performed in order to derive useful conclusions. The influence of conflicting parameters, i.e., parameters which exhibit an opposite influence, in this case for example pedestrian height vs. vehicle front height have to be assessed carefully and the possibility of a nonunique solution to the posed problem has to be thoroughly evaluated.

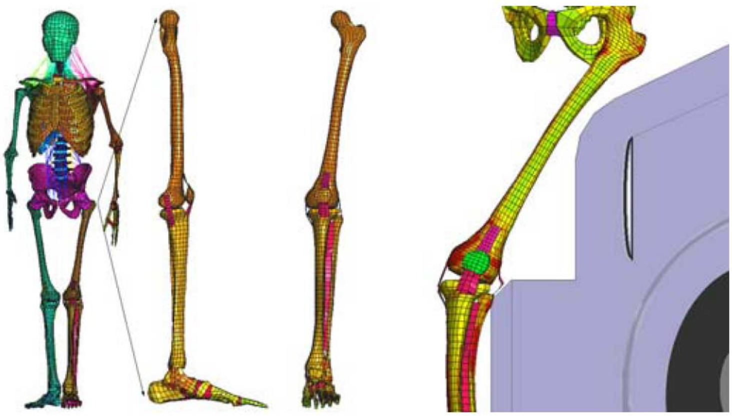

Figure 10. Lateral impact on a pedestrian by a vehicle front with 10 m/s, FE model.

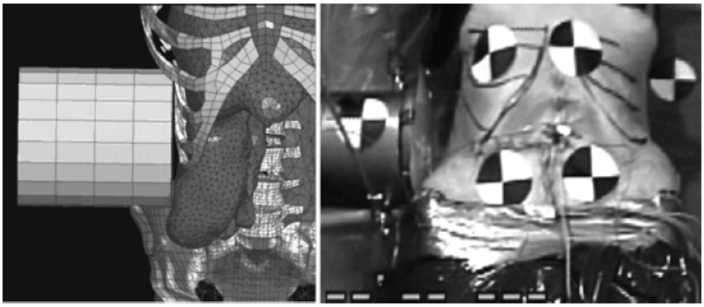

Figure 11. Blunt impact in the abdominal region. Left: FE model; right: corresponding measurement in a post mortem test object.

5. Conclusions

Substantial progress has been achieved through the last 20 – 30 years with respect to the noninvasive imaging of biological tissues. A documentation of the spatial fibrous tissue architecture has in particular become feasible. As a result, much effort in biomechanics is devoted to the analysis of the relation between organ and tissue structure on the one hand and mechanical function on the other. The connection between structure and function is thereby provided by constitutive relations that model the nonlinear, anisotropic and viscoelastic properties adequately. Yet, given the complex composition of biological tissues, this is not achieved in a straightforward manner. The formulation of such relations depends among other on the possibility to perform force-deformation measurements on intact tissues and organs under physiological conditions which in turn requires imaging and mechanical analysis.

In view of the dramatic increase in computational power, gradually more advanced numerical models can be formulated. Model validation and parameter sensitivity studies require concurrently an increasing amount of calculation efforts in order to produce reliable and useful results.

References

[1] M. Bergdorf, P. Koumoutsakos, A Lagrangian particle-wavelet method, *Multiscale Modeling & Simulation* 5 (2006), 980-995

[2] I.F. Sbalzarini, J.H Walther, B. Polasek, P. Chatelain, M. Bergdorf, S.E. Hieber, E.M. Kotsalis, P. Koumoutsakos, A software framework for the portable parallelization of particle-mesh simulations, *EURO-PAR 2006,* Parallel Processing, Lecture Notes in Computer Science 4128 (2006), 730-739

[3] G. Szekely, C. Brechbuhler, R. Hutter, A. Rhomberg, N. Ironmonger, P. Schmid, Modeling of soft tissue deformation for laparoscopic surgery simulation, *Medical Image Analysis* 4 (2000), 57-66

[4] S. Tuchschmid, M. Grassi, D. Bachofen, P. Fruh, M. Thaler, G. Szekely, M. Harders, A flexible framework for highly-modular surgical simulation systems, Biomedical Simulation, *Lecture Notes in Computer Science* 4072 (2006), 84-92

[5] R. Hutter, K.-U. Schmitt, P. Niederer, Mechanical modeling of soft biological tissues for application in virtual reality based laparoscopy simulators, *Tech. & Health Car*e 8 (2000), 15-24

[6] J.P. Bilezikian, L.G. Raisz, G.A. Rodan (eds.), *Principles of bone biology,* Academic Press, San Diego, 2002

[7] J. Dequeker, G. Vander Perre, C. Langton, Assessment of quality of bone in osteoporosis-BIOMED I: Fundamental study of relevant bone, *Clin. Rheumatol.* 13 Suppl. (1994), 7-12

[8] C. Chesnut, S. Majumdar, J. Gardner, A. Shields, D.C. Newitt, E. Erickson, M. Glott, A. Kriegman, L. Mindeholm, Assessment of bone quality, quantity, and turnover with multiple methodologies at multiple skeletal sites, *Adv. Exp. Med. Biol.* 496 (2001), 95-

[9] R. Müller, G.H. van Lenthe, Microarchitectural aspects of quality and competence of bone, *Adv. Osteoporotic Fract. Manag.* 3 (2004), 2-12

[10] D.N. Kahn, Bone, Handbook of Physiology, Sect. 11: Aging (E.J. Masoro ed.) *Am. Physiol. Soc.*, Oxford University Press, 1995

[11] P. Rüegsegger, A. Laib, 3D computed tomography - its contribution in the assessment of bone structure in vivo and in vitro, *J. Bone Miner. Res.* 15 (2000), 796

[12] H. Feneis, Das Gefüge des Herzmuskels bei Systole und Diastole, *Morph. Jahrb.* 89 (1943/44), 371-406

[13] W. Hort, Makroskopische und mikrometrische Untersuchungen am Myokard verschieden stark gefüllter linker Kammern, *Virchows Arch. Path. Anat. Physiol.* 333 (1960), 523-564

[14] D.D. Streeter Jr., Gross morphology and fiber geometry of the heart, Berne, R. M., Sperelakis, N., Geiger, S. R. (Eds.), *Handbook of Physiology, Section 2:* The Cardiovascular System, vol. 1. Am Physiol Soc, Bethesda, MD (1979) 61-112.

[15] P.M.F. Nielsen, I.J. LeGrice, B.H. Smaill, P.J. Hunter, Mathematical model of geometry and fibrous structure of the heart, *Am. J. Physiol.* 260 (1991), H1365H1378.

[16] I.J. LeGrice, Y. Takayama, J.W. Covell, Transverse shear along myocardial cleavage planes provides a mechanism for normal systolic wall thickening, *Circ. Res.* 77 (1995), 182-193

[17] K.D. Costa, Y. Takayama, A.D. McCulloch, J.W. Covell, Laminar fiber architecture and three-dimensional systolic mechanics in canine ventricular myocardium, *Am. J. Physiol.* 276 (1999), H595-H607

[18] B.H. Smaill, P.J. Hunter, Structure and function of the diastolic heart: material properties of passive myocardium, Glass L., Hunter P. J., McCulloch A. D. (Eds.), *Theory of Heart: Biomechanics, Biophysics and Nonlinear Dynamics of Cardiac Function*, Springer, New York (1991) 1-29

[19] P.H.M. Bovendeerd, J.M. Huyghe, T. Arts, D.H. van Campen, R.S. Reneman, Influence of endocardial-epicardial crossover of muscle fibers on left ventricular wall mechanics, *J. Biomech.* 27 (1994), 941-951

[20] P. Schmid, P. Niederer, P.P. Lunkenheimer, F. Torrent-Guasp, The anisotropic structure of the human left and right ventricles, *Tech. & Health Care* 5 (1997), 29-43

[21] P.P. Lunkenheimer, K. Redmann, N. Kling, X. Jiang, K. Rothaus, C.C. Cryer, F. Wübbeling, P. Niederer, Ph. Heitz, S.Y. Ho, R. Anderson, Three-dimensional architecture of the left ventricular myocardium, *Anat. Rec. Part A* 288A (2006), 565578

[22] P. Schmid, T. Jaermann, P. Boesiger, P.F. Niederer, P.P Lunkenheimer, C.W. Cryer, R.H. Anderson, Ventricular myocardial architecture as visualised in postmortem swine hearts using magnetic resonance diffusion tensor imaging, *Eur. J. Cardiothor. Surg.* 27 (2005), 468-472

[23] F. Dorri, P. Niederer, P.P. Lunkenheimer, A finite element model of the left ventricular systole, *CMBBE Comp. Meth. Biomech. Biomed. Eng.* 9 (2006), 319-341

[24] S.P. Bell, J. Fabian, A. Higashiyama, Z. Chen, M.D. Tischler, M.W. Watkins, M.M. LeWinter, Restoring forces assessed with left atrial pressure clamps, *Am. J. Physiol.* 270 (1996), H1015-H1019

[25] D.-E. Bettendorff-Bakman, P. Schmid, P.P. Lunkenheimer, P. Niederer P, A finite element study relating to the rapid filling phase of the human ventricles, *J. Theor. Biol*. 238 (2006), 303-316

[26] K. Goerttler, Der funktionelle Bau des menschlichen Uterus, *Anatomischer Anzeiger* 67 (1929), 122-130

[27] R. Wetzstein, K.H. Renn, Zur Anordnung der glatten Muskulatur im Corpus Uteri des Menschen, *Verh. Anat. Ges.* 64 (1970), 461-468

[28] St. Weiss, T. Jaermann, P. Schmid, P. Staempfli, P. Boesiger, P. Niederer, Three dimensional fiber architecture of the nonpregnant human uterus determined ex vivo using magnetic resonance diffusion tensor imaging, *Anat. Rec. A Discov. Mol. Cell. Evol. Biol.*, in press

Medicine Meets Engineering
J. Hammer et al. (Eds.)
IOS Press, 2008

Trabecular bone remodeling phenomenon as a pattern for structural optimization

Michal NOWAK [1]
Poznan University of Technology, Division of Machine Design Methods

Abstract. The contemporary virtual engineering environment enables a wide range of optimization procedures. The geometrical shape optimization is one of the most important tasks in this area. In the paper the trabecular bone surface remodeling process is formulated in terms of structural optimization and on the basis of this formulation the optimization algorithm useful in mechanical design is proposed. The developed system, based on the functional adaptation phenomenon is able to mimic trabeculae topology evolution, and enables investigations concerning different scenarios of bone remodeling. Some computation results of trabecular bone functional adaptation as well as mechanical design optimization, using the developed system are presented.

Keywords. Biomechanics structural optimization biomimetics

Introduction

Trabecular bone is able to adapt to the mechanical stimulation [1,2,3]. The process of adaptation is called remodeling and has two main attributes: mechanosensitivity and the place of the bone rebuilding process - the trabecular surface. The research of the remodeling of trabecular bone is in the main area of many medical research centers, but the phenomena of bone mass losing is also very important during the space exploration. The mechanical stimulation is one of the most important factors of the normal bone functionality. Also for the mechanical design the idea of creating the optimal structure as a redistribution of the material is very attractive and can be an efficient tool on important early stage of mechanical design procedure.

1. Remodeling simulation

To create a biomimetics optimization system useful in mechanical design area, formerly the model of the biological phenomena must be prepared. The progress in computer hardware technology and parallel computations enable now modeling of the bone adaptation process using the real topology of the trabecular bone with use of a linear model of the trabecula [4, 5]. The latter is justified by experimental investigations stating that on

[1]Corresponding Author: dr Michal Nowak, Poznan University of Technology, Division of Machine Design Methods, ul. Piotrowo 3, 60-965 Poznan, Poland; E-mail: Michal.Nowak@put.poznan.pl

the trabecular level the bone can be treated as an linear material [6]. For the preparation of the optimization system the algorithm of bone remodeling stimulated by mechanical loading is used [7]. The beams of trabecular bone are assumed to be an isotropic linear material, where the marrow space is treated as voids. The simulation of the remodeling process needs both finite element mesh generation and evolution, and structural stress and strain analysis.

Surface adaptation and mechanosensitivity of trabecular bone can be described from the point of view of mechanics. Bearing in mind the design with optimal stiffness [8], for the local design parameter h_e in the domain, that change the design in the domain only the following formula can be employed:

$$\frac{dU_\epsilon}{dh_e} = -(\frac{\delta((\bar{u}_\epsilon)_e V_e)}{\delta h_e})_{fixed\ strains} \tag{1}$$

where dU_ϵ is the elastic energy, $\bar{u}_\epsilon$ is the mean value of the strain energy density and V_e is the domain volume. When, in turn, we assume localized energy change, fixed volume and take into account the necessary condition for optimality:

$$dU_\epsilon = 0 \tag{2}$$

we can conclude that for the stiffest design the energy density along the shape u_{ϵ_s} to be designed must be constant:

$$u_{\epsilon_s} = const. \tag{3}$$

In the case of bone, the remodeling scenario described above, based on the phenomenological model, seems to realize the postulate of the constant value of the strain energy density. By balancing the SED value on the bone surface, the stiffness of the entire structure is ensured. In ideal conditions, when the bone structure is only rebuild, also the volume constraint:

$$\Sigma_e \frac{dV_e}{dh_e} = 0 \tag{4}$$

So, the fixed volume constraint, resulting from the minimum compliance discussion is not a case in the bone remodeling. The optimization goal can be also formulated as a minimum volume problem with assumed fixed strain energy, what is described in [9]. The resulting condition concerning the strain energy density is the same like in the case of the minimum compliance, so the value of the strain energy density on the designed surface must be equal, when the volume is minimal by the assumed value of the strain energy in the structure.

In the model of bone remodeling, there is a special value of the strain energy density - the energy of homeostasis, when the balance between resorption and formation of the bone tissue is perfect. Based on these assumptions a simulation model of trabecular bone adaptation has been developed. On Figure 1 the simulation results of trabecular structure evolution are presented. On Figure 1(a) the initial structure is presented. The trabecular bone structure as a result of simulating loading in different direction is presented on Figure 1(b), when the case with one direction loading only (compression) is presented on Figure 1(c). The one direction loading results in the form of parallel rods. Therefore the obtained structure is aligned to the loading direction. The presented results are similar to those obtained by [1].

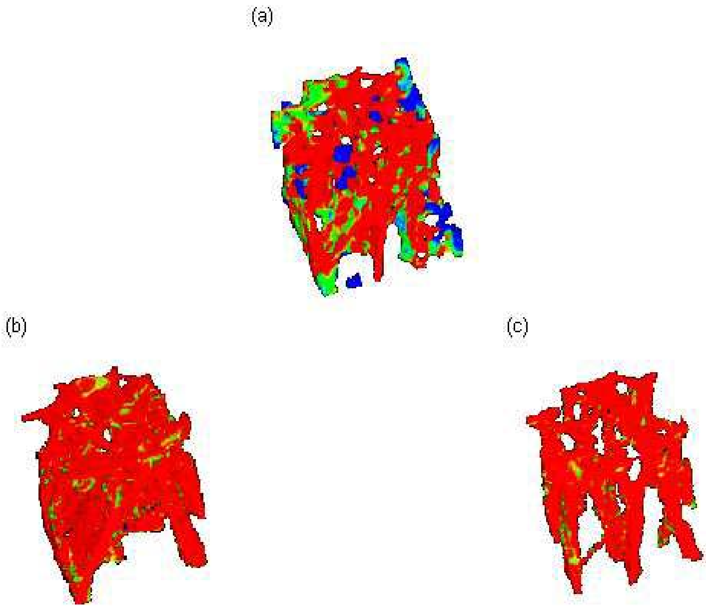

Figure 1. The simulation results of trabecular structure evolution. (a) The initial trabecular structure. (b) The final trabecular structure as a result of simulating loading in different direction. (c) The final trabecular structure as a result of simulating loading in one direction only (compression).

2. The structural optimization method based on trabecular bone remodeling phenomenon

The optimization system is based on the developed for the trabecular bone surface adaptation simulation procedures. The developed system of structural optimization based on biological principle of trabecular bone remodeling consists of input data processing interface, robust 3D mesh generation tool, mesh evolution tool, remodeling scenario, and parallel FEM software and environment. To compare the optimization procedure, based on the trabecular bone surface adaptation, to the standard optimization method, topology optimization was chosen. As an example, the standard topology optimization method example i.e. the bending cantilever beam was chosen. But instead of defining the "ground structure domain", the starting configuration was limited to the simplest fixing (boundary condition - nodes were clamped on the wall) and load (bending force) connection. In Figure 2, the solution obtained using of the system is depicted. The result is very similar to the 3-dimensional solution well known from the topology optimization method [10], but it is not possible to achieve the result using the standard method of topology optimization. This feature, which facilitates adaptation of the structure conserving functional configurations optimization, necessary in case of biological structures, can also be valuable for mechanical structures (in space or civil engineering).

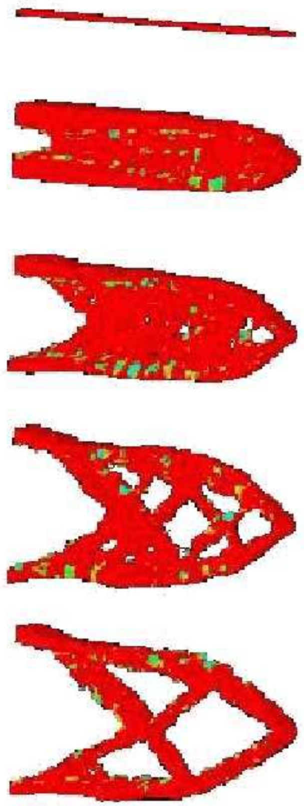

Figure 2. Optimization results of the cantilever beam using of the presented system, based on the trabecular bone surface adaptation. The starting confi guration limited to the simplest fi xing (boundary condition - nodes clamped on the wall) and load (bending force) connection.

3. Conclusions

The presented method is able to produce results similar to the topology optimization method and has some special features, such as domain independence, which can be useful in mechanical design especially in case when the functional structures are needed during the optimization process. The used algorithm is very flexible and the system can be used both for the trabecular bone surface adaptation simulation as well as for the structural optimization in mechanical design. The optimization procedure comprise the optimization of the size, shape and topology, related to the material properties what is natural to biological structures. Presented method can illustrate the core of the term biomimetics the observed biological phenomenon in utilized in mechanical design process.

References

[1] Ruimerman R. et al. A 3-dimensional computer model to simulate trabecular bone metabolism. *Biorheology*, 40, 315-320, 2003.

[2] Lekszycki T. Modelling of Bone Adaptation Based on an Optimal Response Hypothesis. *Meccanica*, 37:343-354, 2002.

[3] Huiskes H.W.J. et al. Effects of mechanical forces on maintenance and adaptation of form in trabecular bone. *Nature*, 404, 704-706, 2000.

[4] Niebur, G.L., Feldstein, M.J., Yuen, J.C., Chen, T.J., and Keaveny, T.M. High resolution fi nite element models with tissue strength asymmetry accurately predict failure of trabecular bone. *J. Biomech.*, Vol. 33, pp. 1575-1583, 2000.

[5] Adachi, T., and Tomita, Y. Functional Adaptation of Cancellous Bone in Human Proximal Femur Predicted by Trabecular Surface Remodeling Simulation toward Uniform Stress State. *J. Biomech.*, Vol. 35, pp. 1541-1551, 2002.

[6] Kowalczyk P. Review of constitutive models for living tissues. *Mechanika Techniczna i Stosowana*, 29, 333-353, 1991.

[7] Nowak M. Structural optimization system based on trabecular bone surface adaptation, Journal of Structural and Multidisciplinary Optimization, Springer Berlin / Heidelberg, 2006, pp. 241-251

[8] Pedersen P. Optimal Designs - Structures and Materials - Problems and Tools. ISBN 87-90416-06-6, 2003.

[9] Dzieniszewski W. Shape Optimization with Elastic Theory Assumptions, Structural Strength Optimization, Institute of Fundamental Technological Research. *ISBN 83-04-011348-7, OSSOLINEUM, 1983,(in Polish).*

[10] Bendsoe M.P., and Sigmund O. Topology Optimiztion - Theory, Methods and Applications. *ISBN 3-540-42992-1, Springer Verlag, 2003.*

Medicine Meets Engineering
J. Hammer et al. (Eds.)
IOS Press, 2008

Numerical Human Models for Accident Research and Safety - Potentials and Limitations

Dr. Norbert Praxl, Jiri Adamec Ph.D., Dr. Holger Muggenthaler, Katja von Merten
Munich University, Institute for Legal Medicine

Abstract The method of numerical simulation is frequently used in the area of automotive safety. Recently, numerical models of the human body have been developed for the numerical simulation of occupants. Different approaches in modelling the human body have been used: the finite-element and the multibody technique. Numerical human models representing the two modelling approaches are introduced and the potentials and limitations of these models are discussed.

Keywords Human body models, computer simulation, vehicle safety

Introduction

A few years ago the development and evaluation of occupant safety systems was done almost exclusively by means of (crash) tests with the use of dummies. Since a dummy must be durable to withstand a crash test without defects and to be statically stable in order to maintain its position after inserting it into the vehicle a dummy is only a very simplistic representation of a human beeing.

Crash tests with dummies induce high costs, since a prototype of the vehicle or safety system must be manufactured which frequently can be tested only once. With the improvement of modern computer technology and simplification of specific software crash tests were shifted increasingly towards the computer. That is, using mathematical models of the vehicle and the occupant the physical sequence of the crash test is computed and visualized on a computer and monitor respectively.

A simulation of a crash test is also called a virtual test and saves time and costs. Since new vehicles must fulfill an increasing number of safety regulations, the European Commission recommends in its report CARS 21 (Competetive Automotive Regulatory System for the 21st century) [1] the successive introduction of virtual tests as partial replacement for the expensive physical tests. If occupant safety systems in the future will be developed and evaluated by virtual tests then it is no longer meaningful to use computer models of dummies for the simulation. In the virtual or mathematical "world" of the computer the biomechanical characteristics of the human can be modelled directly and without the construction-conditioned restrictions of the dummy.

The transformation of the biomechanical characteristics of humans onto a computer model is usually called a human model or human body model. If in the future physical crash tests will be replaced by virtual crash tests, then in the future also the dummy models will be replaced by human models. This shows up also in the roadmap of the APSN (Advanced Passive Safety Network): in the years 2015-2020 it is planned to replace the dummy models gradually by numerical human models.

1. Human Models

The method of numerical simulation is frequently used in the area of automotive safety. All simulations in automotive safety like calculation of structural integrity of the car body or deployment of the airbag have the same ultimate goal - the prevention of injuries. Therefore at the very end all technical simulations have to answer the question if a certain crash will result in an injury or not. To answer this question mostly numerical models of crash test dummies used in physical crash tests are employed. Recently, numerical models of the human body (as opposed to anthropometric testing devices) have been developed for the application in automotive safety.

A numerical human model in the context of accident research and safety is a mathematical representation of the biomechanical properties of the human body. Different approaches in modelling the human body are being used. In principle two different model types can be distinguished:

- Human models with the use of the Finite-Element methode
- Human models with the use of the Multibody methode

Subsequently two numerical human models representing the two different modelling approaches are introduced and the potentials and limitations of these models are discussed on the basis of specific applications in automotive safety.

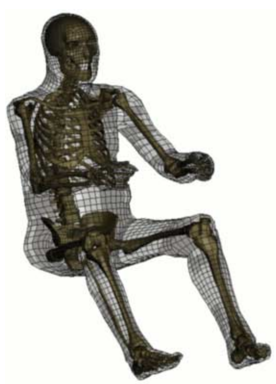

Figure 1. HUMOS-Model

2. Finite Element Model of the Human Body

In the last years different human models were developed in Finite Element technique like the H-Model by ESI [2], the THUMS-Model by Toyota [3] or the HUMOS-Model (Figure 1) [4]. The HUMOS-Model (Human Models for Safety) was developed within a 6-year project funded by the European Commission. A male cadaver was frozen in driving position and subsequently cut in thin slices, for each slice a picture was taken and digitised. From these data a three dimensional grid of the human body was generated. This grid represents the geometry of the finite element model of the human body and is defined by nearly 90.000 elements. Bones, soft tissues, ligaments and organs are modelled. The mechanical properties of the diverse tissues are characterised by more than 500 different material properties. The material properties were taken from the literature or measured within the project. On the basis of these material properties adequate material models have been chosen and applied for the respective body parts.

The model was intensively validated against PMHS (Post Mortem Human Subjects) tests documented in the literature as well as PMHS tests performed during the project [4].

2.1.Application of the HUMOS-Model

A sled test with a side impact of the occupant was simulated with a side impact dummy and the HUMOS-Model to show the advantages a Human FE-Model can offer compared to the dummy:

- Detailed analysis of rib fractures
- Localisation of stresses and strains in the pelvis
- Biomechanical meaningful load of the spine

To show that the HUMOS-Model is predictive and capable to reproduce injuries in a real vehicle accident a reconstructed fatal real world accident was simulated with this model. The accident was a frontal crash against a rigid, concrete wall. The driver a 75 year old female wasn't belted and the technical expertise stated an impact speed of approximately 40 kph.

The impact of the car against the wall were simulated by using the car acceleration taken from the reconstruction of the accident, a simplified model of the occupant compartment (seat and steering wheel) and the 5th percentile HUMOS-Model (Figure 2). The 5th percentile HUMOS-Model is a scaled down version of the original HUMOS-Model to match a 5th percentile female human body.

All injuries of the driver, which are the basis for the evaluation process, were documented in the autopsy report: a rupture of the aorta near the aortic arch, a hemothorax, a flail chest with rib fractures 1-10 bilaterally, two transverse fractures of the sternum and injuries on arms and legs. The cause of death was the rupture of the aorta.

The evaluation of the (5th percentile) HUMOS-Model was done by means of comparison between the injuries found in the autopsy and the injuries and strains predicted in the simulation [5]:

- The aortic rupture was reproduced in the numerical simulation. High strains near the aortic arch were seen in the simulation results indicating a high risk of aortic rupture.
- Rib fractures were predicted in the simulation by element elimination. The rib fractures in the simulation correlated well with the rib fractures found in the autopsy. Due to the high age of the victim more fractures were found in the autopsy compared to the number of predicted rib fractures in the simulations.
- High strains in the sternum bone were also seen in the simulation results, but the two transverse fractures in the real scenario weren't predicted exactly.

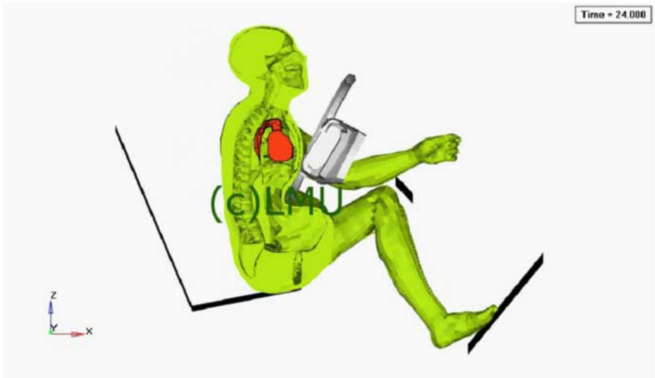

Figure 2. Frontal impact simulation with the 5th percentile HUMOS-Model

2.2.Potentials and Limitations of the HUMOS-Model

As demonstrated by this example, finite-element models of the human body are on the one hand very valuable tools in injury biomechanics research to better understand the causation of injuries and on the other hand they are a useful tool for the evaluation of passive safety devices or injury countermeasures in the automotive industry.

But the finite-element models for safety have their drawbacks. The CPU load and therefore the calculation time are high, the positioning of the model in the car can be a very time consuming procedure and sometimes numerical instabilities may occure. In addition it is to mention that the validation of the human model is by far not complete. To ensure reliable results for all different kinds of impacts (on different body parts as well as with different energy levels and impact directions) more validation work has to be done.

The HUMOS-Model is still a human model representing a completely passive human being. Thus, forces produced by muscle activation are not taken into account neither for the impact dynamics nor for the whole body kinematics.

3. Multi Body Model of the Human Body

The software package MADYMO is commonly accepted in the field of passive safety. Beside the ordinary dummy models MADYMO also offers human body models using the multibody technique and so called facets (Figure 3) [6]. In contrast to the finite-element models the human body model does not consist of numerous small elements but instead consists of body segments like the head, arms, upper torso and so on. Each segment is modelled as a discrete body with mass, center of gravity and inertia which are connected to the nearby segment via kinematic joints. The body segments are based on anthropometric measurements, they do not have material properties like the finite-element models, if a contact with the facet which describes the outer shell of the body is detected the contact force is calculated by a pre-defined force-deflection-characteristic.

The MADYMO human body model was validated against various PHMS tests in high severity impacts and with volunteer tests in the low severity region.

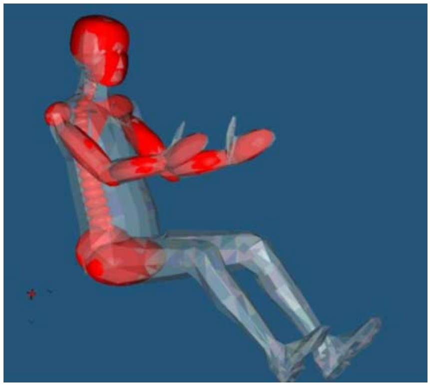

Figure 3. MADYMO Human Body Model

3.1.Application of the MADYMO Human Body Model

Series of experiments with volunteers and the Hybrid III dummy were carried out on a motion base that imitated the first phase of a rollover accident [7]. The kinematics of the volunteers and the dummy sitting belted in a car seat were measured with a 3D motion capturing system.

The experimental setup including the seat and belt was modelled with MADYMO and was simulated using the recorded motion of the motion base. The MADYMO human body model was used in the simulation as well as the Hybrid III dummy model.

By comparing the results of the experiments and the simulations the validity of the kinematics predicted by the human body model was evaluated. The results of the evaluation clearly show the good prediction of the human body model especially compared to the dummy (Figure 4).

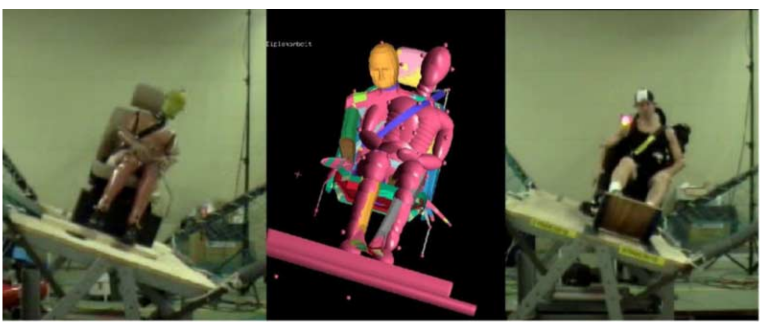

Figure 4. Comparison of dummy, volunteer, dummy model and human body model

Beside the application in the simulation of a laboratory test the model was also used in a simulation of a rollover crash test [8]. Therefore the vehicle kinematics of a physical rollover crash test performed on a crash facility with a widely accepted dummy type (Hybrid III) was measured. These kinematic data were used to prescribe the motion of a vehicle model in a computer simulation. The simulation was performed with the Hybrid III dummy as well as with the Madymo human body model. The simulation results showed big differences between the kinematics of the dummy and the human model (Figure 5).

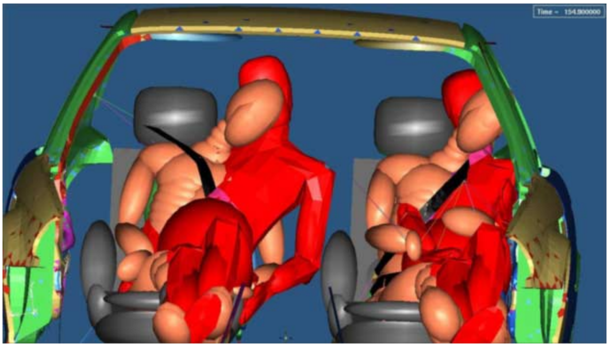

Figure 5. Comparison of dummy and human model in a rollover simulation

3.2.Potentials and Limitations of the MADYMO Human Body Model

The main benefit of the MADYMO human body model is the realistic prediction of the kinematics due to the flexible spine modelled by single vertebraes.

The multibody model is valid for different impact or acceleration directions, needs only a short calculation time and can be easily placed in any biomechanical meaningful position. Furthermore the human model is numerical robust although not as robust as the dummy model. If the structural behaviour of tissue is not of interest the multibody facet model is a useful tool to calculate the kinematics and the forces acting on the human body in a very efficient way.

But the MADYMO human body model is a passive model. The influence of muscular activity is not addressed. For accidents with a long pre-impact phase and low acceleration the muscle action plays an important role in the overall kinematics of the occupant. To improve the performance of the human model in this context active or at least re-active human models have to be developed. Although first basic active models exist up to now no generally applicable validated (re-)active model is available (Figure 6). The development of active human models is the next challenge for the biomechanics research community to provide models which can be used in passive as well as in integrated safety.

Figure 6. Active and passive (bright) human body model

References

[1] European Commission: CARS 21 – A Competitive Automotive Regulatory System for the 21st century. Luxembourg: Office for Official Publications of the European Communities; 2006.
[2] ESI Group, www.esi-group.com
[3] Toyota Central R&D Labs, www.tytlabs.co.jp
[4] HUMOS: Human Model for Safety, Public Report: Contract Number: BRPR-CT97-0475, Project Number: BE96-4169.
[5] vMerten, K.: Using HUMOS2 model for the reconstruction of accidents with thoracical injurues. J. Biomech. Vol. 39 Suppl. 1, p 165, 2006.
[6] MADYMO, www.madymo.com
[7] Praxl, N., Adamec J., Muggenthaler H.: The Response of Hybrid III, EuroSID and Volunteer in the First Phase of a Rollover Accident. Proceedings of the 19th International Technical Conference on the Enhanced Safety of Vehicles, 2005, Paper No. 05-0254.
[8] Praxl, N.; Schönpflug M.: Simulation of Occupant Kinematics in Vehicle Rollover – Dummy Model versus Human Model. Proceedings of the 18th International Technical Conference on the Enhanced Safety of Vehicles, 2003, Paper No. 202.

Medicine Meets Engineering
J. Hammer et al. (Eds.)
IOS Press, 2008

Human cortical bone: the SINUPROS model

Dr M. Predoi-Racila *, Pr J.M. Crolet **

** University of Craiova, Romania*
*** University of Franche-Comte, France*

Abstract: Several modelizations have been investigated on human cortical bone in our team and we have often observed that the introduction of a new geometrical parameter induces significant perturbations on the numerical values obtained with previous models. We have therefore decided to take into account the totality of all possible parameters in a modelization which is physically and physiologically plausible. In order to do this, we have analyzed the architecture of cortical bone and exhibited all parameters that occur. To determine physical properties at each architectural level, the best adapted tool is without any doubt the mathematical theory of homogenization. All the necessary algorithms have been implemented into SINUPROS software (websites of the Universities). Its main interest is the evaluation of macroscopic physical properties for a given configuration. It can also be used to seek, by successive tests, configurations corresponding to properties experimentally measured. Computation time being too high (10 to 45 minutes according to tested configurations), a fast version based on approximation theory has been developed and thus the obtaining of the results is immediate. The researched configuration being thus obtained, it has then to be validated by the original version.

Keywords: Human cortical bone, Homogenization, Piezoelectricity, Bony mineralization, Multi-scale, CPU time

1. Introduction

SINUPROS is a model of the human cortical bone that takes into accounts the architectural, multiphysics and multi scale aspects of this medium. We have built this model in which bony architecture is organized in a hierarchical way, each level contributing to the overall properties. The present modelization of the cortical bone leans on previous studies [1, 3] but this one is more complete because it takes into account many parameters characterizing the complex architecture of cortical bone which were ignored before.

The model contains five architectural levels, 28 parameters and provides detailed information at each level of the bony architecture, including micro and nano levels. We use the mathematical homogenization theory as a modelization tool and the finite element analysis for simulating the mechanical properties of the cortical bone at each architectural level.

The numerical algorithms are implemented in a software based on Matlab which allows easily simulating the effects of each parameter on the overall properties but the computational time is too large.

2. Modelization

Human cortical bone can be considered as a composite medium, the fibbers being the osteons embedded in the interstitial system (IS) i.e. a medium made of surmineralized osteons which have been destroyed during the remodelling phase. The most important entities are the mineralization and the osteon, which, by its tubular geometry, is characterized by a diameter and porosity. These channels called Haversian channels are oriented according to the longitudinal direction and are linked by Volkmann channels located in transverse plans. The following parameters have to be considered: distance between two osteons, distance between an osteon and the IS (called the cement line), distance between two Volkmann channels and the Volkmann porosity.

The osteon is not homogeneous. Being composed by the concentric lamellae encased the one in the others, it is parameterized by the lamellar and interlamellar thicknesses. These lamellae are crossed by small channels (canaliculae) and this canalicular volume is taken into account simultaneously for the current osteon and the IS.

The nonhomogeneous lamella is considered as a composite, the fibers (the collagen sticks which one considers as cylinders) being embedded in a medium made of hydroxyapatite (Hap) crystals and fluid. Then it is necessary to introduce the cylinder diameter, the distance between two such cylinders and their orientation according the longitudinal axis.

Concerning the mineralization, an abstract entity, (the Elementary Volume of Mineral Content or EVMC) has been introduced [5,7]. The associated parameters are the percentages of EVMC and linked water respectively in the current osteon and in the IS. A coefficient of nanoscopic anisotropy is added.

According this description, the SINUPROS model contains 18 structural parameters, distributed as following: 6 for the Haversian system, 4 for the osteon, 3 for the lamellar architecture and 5 for the mineral structure. All the physical properties (10 parameters) have to be added: density of collagen and Hap, Young's moduli of collagen and Hap, Poisson's ratios of collagen and Hap, piezoelectric and dielectric tensors of collagen, dielectric tensors for the EVMC and the fluid. In conclusion, this geometrical and architectural description makes the SINUPROS model particularly complete.

3. Homogenization algorithm for the SINUPROS model

In our model, the process used for the computation of the physical properties is based on the mathematical theory of homogenization [6] that needs the knowledge of the periodic (or pseudo periodic) architecture and the properties of the basic components. In all the models previously studied, the basic components were the collagen fibers and the Hap. Three steps are necessary: from the basic components to the lamella, from two consecutive lamellae to an osteon and from a set of osteons to the cortical bone. This algorithm was already presented in [7]. The main point of this algorithm is that it is quite CPU time penalizing and this cannot be improved: for instance, the computation of the characteristic functions is made too many times: 90 times for a mono architectural configuration and more for other cases.

This algorithm has been implemented into a software called SINUPROS based on Matlab and which allows obtaining the physical properties of cortical bone at each architectural level and also of the behavior laws at the same levels. This software is in free access on the website http://www-math.univ-fcomte.fr/sinupros/sinupros.zip [11]. The interest of this software is to evaluate physical properties for a given configuration, but also to be able to seek, by successive tests, the configurations corresponding to already measured properties. The calculation time being relatively long, from 10 minutes for a mono-architecture to 45 minutes for architecture with 3 or 4 types of osteonal architectures, the research of such a configuration could take hours. This thing is not neglectable knowing that many experimental values can be found in the literature but none give any information on the architectural characteristics of the studied sample. For this reason we have built a fast version of this software (SINUPROS-Fast) based on a database of results and on the approximation techniques. This version will be also proposed in free access in a close future.

4. Algorithm for SINUPROS FAST

The main idea of this fast version is quite simple and consists in building a data base of values of mechanical properties of cortical bone at the macroscopic level (a similar study could be done at the other levels). The using of this data base coupled with a method of the approximation theory allows the obtaining of the architectural configuration of the sample whose some mechanical properties are experimentally measured. The main advantage of the Fast version is that the obtaining of the results is immediate. Once the researched configuration has been thus obtained, it has then to be validated by the original version of the software SINUPROS.

This data base of values is obtained using the SINUPROS software, in two steps:

- Firstly, a reference configuration is built and the properties for this “reference configuration” are calculated using the SINUPROS program. This reference configuration is obtained for the values of the parameters that give a percentage in mass of 63 % for Hap and 37 % for the collagen. Some of this values are get from the literature [2, 10] and the others are introduced in the modelization of the mineral phase (percentages of EVMC and percentages of linked water respectively in the current lamella and in the interstitial system and coefficient of nanoscopic anisotropy). For them, there is no possible information in the literature or by measurements and the values have been chosen in respect with the numerical problem and a plausible physical signification. The reference configuration is not important for itself but it is necessary to organize the parametric study of our model.

- Secondly, we study the influence of each parameter on the macroscopic properties of the cortical. More precisely, by varying only one parameter, on compute the cortical properties using the SINUPROS program and we study the influence that it could has on these properties. All the computed properties are stoked in our data base.

With this data base one can make, using the Excel component of Microsoft Office Suite, the polynomial approximations (of fourth order) which will give later the possible values of the parameters which could give the exact bony properties that we researched.

5. Results

Several types of studies can be pursued with this model. The results at the macroscopic level which have been obtained with the SINUPPROS software [8] show in general a good agreement when compared to those found in the literature [4, 5, 9]. In this paper, we present only some examples which show comparisons between the two versions (the original and the fast version).

The values taken for the reference configuration are the following: osteonal diameter: 140 μm, distance between two osteons: 10 μm, distance between two Volkmann channels: 250 μm, thickness of the cement line: 2 μm, thickness of a lamella: 4 μm, interlamellar thickness: 10 nm, haversian porosity: 8 %, Volkmann porosity: 6 %, diameter of a collagen stick: 4 nm, distance between two collagen sticks: 1.6 nm, volume of canaliculae in a current lamella: 3 %, volume of canaliculae in interstitial system : 1.8 %, degree of mineralization in a current lamella: 38 %, degree of mineralization in interstitial system: 70 %, percentage of linked water in a current lamella: 8 %, percentage of linked water in interstitial system: 5 %, Hap density : 3153 g/cm3, collagen density: 1200 g/cm3, coefficient of nanoscopic anisotropy: 1.

This configuration of reference being arbitrarily fixed, we can make evolve each parameter separately in an appropriate interval of values. We obtain our data base with the results obtained with SINUPROS for these different configurations. SINUPROS Fast version corresponds to all the polynomial approximations of fourth order that we have determined for each parameter.

It is interesting to be able to know the error between the two versions of computation (Matlab and Excel).

We consider the previous reference configuration and firstly we make vary only the first six parameters (Table 1) of the haversian structure. In Table 2 we present the results that one obtains using the fast version of the program and the results that we could obtain if we use the original version of the SINUPROS program only for the diagonal terms because these terms are the most experimentally measured. The error is also presented for all these values obtained with the two versions.

	Varying Parameters	Value	Units
1	osteonal diameter	160	µm
2	haversian porosity	10	%
3	distance between two osteons	12	µm
4	thickness of the cement line	4	µm
5	Volkmann porosity	8	%
6	distance between Volkmann channels	350	µm

Table 1. Variations of the parameters of the haversian structure

Version		Original	Fast	Error
Orientation of collagen 45°/-45°	C_{11}	14.58	14.62	0.3 %
	C_{33}	21.54	21.63	0.4 %
	C_{44}	6.61	6.63	0.3 %
	C_{66}	5.08	5.11	0.6 %
Orientation of collagen 0°/0°	C_{11}	12.51	12.58	0.6 %
	C_{33}	27.35	27.43	0.3 %
	C_{44}	5.56	5.56	0.0 %
	C_{66}	4.94	4.97	0.6 %

Table 2. Results obtained by using the two versions varying only the haversian structure's parameters

Let us now consider variations of only the four parameters (Table 3) characterizing the lamellar structure, all the other parameters being exactly those considered in the reference configuration. Here are the results (Table 4) that one obtains with SINUPROS-Fast and the original SINUPROS version:

	Varying Parameters	Value	Units
1	thickness of a lamella	5	µm
2	interlamellar thickness	12	nm
3	canaliculae volume in current lamella	5	%
4	canaliculae volume in interstitial syste	4	%

Table 3. Variations of the parameters of the lamellar structure

Version		Original	Fast	Error
Orientation of collagen 45°/-45°	C_{11}	15.87	15.85	0.1 %
	C_{33}	23.75	23.72	0.1 %
	C_{44}	7.31	7.30	0.1 %
	C_{66}	5.55	5.56	0.2 %
Orientation of collagen 0°/0°	C_{11}	13.56	13.56	0.0 %
	C_{33}	30.18	30.18	0.0 %
	C_{44}	6.09	6.08	0.2 %
	C_{66}	5.41	5.42	0.2 %

Table 4. Results obtained by using the two versions varying only the lamellar structure's parameters

If only the diameter of collagen sticks and the distance between two collagen sticks can have variations, we obtain, for the macroscopic elastic properties the following values (Table 5):

Version		Original	Fast	Error
Orientation of collagen 45°/-45°	C_{11}	15.14	15.19	0.3 %
	C_{33}	22.70	22.81	0.5 %
	C_{44}	6.95	6.97	0.3 %
	C_{66}	5.21	5.24	0.6 %
Orientation of collagen 0°/0°	C_{11}	13.04	13.09	0.4 %
	C_{33}	28.91	29.03	0.4 %
	C_{44}	5.85	5.84	0.2 %
	C_{66}	5.10	5.14	0.8 %

Table 5. Results obtained by using the two versions varying only the collagen structure's parameters

Finally, if we make vary only the five parameters concerning the mineral structure (Table 6), the results and the errors obtained are summarized in Table 7.

	Varying Parameters	Value	Units
1	% of EVMC in current lamella	50	%
2	% of linked water in current lamella	10	%
3	% of EVMC in interstitial system	80	%
4	% of linked water in interstitial system	7	%
5	anisotropy coefficient at nanoscale	1.05	

Table 6. Variations of the parameters of the mineral structure

Version		Original	Fast	Error
Orientation of collagen 45°/-45°	C_{11}	12.94	12.87	0.5 %
	C_{33}	20.69	21.07	1.8 %
	C_{44}	6.29	7.13	13.4 %
	C_{66}	4.51	4.53	0.4 %
Orientation of collagen 0°/0°	C_{11}	10.22	10.15	0.7 %
	C_{33}	29.77	29.10	2.3 %
	C_{44}	4.91	4.94	0.6 %
	C_{66}	4.24	4.43	4.5 %

Table 7. Results obtained by using the two versions varying only the mineral structure's parameters

Let us now make vary all the architectural parameters (Table 8). This is the most complex situation that one could have. We give in Table 9 the results and errors obtained when using the two versions of the program.

	Varying Parameters	Value	Units
1	osteonal diameter	160	µm
2	haversian porosity	10	%
3	distance between two osteons	12	µm
4	thickness of the cement line	4	µm
5	Volkmann porosity	8	%
6	distance between Volkmann channels	350	µm
7	thickness of a lamella	5	µm
8	interlamellar thickness	12	nm
9	canaliculae volume in current lamella	5	%
10	canaliculae volume in interstitial syste	4	%
11	diameter of collagen sticks	5	nm
12	distance between collagen sticks	2	nm
13	% of EVMC in current lamella	50	%
14	% of linked water in current lamella	10	%
15	% of EVMC in interstitial system	80	%
16	% of linked water in interstitial system	7	%
17	anisotropy coefficient at nanoscale	1.05	

Table 8. Variations of all the parameters of the bony structure

		Sinupros	Fast	Error
Orientation of collagen 45°/-45°	C_{11}	11.93	10.91	8.5 %
	C_{33}	18.62	17.96	3.5 %
	C_{44}	5.60	6.11	9.1 %
	C_{66}	4.11	3.79	7.8 %
Orientation of collagen 0°/0°	C_{11}	9.61	8.69	9.6 %
	C_{33}	26.42	25.18	4.7 %
	C_{44}	4.53	4.16	8.2 %
	C_{66}	3.86	3.72	3.6 %

Table 9. Results obtained by using the two versions varying all the bony structure's parameters

6. Conclusions

Firstly, one must remark that for the parameters characterizing the haversian, lamellar and collagenic structures, the obtained errors when using the two versions of the program are always near zero.

Concerning the parameters associated to the mineral structure, when we use the original and the fast versions, the errors are slightly superior (1 - 4 % excepted for C_{44} and C_{66}) and again more superior when all the parameters are varying together. This fact is normal, because of the already known influence that both the mineralization and anisotropy have on the bony properties.

Dealing with the CPU time, the Fast version is extremely convenient, because the results are instantaneously obtained. The main interest of such a performance is the research of a possible architectural configuration for a sample whose the elastic diagonal properties have been experimentally measured.

References

[1] Aoubiza B., Crolet J. M., Meunier A., "On the mechanical characterization of compact bone structure using the homogenization theory", Journal of Biomechanics, vol. 29, no. 12, pp. 1539-1547, 1996
[2] Cowin S., Bone Mechanics Handbook, CRC Press, 2001
[3] Crolet J.M., Racila M., Mahraoui R., Meunier A., New numerical concept for hydroxyapatite in human cortical bone, Computer Methods in Biomechanics and Biomedical Engineering, Vol. 8 (2), pp. 139-143, 2005
[4] Katz J.L., Meunier A., The elastic anisotropy of bone, J. Biomech, Vol. 20, N° 11/12, pp 1063-1070, 1987
[5] Meunier A., Riot O. Christel P., Katz J.L., Sedel L., Inhomogeneities in anisotropic elastic constants of cortical bone, Ultrasonics symposium, pp 1015-1018, 1989
[6] Panasenko G., Multiscale Modelling for Structures and Composites, Springer, Dordrecht, Netherlands, 2005
[7] Racila M., Crolet J. M., Human cortical bone: computer method for physical behavior at nano scale. Constant pressure assumption, Technology and Health Care – Journal of the European Society for Engineering and Medicine, IOS Press, Vol. 14, No. 4,5, pp. 379-392, 2006
[8] Racila M., Crolet J. M., Nano and macro structure of cortical bone: numerical investigations, International Journal of Computers and Structures, Special Issue on Structural and Multidisciplinary Optimization (to appear in juin 2007)
[9] Rho J.Y., An ultrasonic method for measuring the elastic properties of human tibial cortical and cancellous bone, Ultrasonics, vol. 34, pp. 777-783, 1996
[10] Rho J-Y, Kuhn-Spearing L, Zioupos P, Mechanical properties and the hierarchical structure of bone, Medical Engineering & Physics, 20, pp. 92-102, 1998
[11] SINUPROS website: http://www-math.univ-fcomte.fr/sinupros/sinupros.zip

Medicine Meets Engineering
J. Hammer et al. (Eds.)
IOS Press, 2008

Unstable Operators in Image Processing

Dietwald SCHUSTER [a]
[a] *University of Applied Sciences, Regensburg*

Abstract. Digital image processing is a powerful tool in biomedical applications and is used for image enhancement, segmentation or classification. Unfortunately, some of the processes in image analysis are unstable operators. Even small perturbations in the image data can cause significant errors in the result. The corresponding practical algorithms are sensitive to deviations in the input data and the behaviour is similar to linear systems with ill conditioned matrices. This property is related to the so called ill posed problems. We review the framework of ill posed problems and regularization in image analysis. We examine a few examples related to biomedical imaging: segmentation by thresholding, edge detection, length estimation, orientation.

Keywords. Unstable operators, ill posed problems, image processing

Introduction

In image analysis one always must take into account the effects of noise. It is caused by various disturbing effects in the imaging process and creates random fluctuations in the image intensities. Instability in a particular image processing algorithm and noise has important consequences in practical applications. The task of recovering information from images becomes difficult and "what you see is not what you get!" The deficiencies of an ill posed problem can be partially removed by imposing constraints on the output function. These constraints are usually based on additional properties like smoothness and are called regularization methods.

1. Segmentation

1.1. Thresholding

We can extract light objects on a dark background in an image by selecting a gray-level threshold s. A pixel with value above s is classified as an object pixel in an output image. Let the image function on a rectangular region R be $B : R \to G$ with gray values $G = \{0,1,2,...,g_{max}\}$. The thresholded output image is the binary image $T_s(B(x,y))$ defined by

$$T_s(B(x,y)) = \begin{cases} 1 \text{ if } B(x,y) \geq s, \\ 0 \text{ if } B(x,y) < s \end{cases}$$

In general the determination of a suitable threshold value is not a simple matter. In figure 1 (a) a square object of length 100 pixel and constant gray value 120 is included in an image of size 256^2. Inside the square object there is an other smaller square of constant gray value 121. Applying the threshold operator with $s = 120$ gives an image with the big square (figure 2 (a)) and a threshold value of $s = 121$ detects the small square (figure 2 (b)). The result of the threshold operator is sensitive to the threshold value.

We consider again the example with the fixed threshold $s = 121$. If the image values of $B(x,y)$ are increased by 1, the slightly modified image $\hat{B}(x,y) = B(x,y) + 1$ does not show any difference to the viewer. Thresholding with $s = 121$ results in two very different output images. (figure 2). This is the ill posed property of the operator. Small changes in the input image can cause significant differences in the output. The threshold operator is unstable or discontinuous as a mapping between image function spaces. This property makes segmentation a difficult task. We can accomplish it with additional information about the gray value distribution or with interactive control.

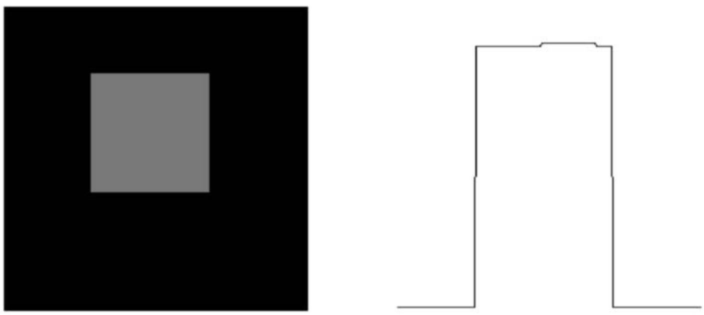

(a) (b)

Figure 1. (a) Test image (b) horizontal gray value profile through the image center

(a) (b)

Figure 2. Thresholding result (a) $s = 120$ applied to B, $s = 121$ applied to$\hat{B}$ (b) $s = 121$ applied to B

1.2. Edge Detection

Edges are the boundary lines between image regions assumed as objects and background. Edge detection methods are based on the computation of a local derivative operator. In two dimensional images the magnitude of the gradient is used and approximated with finite differences. The lack of stability for gradients is well known and discussed in many references ([5]). Differentiation is a typical ill posed problem. The result of numerical differentiation is sensitive to noise giving wrong edges or gaps in the border lines. Methods to improve robustness are based on regularization techniques and involve smoothing of the noisy data. One of the most prominent regularized edge operator is due to Canny ([1]).

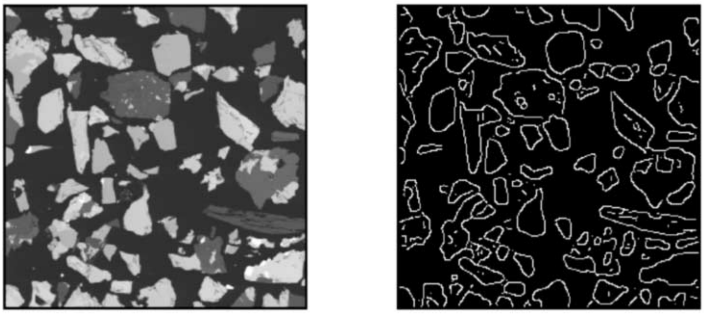

(a) (b)

Figure 3. (a) Input image (microscopy) (b) edge detection with Canny operator

2. Geometric Features

2.1. Length Estimation

Length and perimeter estimation of digitized planar objects depend on the pixel model. If we assume a pixel being a square then the length of a discrete object is in a simple approach the count of the "cracks" on the border of the object. In the following example (figure 4) the perimeter is $p_{crack} = 12$.

Using the midpoint of an pixel and the lines joining these points we get a different border line and a perimeter $p_8 = 4 + 2\sqrt{2} = 6.828....$ The different values show the importance of the discrete image model.

An other example is the digitized disc. Assuming the radius r we can find

$$p_{crack} = 8r, \quad p_{exact} = 2\pi r$$

The relative error is independent of r and equals $4/\pi - 1 = 0.273...$ that is 27%. Analyzing an numerical example with $r = 160.5$ in an image of size 512^2 we have

$$p_{crack} = 4 \cdot 321 = 1284, \quad p_{exact} = 2\pi 160.5 = 1008.45.$$

From an image processing software we see that $p_8 = 1059.74$ is a better estimate with a relative error of 5%. The smoothness of the circle line is partially considered in the p_8-model. The digitized circle in figure 5 has a border consisting of cracks, so p_{crack} is actually the correct geometrical length of the borderline. While the digitized disc is a rather good approximation of the continuous disc, the perimeters differ significantly.

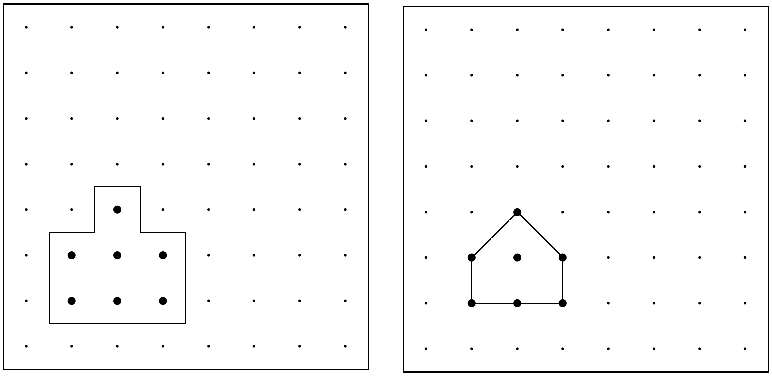

Figure 4. Pixel model and length estimation

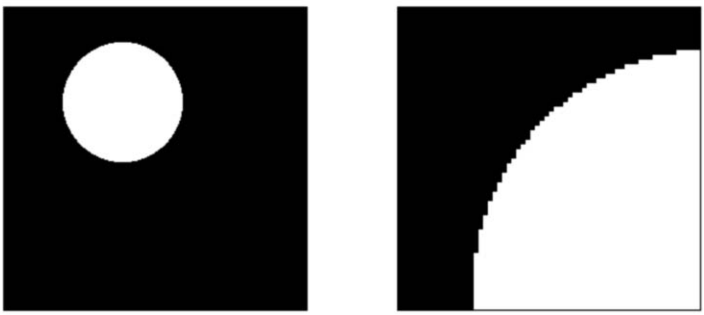

(a) (b)

Figure 5. (a) Digitized disc, (b) zoomed digitized border

Length estimation is an unstable process. We conclude that there is no general length estimation method. Additional input like smoothness has to be provided.

Finally we show that the area value for the digitized disc is a very good approximation to the continuous disc area.

$$F_{exact} = 80424.77, \quad F_{crack} = 80877.$$

The relative error is only 0.56% and the area is a robust parameter.

2.2. Orientation

Using the gray values of an image object as a density function we can find the moments of inertia in a mechanical model. The principal axes of inertia provide the orientation of an elongated object with the assumed density.

The orientation can be used for anisotropy measurement or analysis of biomechanical properties. The application on CT images of bone shows the detection of a dominant direction. The direction in figure 6 (a) seems reliable, in 6 (b) the result however, differs from the expected anisotropy. The density coded in the gray values of 6 (b) influences the axis significantly.

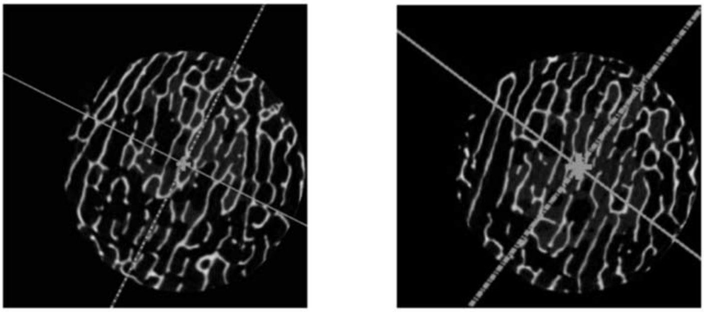

(a) (b)

Figure 6. (a) CT image bone, reliable orientation , (b) unexpected orientation

The orientation from the axis of inertia is an unstable parameter as we show in the example 7. Small deviations in the simulated disk image cause the significant change in the axis of inertia.

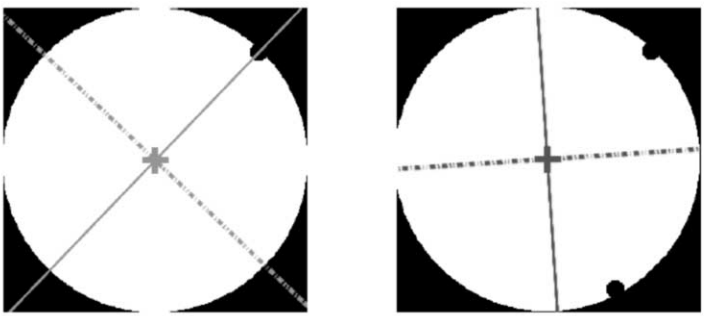

(a) (b)

Figure 7. (a) Test object with axis of inertia , (b) Modified object

References

[1] J. Canny: A Computational Approach to Edge Detection, *IEEE-Transactions, PAMI-8,* (1986), 679–698
[2] R. C. Gonzalez; R. E. Woods: Digital Image Processing, Addison-Wesley, 1993
[3] J. Koplowitz; A. M. Bruckstein: Design of Perimeter Estimators for Digitized Planar Shapes, *IEEE-Transactions, PAMI-11,* (1989), 611–622
[4] J. Kurz: Bestimung von Strukturkennwerten der Spongiosa, Diplomarbeit, FH Regensburg 2006
[5] V. Torre; T. A. Poggio: On Edge Detection, *IEEE-Transactions, PAMI-8,* (1986), 147–163

Medicine Meets Engineering
J. Hammer et al. (Eds.)
IOS Press, 2008

Bone as a Structural Material: How Good Is It?

David TAYLOR
Trinity Centre for Bioengineering
Trinity College, Dublin, Ireland

Abstract. As a structural material, bone is not very good; compared to engineering materials such as metal alloys and fibre composites, its mechanical properties are mediocre. In fact, the really amazing thing about bone is that it is able to achieve even these mediocre properties with the ingredients available: hydroxyapatite, collagen and water. Drawing on previous research, and some simple fracture mechanics calculations, we can see how bone optimises the use of these materials in a composite structure which has important features at two different scales: the nanometre scale and the hundred-micron scale.

Keywords. Bone, strength, toughness, nanocomposite

1. Bone Compared to Engineering Materials

Discussions about bone frequently take the line "Isn't Nature Wonderful?", but really bone is not particularly good when compared to the kinds of materials which we now routinely make for engineering purposes. As Table 1 shows, we can make metal alloys and fibre composites with much higher strength and toughness, making them inherently more suitable as load-bearing materials.

Of course there is also the issue of biocompatibility, but metals such as titanium and stainless steel have shown themselves to be very satisfactory in this respect. Bone can repair itself, and adapt its shape and properties to changes in its loading environment; this is a clever trick, but one which a titanium alloy bone wouldn't need to do. The typical maximum cyclic stresses experienced by our bones, of the order of 50MPa, are about ten times lower than the fatigue strength of a titanium alloy, so it would function for thousands of years without any risk of fatigue failure.

Density is another important factor. Bone saves weight by having a lower density than metals, so to be fair we should take this into account. Consider a typical long bone; if we want to make this from titanium, since we can't change the length we will need to reduce the area of the cross section by a factor of 2 (the density of titanium being 4.5g/cm^3 and that of bone being just over 2g/cm^3). Bones are subjected to both bending and axial tensile stresses. Reducing the cross section by a factor of 2 will simply increase any tensile and compressive stress by the same factor. We can calculate

Table 1: Typical Mechanical Properties for Various Materials

	Young's Modulus (GPa)	Tensile Strength (MPa)	Strain to Failure (%)	Fracture Toughness $MPa(m)^{1/2}$
Bone – compact, primary	20	170	2	2-6
Bone – compact, secondary	16	140	2	1.5-4
Bone – cancellous	0.07-0.7	1-8		
Tendon and Ligament	1.5	100	20	
Enamel	50	35		0.75
Dentin	12	160		3
Hydroxyapatite	165			0.5
Collagen	1	100		
Steel	200	700	20	100
Titanium Alloy	100	800	10	80
Carbon Fibre Composite	50	600		40

its effect on bending stresses using standard mechanics equations, which state that the maximum stress in a tube of radius r subjected to a bending moment M is:

$$\sigma = \frac{Mr}{I} \tag{1}$$

…where the moment of inertia I is a function of radius r and thickness t:

$$I = \frac{\pi}{4}\left(r^4 - (r-t)^4\right) \tag{2}$$

The ratio of stress in the original bone to stress in the new titanium bone is simply the ratio of their I values. Using some typical dimensions for a long bone (diameter 25mm, cortical thickness 7mm) and reducing the thickness by half for the titanium bone, the result is an increase in stress by a factor of 1.3. Different bones experience different ratios of bending and tensile loads, but even in the worst case the stresses in the titanium bones will be less than 100MPa, which is about one fifth of the fatigue strength of this material. Carbon fibre composites have about the same density as bone so this argument doesn't apply to them.

Another argument for the superiority of bone is that it has a unique *combination* of properties. Specifically, bone has rather good strength and toughness considering its rather low Young's modulus. Certainly metals, and most fibre composites, have higher E values; composites can be made with E values which are the same as bone but this is achieved by using rather low proportions of fibres (or by using short-length fibres or particulate reinforcement) which tends to bring down the strength and toughness as well.

What is the significance of the low E value? It may be useful in terms of absorbed energy. In an impact situation, a material can absorb a lot of energy if there is a large area under its stress/strain curve; this area is the amount of energy absorbed per unit volume of material. This is a property which is similar to, but distinctly different from, the fracture toughness; materials with good impact resistance sometimes have low toughness – certain polymers for example – so we should also consider this property. Table 2 shows estimates of the impact energy for various materials. It is clear that bone has about an order of magnitude less capacity to absorb impact energy than metals: carbon fibre composite is about the same as bone in this respect. Interestingly tendons and ligaments are much better. The mechanism of energy absorption is better too: in an accident, a titanium bone would bend (and will have to be re-straightened) whilst a bone will crack and snap.

Another useful energy parameter is the amount of elastic energy that can be absorbed whilst operating at a safe stress level. The importance of the soft tissues in this respect was made by Alexander when he noted that, during running, most of the stored elastic energy is found in our muscles, tendons and ligaments [1]. It used to be said that cartilage also has a significant shock-absorbing effect but this turns out to be incorrect: as a material it can absorb quite a lot of energy but in joints it exists only in small volumes. Table 2 shows this "Safe Elastic Energy" which I have defined as the area under the stress/strain curve up to half the yield strength. Titanium and carbon-fibre materials are again much better than bone.

Table 2: Energy Parameters for Various Materials (Typical Values)

Material	**Impact Energy (MJ/m^3)**	**Safe Elastic Energy (MJ/m^3)**
Bone	2.7	0.09
Tendon/Ligament	17	0.16
Steel	69	0.1
Titanium Alloy	37	0.45
Carbon Fibre Composite	3.6	0.9

I conclude the case in favour of engineering materials by mentioning the athlete Oscar Pistorius, a below-knee amputee who has artificial legs and feet made from carbon fibre composite. His performance on the running track rivals that of the best able-bodied athletes. He could probably achieve the standard necessary to compete in the next Olympic Games, but some sporting associations have banned him from competing on the grounds that his prostheses give him an unfair advantage!

2. How Bone Achieves Its Properties

Perhaps I shouldn't be so critical of Mother Nature – she is trying as hard as she can with the limited materials that are available, and in fact she is doing very well. The only material found in the human body which has high stiffness and (potentially) high strength, is hydroxyapatite (HA), so making a composite material with HA and collagen is really the only option, not only for bone but for other hard structures in animals such as teeth and antlers. Table 1 includes some mechanical property values for HA and collagen. It is worth noting that there are some other, quite different structural material elsewhere in nature, in plants, sea-shells etc, but they are beyond the scope of this article.

Regarding the HA/collagen/water composites that make up our body's structural materials, at one extreme we have tooth enamel, which has 95% HA by weight and no living cells inside it to create porosity. This enables it to achieve a stiffness three times that of bone, but at the expense of toughness and strength. Its toughness is only slightly higher than that of pure HA and its tensile strength is only one quarter that of bone. This is a material which is only suitable as a surface layer and not as a bulk load-bearing material. Using less HA and more collagen, Nature has produced a spectrum of materials with decreasing strength and increasing toughness, including dentine, bone and antler. The way in which strength and toughness are juggled to produce materials with different functions has been very well discussed by Curry [2].

Researchers have tried to imitate nature, making artificial composite materials using HA in conjunction with polymers such as polyethylene [3]. The resulting mechanical properties have been much worse than those of cortical bone. Why is this? A key feature is the scale of the structures involved, as discussed in the next two sections.

3. The Nano Scale

One difference between bone and these artificial materials is the scale at which the composite structure is achieved. Some simple calculations can demonstrate this, as follows. The ideal, theoretical strength of a material, essentially the strength of its atomic bonds, can be estimated as a function of its Young's modulus. A suitable value for HA is E/30, which is about 5,500MPa. It is very difficult to achieve this strength in practice, because HA has very low toughness, so even tiny defects and cracks will compromise its strength, causing a failure by brittle fracture. We can estimate the stress for brittle fracture, σ_f, as a function of the length a of a crack or defect in the material:

$$\sigma_f = \frac{K_{IC}}{\sqrt{\pi a}} \tag{3}$$

This equation is approximate – for a more precise estimate we would need to take account of the shape of the crack – but it is sufficient for our present purpose. As fig.1 shows, the fracture stress rises rapidly with decreasing crack length, becoming equal to the idea strength at a crack length of 2.6nm. It can be no coincidence that this is very similar to the diameter of HA crystals in bone, which are typically 5nm across. This implies that optimum strength of the material can be achieved because the individual crystals are too small to contain damaging defects. This is the essential principle on which nano-composite materials are based. The HA particles used in artificial composites are typically 1-10μm in size, [3] implying a maximum theoretical strength of the order of 100MPa, even before the collagen is taken into account.

Problems arise with nanomaterials when you try to make big pieces, which will have big defects in them. In bone, the HA crystals are separated by surrounding them with collagen, thereby reducing strength and stiffness. Further compromises are needed to ensure reasonable properties in three dimensions, which implies that some HA fibres will lie in off-axis orientations. It's not all bad news, however, because the addition of collagen increases toughness. Energy can be dissipated in the collagen in plastic deformation and viscous flow, the physical manifestation of which is blunting of the crack tip.

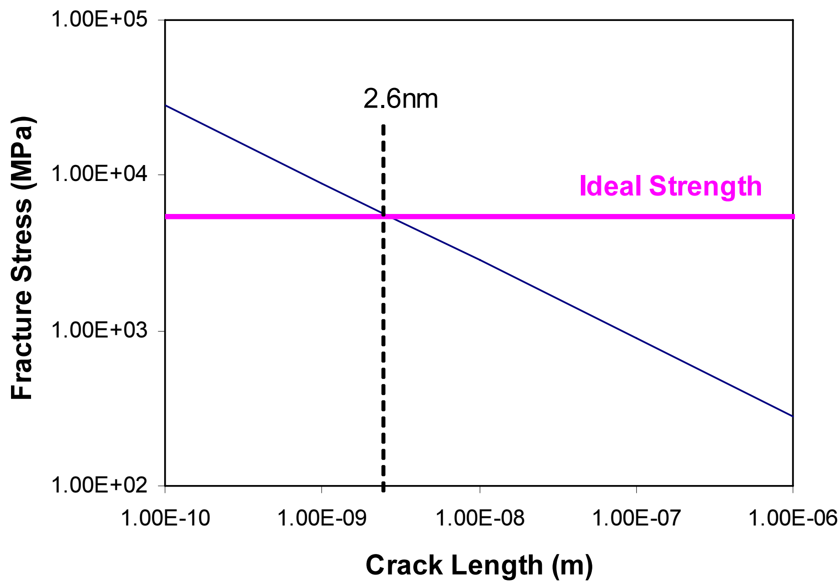

Figure 1: Theoretical analysis of hydroxyapatite shows that it reaches its ideal strength in crystals less than a few nanometres in size.

Thanks to some recent investigations into the mechanisms of toughening (discussed in the next section), we can estimate that the addition of collagen to HA improves its toughness from 0.5MPa(m)$^{1/2}$ to approximately 2MPa(m)$^{1/2}$; during aging this figure reduces to about 1MP(m)$^{1/2}$. Further improvements in toughening are achieved by introducing structure on a larger scale into the material.

4. The Micro Scale

Nanocomposites need to have some structure also at a larger scale in order to achieve reasonable properties. In the case of our hard tissues this happens at the scale of a few hundred microns, through the presence of osteons, plexiform bone units, enamel prisms etc. We can see the effectiveness of this microscopic structure in the change in K_{IC} with

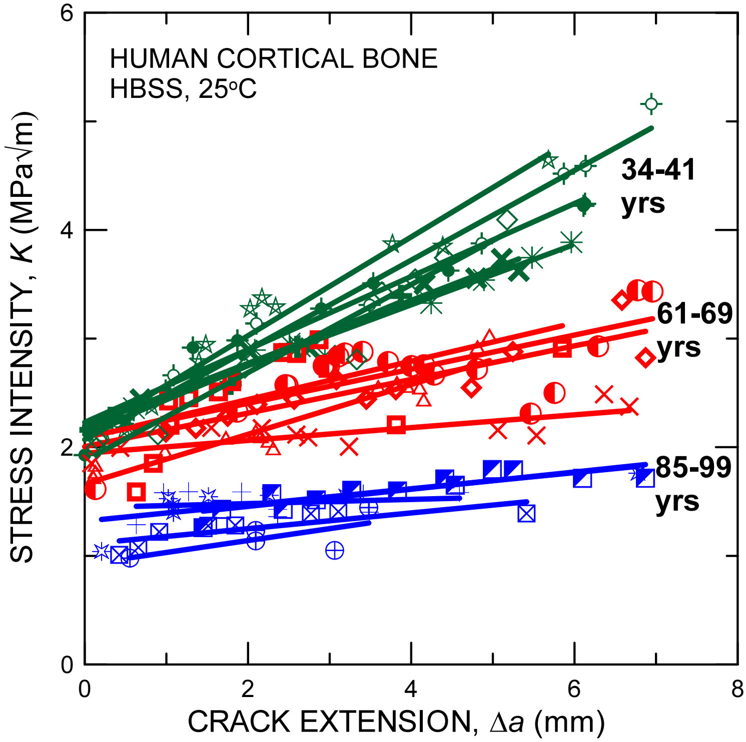

Figure 2: Data from Nalla et al [4] showing R-curve toughening for bone of different ages.

crack length – the so-called resistance curve or R-curve. Fig.2 shows an example, due to Nalla et al [4]; clearly K_{IC} is not a constant in this material. The reason for the increase in toughness with crack length is that, as the crack grows, it encounters features in the microstructure which make further growth more difficult. Extrapolating the data of fig.2 to zero crack length gives us an idea of the intrinsic toughness, i.e. the toughness of the underlying nanocomposite; this is where I obtained the values quoted in the previous paragraph. As the crack grows by a few millimetres, its toughness increases to as much as $5\text{MPa(m)}^{1/2}$ (less so for older people and those with osteoporosis). This increase is due to several different mechanisms, the understanding of which is a subject of ongoing research. For example Nalla et al argue that the major contribution comes from uncracked ligaments of material behind the crack tip, whilst others emphasise the role of microdamage in the region ahead of the crack tip. The main point is that there is a region of the order of a millimetre surrounding the crack tip in which tens or hundreds of structural units exist and are responsible for various toughening mechanisms.

There is a simple calculation which can be used to find the so-called 'critical distance' L, which tells us, without getting involved in the details of toughening mechanisms, the length scale at which toughness is achieved [5]. It is a function of the material's toughness K_{IC} and tensile strength σ_u:

$$L = \frac{1}{\pi}\left(\frac{K_{IC}}{\sigma_u}\right)^2 \tag{4}$$

The value of L turns out to be around 200-400μm in all types of bone, and also for tooth enamel, reflecting the microstructures that exist in these materials.

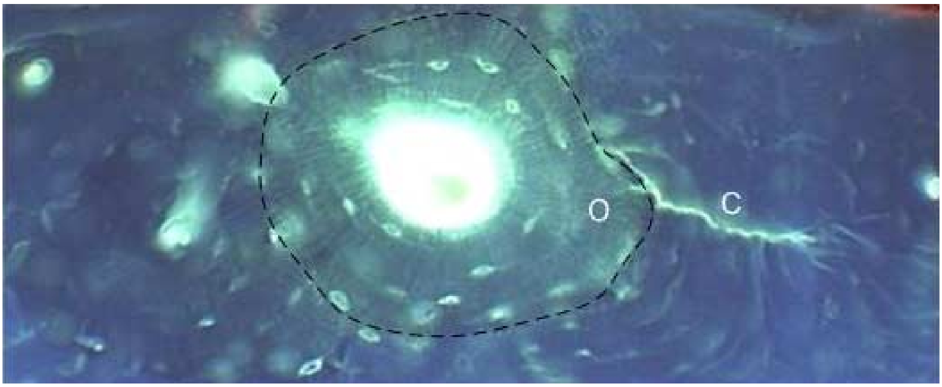

Figure 3: A small fatigue crack C, approximately 100μm long, stops growing when it encounters the cement line surrounding an osteon O. Photograph from O'Brien et al [6].

5. Fatigue and Repair

Microstructural features such as osteons are also very instrumental in improving long-term fatigue resistance; fatigue cracks tend to stop when they hit the cement lines surrounding osteons, (see fig.3) and by this means most of the fatigue cracks never grow beyond a length of 100μm. At this length the cracks can be repaired by BMUs – systems of osteoclast and osteoblast cells which remove damaged bone in tunnels of diameter 200μm, filling in the tunnels to produce new osteons. The size of these replacement units just matches the size of the fatigue cracks which need to be removed.

If bone did not repair itself, it would fail by fatigue after a relatively short time, even for people carrying out normal everyday activities. This fact is not immediately obvious when you look at the data from fatigue tests. The problem is that the fatigue strength measured from small test specimens in much higher than the strength of larger volumes such as whole bones. This is another example of the importance of size scale effects; it can be analysed using the well-known Weibull method, which is based on the idea that failure occurs from the weakest location in a material whose properties have some statistical distribution. We can predict the effect of stressed volume on the fatigue strength, defined as the stress range causing failure in a certain number of cycles [7]. Given a bone such as the tibia, for which stress varies from place to place and varies also depending on the type of exercise undertaken, we can predict the probability of failure as a function of time.

Fig.4 shows results for an extreme case – military recruits undergoing a very strenuous training regime, but even for more normal usage the predictions show that all bones will fail within a relatively short time period. Introducing the repair function, which in this prediction is imagined to start at time zero, shows how effectively it can prevent failure from occurring [8].

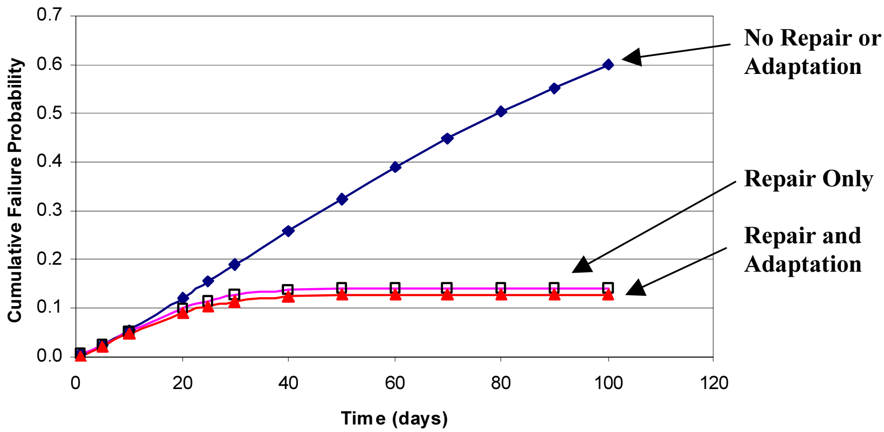

Figure 4: Predictions of fracture probability in the human tibia as a function of time during strenuous exercise, including the effects of repair and adaptation [8].

6. Conclusions

1) Bone is not as good as many engineering materials. Metal alloys such as titanium have better mechanical properties, are biocompatible and could last forever subjected to human body loadings without failure.

2) What is clever about bone is that it achieves moderately good structural properties with the very poor materials which are available, namely hydroxyapatite and collagen. This is achieved by making a nanocomposite, crucially keeping the size of HA crystals so small that their ideal strength can be achieved.

3) When this nanocomposite is scaled up to the size of a whole bone, further structure is needed at the hundred micron scale. The purpose of this structure is to increase toughness via various different mechanisms, and to trap growing fatigue cracks, keeping them small enough to be repaired.

References

[1] Alexander RM: Journal of Theoretical Biology 109 (1984), 621-636
[2] Curry JD: Journal of Biomechanics 12 (1979), 313-319
[3] Wang M, Joseph R, Bonfield W: Biomaterials 19 (1998), 2357-2366
[4] Nalla RK, Kruzic JJ, Kinney JH, Ritchie RO: Bone 35 (2004), 1240-1246
[5] Taylor D: *The Theory of Critical Distances: A New Perspective in Fracture Mechanics*. Oxford, UK, Elsevier, 2007
[6] O'Brien FJ, Taylor D, Lee TC: Journal of Biomechanics 36 (2003), 973-980
[7] Taylor D: Journal of Theoretical Biology 206 (2000), 299-306
[8] Taylor D, Casolari E, Bignardi C: Journal of Orthopaedic Research 22 (2004), 487-494

Medicine Meets Engineering
J. Hammer et al. (Eds.)
IOS Press, 2008

Bone strength in pure bending: Bearing of geometric and material properties

Werner WINTER [1]

Abstract. Osteoporosis is characterized by decreasing of bone mass and bone strength with advanced age. For characterization of material properties of dense and cellular bone the volumetric bone mineral density (vBMD) is one of the most important contributing factors to bone strength. Often bending tests of whole bone are used to get information about the state of osteoporosis. In a first step, different types of cellular structures are considered to characterize vBMD and its influence to elastic and plastic material properties. Afterwards, the classical theory of plastic bending is used to describe the non-linear moment-curvature relation of a whole bone. For bending of whole bone with sandwich structure an effective second moment of area can be defined. The shape factor as a pure geometrical value is considered to define bone strength. This factor is discussed for a bone with circular cross section and different thickness of cortical bone. The deduced relations and the decrease of material properties are used to demonstrate the influence of osteoporosis to bone bending strength. It can be shown that the elastic and plastic material properties of bone are related to a relative bone mineral density. Starting from an elastic-plastic bone behavior with an constant yield stress the non-linear moment-curvature relation in bending is related to yielding of the fibres in the cross section. The ultimate moment is characterized by a shape factor depending on the geometry of the cross section and on the change of cortical thickness.

Keywords. Osteoporosis, Bending strength, elastic-plastic behavior

Introduction

The incidence of osteoporosis continues to increase with progressively aging population. Currently, it is estimated that over 200 million people worldwide have osteoporosis [1]. The reduction in bone material parameter associated with the disease markedly increases the risk of skeletal and non-skeletal fractures. All the fractures of wrist, ribs, vertebrae and hip are associated with considerable morbidity, a decline in quality of life, and increased mortality (see Fig. 1). The dramatic increase in fracture risk is strongly related to a deterioration of bone's mechanical competence, which itself is determined by bone structural properties and intrinsic material properties. Structure properties include features such as bone size, bone geometry and also microstructural properties such as bone porosity or bone density [2].

[1]Corresponding Author: Dr.-Ing. Werner Winter, Institute of Applied Mechanics, University of Erlangen-Nuremberg, Egerlandstraße 5, D-91058 Erlangen, Germany; E-mail: winter@ltm.uni-erlangen.de.

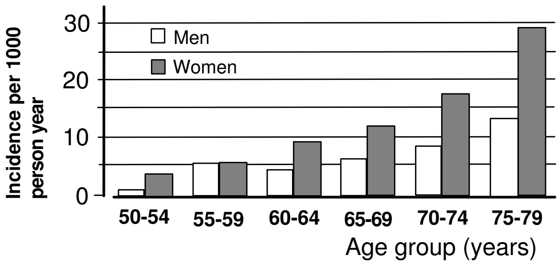

Figure 1. Incidence of vertebral fractures in women and men by age group. Reproduced from [3]

The volumetric bone volume mineral density (vBMD) serves as a surrogate measure for mechanical competence of bones and is used as direct measure of an individual's fracture risk. Risk assessment is focused on sites rich in trabecular bone, such as the spine, the intertrochanteric region of the femur or the distal radius.

The femur and the distal radius are primary loaded through bending moments. Thus, usually 3-point bending test or 4-point bending test of whole bones are carried out for characterization of the state of osteoporosis (see Fig. 2a). By means of the force-displacement curve of the bending test bone's mechanical competence is discussed. Mostly the items of the classical elastic theory for bending of beams such as the second moment of area (also called: moment of inertia of the cross section), bone strength, limit load up to yielding and maximal load (see Fig. 2b). The fracture risk is appraised by means of bone density whereas the thickness and density of the cortical bone plays a significant rule. Thus, the aim of this paper is to put out the influence of cortical and trabecular bone density and the influence of geometrical properties such as whole bone geometry to the load bearing behavior in view of bending in the elastic-plastic range.

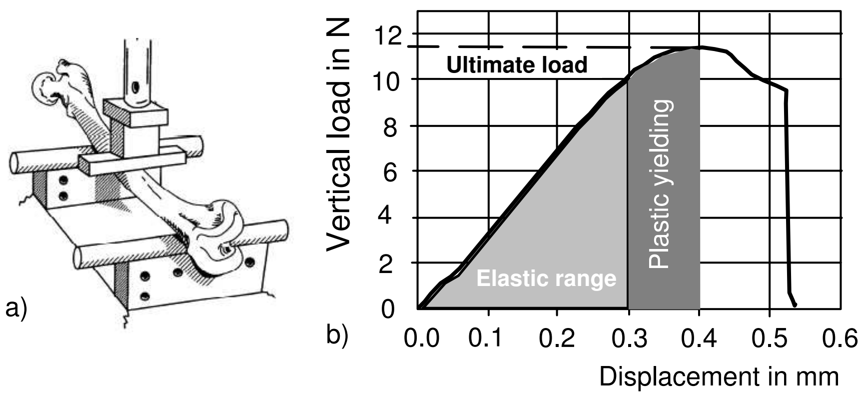

Figure 2. Whole bone: a) 3-Point bending test (schematical); b) Force-displacement curve of a whole bone specimen (3-Point bending test). Reproduced from [4,5]

1. Relative volumetric bone mineral density

For the bone density of the rigid bone the item bone volumetric bone mineral density (b-vBMD)

$$\text{b-vBMD} = \frac{m_b}{V_b} \tag{1}$$

is adopted wheras m_b is the bone mass and V_b is the bone volume. For a bone with pores a smeared bone density (s-vBMD)

$$\text{s-vBMD} = \frac{m_b}{V_b + V_p} \tag{2}$$

can be used with V_p as the volume of the pores. With the porosity (POR)

$$\text{POR} = \frac{V_p}{V_b + V_p} \tag{3}$$

the relative volumetric bone mineral density r-vBMD

$$\text{r-vBMD} = \frac{V_b}{V_b + V_p} = 1 - \frac{V_p}{V_b + V_p} = 1 - \text{POR} = \frac{\text{s-vBMD}}{\text{b-vBMD}}. \tag{4}$$

can be specified.

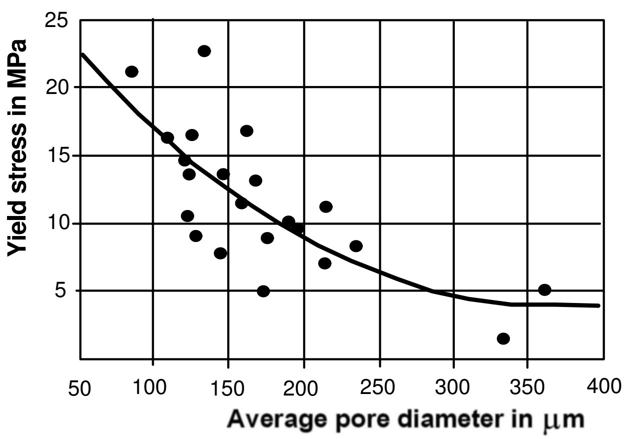

Figure 3. Cortical bone and pore size: Yield stress depending on pore size (porosity). Reproduced from [6]

2. Related elastic-plastic material parameters

In aged-related osteoporosis the elastic and plastic material properties change in view of pores. This change of yield stress depending of pore size is depicted in Fig. 3. Similarly the elastic bone material properties depend on the porosity. Mostly the Young's modulus is regarded and it is assumed that the Poisson's ratio ν^e doesn't change. If we assume for dense bone an ideal Young's modulus E_b and an ideal yield stress σ_{ys_b} we can formulate related or relative material properties. Using the relative volumetric bone mineral density r-vBMD in Eq. (4) a related or relative Young's modulus $E_r = \frac{E}{E_b}$ can be defined. For the dependence of the relative Young's modulus on the r-vBMD in cellular materials with $0 <$ r-vBMD < 0.4 the power function

$$E_r = \frac{E}{E_b} = B\,(\text{r-vBMD})^{\alpha} \tag{5}$$

is often used with the material properties B and α. In order to cover the complete range $0 <$ r-vBMD ≤ 1.0 of the r-vBMD the function

$$E_r = \frac{E}{E_b} = \frac{(\text{r-vBMD})^{n^e}}{(3 - 2\,\text{r-vBMD})^{m^e}} \tag{6}$$

is assumed for the related or relative Young's modulus E_r and

$$\sigma_{ys_r} = \frac{\sigma_{ys}}{\sigma_{ys_b}} = \frac{(\text{r-vBMD})^{n^p}}{(3 - 2\,\text{r-vBMD})^{m^p}} \tag{7}$$

for the related or relative yield stress σ_{ys_r}, respectively. The exponents n^e, m^e and n^p, m^p can be used to adapt real bone behavior.

3. Bending in the elastic range

As is generally known from the classical theory of beams that in pure bending (the bending moment is constant) the strain $\varepsilon(z)$ is related to the radius of curvature R_c and the curvature κ, respectively. Assuming small strains one gets

$$\varepsilon(z) = \frac{z}{R_c} = \kappa\, z \tag{8}$$

for the distribution of strains in a cross section. Is the strain $\varepsilon(R) = \kappa\, R$ (R : radius of the whole bone, see Fig. 4a) smaller than the elastic strain limit ε^e the behavior is a pure elastic behavior. From Eq. (8) the elastic limit curvature κ^e follows

$$\kappa^e = \frac{\varepsilon^e}{R}. \tag{9}$$

Assuming linear elasticity with the Young's modulus E_c for the cortical bone and Young's modulus E_t for the trabecular bone inside the whole bone (see Fig. 4b) over the relation for the brending moment M

$$M = \kappa \left[\int_{A_t} E_t\, z^2 dA_t + \int_{A_c} E_c\, z^2 dA_c \right]. \tag{10}$$

(A_c: cross section of the cortical bone; A_t: cross section of the trabecular bone) and

$$M = \kappa\, E_c \underbrace{R^4\, \frac{\pi}{4}[1 - (1 - \frac{c}{R})^4] \left[1 + \frac{E_t}{E_c} \frac{(1 - \frac{c}{R})^4}{[1 - (1 - \frac{c}{R})^4]} \right]}_{\text{effective second moment of area}} \tag{11}$$

an effective second moment of area I_{eff}

$$I_{eff} = R^4 \, \frac{\pi}{4}[1-(1-\frac{c}{R})^4] \left[1+\frac{E_t}{E_c}\frac{(1-\frac{c}{R})^4}{[1-(1-\frac{c}{R})^4]}\right] \tag{12}$$

can be defined whereas c is the thickness of the cortical bone (see Fig. 4b and c). The product $E_c \, I_{eff}$ is also referred to as the effective flexural rigidity or effective bending stiffness.

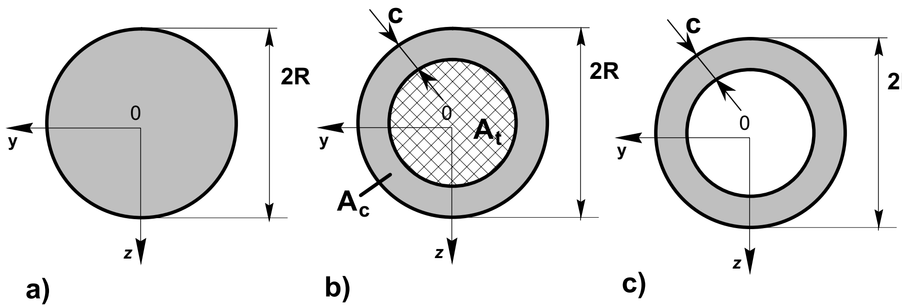

Figure 4. Circular cross section for whole bone: a) Solid cross section; b) Cross section with cortical and trabecular bone (sandwich type bone); c) Thin-walled cross section without trabecular bone

Since a whole bone with brittle-rigid behavior fails by a limit curvature κ^e, Eq.(11) leads to the elastic limit moment M_f^e (Failure moment)

$$M_f^e = \varepsilon_f^e \, E_c \, R^3 \, \frac{\pi}{4}[1-(1-\frac{c}{R})^4] \left[1+\frac{E_t}{E_c}\frac{(1-\frac{c}{R})^4}{[1-(1-\frac{c}{R})^4]}\right], \tag{13}$$

whereas ε_f^e is a material property to characterize brittle bone behavior.

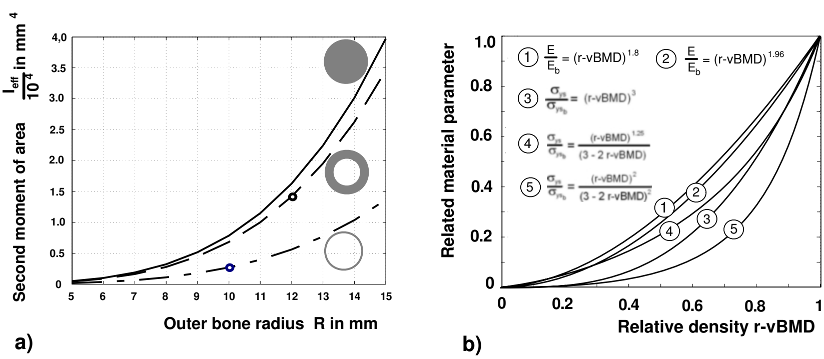

Figure 5. Second moment of area and related material properties: a) Second moment of area depending on the radius of the whole bone and the thickness of cortical bone; b) Young's modulus and yield stress depending on the relative volumetric bone density

In Fig. 5a the influence of osteoporosis on the effective second moment of area due to the change of the radius R and the change of the thickness of the cortical bone is depicted. The small circles demonstrate the change of the second moment of area due to a change of the outer bone radius from 12 mm to 10 mm and a change of cortical thickness as is shown in Fig. 5a, too. For approximation of the related material parameters Fig. 5b shows different curves for the related Young's modulus and the related yield stress depending on the relative volumetric bone density r-vBMD. A nonlinear relation between the material parameters and the relative bone density can be seen.

4. Loading part of trabecular bone

In osteoporosis a change in thickness of cortical bone and density of the trabecular part of the whole bone can be observed. This change effects the effective second moment of area as shown in Eq. (12). The factor in the square bracket in Eq. (12) clarifies the stiffness part of the trabecular bone and is depending on the cortical thickness or the geometrical ratio $\frac{c}{R}$ and the Young's modulus of cortical and trabecular bone or the material ratio $\frac{E_t}{E_c}$. The influence of osteoporosis is demonstrated in Fig. 6 for a whole bone with a constant outer radius. For small values of the ratio $\frac{c}{R}$ the loading part of the trabecular bone to the part of cortical bone grows, that means that during the process of osteoporosis the material properties of the trabecular bone become an important factor.

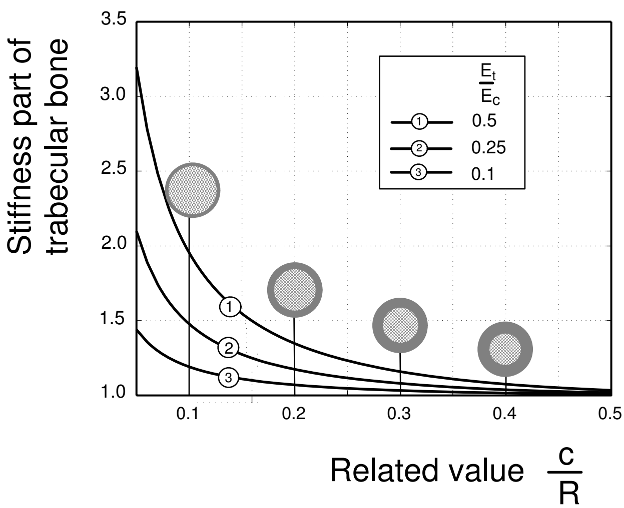

Figure 6. Loading part of trabecular bone due to osteoporosis

5. Bending in the elastic-plastic range

As shown from experiments of real bone material the healthy bone can be deformed in the plastic range. Thus, assuming an elastic-plastic material behavior the whole bone can be loaded beyond the elastic limit of curvature κ^e in Eq. (9). If the fibres at the top and the bottom of the beam reach the limit strain $|\varepsilon^e|$ plastic strains occur in the outer fibres whereas the yield stress σ_{ys_c} is constant. Fig. 7a shows the elastic range and the plastic zones and in Fig. 7b the distribution of stress is depicted. In the ultimate state one-half of the area is loaded in tension and compression. Thus, the ultimate moment M^U can be calculated whereas for the solid cross section in Fig. 4a the ultimate moment M^U yields $M^U = \frac{16}{3\pi} M^e = 1,69\, M^e$.

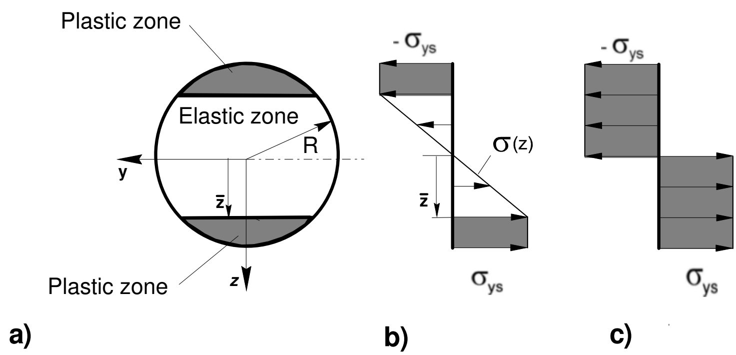

Figure 7. Plastic zones in a solid circular cross section: a) Plastic zones in the cross section; b) Distribution of stress; c) Distribution of stress in the plastified cross section

The shape factor m specifies the transition from the pure elastic state to the ultimate plastic state which is defined as the ratio of the ultimate plastic moment M^U to the elastic moment M^e in Eq. (13). Substituting the product $\varepsilon^e\, E_c$ by the yield stress σ_{ys_c} one gets

$$M^e = \sigma_{ys_c}\, R^3\, \frac{\pi}{4}[1-(1-\frac{c}{R})^4]\left[1+\frac{E_t}{E_c}\frac{(1-\frac{c}{R})^4}{[1-(1-\frac{c}{R})^4]}\right]. \tag{14}$$

For a whole bone with circular cross section the shape factor m yields depending on the curvature $\kappa > \kappa^e$

$$m(\frac{\kappa}{\kappa_e}) = \frac{M^U}{M^e} = \frac{2}{3\pi}\left[5-2(\frac{\kappa_e}{\kappa})^2\right]\sqrt{1-(\frac{\kappa_e}{\kappa})^2} + \frac{2}{3\pi}\left[3\frac{\kappa}{\kappa_e}\arcsin(\frac{\kappa_e}{\kappa})\right] \tag{15}$$

with the ultimate $m^U = \frac{16}{3\pi} = 1.69$ and for a whole bone with a thin thickness of the cortical bone $c << R$

$$m(\frac{\kappa}{\kappa_e}) = \frac{2}{\pi}\left[\sqrt{1-(\frac{\kappa_e}{\kappa})^2} + \frac{\kappa}{\kappa_e}\arcsin(\frac{\kappa_e}{\kappa})\right] \tag{16}$$

with the ultimate value $m^U = \frac{4}{3\pi} = 1.27$.
By approximation the shape factors in Eq. (15) and Eq. (16) can be replaced with adequate accuracy by the function

$$m(\frac{\kappa}{\kappa_e}) = 1+\beta\left[1-\left(\frac{\kappa_e}{\kappa}\right)^2\right] \tag{17}$$

whereas the parameter β lies between $0.27 \leq \beta \leq 0.69$ for the whole bone with thin cortical thickness and whole bone with solid cross section, respectively. Assuming a material behavior depicted in Fig. 8a for the fibres in the whole bone one gets moment-curvature curves as shown in Fig. 8b. The curves show nonlinear characteristic influenced by the geometry of cross section (see Fig. 8b, curve 1).

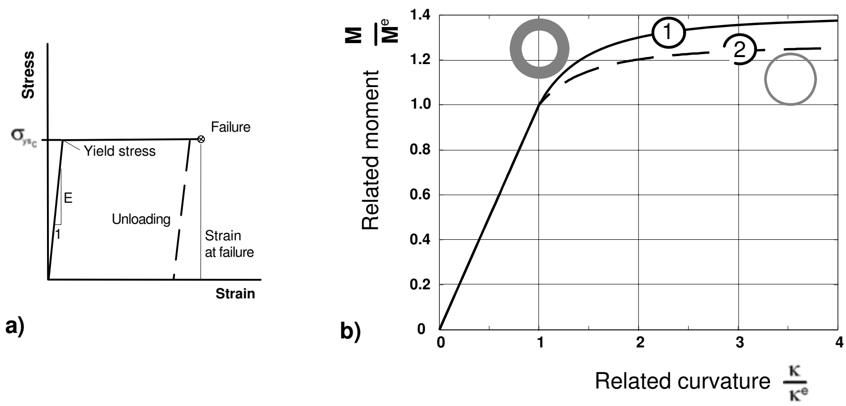

Figure 8. Moment-curvature curves due to elastic-plastic bending: a) Elastic-plastic material behavior in a fibre of the cross section; b) Moment-curvature curves influenced by the change of the shape factor due to osteoporosis

In particular the decease of the thickness of the cortical bone provokes a reduction of the shape factor m (see Fig. 8b, curve 1 and curve 2). Further, the nonlinear moment-curvature curves in Fig. 8b are related to the process of yielding in the cross section and don't reflect material yielding with hardening. Resulting the failure of a whole bone is not a stress problem it is a strain problem. Today no experimental verified value for the whole bone exists and for the change due to osteoporosis, too.
The aim of this project was to compile elastic and plastic parameter in view of geometry and bone material behavior to describe pure bending of circular cross section. These results can be used as basics for calculation of force-displacement behavior of the 3-Point- and 4-Point bending test. This will be done in a further work.

References

[1] C. Cooper: Epedemiology of osteoporosis, *Osteoporos Int* **9** (Suppl 2) (1999), S2–S8.

[2] C.R. Russo, F. Lautetani, E. Seeman, B. Bartali, S. Bandinelli, A. Di Iorio, J. Guralnik, L. Ferrucci: Structural adaption to bone loss in aging men and women, *Bone* **38** (2006),112–118.

[3] J.-Y. Reginster, N. Burlet: Osteoporosis: A still increasing prevalence, *Bone* **38** (2006), S4–S9.

[4] K. Srømsøe, A. Høsert, A. Alho, W.I. Kok: Bending strength of the femur in relation to non-invasive bone mineral assessment, *J. Biomechanics* **28** (7) (1995), 857–861.

[5] J.L. Schriefer, A.G. Robling, S.J. Warden, A.J. Fournier, J.J. Mason, C.H. Turner: A comparsion of mechanical properties derived from multiple skeletal sites in mice, *J. Biomechanics* **38** (2005), 467–475.

[6] P. Augat, S. Schorlemmer: The role of cortical bone and its microstructure in bone strength, *Age and Ageing* **35-S2** (2006), ii27-ii31.

Medicine Meets Engineering
J. Hammer et al. (Eds.)
IOS Press, 2008

Bone quality issues and matrix properties in OP cancellous bone

P. ZIOUPOS [a] [1], R. COOK [b], R.M. ASPDEN [c] and A.M. COATS [d]
[a] *Dept. Materials and Applied Science, Cranfield University, Shrivenham, UK*
[b] *Dept. Oral Rehabilitation, Univ. of Dunedin, New Zealand*
[c] *Orthopaedic Surgery, Univ. of Aberdeen, Aberdeen, Scotland, UK*
[d] *Dept. Chemistry, Univ. of Aberdeen, Aberdeen, Scotland, UK*

Abstract. There is increasing evidence nowadays that diseases or conditions, like osteoporosis (OP), which are conventionally defined in terms of bone quantity/ mass, are also associated with concomitant changes at the bone matrix level. The present study examined the composition, density and mineral content of OP cancellous bone at the tissue level and the hardness values at the trabecular level to establish correlations between these variables. The results showed that changes in porosity (Bone volume/Tissue volume) are accompanied by changes in mineral content and in the hardness of individual trabeculae. In other words in OP there are both quantitative and qualitative effects that take place with the progress of this condition.

Keywords. Cancellous bone, mass, density, quality, osteoporosis

1. Introduction

Osteoporosis (OP) is commonly defined as a condition where there is 'less bone, but whatever bone there is, is normal'. The WHO criterion for OP, for instance, is on the basis of a bone mineral density (BMD) value ≤ by 2.5 SD of the value of a normal adult of the same sex [1]. The fear is that such rules address the issue of OP only in quantitative terms and have in the long term 'conditioned' the mind of many (including clinicians) to think only in terms of bone mass/ density, rather than actual bone fragility. As shown in Figure 1 bone density is a major factor in determining cancellous bone stiffness and strength, but even when trabecular orientation, skeletal site, structural design (struts vs. plates, open vs. closed cell architecture) are controlled the percentage of variability that can be explained this way rarely exceeds R^2=0.80.

The fact that there must be other factors at play is deduced from a variety of clinical observations. Older patients are more susceptible to fracture than younger patients with the same BMD value [2]. Individuals with one or more spinal fractures are more likely to have a subsequent fracture and more interestingly individuals at the higher tertile of bone mass with a fragility fracture were more likely to develop another fracture than individuals at a lower tertile of bone mass who had sustained no previous fracture [3]. Assessment of bone status by means of quantitative ultrasound (QUS), which measures a combined effect of structure-mass-material quality, showed that

[1] Corresponding Author: Dr P. Zioupos, Biomechanics laboratories, Dept. of Materials and Applied Science, Cranfield University, Shrivenham SN6 8LA, UK; E-mail: p.zioupos@cranfield.ac.uk

individuals with OP fractures, matched for bone mass, had in fact comparatively lower QUS velocities [4]. Fluoride treatment has been shown to increase bone mass in the spine, but does not improve vertebral fracture rates [5]. Age, as a factor, has shown that clinical fractures incidence is not related to bone density for women over 70 [6].

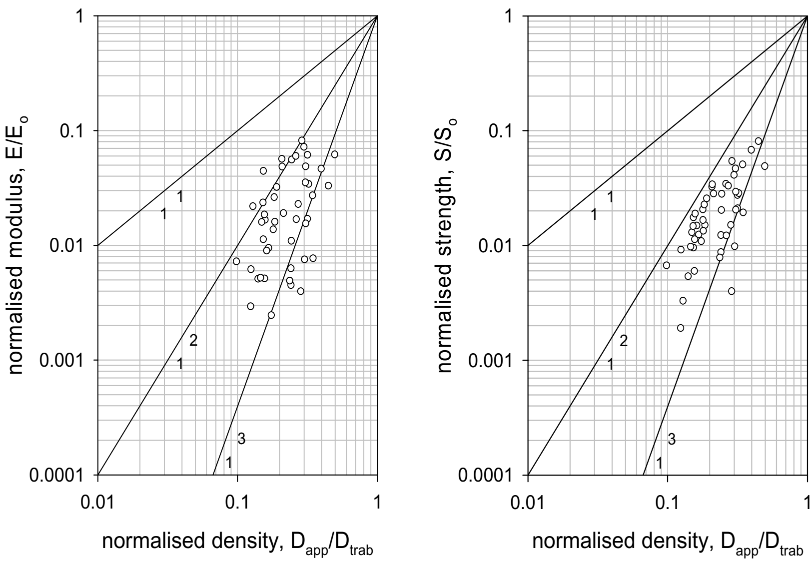

Figure 1. Elastic modulus and strength of femoral head cancellous bone cores aligned along the predominant trabecular direction (groups-2 samples of the present study) vs. normalized density values. For normalization the modulus and strength of bone matrix was taken to be E_o=18 GPa, S_o=190 MPa. Normalized density is D_{app}/D_{trab}= (apparent density / trabecular density) as measured for each specimen. Log-log plots show that the dependency of modulus and strength vs. density is a power between 1.5 and 3.

In addition to these controversial clinical observations, increasingly nowadays laboratory evidence accumulates that there are both structural and material alterations in the bone matrix of OP and ageing bone [7, 8]. Ageing human bone has been shown to change in structure, architecture, physicochemical and material characteristics with age [8]. In other words, changes are both of a quantitative and qualitative kind.

The majority of the published biomechanical studies of the properties of OP cancellous bone were of the structural kind attempting to relate macromechanical data to the architecture and the apparent density of the tissue. Very few studies have considered the bone matrix (trabecular material=hard tissue) properties and the effect they may have at the structural level and those they did so, were computational and thus unable to experimentally verify any hard tissue level effects [9, 10].

There have been few direct comparisons, for instance, between bone composition and mechanical properties at the same local sites and at the micromechanical level. The present study provides a detailed examination of these material/quality aspects of OP bone and attempts to establish trends with the severity of OP, the severity being defined by the porosity of the tissue. For this aim, we employed an examination of the mineral content, the density of the structure, and that of the trabecular material, the trabecular tissue properties by microhardness measurements and the composition by electron probe microanalysis (EPMA) to try to correlate directly the local composition of the bone matrix with the hardness values.

2. Materials and methods

In total 67 femoral heads were collected over a period of 4 years from fracture neck of femur patients from three major UK NHS hospitals (GWH-Swindon, 12♀-1♂; ARI-Aberdeen, 14♀-10♂; GRH-Gloucester, 21♀-9♂) and were analysed in two independent research centres in the UK. *In group-1*: 25 cores were taken (GRH-ARI) from 25 different OP femoral heads and were analysed whole without further dissection in terms of mineral content, trabecular hardness and density values. *In group-2:* 40 cylindrically shaped cores were drilled from 30 femoral heads (GWH) and were analysed whole in terms of elastic modulus, strength, mineral content and density values. *In group-3:* A balanced test was performed where 24 cylindrically shaped cores (ARI) were drilled from the superior and the inferior site of 12 femoral heads from 12 patients (6♀, 6♂, age matched) to coincide with areas that experience higher or lower loads respectively. These cores were also cut diametrically along their length and dissected transversely up to five levels (Figure 2) from the articular surface [11].

Apparent (D_{app}=wet weight/ specimen volume), trabecular material (D_{trab}=wet weight/ trabecular volume) densities, porosity ($P=1- D_{app}/ D_{trab}$) and the mineral content (MinC) were determined by well-established methods [12, 13] for all samples whether full cores or small semi-circular cuts. Microhardness measurements and EPMA analysis were carried out for groups 1 and 3 at a mid-dissection plane after the samples had been embedded in resin.

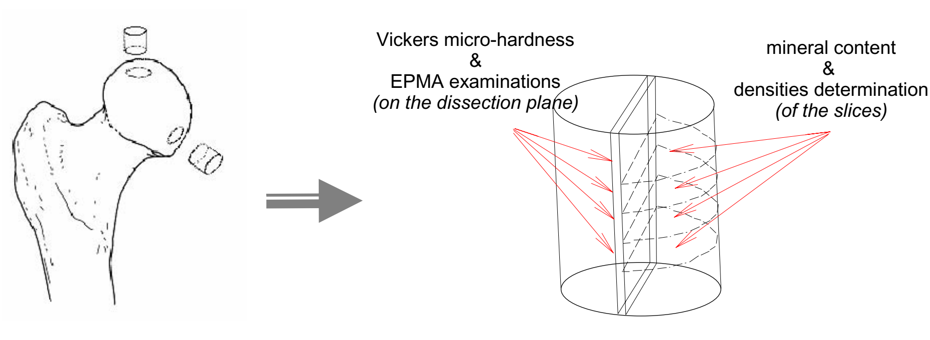

Figure 2. Collection of OP cores and dissection down the middle plane in group-3 tests.

The mineral, water and organic content were determined by using EDTA for demineralisation and measuring the wet, dry and dry demineralised weight [13]. The semi-cylindrical halfcore specimens were air-dried and embedded with their plane facing uppermost in Buehler MetSet (SW type) resin, to avoid exothermic reactions, and placed for 10-15 hours in a Buehler Vacuum impregnation machine. The moulds were then polished carefully using a purpose-built jig to expose the bone trabecular network using progressively finer grades of silicon carbide papers under continuous water irrigation. They were finally brought to a mirror finish with Struers (Struers, Glasgow, UK) alumina slurry (0.05 µm).

Vickers microhardness (VHN) of individual trabeculae was measured using an Indentec model HWDM7 testing machine at 10 and 50 grammes-force (gf) applied for appr.20 s on dry specimens at room temperature at 5 different depth levels in the bone. (Indentations were also made in the embedding resin to check for its consistency. From each indentation test an estimate value for the Young's modulus of bone *E*, can be produced using $E = 0.561 \times VHN^{0.747}$ based on previous studies [11,13], which showed a correlation between these parameters with an $R^2 = 0.95$.)

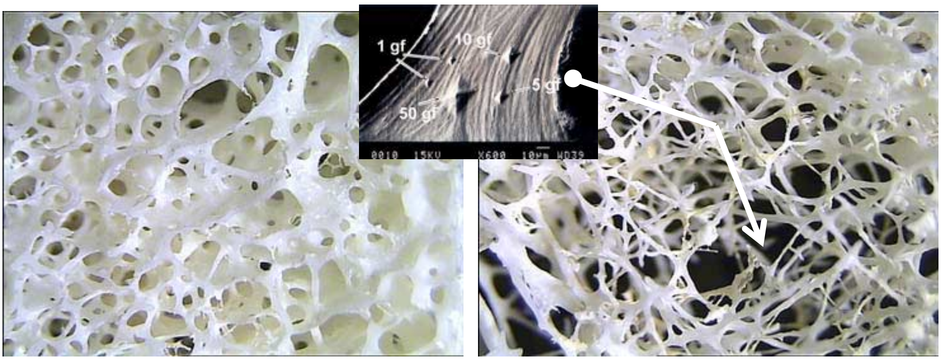

Figure 3. Cancellous bone tissue from the neck of the femur in a 54 yr old female (left) and a 74 yr old female (right). The insert shows examples of indentations performed at the trabecular level at 1, 5, 10 and 50 grams force.

EPMA measurements were made at the same sites immediately adjacent to each indentation. Calcium, phosphorus, sulphur and oxygen contents were measured. These were expressed as percentage of the total mass. A measure of the composition was obtained from the percentage by weight of the oxides CaO and P_2O_5, based on an assumed valency for each element and the stoichiometry of the mineral. For the purposes of the analysis, this is based on an ideal hydroxyapatite formula [$Ca_5(PO_4)_3OH$], one oxygen being assumed lost due to beam damage, and in this case the ideal Ca/P ratio is 1.67. The total weight percentage is a measure of the amount of material present, the remainder being porosity, and is the conventional mineralogical means of presenting the data.

3. Results & Discussion

Results within each of the 3 groups showed that there was a negative relationship between *trabecular* and *apparent* density in OP bone (Figure 4). This was a finding our group made first sometime ago [14] and we have since confirmed it to apply to normal and osteoarthritic bone too. There is no evidence in the literature that such a significant relationship has been reported before, although there is indirect evidence that the strength of cancellous bone increases with apparent density and decreases with material density [15] and similarly the cancellous Young's modulus increases with apparent density, while the trabecular material modulus decreases with apparent density [16].

Our observation is that 'the more porous the bone the higher the trabecular material density is'. This is by no means an innocuous, or trivial observation and we can illustrate why by means of Figure 5. It has been a long established belief, or better say misconception, that the transition of bone from a cortical to a cancellous form is primarily a structural adaptation. In other words, the same substance of bone can be turned into cancellous if one simply increases the pore size. To conceptualise this progression: if one was to calculate the porosity within frames '*a'* to '*d'* (Figure 5) then as apparent density increases the upper limit it reaches is that of the density of the bone material itself (~2.2 g/cm^3). This is, and by far, remote from what actually happens. Porosity appears to be calculated over an area such as in frame '*e'* where the bone *material* is in fact different.

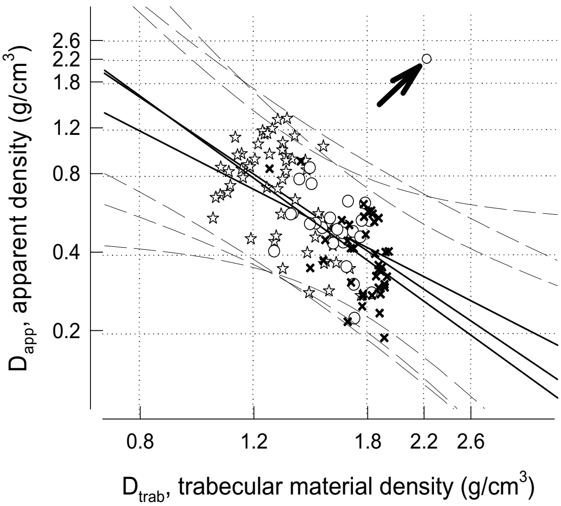

Figure 4. Apparent vs. trabecular material density in OP bone. Group-1 (circles); group-2 (crosses), group-3 (stars). Linear regression lines and the 95% prediction intervals for the data. (The arrow shows the limit of the a-d process shown in fig.5)

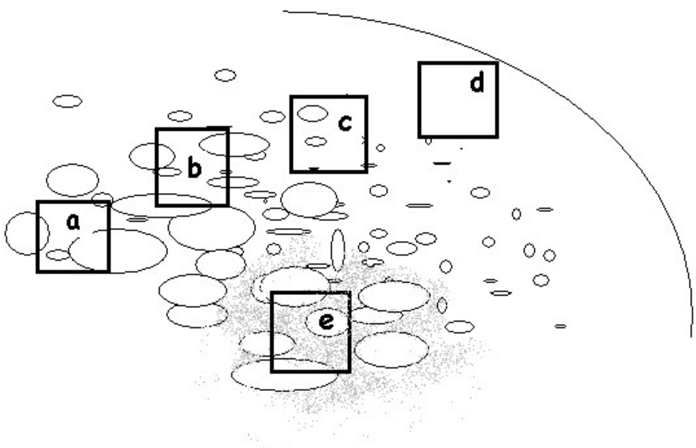

Figure 5. The physiology of cancellous bone involves material change; it is more profound than a simple structural adaptation. (Bone matrix in frame 'e shaded grey to show change in material substance)

There can be a number of possible explanations for this, but they will stay as conjectures till final clarification. We can lists two possibilities: (i) from a teleological point of view it makes sense in evolutionary terms if the less bone mass there is the denser the remaining material is to compensate and counteract the detrimental effects on the structure as a whole (assuming that bone knows what it is that is aiming for); (ii) in term of chemistry of remodelling actions it may be simply the result of an increased mineral solubility of areas of lesser density, the denser trabeculae survive as OP progresses precisely because they are denser and more resilient to the osteoclastic activity.

Age effects: these are important in terms of biomedical engineering applications and the clinical management of fractures. D_{app} decreased significantly with age as expected (P=0.05), while material density increased and the microhardness values decreased insignificantly with age (Figure 6, irrespective of sex and site of harvest).

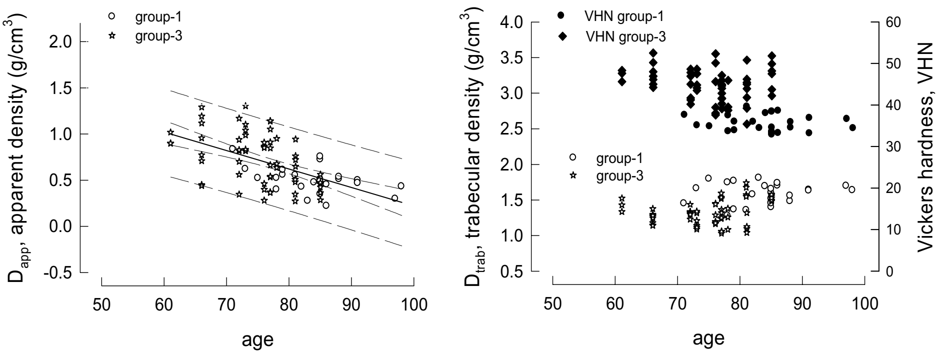

Figure 6. D_{app}, D_{trab} and Vickers hardness of cancellous bone with age.

However, careful inspection of Figures 6 and 4 reveals a contradiction: a decrease in D_{app} is concomitant to an increase in D_{trab} (Figure 4), but when plotted *vs* age (Figure 6) the data suggests that there is a decrease of VHN with an increase in D_{trab}. This is not rational as material density and VHN should go hand in hand. The conundrum is solved when one looks in group-3 data of mineral content (MinC) and VHN vs. D_{trab}.

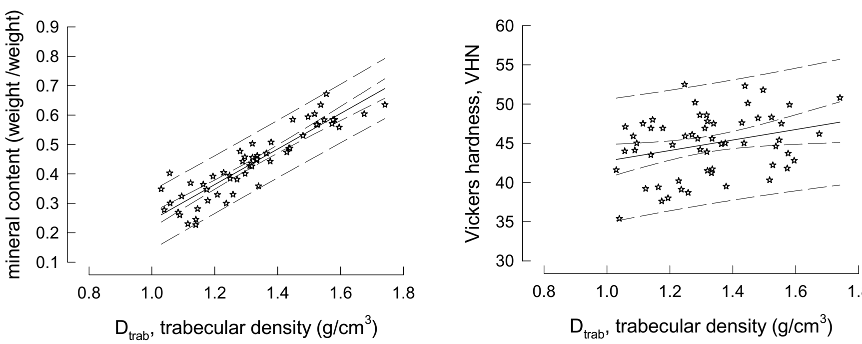

Figure 7. Both VHN and mineral content related, as expected, significantly to the trabecular material density (group-3 data). Regression lines with their 95% prediction intervals and 95% data confidence intervals.

Intra-individual effects: Group-3 tests examined a greater number of smaller subsections from within each femoral head and allowed any intra-specimen (intra-individual) variability to become apparent. By comparison, examination of results in group-1 reveals only inter-individual and generic age effects, as there was just one datum from each femoral head. Conversely, examining the data of group-3 as a function of age (Figure 6) performs an averaging of the intra-individual variations too, as it makes the data set from group-3 resemble the inter-individual variations shown by group-1 results. Figure 7 shows clearly that the increased density of the OP trabeculae is caused mostly by a higher mineral content. Consequently trabecular micro-hardness increases with increasing trabecular material density and with the mineral content. This material relationship is generic and holds true for all material samples big or small, irrespective of age, sex and site of harvest. However, the composition (Ca/P ratio), as shown by EPMA tests, was not different with age or site of harvest (inferior/superior) and there were no intra-individual effects, or correlation of Ca/P to hardness values.

The significant 'tissue level specific' alterations are worth examining further. Microhardness (and by implication tissue modulus) increases with porosity, with trabecular density, with mineral content and decreases with apparent density within each femoral head. Similarly, to the observed relationship between D_{app} vs. D_{trab} this may be due to a number of reasons and generates in itself legitimate curiosity. Why is it that denser trabeculae remain and progressively get more and more mineralised? After all mineralisation beyond a certain threshold brings about the detrimental effect of increased brittleness as it has been documented elsewhere [13]. From the mechanobiological point of view denser trabeculae may experience lesser strain, for a level of exerted stress, and this may protect them from damage and resorption. However, with the same token bone reacts positively to strain and maintains mass, and in turn, if it experiences reduced strain levels it may start resorbing.

In a similar vein, it appears that in OP the bone itself changes in a way we have already seen in ageing processes [17] by shifting its mineralisation profile to higher values and becoming more heterogeneous and nonuniform. Bone loss in OP is usually attributed to and associated with an increased bone turnover rate. The present results question what the term 'turnover rate' actually means. OP is caused by increased resorption and decreased new bone formation, which together upset the balance that maintains bone mass. But what is it primarily: a greater reduction in osteoblastic activity, or a proportionally bigger increase in osteoclastic activity? The former was the view in the early days and the latter is the prevailing belief recently [18]. One has to question then, how a proportionally faster resorption is able to shift the mineralisation profile to higher values, instead of the more logical explanation that there must be a proportionally more severe reduction in the rate of deposition of new bone.

4. Conclusions

The majority of the cancellous bone research has been concerned with deriving structural properties as a function of architecture and porosity, but there are no reports of correlations between porosity and the quality of the trabecular material. The present study: (i) confirmed that there is an inverse (negative) relationship between the *apparent* and the *trabecular material* density in cancellous bone (whether this refers to the average values for a femoral head, or to a site in the femoral head); (ii) an increase in mineral content is accompanied by an increase in material density and in the microhardness values of the tissue at any point at the microscale; (iii) meanwhile with an increase in age the average value for trabecular density increases and the average value for microhardness for the femoral head decreases, but only moderately.

The present results demand a distinction to be made between inter-individual (often age related) and intra-individual (bone regulation, site specific) effects and confirm other studies, which infer similar effects by using FEA methods [19].

Acknowledgements

The authors acknowledge the financial support of the EPSRC (GR/N33225; GR/N33102; GR/M59167), the MRC, the Sir Halley Stewart Trust and the efforts of Dr B.Li, Dr K.Winwood, Mr E.Noriega and Mrs V.Wise.

References

[1] J.A. Kanis *et al.* The diagnosis of osteoporosis. *J Bone Mineral Res.* **9** (1994), 1137-41.
[2] S.L. Hui *et al.* Age and bone mass as predictors of fracture in a prospective study. *J Clinical Invest.* **81** (1988), 1804-1809.
[3] P.D. Ross et al. Pre-existing fractures and bone mass predict vertebral fracture incidence in women. *Annals Intern. Medic.* **114** (1991), 919-923.
[4] D.B. Kimmel et al. Patellar ultrasound velocity in osteoporotic and normal subjects of equal forearm of spinal bone density. *J Bone Mineral Res.* **6** (1991), 175.
[5] M. Kleerekoper and R. Balena. Fluorides and osteoporosis. *Ann. Rev. Nutrit.* **11** (1991), 309-324.
[6] P.Gardsell *et al.* Predicting fractures in women by using forearm bone densitometry. *Calc. Tiss. Intern.* **44** (1989), 235-242.
[7] A.J. Bailey *et al.* Biochemical changes in the collagen of human osteoporotic bone matrix. *Conn. Tiss. Res.* **29** (1993), 119-132.
[8] P. Zioupos. Ageing human bone: factors affecting its biomechanical properties and the role of collagen. *J Biomater. Applic.* **15** (2001), 187-229.
[9] F.J.Hou *et al.* Human vertebral body apparent and hard tissue stiffness. *J Biomechanics* **31** (1998), 1009-1015.
[10] J Homminga *et al.* Cancellous bone mechanical properties from normals and patients with hip fractures differ on the structure level, not on the bone hard tissue level. *Bone* **30** (2002), 759-764.
[11] A.M. Coats *et al.* Material properties of subchondral bone from patients with osteoporosis or osteoarthritis by microindentation testing and electron probe microanalysis. *Calc Tiss Intern.* **73** (2003), 66-71
[12] B. Li and R.M. Aspden. Mechanical and material properties of the subchondral bone plate from the femoral head of patients with osteoarthritis and osteoporosis. *J Bone Miner. Res.* **12** (1997), 641-651.
[13] P. Zioupos *et al*. Exploring the effects of hypermineralisation by using an extreme biological example. *Conn. Tiss. Res.* **41** (2000), 229-248.
[14] P. Zioupos and R.M. Aspden. Density, material quality and quantity issues in OP cancellous bone. *Proc. Eur. Soc. Biomechanics 2000*, p.327, Dublin, Ireland.
[15] P.H.F. Nicholson *et al*. Structural and material mechanical properties of human vertebral cancellous bone. *Med Eng Physics* **19** (1997), 729-737.
[16] J. Galante *et al.* Physical properties of trabecular bone. *Calc Tiss Intern*. **5** (1970), 236-246.
[17] P.I. Croucher *et al.* Structural mechanisms of trabecular bone loss in primary osteoporosis: specific disease mechanism or early ageing? *Bone & Mineral* **25** (1994), 111-121.
[18] D.N. Kalu. Evolution of the pathogenesis of postmenopausal bone loss. *Bone* **17** (1995), S135-144.
[19] Y. Yeni *et al.* Trabecular shear stress in human vertebral cancellous bone: intra- and inter-individual variations. *J Biomechanics* **34** (2001), 1341-1346.

Author Index

This page intentionally left blank

This page intentionally left blank